Studies of the Faint Galaxy Population

Boudewijn François Roukema
Mount Stromlo and Siding Spring Observatories
Institute of Advanced Studies
Australian National University

A thesis submitted for the degree of
Doctor of Philosophy
of The Australian National University

(As of January 21, 1993, this thesis has not yet been examined.)

January 1993

Contribution of Candidate

All the work here is my own apart from any exclusions listed in the following. (Much of the use of the pronoun "we" in fact refers to myself; this is intended as a scientific "we", not a royal "we".)

The AAT observations were taken by Bruce Peterson and Joe Silk.

Bruce Peterson assisted me with defining the criteria for selecting the low surface brightness galaxies from the Schmidt plate copies, though I did the eye-searches myself. Bruce also helped me with some of the observations on the 2.3m and the 40-inch.

The N-body simulations were run by the Mike Warren, Peter Quinn, John Salmon, Wojcek Zurek collaboration. All the processing from these sets of masses, positions and velocities was done by me. A display program called "Magnum" written by PJQ was used for interactive examination of the simulations and sets of density peaks found. Bruzual's galaxy evolutionary population synthesis code was provided, naturally, by Bruzual.

Signature removed at request of author

January 21, 1993

Acknowledgements

Well, I guess I'd better put some soppy and sentimental and maybe even some scientific acknowledgements here. All those long hours partying and raging here at MSSSO require it I guess.

I certainly wish to thank Bruce Peterson and Peter Quinn for all the scientific discussions we've had. You both have your own scientific styles of discussion, which I appreciate for what they are. There have been a few difficult times, but the good times make them worth it. Thanks, Michael Gregg, for taking the time to do some pretty thorough proofreading; Mike Bessell, for putting in a few hurdles in order to make getting a thesis done a bit more challenging, but also for your support at other times; and arigato, Yoshii, for plenty of interesting discussions over the past year.

And I want to thank my officemate, Jayanne, for your companionship and our stimulating debates over these years, and the other young astronomers, Angela, who gave me the courage to start the discussion groups, Anton and Haida and Nick and Ruan and Catarina and Chris for keeping the discussion groups going, Sylvie and Stéphanie for *les transcriptions françaises,* Claudia, Dave, Jon and Daniel for your liveliness, Brett for your support and for those interesting conversations while toothbrushing, and Stuart and Ralph for your Stuartness and Ralphness.

And to KCF and Alex and Aleck and Milka and Maggie and Thelma and Peter Wood and Peter tLH and Bluey and Reet and Smetho and PJY and the others here at Stromlo, thanks too.

In the realm beyond our ivory mountain, my greatest support came from my housemates: thanks, Trudie and Antoinette and Monique and Stef and Paul and Frank and Stephen and Janée and Brett and Roger; and from the Musicians[1]: thanks for making me feel accepted, Josie, and thanks for some great tromboning together Cathy and Michael and Lucian and David, thanks Jenny and thanks too Helen and Toby and Malini and Doug and Jane and Robin and Rob and Vanessa and Markus and Michelle and Garry and thanks to Martin too.

And for your support during the last few hectic weeks, thanks Simon and Stuart.

[1] of the Belconnen variety

To Miss Judy Westwood and Mr Graham Jones,

My maths teachers,

Thanks.

There once was an observer at Stromlo,

Whose models of galaxy counts were one[2] low,

But with no L.S. Beeps,

He jumped into MIEPS,

And no longer were his models one low.

(ancient Canberran limerick)

[2]In log_{10}, allowing artistic licence.

Abstract

Recent observations of faint galaxies to $b_J \approx 28$ (e.g., Tyson & Seitzer, 1988) show an excess in number density with respect to simple flat universe models which incorporate K- and E-corrections but unevolving luminosity functions. Low q_0, high z_f models are unfavoured by recent redshift measurements, but merging dominated models and models involving differential evolution between bright and faint galaxies or a new population of faint galaxies remain consistent with the data and a flat universe.

In this thesis, observations and theory which contribute to our understanding of these faint galaxy populations are described. In chapter 2 it is shown that d_L, dV/dz, q_0, z_f, the K- and E- corrections, ϕ^*, M^*, α, and η all affect the faint number counts significantly, though not independently, while the effect of H_0 is small.

A preliminary search for low surface brightness galaxies described in Chapter 3 gave unpromising results, with a number density to $z \approx 0{\cdot}05$ of $n \approx (9 \pm 5){\times}10^{-3}h^3Mpc^{-3}$, which is about $7 \pm 4\%$ of the number density for normal galaxies in the corresponding magnitude range of $-14 \geq M_B \geq -20$ represented in a Schechter (1976) luminosity function with Efstathiou *et al.*'s (1988) parametrisation. Only about half of this low surface brightness galaxy population is likely to be excess to that represented in the Schechter function. The diameters of the population observed are inconsistent with the hypothesis that they are the low-redshift counterparts of the excess faint galaxies if the latter are assumed to have a typical redshift of $z = 0{\cdot}25$ at $B \approx 24$ (as in Cowie *et al.*, 1991), though their magnitudes are consistent.

The angular two-point correlation function has been measured for a field of faint galaxies to $v \approx 26{\cdot}5$ at the South Galactic Pole. The clustering of these faint galaxies is shown to be as low as that found by Efstathiou *et al.* (1991), but Neuschaefer *et al.*'s (1991) rising correlation function amplitudes as a function of median sample magnitude are not found. The former implies that clustering growth is faster than it would be if clustering were fixed in proper coordinates, i.e., $\epsilon > 0$ (eqn (4.25)). If for some reason we have overestimated the uncertainties in our measurements, this result would be even stronger. Efstathiou *et al.* feel that $\epsilon > 0$ is unlikely, so their favoured explanation is that the weakness in clustering is due to the excess faint galaxies being an intrinsically faint, low redshift, more weakly clustered than normal population. N-body models used in this thesis do in fact predict $\epsilon < 0$ in agreement with Efstathiou *et al.* (§6.4), but they also have a spatial correlation function amplitude which is far lower than cosmological amplitudes, so this does not seriously overrule the N-body results of Melott (1992)

or Yoshii *et al.* (1993) or the observational data of Warren *et al.* (1993), which all indicate that $\epsilon > 0$. Instead, it provides a constraint with which to check future N-body simulations which are normalised with the intention of having correlation functions at a cosmological scale.

Merger-induced evolutionary population synthesis (MIEPS) models are defined and results shown in Chapters 5 and 6. Apart from two caveats on spatial correlation function normalisation and the size of the time interval between time stages used, these models look like a good candidate for explaining the faint counts, as expected. Burst-only star formation rate models are found to be necessary, as exponentially decaying star formation rates do not flatten the faint end of the mass function enough in converting it into a luminosity function. The burst-only models with initial perturbation spectra as power law spectra with indices of $n = 0$ and $n = -2$ and detection thresholds of $r_{thresh} = 5$ and $r_{thresh} = 1000$ were run. The model with the most expected parameters ($n = -2$, $r_{thresh} = 1000$) gives a luminosity function which roughly fits a Schechter function at $t \approx t_0$, but gives number counts which clearly don't fit the observations; while a model with less likely parameters ($n = 0$, $r_{thresh} = 5$) gives a luminosity function which has the slope of a Schechter function and fits a Schechter function overall if the compensatory factor A is allowed, in which case the number counts fit reasonably well to the observations apart from the faint end. An increase in time resolution of the N-body output is likely to improve the fit of the latter model more than that of the former.

Hence, these models favour a white-noise-like initial perturbation spectrum ($n \approx 0$) with a low detection threshold ($r_{thresh} \approx 5$) and a correction factor $A = 7$ as a candidate for explaining the excess of faint galaxies; while a CDM-like spectrum on these scales ($n \approx -2$) appears less likely.

An additional result from the N-body galaxy evolutionary modelling is that the individual merger rates can be very different from the average merger rates and that the fraction of mass coming from accretion can be quite high. For example, for the $n = 0$, $r_{thresh} = 5$ model, the mean number of peaks which collapse from the intergalactic medium at any time stage and end up in a peak at the final time stage is 7·4, while the standard deviation in this quantity is 20·7. While this result is likely to quantitatively change with the new N-body simulations, qualitatively it is unlikely to.

Contents

List of Figures

List of Tables

Chapter 1

Introduction

The study of faint galaxies ($b_J \approx 24 - 28$) offers the hope of an alternative method of deriving the values of cosmological parameters, in particular, q_0, in contrast to the more direct and traditional method of using the magnitude-redshift relation. The study of these galaxies involves an attempt to derive information from galaxies which are too faint to have redshifts measured, and whose distribution therefore has to be modelled indirectly. As redshift information becomes available for successively fainter galaxy populations, these indirect models will be (and already some have been) either confirmed or denied. At these faint magnitudes, the evolutionary properties of galaxies, individually and as a population, are as important as cosmology in interpreting the data. Hence, the interpretation of the data is nontrivial, and the quest to determine the curvature of the Universe is not yet over.

In this thesis I describe two properties of the faint galaxy populations, adding to the work of previous authors in attempting to reconcile the observations with the theoretically popular flat, pressure-free universe ($q_0 = 0{\cdot}5, \lambda_0 = 0$).[1] I describe models and observations relating to the differential number counts of faint galaxies ($d^2N(< m)/d\Omega\, dm$) and I describe observations of the angular two-point autocorrelation function ($w(\theta)$) of these faint galaxies.

The recent differential number counts obtained by Tyson (1988) from observations by Tyson & Seitzer (1988) to magnitudes of $b_J \approx 28$ show an excess of galaxies in comparison to the numbers predicted by the indirect models made by many independent authors. These authors have independently concluded that with the assumption of conservation of galaxy comoving number density the best interpretation of the data is that the Universe must be open ($q_0 < 0{\cdot}5$) and the epoch of galaxy formation high ($z_f \gtrsim 5$). These authors include Tyson (1988), who also considers a biassed cold dark matter (CDM) model with $z_f = 2$ to be

[1] $\lambda_0 = (\Lambda c^2)/(3H_0^2)$ is the normalised cosmological constant.

consistent with the data; Koo (1990), Guiderdoni & Rocca-Volmerange (1990) and Yoshii & Peterson (1991). The models used by these authors involve many parameters. These include: the cosmological parameters q_0, H_0 and z_f—the effects of different values of H_0 are small, while λ_0 is usually assumed to be zero by Occam's Razor; the K-correction—the effects of sampling different parts of the spectrum of a galaxy due to redshifting; the E-correction—the effects of galaxies' spectra evolving due to stellar formation and evolution; and the present epoch luminosity function, modelled by all these authors as a Schechter function (Schechter, 1976) with slight variation in the particular parameters used (ϕ^*, M^*, α). In Koo (1990) the K- and E- corrections are modelled in a simple algebraic manner, while the other authors, Tyson (1988), Guiderdoni & Rocca-Volmerange (1990) and Yoshii & Peterson (1991) use galaxy evolutionary population synthesis models: those of Bruzual (1981, 1983), Guiderdoni & Rocca-Volmerange (Guiderdoni & Rocca-Volmerange, 1987, Rocca-Volmerange, 1989) and Arimoto & Yoshii (1986, 1987) respectively.

In order to demonstrate the different contributions that these parameters make to the differential number counts, I describe them separately and in combination in Chapter 2.

While the low q_0, high z_f models are favoured by the above authors, ways in which the counts could be consistent with a flat universe have been considered. Koo (1990) shows two separate ways in which a $q_0 = 0{\cdot}5$ universe could be made consistent with the observed counts. These are (a) an increase in comoving number density proportional to about $(1+z)^{2{\cdot}5}$ (with a (K+E)-correction equal to the K-correction for galaxies with $f_\lambda = constant$), and (b) an evolution in α, the slope of the faint end of the galaxy luminosity function, according to $\alpha(1+z)^{1{\cdot}1\pm0{\cdot}1}$. The latter is inspired by Broadhurst *et al.*'s (1988) suggestion that what would otherwise be low luminosity galaxies at high redshifts are brightened by starbursts, effectively making the slope of the faint end of the luminosity function steeper at high redshifts than the present-day slope. This suggestion is based on the results of redshift data of objects to $b_J \approx 21{\cdot}5$, which show a redshift distribution consistent with that of a population in which the brighter galaxies do not evolve. Ellis (1990) also describes a model in which short starbursts in high redshift, low luminosity galaxies may fit the counts in a flat universe.

Rocca-Volmerange & Guiderdoni (1990) model the effects of an increase in comoving number density at higher redshift in more detail than Koo, i.e., on the basis of full galaxy evolutionary population synthesis models, and with a number density evolution that conserves light (unlike that of Koo). They show that number density evolution proportional to about $(1+z)^{1{\cdot}5}$ is sufficient to

fit the observed number counts. Broadhurst *et al.* (1992) also describe a model involving nonconservation of comoving number density which fits the observed counts for a flat universe. In both of these models, objects are simply split apart into separate subobjects at high redshift, i.e., the masses (luminosities) decrease in proportion to the increase in number density, so that total mass (luminosity) is conserved at any epoch relative to a model in which comoving number density is conserved.

The use of a merging model (nonconservation of comoving number density) is also favoured by Cowie *et al.* (Cowie *et al.*, 1991, Lilly *et al.*, 1991). On the basis of redshift data for a small sample of galaxies in the range $23 < B < 24$ and observations in the infrared K band (Cowie *et al.*, 1990), they find the best models for the faint galaxies to be either a merging dominated model or a model incorporating a change in the faint end of the luminosity function at redshifts of $z \approx 0{\cdot}25$ due to a new population, suggesting a population of "flat spectrum" ($f_\nu = constant$) galaxies (Cowie *et al.*, 1988) as a candidate.

The need to consider models such as these which may save a flat universe has become necessary due to the redshift results of Broadhurst *et al.* (1988) and Colless *et al.* (1990). Colless *et al.* (1992) argue that the low q_0, high z_f models are ruled out on the basis of these recent redshift data to $b_J \approx 23$, but that both merging dominated models and models with starbursts in dwarf galaxies (evolution in α) remain consistent with these redshifts. The main basis of ruling out the low q_0, high z_f models ("mild luminosity evolution") models is that these models predict that almost all galaxies fainter than $b \sim 22{\cdot}5$ having $B - I < 1$ should be at redshifts greater than $z = 1$ (Koo, 1990, Figs 1a,1c, Yoshii & Peterson, 1991, Fig. 3a) but all six objects in the sample observed by Colless *et al.* satisfying these two criteria have $z < 1$ (Fig. 11, Colless *et al.*, 1993). This is consistent with Guhathakurta *et al.*'s (1990) earlier result that Tyson & Seitzer's (1988) faint galaxies mostly have $z \lesssim 3$ since the shift of the Lyman break into the U band is not seen.

In order to model the evolution of the luminosity function, Silk and Lacey (Silk & Lacey, 1990, Lacey & Silk, 1991) have recently used galaxy evolutionary population synthesis in combination with the hypothesis that star formation is induced by galaxy interactions (merging or tidal effects), modelling the latter analytically. This work is continued in Lacey *et al.* (1992), in which the model is found to successfully fit the observed counts, as well as several other observational properties of the galaxy populations, though the present-day luminosity function is too steep and there is a deficit of red, bright galaxies.

As these models predict the existence of a large number of gas-rich, low sur-

face brightness galaxies, and authors such as Impey *et al.* (1988) argue that our knowledge of galaxies is biassed against the detection of such galaxies, the first observational part of my thesis was to conduct a preliminary survey for low surface brightness galaxies in the field. If the result of this search had been promising, a further, more thorough survey could have been made. This survey and its results are described in Chapter 3.

As the understanding of any scientific phenomenon is advanced by having different types of observational[2] evidence to constrain theories, the other observational part of my thesis is an analysis of the two-point angular correlation function of faint galaxies (to $v \approx 25{\cdot}5$). Efstathiou *et al.* (1991) and Neuschaefer *et al.* (1991) already have similar observations, but the results described here certainly add a different perspective to their results. The reduction and analysis of the observations and resulting correlation functions are discussed in Chapter 4.

The merging models mentioned above (Rocca-Volmerange, 1990 and Broadhurst *et al.*, 1992) ignore starbursting activity which is likely to occur when galaxies merge, while the starbursting models (Broadhurst *et al.*, 1988, Ellis, 1990) and the luminosity evolution models of Lacey *et al.* (1992) assume conservation of comoving number density.

Hence, the theoretical part of my thesis is a model based on N-body simulations which aims to simultaneously model the luminosity and number evolution of galaxies. This is done by detecting density peaks (dark matter galaxy haloes) in the N-body simulations at a range of time steps, making representations of how these peaks merge into one another, supposing that one galaxy exists in each of these haloes, and hypothesising either that the star formation rate is exponentially decaying as a function of time, that it occurs as a burst whenever galaxies merge, or a combination of the two.

The N-body simulations of Warren *et al.* (1992) and an updated version of Bruzual's (1983) galaxy evolutionary population synthesis code are used. The star formation rate during bursts and the durations of the bursts are parametrised in a simple but observationally inspired manner, described in §5.5. The definition and implementation of these models is described in Chapter 5, while the results are described in Chapter 6.

The results of these observations and models are summarised in the conclusion of the thesis (Chapter 7).

[2](or experimental, in experimental sciences)

Chapter 2

Factors Affecting Faint Galaxy Number Counts

Abstract

The different factors which contribute to the faint galaxy number counts ($d^2N(< m)/d\Omega\, dm$), i.e., luminosity distance, differential volume element, deceleration parameter, formation redshift, K- and E- corrections, the comoving (i.e., present-day) luminosity function and merging of galaxies are described and shown in this chapter.

2.1 Introduction

In this chapter I outline the various factors which affect the faint number counts of galaxies ($(d^2N(< m)/d\Omega\, dm)$) expected according to different astrophysical parameters. To conceptualise these counts, it is helpful to imagine a cone projecting outwards from the observer, bounding the galaxies which are projected onto a single "celestial" surface in the observing process. This cone is a three-dimensional cross-section through four-dimensional space-time. Close to the observer, one can ignore the time factor and consider this to be merely a cone projecting into space. Further from the observer, cosmological effects start occurring. A fundamental boundary provided by any cosmology with a big bang singularity is that no information can reach an observer from an event at $t < 0$. More precisely, the locus of events for which photons take the age of the Universe to reach the observer is termed the particle horizon. This horizon can be thought of as the bottom of the cone.

Even if we ignored everything else in cosmology but the finite horizon, this alone would guarantee that we could see no galaxies beyond some fixed distance.

In proper units, the horizon is

$$\begin{aligned} r_{horiz} &= \frac{c\, cosh^{-1}[(1-q_0)/q_0]}{H_0\sqrt{1-2q_0}}, \quad q_0 < \frac{1}{2} \\ &= \frac{2c}{H_0}, \qquad\qquad\qquad\quad q_0 = \frac{1}{2} \\ &= \frac{c\, cos^{-1}[(1-q_0)/q_0]}{H_0\sqrt{2q_0-1}}, \quad q_0 > \frac{1}{2} \end{aligned} \tag{2.1}$$

where c is the conversion factor between space and time units[1] and h is the Hubble constant in units of $100\, km\, s^{-1}\, Mpc^{-1}$, (Weinberg, 1972). A galaxy at the shoulder of the Schechter (1976) luminosity function, of magnitude $M_B^* = -21{\cdot}1 + 5log_{10}(h/0{\cdot}5)$ (Efstathiou *et al.*, 1988), would have apparent magnitude $m_B = 24{\cdot}3$ at this horizon for a flat universe ($q_0 = 0{\cdot}5$) if we ignore all cosmological effects apart from the horizon itself. A lower density universe, say, $q_0 = 0{\cdot}05$, would stretch this to $m_B = 25{\cdot}7$. Hence, if we ignored all cosmology apart from the horizon distance, we would have a guarantee that the magnitudes at which we are presently observing galaxies should give us clear cosmological effects. Unfortunately, as is described in this chapter, other cosmological and evolutionary effects make extraction of the cosmology from the number counts more difficult.

In this chapter I discuss the effects of realistic cosmology in contrast to a naively simple model in §2.2, the effects of different values of q_0, H_0 and z_f in §2.3, the effects of sampling different parts of the same spectrum or different spectra altogether (the K- and E- corrections) in §2.4, the effect of the luminosity function in §2.5 and the effects of a simple merging model in §2.6.

2.2 Basic Cosmological Effects: d_L, dV/dz

To see the basic effects of a hot big bang cosmology in contrast to a simple, non-cosmological conception of space, let us start with a naively simple case. Let us suppose that all galaxies have the same intrinsic luminosity (i.e., the luminosity function is a Dirac delta function), that space is Euclidean, that the Universe is static and that the galaxy number density in this naive universe is the same everywhere. Then a galaxy at a distance r in Mpc has apparent magnitude $m = M + 5log_{10}[r/(10^{-5}\, Mpc)]$ and the total number of objects brighter than m would be exactly proportional to the volume contained up to r, i.e., proportional to r^3, no matter how large the value of r. Hence, $dN(<m)/dm = dN[<r(m)]/dr \times dr/dm \propto d/dr(r^3)\, r = 3r^3 \propto (10^{m/5})^3 = 10^{0{\cdot}6m}$. This is relatively easy to conceptualise in our imaginary cone.

[1] "speed of light" for those sceptical about special relativity.

In Figure 2.1, we use an approximation to a Dirac delta function to compare the number counts predicted by this naive model in contrast to those predicted with more realistic cosmological parameters. A recent parametrisation of the luminosity function is that of Efstathiou *et al.* (1988), i.e.,

$$\phi(L)dL = \phi^* \left(\frac{L}{L^*}\right)^{\alpha} exp\left(-\frac{L}{L^*}\right) d\left(\frac{L}{L^*}\right) \tag{2.2}$$

where $\phi^* = 1{\cdot}95{\times}10^{-3}(h/0{\cdot}5)^3 Mpc^{-3}$, $\alpha = -1{\cdot}1$ and $M_B^* = -21{\cdot}1 + 5log_{10}(h/0{\cdot}5)$ is the characteristic magnitude corresponding to L_B^*. The delta function approximation is chosen to be nonzero at this M_B^*; it has an integral of the value of the Schechter function at M_B^*, i.e., $\int_{-\infty}^{+\infty} \phi_\delta(L)dL = \int_{-\infty}^{+\infty} \psi_\delta(M)dM = \phi^* e^{-1}$; and it is zero anywhere more than half a magnitude from M_B^*. All the calculations made with this approximated delta function are therefore a measure of how many galaxies are contributed to the number counts by $M_B^* \pm 0{\cdot}5$ galaxies. Since we know that there are brighter and fainter galaxies than $M_B^* \pm 0{\cdot}5$, these calculations therefore underestimate the total number of galaxies.

For the plot of our naive model in Fig. 2.1, (the solid line), we also use a horizon distance cutoff. The naive model without such a cutoff would merely be a straight line with the same slope and normalisation that the plotted curve has for magnitudes brighter than $m_B \approx 23{\cdot}5$. The value of the horizon distance cutoff is $r_{horiz} = 12Gpc$ (eqn (2.1)), where $(q_0, h) = (0{\cdot}5, 0{\cdot}5)$. We choose to compare to $q_0 = 0{\cdot}5$ since it is a theoretically desirable value, and $h = 0{\cdot}5$ since this gives the oldest age of the Universe, $13Gyr$, for an observationally credible value of h this value of q_0, i.e., making the Universe nearly as old as the oldest globular clusters. In this "naive" model, distance is $r = zc/H_0$, so we call this a "horizon redshift", though this is of course in a loose sense.

Five variants on the naive model are plotted in comparison in Fig. 2.1. Each of these uses the same "horizon redshift", except that the variant with both a correct luminosity distance and a correct volume element is plotted both with this "horizon redshift" and with a formation redshift effectively at $z_f \rightarrow \infty$. These variants are not intended as self-consistent cosmological models (except for the naive case and the case with cosmologically correct d_L and dV/dz); they are intended to isolate the functional effects of the different parameters.

Variants with a proper distance instead of either a "naive" distance or a luminosity distance are included. The proper distance to a galaxy,

$$d_{prop} = \frac{c}{H_0 q_0^2}\left[\frac{q_0 z + (q_0 - 1)\left(\sqrt{1 + 2q_0 z} - 1\right)}{1 + z}\right] \tag{2.3}$$

is the integral of the spatial component of the metric along the world line (path) of a photon which travels between a galaxy and the observer (e.g., Weinberg,

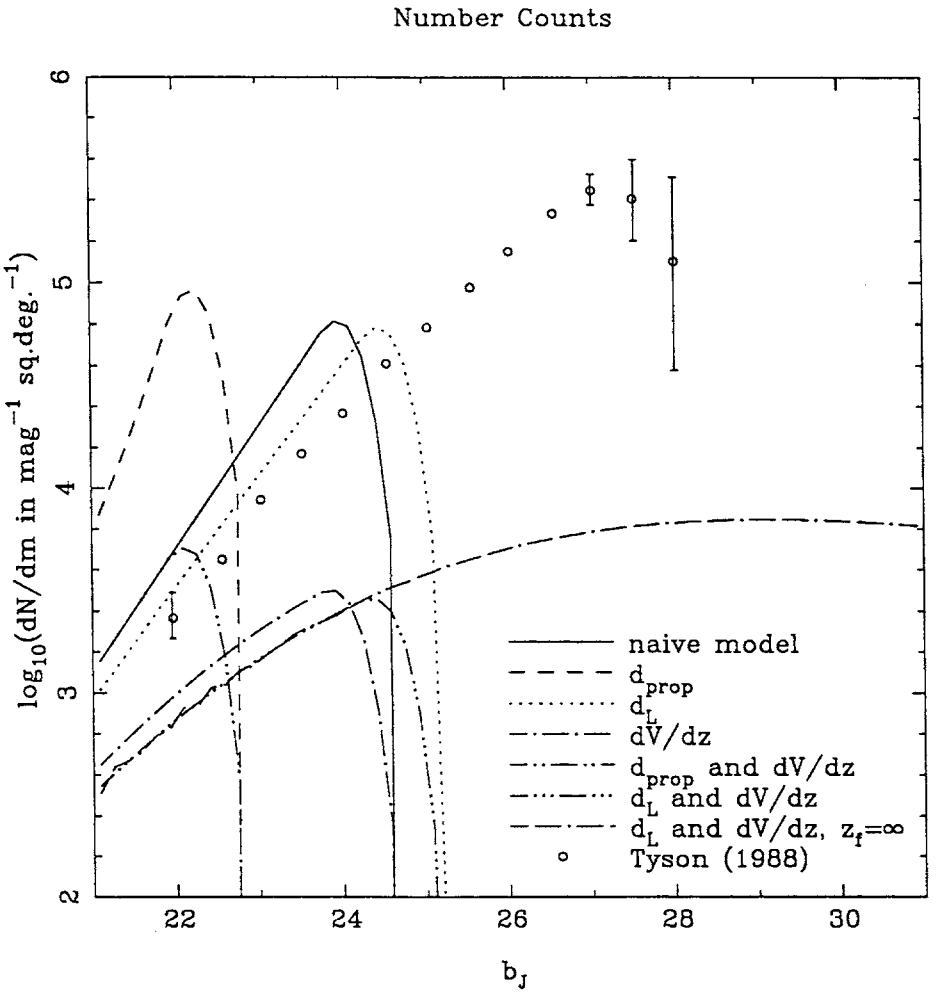

Figure 2.1: Effects of basic cosmological variables (d_L and dV/dz) on number counts for a delta luminosity function. The model labelled "naive" assumes a static, Euclidean universe, with galaxies existing to the horizon distance for $q_0 = 0{\cdot}5, h = 0{\cdot}5$, which in this naive model is defined by a "horizon redshift" of $z_h = 1/q_0 = 2{\cdot}0$. The next two models show the effects of putting in a proper distance for the appropriate redshift (ignoring $(1+z)^2$ dimming) or a correct luminosity distance (d_L) respectively. The next three models correspond to the first three for object distances, but a correct cosmological volume element (dV/dz) is used. Each of these models assumes that galaxies have formed at redshift $z_f = z_h$. The seventh model has correct cosmological d_L and dV/dz and has $z_f = \infty$.

Tyson's (1988) corrected counts are also plotted. (These same counts are plotted in further figures in this chapter as well.)

1972). This is shorter than the naive distance. It has the limiting approximations $d_{prop} \sim cz/H_0, \quad z \ll 1$, $d_{prop} \sim c/(H_0 q_0), \quad z \gg 1$. The latter shows the horizon distance as mentioned above. As the naive distance, $d = zc/H_0$, increases without bound as z increases without bound, d_{prop} must be significantly lower than this for $z \gg 1$. In Fig. 2.1 this is clear, with the curves using proper distances truncating about $1{\cdot}5mag$ brighter than the curves with the naive distance.

Due to cosmological redshifting, the amount of energy per second coming from photons emitted by a galaxy is decreased by two factors of $(1+z)$ on arrival at the observer. These two factors can be thought of as a change in energy per photon and a time delay effect in the rate at which photons arrive at the observer. These two factors are incorporated into the concept of luminosity distance. This is defined as the distance at which a galaxy would have to be in order that a calculation of the distance modulus which ignores these two factors in fact gives the correct distance modulus. Hence,

$$d_L = (1+z) d_{prop}. \tag{2.4}$$

This is, therefore, greater than the proper distance, and as Fig. 2.1 shows, only slightly larger than the naive distance. Hence, the luminosity distance does not have a great effect in contrast with the naive distance, though it does have a large effect relative to the proper distance.

The differential volume element, dV/dz, on the other hand, does have a big effect. In our conceptual cone, the only effect of using the proper distance and then the luminosity distance to shift the galaxies back and forth in the line of sight direction. In contrast, the volume element involves both a decrease in the cross-sectional area and the incremental distance in the line of sight direction, and shrinks towards zero as z increases without bound. From eqn (2.3), it follows that

$$\frac{dV}{dz} = \frac{4\pi c\, d_L^2}{H_0 (1+z)^6 \sqrt{1+2q_0 z}} \tag{2.5}$$

is the differential volume element in proper coordinates. The comoving volume element is of course $(1+z)^3$ times this expression. As is clear from Fig. 2.1, the differential volume element for $q_0 = 0{\cdot}5$ already has a large effect at relatively bright magnitudes, e.g., it decreases the number counts by a factor of ~ 15 at $m_B = 24$.

Figure 2.2 shows the effect that a full Schechter function (with the above Efstathiou *et al.*, 1988 parametrisation) has on these models. It reduces the small effects of the different distance variables, while the difference in dV/dz at the truncation magnitude is preserved faintwards of $m_B \approx 25$, and the effect of the

unbounded z_f is reduced from being unbounded itself to being finite, but still a factor of about 4 at $m_B \approx 30$. The Schechter function shown in the same diagram indicates why it has these effects.

2.3 Effects of Cosmological Parameters: q_0, H_0 and z_f

Now that the basic cosmological factors have been discussed, we can present a preliminary expression with which to evaluate the number counts:

$$\begin{aligned} \frac{d^2N(<m)}{d\Omega\, dm} &= \frac{d}{d\Omega}\int_{z=0}^{z=z_f}(1+z)^3\psi[m+(M-m)]\frac{dV}{dz}dz \\ &= \frac{1}{4\pi}\int_{z=0}^{z=z_f}\frac{(1+z)^3}{h^3}\psi[m+(M-m)]h^3\frac{dV}{dz}dz \end{aligned} \tag{2.6}$$

where $\psi(M)$ is the magnitude form of the luminosity function ($\psi(M)dM = \phi(L)dL$) and the distance modulus is

$$\begin{aligned} M-m &= -5log_{10}\left(\frac{d_L}{10pc}\right) \\ &= -5log_{10}\left(\frac{h\,d_L}{1Mpc}\right) + 5log_{10}h - 25. \end{aligned} \tag{2.7}$$

This expression conserves comoving number density, hence the factor of $(1+z)^3$ in front of the present-day luminosity function to convert it to proper coordinates, as the volume element is also in proper coordinates.

The explicit use of h here is to show the independence of the faint counts (at this basic stage) from the Hubble constant. Equations (2.3) and (2.4) show that $h\,d_L$ is independent of h. Provided that M^* is given in the form including the term $+5log_{10}h$, as above, $M^* - M = M^* - [m + (M-m)]$ is therefore independent of h, and so the corresponding quantity L/L^* is independent of h. The normalisation of the luminosity function, ϕ^*, is proportional to h^3. Hence, by eqn (2.2), $h^{-3}\psi(M)$ is independent of h. From eqns (2.3), (2.4) and (2.5), it can be seen that dV/dz is proportional to h^{-3}, so $h^3\,dV/dz$ is independent of h. Hence, $d^2N(<m)/d\Omega dm$ is independent of the Hubble constant as far as it has been modelled to this point of the chapter.

Figure 2.3 shows the comoving volume element for various values of q_0. The lower plot shows how dramatic a difference there is in the volume elements for different geometries. At $z = 1$, $(1+z)^3 dV/dz$ in an open universe with $q_0 = 0{\cdot}05$ is already twice as large as that in a flat universe ($q_0 = 0{\cdot}5$).

One way to conceptualise why this difference is so large is to imagine our conceptual cone at a constant cosmological time, instead of having cosmological time

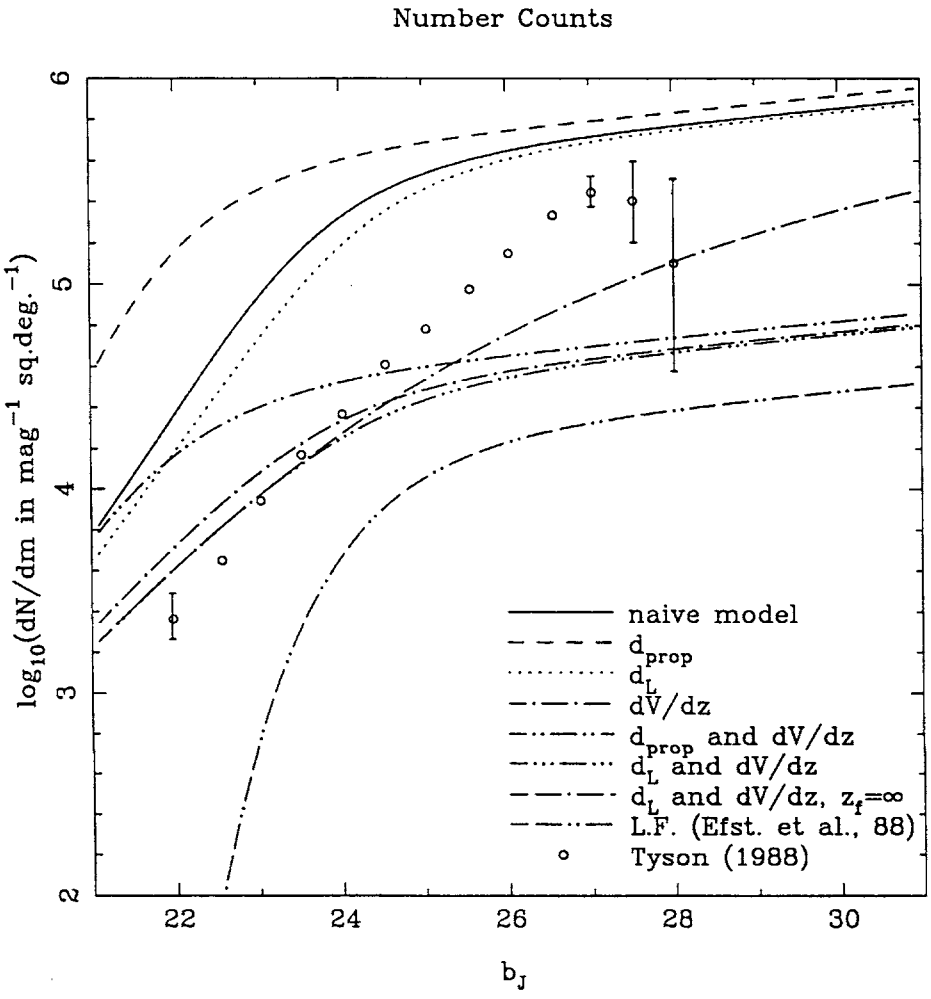

Figure 2.2: Effects of basic cosmological variables (d_L and dV/dz) on number counts for a Schechter luminosity function. These are the same as Figure 2.1 apart from the difference in luminosity functions. A Schechter luminosity function with $M_B^* - log_{10}h$ scaled to $m_B = 24{\cdot}3$ and multiplied by a volume of $10^7 h^{-3} Mpc^3$ is also plotted for comparison.

decrease as distance from the observer increases. In a hypersurface of constant cosmological time in an open universe, the cross-sectional area is proportional to $sinh^2\chi$, (where the line element is $dl^2 = R_0^2[d\chi^2 + sin^2\chi(d\theta^2 + sin^2\theta\, d\phi^2)]$) rather than just χ^2, as in a flat universe. While this means a small difference close to the observer, this difference is exponential, so quickly becomes larger. The case for a closed universe is, of course, the opposite. The cross-sectional area is proportional to $sin^2\chi$, so it reaches a maximum and decreases to zero.

This is not, of course, the same as the actual observational cone, but gives us a feeling for the difference among the different volume elements. The observational cone projects backwards in cosmological time, so that one can try to think of a series of cross-sections and differential distance elements at successively earlier cosmological times and greater proper distances from the observer, with this proper distance approaching a limit at the particle horizon, and then compensating for the fact that the volume element is a derivative with respect to redshift, not proper distance.

The contrast between the volume element in the naive model of the geometry of the Universe and the various ordinary (cosmological) models is stronger than among the various ordinary models alone. As shown in Figure 2.3, even at a redshift as low as $z = 0{\cdot}03$, the naive model has about 10% more volume than a flat model, while the difference between the various ordinary models is only a small fraction of this.

The effects of these different volume elements, as well as the effects of the formation redshift are shown in Figures 2.4 and 2.5. In Fig. 2.4, which is for the Dirac delta luminosity function mentioned above, it can be seen that either increasing formation redshift (z_f) or decreasing q_0 increases the magnitude at which the counts truncate. This is via the luminosity distance (eqns (2.3), (2.4)). Use of the full Schechter function (Fig. 2.5) reduces this effect into a small change in the slope at the faint end, leaving the effect of the volume element as the major effect of changing either of z_f or q_0.

2.4 K and E corrections

2.4.1 Definitions

Although the major effects which are primarily cosmological properties rather than intrinsic properties of galaxies have already been discussed, there is one such factor remaining to be discussed - the "K-correction". Although we have

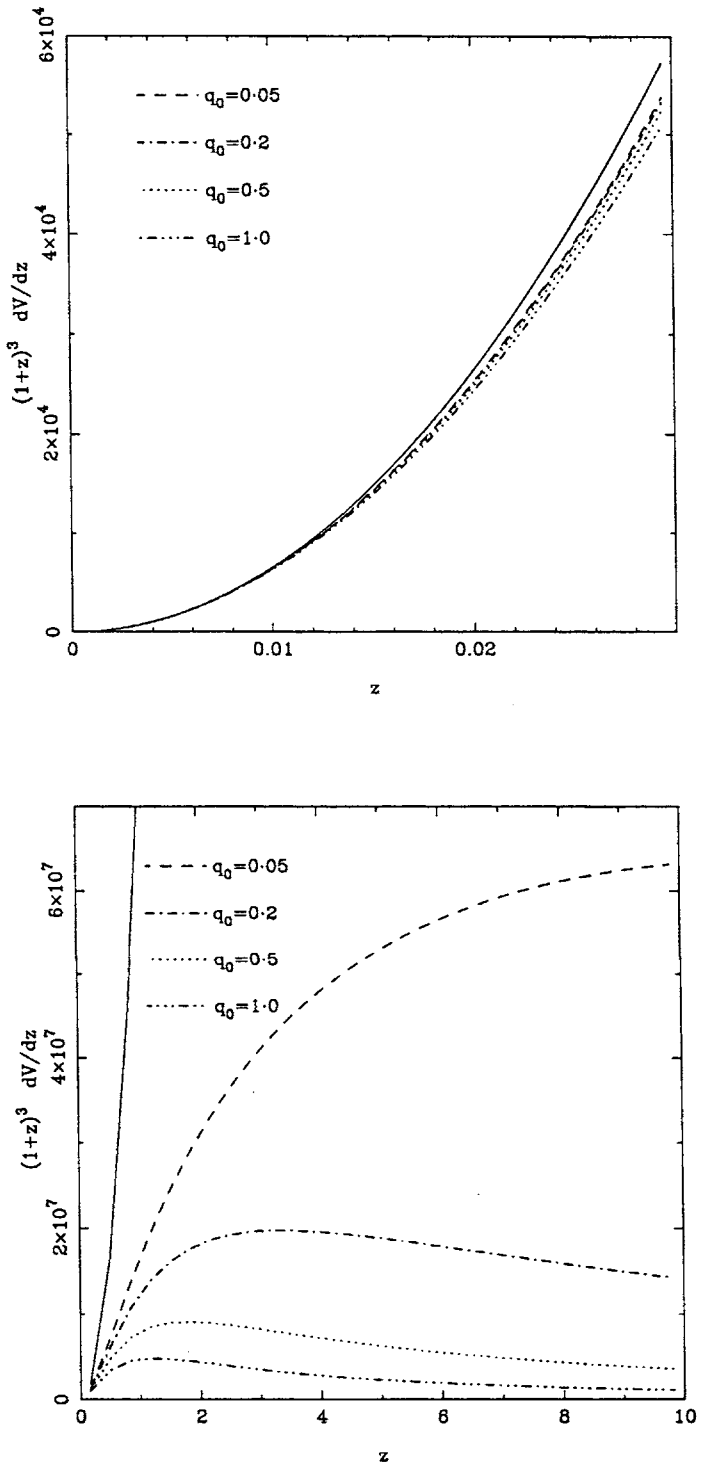

Figure 2.3: Volume element. For $h = 0{\cdot}5$, the comoving volume element $(1+z)^3 dV/dz$ is plotted against redshift for a range of values of q_0, at low redshift and at higher redshift. The solid line shows the volume element for a "naive" universe, in which $V = 4\pi/3\,(zc/H_0)^3$.

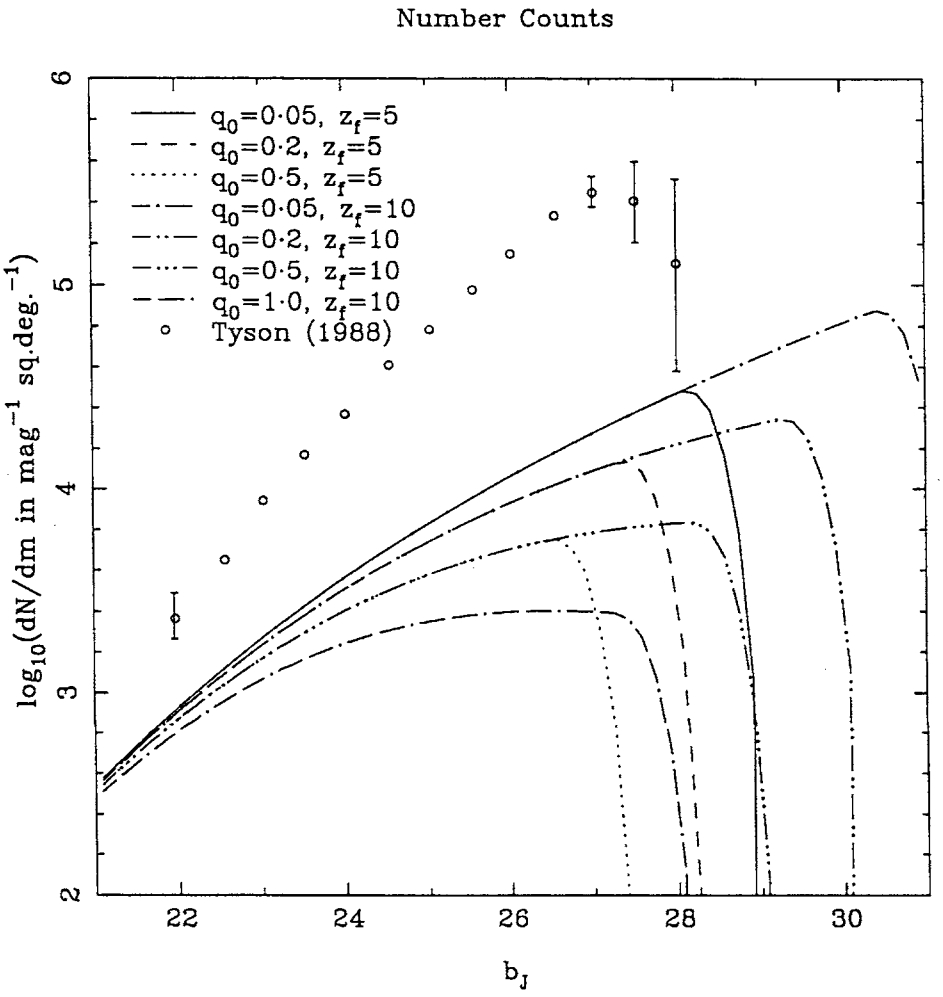

Figure 2.4: Effects of changing z_f, q_0. Number counts are plotted for a range of values of q_0 and z_f for a Dirac delta luminosity function, i.e., the contribution of M^* galaxies is shown.

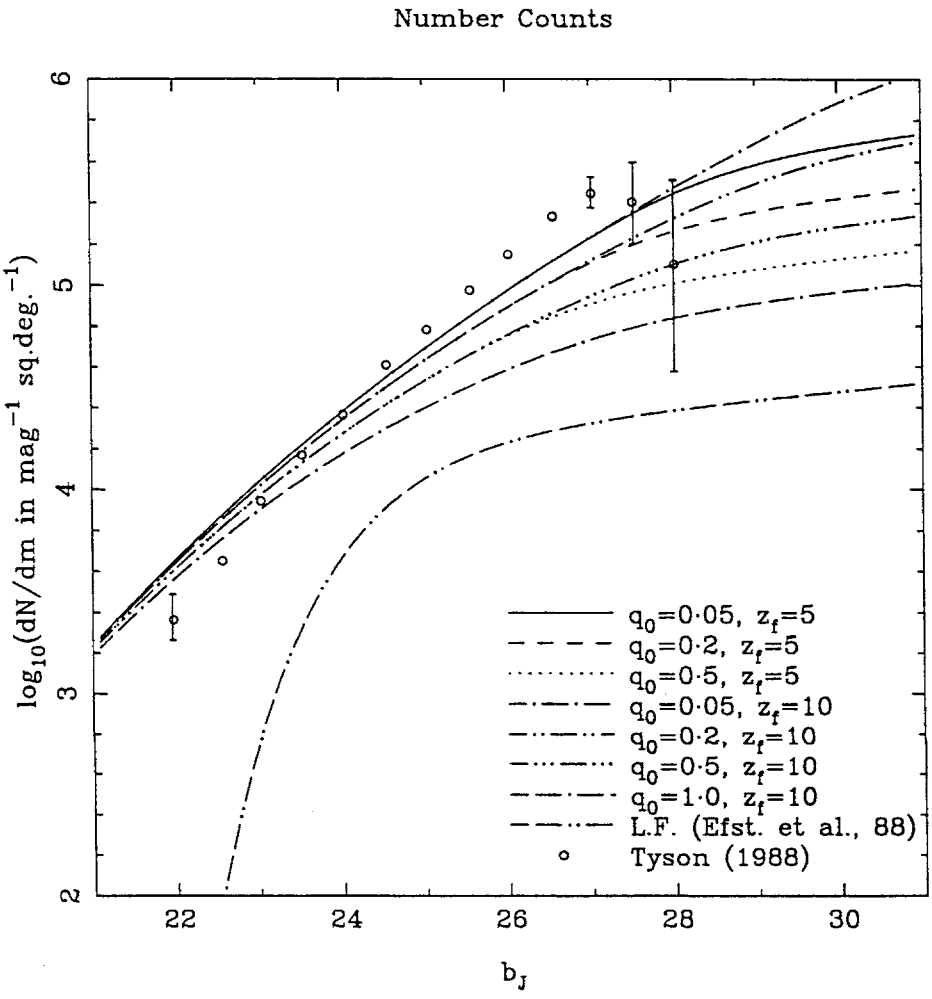

Figure 2.5: Effects of changing z_f, q_0. Number counts are plotted for a range of values of q_0 and z_f for a Schechter luminosity function. A Schechter luminosity function with $M_B^* + log_{10}h$ scaled to $m_B = 24{\cdot}3$ and multiplied by a volume of $10^7 h^{-3} Mpc^3$ is also plotted for comparison.

already taken into account the decrease in flux due to the increase in energy of each photon and the decrease in the rate at which photons arrive due to the time delay via the concept of luminosity distance, this is only valid if we are measuring flux across all wavelengths, i.e., bolometric flux. Since in practice we use finite wavebands which exclude significant proportions of the total flux, we also need to take account of the difference in the wavelengths at which the flux is emitted with respect to the wavelengths at which it is actually measured. This additional factor is termed the K-correction, K_X, (where X is the waveband) and can be derived as follows.

We initially include the time delay and energy change factors in this derivation, since this makes direct sense physically, and separate them out afterwards.

Denote the emitted and observed fluxes in $photons\, cm^{-2}s^{-1}\text{Å}^{-1}$ as $f_1(\lambda)$ and $f_2[(1+z)\lambda]$ respectively, the fluxes in $erg\, s^{-1}cm^{-2}s^{-1}\text{Å}^{-1}$ as $f_{\lambda_1}(\lambda)$ and $f_{\lambda_2}[(1+z)\lambda]$ and consider photons with observer wavelengths between λ_a and λ_b, where the waveband X falls between λ_a and λ_b. Then

$$f_2[(1+z)\lambda]\, d[(1+z)\lambda] = \frac{1}{(1+z)} f_1(\lambda) d\lambda \tag{2.8}$$

incorporates the time delay factor. To see that this is correct, note that

$$\int_{\lambda_a}^{\lambda_b} f_2[(1+z)\lambda]\, d[(1+z)\lambda] = \frac{1}{(1+z)} \int_{\frac{\lambda_a}{(1+z)}}^{\frac{\lambda_b}{(1+z)}} f_1(\lambda) d\lambda, \tag{2.9}$$

i.e., the integrated numbers of $photons\, cm^{-2}s^{-1}$ in the physically corresponding wavelength interval is decreased by $(1+z)$ due to the time delay but otherwise the same.

From eqn (2.8),

$$f_2[(1+z)\lambda]\, d(\lambda) = \frac{1}{(1+z)^2} f_1(\lambda) d\lambda \tag{2.10}$$

or

$$f_2[(1+z)\lambda] = \frac{1}{(1+z)^2} f_1(\lambda). \tag{2.11}$$

The energy change factor comes in by relating

$$f_{\lambda_1}(\lambda) = \frac{hc}{\lambda} f_1(\lambda) \tag{2.12}$$

and

$$f_{\lambda_2}[(1+z)\lambda] = \frac{hc}{(1+z)\lambda} f_2[(1+z)\lambda]. \tag{2.13}$$

Hence

$$\begin{aligned} f_{\lambda_2}[(1+z)\lambda] &= \frac{1}{(1+z)} \frac{hc}{\lambda} \frac{1}{(1+z)^2} f_1(\lambda) \\ &= \frac{1}{(1+z)^3} f_{\lambda_1}(\lambda). \end{aligned} \tag{2.14}$$

Integrating this gives

$$\begin{aligned}\int_{\lambda_a}^{\lambda_b} f_{\lambda_2}[(1+z)\lambda]\; d[(1+z)\lambda] &= \int_{\lambda_a}^{\lambda_b} \frac{1}{(1+z)^3} f_{\lambda_1}(\lambda)\; d[(1+z)\lambda] \\ &= \int_{\frac{\lambda_a}{(1+z)}}^{\frac{\lambda_b}{(1+z)}} \frac{1}{(1+z)^3} f_{\lambda_1}(\lambda)(1+z)\; d\lambda \\ &= \frac{1}{(1+z)^2} \int_{\frac{\lambda_a}{(1+z)}}^{\frac{\lambda_b}{(1+z)}} f_{\lambda_1}(\lambda) d\lambda. \qquad (2.15)\end{aligned}$$

That is, the integrated intensity in $ergs\, cm^{-2} s^{-1}$ received by the observer is that from the physically corresponding wavelength interval but decreased by exactly $(1+z)^2$ due to the time delay and the energy decrease.

The fraction of light passed through a filter and absorbed by a CCD or photographic plate, termed the response function, is less than 100% and varies between the limits λ_a and λ_b. If we denote this $S_\lambda[(1+z)\lambda]$, since it is used at observed, i.e., redshifted, wavelengths, the integrated flux can be described from the observer's point of view as

$$I = \frac{1}{(1+z)^3} \int_{[(1+z)\lambda]=\lambda_a}^{[(1+z)\lambda]=\lambda_b} S_\lambda[(1+z)\lambda] f_{\lambda_1}(\lambda)\; d[(1+z)\lambda]. \qquad (2.16)$$

For the K-correction, we remove two factors of $(1+z)$, since these are already included in the luminosity distance. The K-correction is therefore defined

$$K_X(z) = -2{\cdot}5 log_{10} \left(\frac{\frac{1}{1+z} \int_{[(1+z)\lambda]=\lambda_a}^{[(1+z)\lambda]=\lambda_b} S_\lambda[(1+z)\lambda] f_\lambda(\lambda)\; d[(1+z)\lambda]}{\int_{\lambda=\lambda_a}^{\lambda=\lambda_b} S_\lambda(\lambda) f_\lambda(\lambda)\, d\lambda} \right), \qquad (2.17)$$

where the subscript "1" has been dropped off f_λ.

Calculation of the K-correction requires both galaxy spectra and knowledge of the response functions of the filters/detectors being used. In order to calculate the E-corrections (see next paragraph) we use spectra generated by Bruzual's (1983) evolutionary population synthesis code , so we also use these for the K-correction. The filter/detector passbands were provided numerically by Mike Bessell.

The E-correction is the first factor affecting the faint number counts among those which we consider that is best thought of as a galaxy property rather than a cosmological property. The E-correction is the correction for the fact that the stellar populations of galaxies, and hence their spectra, change as a function of time. This is calculated using the ratio of the flux from an present-day galaxy to that of the ancestor of a present-day galaxy, where both of these are calculated at the actual redshift of the galaxy as just shown in deriving the K-correction. Hence, the E-correction is

$$E_X(t,z) = E_X(t_g(z),z)$$

$$= -2{\cdot}5log_{10}\left(\frac{\int_{[(1+z)\lambda]=\lambda_a}^{[(1+z)\lambda]=\lambda_b} S_\lambda[(1+z)\lambda] f_\lambda(t_g(z),\lambda)\, d[(1+z)\lambda]}{\int_{[(1+z)\lambda]=\lambda_a}^{[(1+z)\lambda]=\lambda_b} S_\lambda[(1+z)\lambda] f_\lambda(t_g(z=0),\lambda)\, d[(1+z)\lambda]}\right), \tag{2.18}$$

where the dependence of f_λ and E_X on the age of the galaxy t_g is shown. The dependence of f_λ on t_g is normally thought of as a function solely of the galaxy, independent of cosmology. (Effects of galaxies' environments, e.g., merging, would change this.) However, since we calculate the number counts as an integral over redshift, we need to calculate the age of a galaxy from the time corresponding to the formation redshift of galaxies, t_f, and cosmological time, t, so we use

$$\begin{aligned} t_g &= t_g(q_0, H_0, z, z_f) \\ &= t(q_0, H_0, z) - t_f(q_0, H_0, z_f). \end{aligned} \tag{2.19}$$

2.4.2 Effects

Given an overall star formation rate (SFR) and an initial mass function (IMF), Bruzual's models calculate the number of stars of each mass at each stage of stellar evolution along that mass track, and hence from observational spectra galaxy spectra are calculated. We assume here, as in Yoshii & Takahara (1988) and Yoshii & Peterson (1991), that there are five galaxy types, each of which can be represented by one evolutionary model. We use the proportions of the different types as in Yoshii & Peterson (1991) (f_T = 0·38, 0·16, 0·25, 0·10 and 0·11 for galaxy types T = E/S0, Sab, Sbc, Scd, Sdm respectively), and use Bruzual's μ-models with values μ = 0·7, 0·21, 0·097, 0·037, 0·0015 for the same types respectively, also after Yoshii & Peterson (1991) and Yoshii & Takahara (1988).

We then calculate the number counts as

$$\frac{d^2N(<m)}{d\Omega\, dm} = \frac{1}{4\pi}\int_{z=0}^{z=z_f} \frac{(1+z)^3}{h^3} \sum_T f_T\, \psi[m + (M-m)_T]\, h^3 \frac{dV}{dz} dz \tag{2.20}$$

where f_T is the fraction of galaxies which are of type T ($\sum_T f_T = 1$) and

$$(M-m)_T = -5log_{10}\left(\frac{h\, d_L}{1Mpc}\right) + 5log_{10}h - 25 - K_X(z) - E_X(q_0, H_0, z, z_f). \tag{2.21}$$

Figure 2.6 shows the K- and E- corrections calculated from these models (for the B_J band). The K-corrections are all positive, i.e., the galaxies' light in the UV is not bright enough to overcome the spread in the wavelength interval, while the E-corrections are all negative, i.e., the galaxies are all brighter in the past, due to higher rates of star formation.

Figure 2.7 shows how these affect the number counts. The K-correction alone shifts the counts curve to fainter magnitudes, while the combined (K+E)-correction alters the shape, making a slight "bulge" in the case of the full Schechter function, since the brightening effect of the E-correction is not felt until fainter magnitudes than at which the effect of the K-correction is felt. In the case of the delta luminosity function, the (K+E)-correction shows a complex wiggle. This is in a sense a compression of the redshifts shown across most of Fig. 2.6 into a few magnitudes, hence the oscillations in Fig. 2.6 are exaggerated. These oscillations comprise an effect that is left over from the near cancellation of the K- and E-corrections when added together. While this effect is made totally smooth by use of the full Schechter function, the fact that it does come from the near cancellation of two large functions means that it is a factor in the number counts which may be fairly sensitive to small changes in the parameters.

A consequence of using the E-correction is that the statement in §2.3 that the counts are independent of H_0 no longer holds. This can be seen from equations (2.18), (2.19), (2.20) and (2.21). However, the effects of H_0 still largely cancel out, as can be seen from Figure 2.8. From the delta function curves in this figure, it can be seen that increasing h from 0·5 to 1·0 only brightens the (K+E)- bump by about a magnitude, while for the Schechter function this effect is reduced to about a quarter of a magnitude and disappears totally fainter than $b_J \approx 26$. We therefore retain the value $h = 0{\cdot}5$ throughout the remainder of this chapter unless otherwise specified.

One way of testing the extremes of the effects of the K- and E- corrections without changing the evolutionary parameters (SFR, IMF, etc.) is to suppose that either all galaxies evolve as E/S0's or all galaxies evolve as Sdm's. These extremes are plotted in Figure 2.9. This figure shows that with the smoothing effect of the full Schechter function, the effect of changing the mixture is not quite as large as, say, omitting the K- and E- corrections altogether.

2.5 Luminosity Function

As the previous sections indicate, the fact that galaxies have different absolute luminosities, i.e., that the luminosity function is not a Dirac delta function, affects

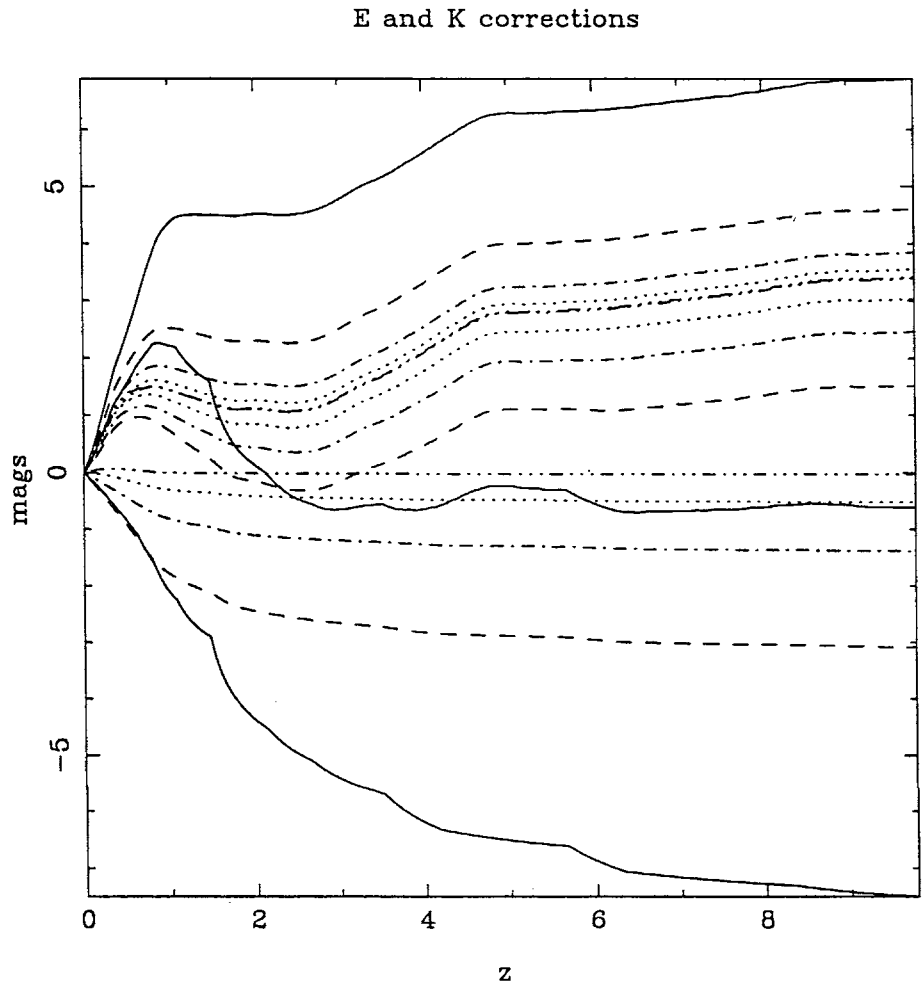

Figure 2.6: K- and E- corrections in B_J. Lines of the same style show K-, (K+E)- and E- corrections from top to bottom respectively, for $q_0 = 0{\cdot}5, h = 0{\cdot}5$. Solid lines are for galaxy type E/S0, dashed lines are for Sab, dash-dotted lines are for Sbc, dotted lines are for Scd and dash-triple-dotted lines are for Sdm type galaxies. The evolutionary models for each galaxy type are referred to in the text.

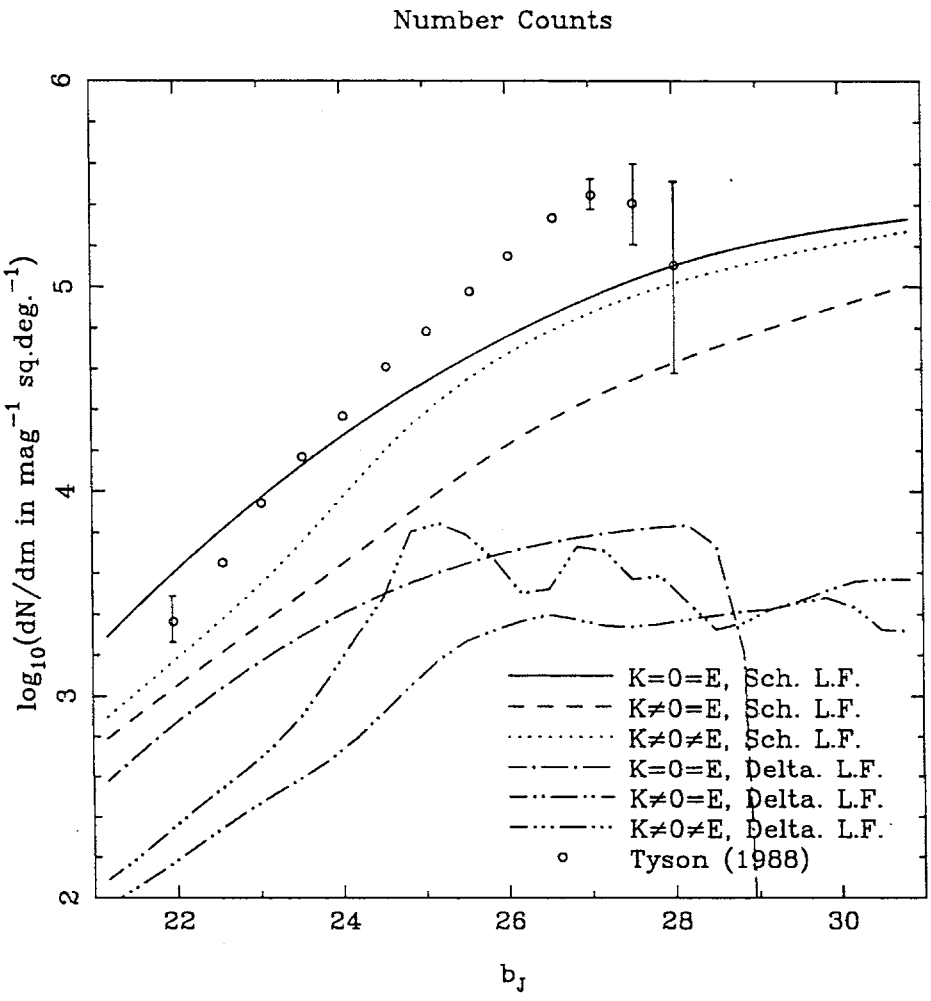

Figure 2.7: Effects of K- and E- corrections on number counts. For a $q_0 = 0{\cdot}5$, $z_f = 10{\cdot}0$ cosmology, the number counts found by incorporating a K-correction ("K≠0=E"), a (K+E)-correction ("K≠0≠E") or no correction ("K=0=E") in the number counts calculated for a Schechter luminosity function; the corresponding curves are also shown for a Dirac delta luminosity function.

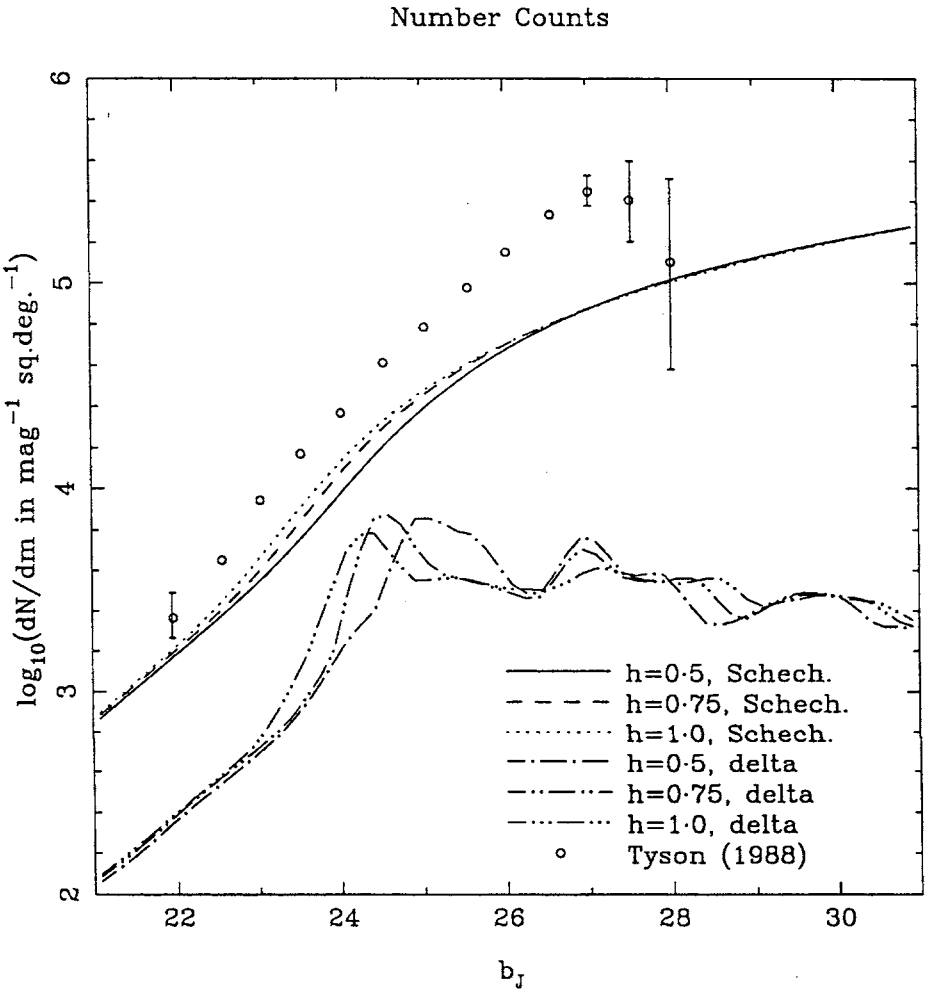

Figure 2.8: Effects of changing H_0, (K+E)-corrections included. For a $q_0 = 0{\cdot}5$, $z_f = 10{\cdot}0$ cosmology, the effects of changing H_0 ($h \equiv H_0/(100\,km\,s^{-1}\,Mpc^{-3})$) are shown for a Schechter luminosity function and a Dirac delta luminosity function.

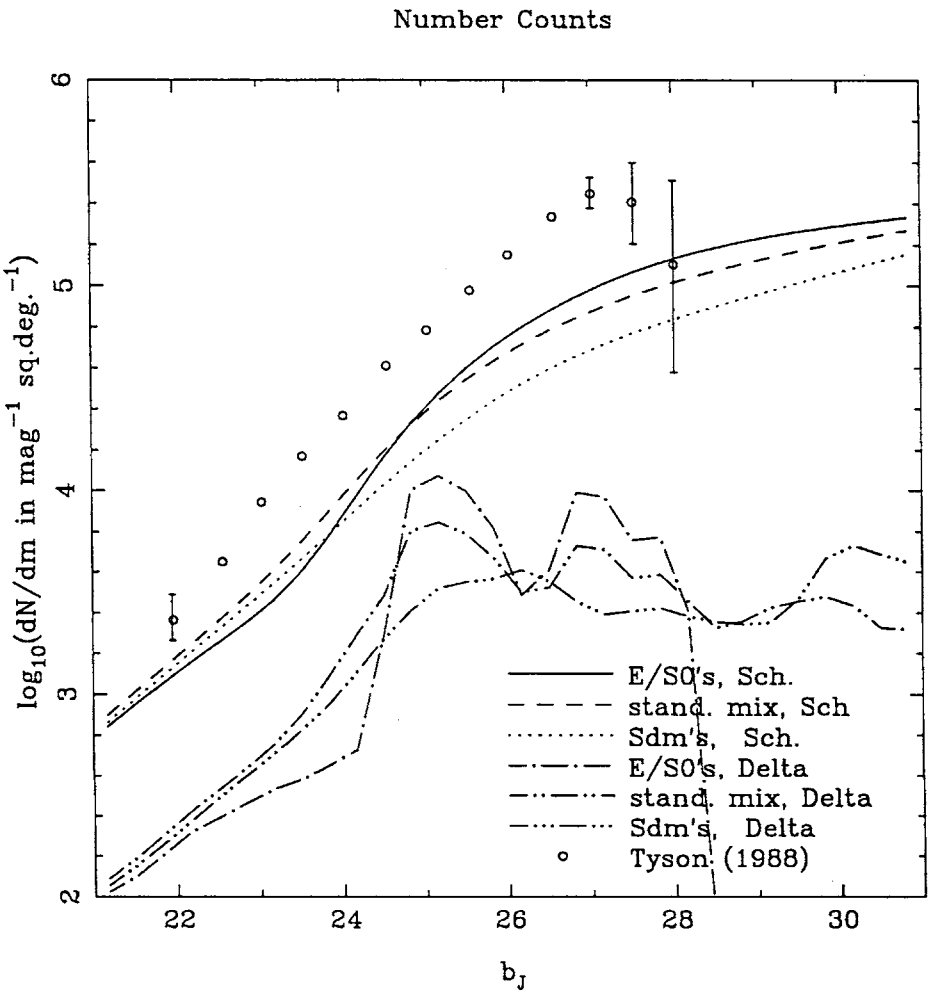

Figure 2.9: Number counts assuming that all galaxies evolve according to one type, either E/S0's or Sdm's (the two extremes), using the (K+E)-correction. These are plotted in comparison to the number counts for a combination of galaxy types as mentioned above in the text, for both Schechter and delta luminosity functions. $q_0 = 0{\cdot}5$, $z_f = 10{\cdot}0$ are used for all these curves.

the number count curves significantly. The three parameters ϕ^*, M^* and α are interdependent in calculating them from a set of observed data, as in Efstathiou *et al.* (1988). However, it is worth at least mentioning their effects on the number counts separately.

Because the luminosity function, expressed in terms of magnitudes, is exactly that, a function of magnitude, the effects of changing ϕ^* or M^* on the faint number counts are straightforward. Changing ϕ^* simply changes the normalisation of the number counts, i.e., shifts the curve up or down; while changing M^* simply shifts the number counts in magnitude, i.e., left or right in the figures shown here. Given the slope of the number counts of say, 0·4, (e.g., for $q_0 = 0{\cdot}5$, $z_f = 10{\cdot}0$, for a Schechter function with full (K+E)-correction, Fig. 2.7 at $b_J \approx 22 - 24$) increasing ϕ^* by $0{\cdot}2dex$ is equivalent to making M^* brighter by $0{\cdot}5mag$.

As the observational normalisation of the number counts at bright magnitudes varies by about to $\sim 0{\cdot}2dex$ between observers (e.g., see Figure 4 of Jones *et al.*, 1991), for comparison with Tyson's observed counts we suppose that the survey on which Efstathiou *et al.*'s (1988) measurement of the luminosity function is underdense for some reason, e.g., it's deficient in rich clusters, and change ϕ^* to $\phi^* = 3{\cdot}1{\times}10^{-3}(h/0{\cdot}5)^3 Mpc^{-3}$ for the purposes of understanding the effects of further parameters. This is used throughout the remainder of this chapter unless otherwise mentioned.

The third parameter in the luminosity function, α, which describes the slope of the faint end of the luminosity function, has a less obvious effect on the number counts. As the luminosity function in clusters indicates the slope may be steeper than the value of Efstathiou *et al.*(1988), e.g., $\alpha = -1{\cdot}25$, (Binggeli *et al.* (1988, pp537, 538)), while the same authors also consider $\alpha \approx -1{\cdot}0$ as a likely (but as yet uncertain) value for the luminosity function of field galaxies, this effect is worth considering. The survey described in chapter 3 was intended to see if an increase in the steepness of the faint end slope was justified observationally, unfortunately coming up with a negative answer, at least as far as a scouting survey of this nature can discern.

Figure 2.10 shows the effect of using different values of α, for $q_0 = 0{\cdot}05, z_f = 5{\cdot}0$ and $q_0 = 0{\cdot}5, z_f = 10{\cdot}0$ geometries. In the open geometry, for which the number counts are already matched, the effect of changing α occurs mainly below where the observations have low uncertainty, while for the flat geometry the effect of α is clearly significant, though a slope as high as about $\alpha = -1{\cdot}5$ would be necessary to fit the observed counts.

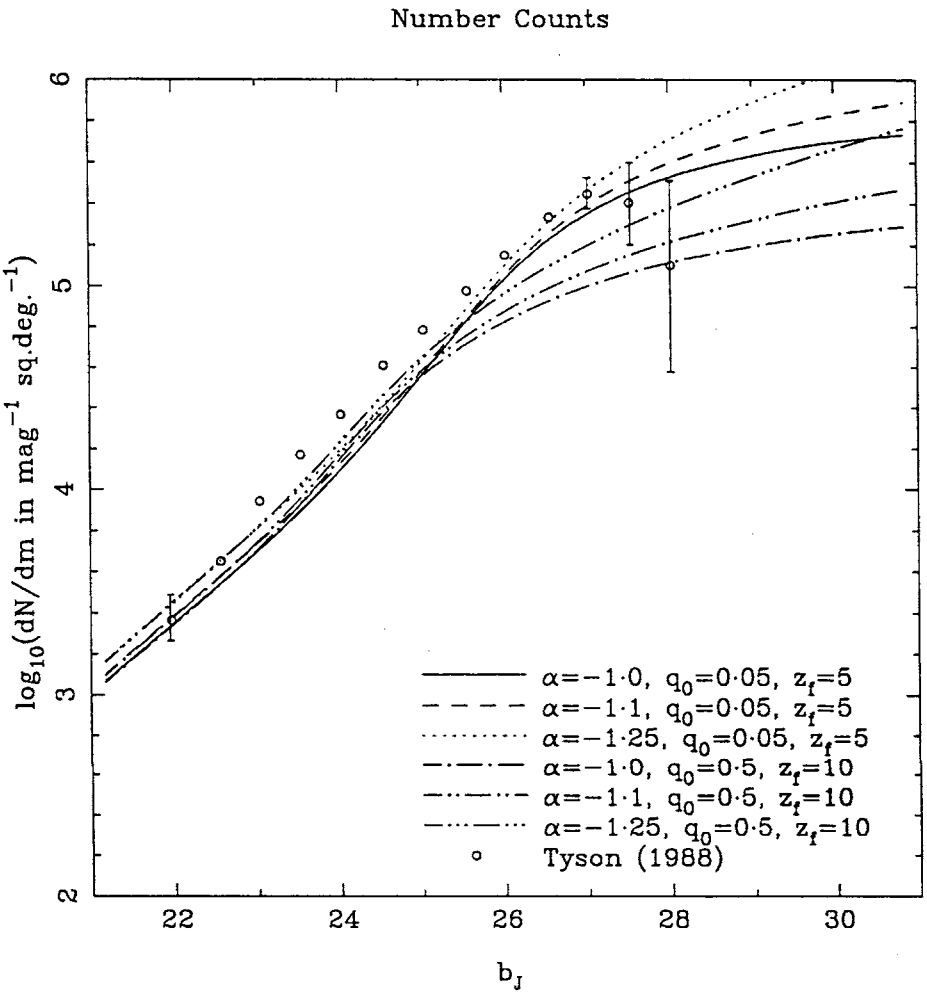

Figure 2.10: Effects of changing α, the slope of the faint end of the luminosity function. For $q_0 = 0{\cdot}05, z_f = 5{\cdot}0$ and $q_0 = 0{\cdot}5, z_f = 10{\cdot}0$ geometries, number counts are shown for $\alpha = -1{\cdot}0, -1{\cdot}1, -1{\cdot}25$. (K+E)-corrections are included. $\phi^* = 3{\cdot}1{\times}10^{-3}(h/0{\cdot}5)^3 Mpc^{-3}$ in this and later figures in this chapter.

2.6 Nonconservation of Comoving Number Density

We know that galaxies do merge (e.g., Tremaine, 1980), so it is necessary if a model of galaxy counts is to be considered realistic to incorporate the effects of merging, i.e., nonconservation of comoving number density. This of course is treated in a detailed model in chapters 5 and 6, but here we consider the very simple phenomenological model of and Rocca-Volmerange & Guiderdoni (1990).[2]

In this model, what was previously considered as a single galaxy at high redshift is now considered as being a set of $(1+z)^\eta$ separate galaxies. The stellar population of each of these separate galaxies is that of the single galaxy scaled down[3] by a factor of $(1+z)^\eta$. This means that total comoving luminosity density at any redshift is conserved in this model, and any changes to the stellar population (and therefore luminosity) that one might expect to occur during merging are ignored. This model can be described by a redshift-dependent luminosity function:

$$\begin{aligned} \phi(L,z)dL &= (1+z)^\eta\,\phi(L(1+z)^\eta, z=0)\,d(L(1+z)^\eta) \\ &= (1+z)^{2\eta}\,\phi(L(1+z)^\eta, z=0)\,dL. \end{aligned} \tag{2.22}$$

Since $\phi(L)dL = \psi(M)dM$, this translates into $\psi(M)$ via

$$\begin{aligned} \phi[L(1+z)^\eta]d[(1+z)^\eta] &= \psi[M - 2{\cdot}5\eta\, log_{10}(1+z)]\,d[M - 2{\cdot}5\eta\, log_{10}(1+z)] \\ &= \psi[M - 2{\cdot}5\eta\, log_{10}(1+z)]\,dM. \end{aligned} \tag{2.23}$$

The effects of this merging parametrisation is clearly seen in Figure 2.11. As with the other factors previously discussed, the delta functions show the effect strongly, while the Schechter function shows it more weakly. While the advantage (in matching the Tyson counts) of increasing the counts at the faint end is strong, this is countered by the problem that galaxies are removed at the brighter magnitudes ($b_J \approx 24-26$), so it is not clear that this simple model is sufficient to model the counts. Rocca-Volmerange & Guiderdoni (1990) compare their models with Tyson's (1988) uncorrected counts, which are lower than the corrected counts plotted here, so they feel that their merging model with $\eta \approx 1{\cdot}5$ best satisfies the observations.

[2]Koo (1990) also considers a simple merging model, which doesn't conserve luminosity, while Broadhurst *et al.* (1992) consider a more complex (analytical) merging model.

[3]Rocca-Volmerange & Guiderdoni (1990) describe this in terms of mass, but the most obvious interpretation of their description is that this translates proportionally into luminosity.

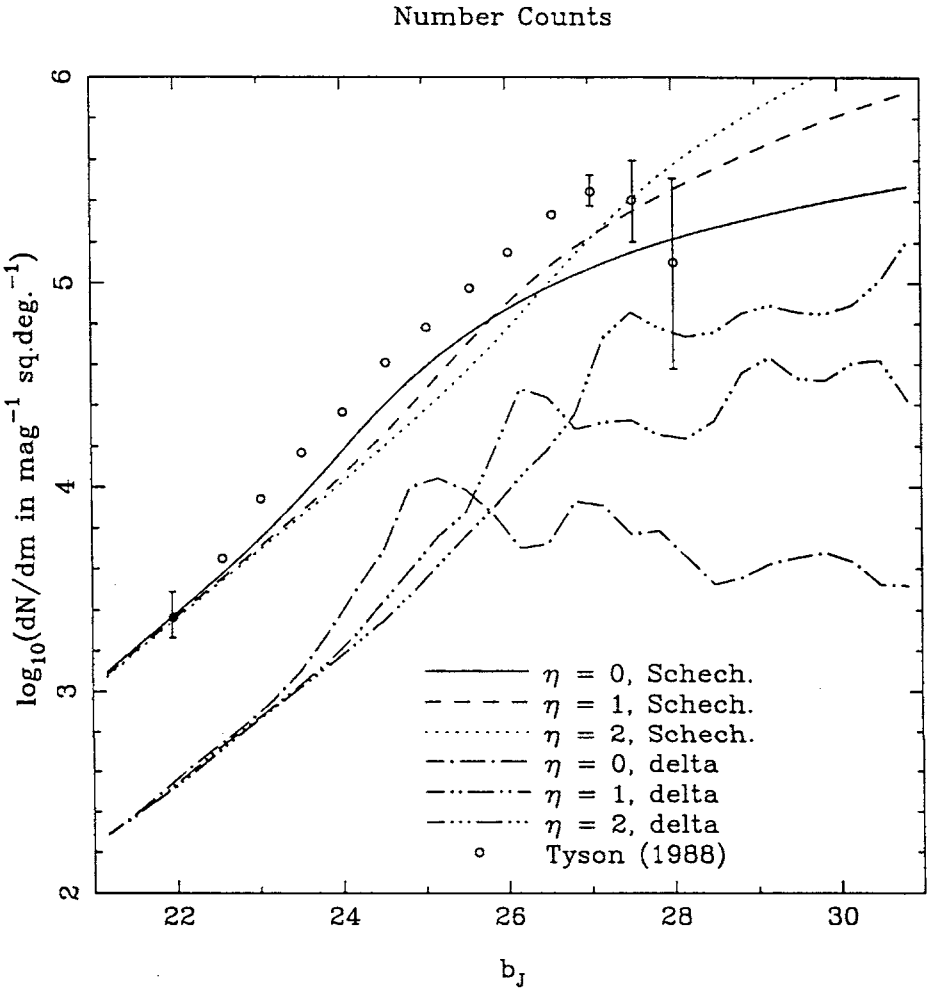

Figure 2.11: Effects of using Rocca-Volmerange & Guiderdoni's (1990) simple merging model, with the values $\eta = 0, 1, 2$ for standard Schechter and delta luminosity functions and $q_0 = 0{\cdot}5, z_f = 10{\cdot}0$.

2.7 Conclusion

The above indicate the effects of the different parameters which affect the faint number counts, dN/dm. The main significant parameter which has been found to *not* significantly affect the number counts is H_0, though relative to a naive model the effect of luminosity distance is also fairly small. The remainder, d_L, dV/dz, q_0, z_f, the K- and E- corrections, ϕ^*, M^*, α, and η all do affect the counts, but are certainly not independent of one another.

As found by the authors discussed in chapter 1, a low q_0, high z_f model is needed if galaxy comoving number density is conserved and a standard Schechter luminosity function is used. The effect of allowing merging, which changes the comoving number density, does increase the numbers at the faint end in a flat universe ($q_0 = 0{\cdot}5$) model, but the decrease in the numbers of brighter galaxies which compensates for this suggests that this simple prescription isn't quite enough to provide a good fit to the data. Hence, the more sophisticated merging model which also models evolution in the luminosity function and is discussed in chapters 5 and 6 has been developed.

Chapter 3

A Survey for Low Surface Brightness Galaxies in the Field

Abstract

We report the results of a preliminary survey for low surface brightness galaxies (LSBG's) in the field, in regions near the SGP. The objects were visually selected from film copies of SERC J Schmidt plates. Spectroscopy and photometry indicate that the resulting sample is better described as a sample of dwarf galaxies in the field than of LSBG's in the field, as the galaxies of lower surface brightness are also of lower total luminosity, similar to other studies in the Virgo and Fornax galaxy clusters. The number density of the population sampled by this survey extends to redshifts of up to $z \approx 0{\cdot}05$ and implies a density of $n \approx (9 \pm 5) \times 10^{-3} h^3 Mpc^{-3}$, which is about $7 \pm 4\%$ of the number density for normal galaxies in the corresponding magnitude range of $-14 \geq M_B \geq -20$ represented in a Schechter (1976) luminosity function having parameters $\alpha = -1{\cdot}1$, $M_B^* = -21{\cdot}1$ and $\phi^* = 1{\cdot}56 \times 10^{-2} h^3 Mpc^{-3}$. About half of the population is probably already represented in such a measurement of the general galaxy luminosity function, making the new contribution of our population fairly small.

Taking into account surface brightness dimming, and assuming that the excess of galaxies observed at $B \approx 24$ (e.g., Tyson, 1988) has a typical redshift of about $z = 0{\cdot}25$ (Cowie *et al.*, 1991), the magnitudes of the galaxies in our sample are consistent with the hypothesis that they are the low-redshift counterparts of the excess galaxies, but the diameters are not.

Hence, the population we have surveyed does not contribute significantly to the general galaxy luminosity function and is not a candidate for explaining the excess of faint galaxies.

3.1 Introduction

Knowledge of the population of galaxies which inhabits the Universe is a major element of present-day cosmological models. The present view is that while galaxies may constitute a minority of the mass density of the Universe, the fact that they are luminous means that they are the primary observable constituent of the Universe on large scales (apart from the cosmological microwave background), and hence are much better known than dark matter. The population of galaxies is most simply described as a distribution over total luminosity: the luminosity function. While there are those who argue that separate luminosity functions modelling different types of galaxies should be used in preference to a general luminosity function (e.g. Binggeli *et al.*, 1988), the Schechter (1976) luminosity function is still largely accepted as a good first order description of the observed galaxy population.

However, in view of the fact that galaxy surface brightnesses[1] are usually no more than a magnitude or two brighter than the background sky (around $22-23\,B\,mag\,arcsec^{-2}$), it has been argued (e.g., Impey *et al.*, 1988) that bivariate distributions of galaxies across both total luminosity and a surface brightness variable (such as projected central surface brightness) show that there are strong selection effects against finding either low surface brightness galaxies or galaxies which are compact enough to be difficult to distinguish from stars (i.e., galaxies having high surface brightness).

The more conventional view is that objects which have been missed due to low surface brightness are also of low total luminosity. Thuan & Seitzer (1979) find for a survey of HI-rich galaxies that Freeman's (1970) constant value of $(S_B)_0 = 21{\cdot}6 \pm 0{\cdot}3$ (for the disks of bright spirals) holds for galaxies brighter than $M_{pg} = -19$ (with the worst disagreement being 2% at $M_{pg} = -19$) even though the sample on which their survey is based goes down to a mean surface brightness of about $(S_{pg})_0 = 25\,mag\,arcsec^{-2}$. In their review of galaxy luminosity functions, while they acknowledge that their discussion assumes that there are no missing low surface brightness galaxies, Binggeli *et al.* (1988) claim that there is a correlation between absolute magnitude and surface brightness for galaxies fainter than $M_{B_T} \sim -19$, so that galaxies fainter in total luminosity have lower surface brightness.

Continuing surveys for dwarfs to very low surface brightnesses in the Virgo and Fornax galaxy clusters may affect these views. In the background of Virgo, Bothun *et al.* (1987) and Impey *et al.* (1989) found a very luminous, very low

[1] flux per solid angle

surface brightness galaxy ("Malin 1") as well as finding 137 low surface brightness galaxies, 27 of these previously undetected, down to $(S_B)_0 \lesssim 26\, mag\, arcsec^{-2}$ with $D_{27} \lesssim 100\, arcsec$ (Impey *et al.*, 1988).

In Fornax, from a sample of 145 dwarf ellipticals (Caldwell, 1987), 33 of these with surface brightnesses in the range $21{\cdot}2 \leq (S_B)_0 \leq 25{\cdot}0$ had CCD photometry taken by Caldwell & Bothun (1987). Those brighter than $(S_B)_0 = 24\, mag\, arcsec^{-2}$ have exponential profiles outside their nuclei while those fainter have a variety of profiles. Caldwell & Bothun's Figure 8 shows a reasonable correlation between total brightness and central projected surface brightness, though this is weak fainter than total magnitude $B \approx 17$ or $(S_B)_0 \approx 23$.

Davies *et al.* (1988) analysed a sample of 189 low surface brightness galaxies (LSBG's) in Fornax with projected central surface brightnesses in the range $(S_B)_0 \approx 22-24{\cdot}5$. In Davies *et al.* (1990) surface brightness profiles and grey-scale images obtained from CCD exposures of some of these objects are shown. Their central projected surface brightnesses go down to $(S_B)_0 \lesssim 26{\cdot}0$ (and $(S_R)_0 \lesssim 25{\cdot}0$).

Bothun *et al.* (1991) discuss another sample of 26 LSBG's with $(S_B)_0 \leq 26{\cdot}3$ (only 3 have $(S_B)_0 > 25{\cdot}0$). Twelve (12) of these are in the Caldwell (1987) catalogue.

These studies all imply that LSBG's cannot easily be written off as having an insignificant contribution to the general population of galaxies. Hence, the purpose of this survey was to perform a preliminary search for LSBG's in the field in order to see if their space density is high enough for them to contribute significantly to the galaxy luminosity function. If this contribution had been found to be high enough, a more ambitious and thorough survey could have been undertaken.

A more specific motive for the survey was to see if these galaxies could be the low redshift counterparts of the excess of faint galaxies observed for $B \gtrsim 24$ (e.g., Tyson, 1988, Cowie *et al.*, 1990, Lilly *et al.*, 1991 or Chapter 4). In that case, if the number density of these galaxies was also high enough, the existence of the excess of the faint galaxies could have been shown to be consistent with the theoretically popular $\Omega_0 = 1{\cdot}0, \lambda_0 = 0$ universe.

In §3.2 we discuss the selection of the objects from the Schmidt plate copies, in §3.3 we describe the spectroscopy and photometry obtained, in §3.4 a calculation indicating the space number density of the sample is explained, in §3.5 we discuss the possible significance of this survey and in §3.6 we summarise our conclusions.

3.2 Selection of Objects

Film copies of SERC J Schmidt plates for ESO/SERC field numbers 410-412, 235-237, 286-288, 341 and 342 were visually scanned for objects of between about $0{\cdot}5mm$ and $1{\cdot}0mm$ in diameter and no darker than a subjectively agreed upon shade of "light grey". Some objects which were "very light grey" but between about $1{\cdot}0mm$ and $1{\cdot}5mm$ were also included. Celestial positions were obtained by scanning these copies with a PDS microdensitometer and using known positions of bright stars. A total of 151 candidate objects were found, 65 of these being in the fields 286-288, 410 and 412. Due to observational time restrictions, most observations were made in these five fields. Of the objects in these five fields, three objects were each listed twice due to being on overlapping plates, while two other objects which should have appeared on overlapping plates in corresponding positions did not. We interpret these two objects as plate defects. This leaves a total of 60 distinct candidate objects in fields 286-288, 410 and 412. Although 6 objects which are in these five fields were not observed, an extra 6 objects which are *not* in these fields *were* observed.

The candidate objects were labelled numerically for each field (e.g. 286.05 is the fifth candidate object in field 286). Table 3.1 lists the number of candidate objects found on each plate, the number of objects on each plate for which spectra, redshifts and photometry were obtained, and the totals of these numbers over all plates and over the five plates used for the main analysis. Our object labels and x and y positions on the plate copies in mm are listed in Table 3.2.

As a cross-check, all our objects listed in Table 3.2 were compared with the ESO-Uppsala Catalogue (EUC) of Galaxies (obtained by visual inspection of ESO Quick Blue Schmidt survey plates, Lauberts, 1982) and the Surface Photometry Catalogue (SPC) of the ESO-Uppsala Galaxies (which is based on PDS micro-densitometer scans of a majority of objects in the ESO-Uppsala catalogue, Lauberts & Valentijn, 1990). Twenty two (22) of the objects in our catalogue were less than $3'$ from objects in the EUC (all but one of them less than $1'$ away) but only 4 objects from our catalogue were between $3'$ and $10'$ from an object in the EUC (all of these being more than $5'$ from an EUC object). Given the size of the objects, an error in position of about an arcminute is reasonable, but one of more than $5arcmin$ is unlikely. This would suggest that the 21 objects matched by less than an arcminute are matches of identical objects, that the object with a $2{\cdot}2'$ match is a possible match and that no other objects in our catalogue have been catalogued in the EUC. For 3 of the 21 objects, redshifts were available both from our catalogue and the EUC. These all agree within their uncertain-

Plate#	Number per plate of :			
	candidates	spectra	redshifts	photometry
235	16	1	0	–
236	19	1	0	–
237	13	1	1	–
286	10	8	5	1
287	8	6	4	1
288	16	10	2	1
342	12	2	0	–
343	13	1	0	–
410	14	14	4	2
411	13	–	–	–
412	17	16	8	2
	151	60	24	7
286, 287, 288, 410, 412 only give :				
	65	54	23	7

Table 3.1: Summary of numbers of objects found on different plates and numbers of observations. Notes: (1) 287.01=286.01, 287.03=286.02, 288.07=287.07; (2) 288.16 and 412.03 are plate defects; (3) 287.01 consists of two objects, but the spectrum of the spectrum has no identifiable emission or absorption lines; (4) Six objects not on the five fields 286,...,412 did have spectra taken (only with identifiable lines) and six objects on 286,...,412 which did have spectra taken did not have identifiable lines.

ties. This supports the statement on matching objects just made. The 22 objects with matches less than 3′ away are those labelled with an EUC designation in Table 3.2. For the objects among these for which SPC data is available but for which we do not have our own data, the SPC data is also listed Table 3.2.

As the EUC was only intended to cover objects with visual angular diameter greater than or equal to an arcminute, we would have expected fewer of our objects to appear in it. However, about two thirds of our sample are not in the EUC, so it is still useful.

An additional check we made was to see whether or not objects in the EUC or SPC which would have been expected to be found in our survey in fact were found. A search for objects in the EUC with a "classification" starting with the string "Dwarf" or with a "description" containing the letter "F " as the first or second character was made, finding seventeen objects (in the five main fields we used). Six of these objects are in our catalogue. For a central projected surface brightness search, the SPC was searched for objects having the variable "bs_oct" (described as "B central surface brightness in fit of generalized exponent to B octants") greater than or equal to 23·0 (again in the five main fields). This

Table 3.2: Catalogue of field survey for low surface brightness galaxies observed. Listed are: object names (the names according to our cataloguing system, not to be confused with the ESO-Uppsala names), x and y positions on the plate copies (i.e. distances from the western and southern edges, excluding black borders if present, in mm), right ascension and declination in 1950.0 coordinates, the wavelength shift $1+z$, the apparent magnitudes found for the objects with photometry, the colour $b-r$, absolute magnitudes found for the five objects with redshifts (for $H_0 = 100\, kms^{-1}Mpc^{-1}$), and projected central surface brightnesses in B and R estimated from the surface brightness profiles. These values are ours if available, otherwise coming from the Surface Photometry Catalogue of the ESO-Uppsala Galaxies. The latter are denoted by an asterisk (*).

object	ESO-Upp	x	y	r.a.	dec.	$1+z$	b	r	$b-r$	B	R	$(S_B)_0$	$(S_R)_0$
235.09	235 G 38	166·8	191·9	20 59 14·4	-49 40 25	—	15·7*	14·6*	1·1*			20.5*	18.2*
236.09		112·4	236·8	21 23 2·9	-48 46 36	—							
237.09	237 G 10	77·4	244·6	21 49 9·4	-48 38 6	1·018	16·3*	15·6*	0·7*			21·7*	19·2*
286.01	235 G 80	280·2	18·6	21 11 53·3	-47 49 13	1·017	15·3*	14·1*	1·2*			22·5*	21·0*
286.02		310·5	31·0	21 15 9·2	-47 33 39	1·017							
286.04		224·2	66·6	21 5 35·7	-46 58 32	1·017							
286.05	285 G 51	11·2	112·3	20 42 35·2	-46 2 1	1·009	16·1	15·5	0·5	-16·1-16·7		24	23·5
286.06		21·0	152·4	20 43 50·8	-45 17 30	—							
286.07		262·8	228·0	21 9 13·1	-43 54 54	1·017							
286.09		86·6	291·6	20 51 13·0	-42 45 37	—							
286.10		104·5	302·2	20 52 59·9	-42 33 54	—							
287.02		121·8	20·5	21 22 19·3	-47 50 40	1·031	16·5	15·6	0·9	-18·4-19·3		21	21
287.04	236 G 6	81·8	25·9	21 17 49·8	-47 43 41	1·009	14·7*	14·2*	0·5*			21·9*	21·1*
287.05		311·8	136·0	21 42 47·2	-45 37 54	1·031							
287.06		89·0	128·7	21 19 0·9	-45 49 7	1·014							
287.07	287 G 52	279·8	170·5	21 39 14·9	-45 1 19	1·007*	13·2*	12·3*	0·9*			20·9*	19·1*
287.08	287 G 37	204·9	198·2	21 31 19·6	-44 32 13	1·009*	13·7*	12·8*	1·0*			21·5*	20·3*
288.01	236 G 36	26·1	4·3	21 39 36·8	-48 5 1	—	15·2*	15·1*	0·1*			22·0*	21·6*
288.04		289·2	109·6	22 8 31·0	-46 9 19	—							
288.05	288 G 49	291·9	126·9	22 8 43·3	-45 50 12	1·037*	14·0*	13·3*	0·7*			21·7*	19·8*
288.08		232·8	186·7	22 2 16·3	-44 45 27	—							
288.09	288 IG 48	291·8	205·2	22 8 24·1	-44 21 33	1·006	16·8	16·0	0·8	-14·5-15·3		23	23
288.10		209·3	244·2	21 59 44·5	-43 41 13	—							
288.12	288 G 28	187·6	260·9	21 57 30·1	-43 22 57	1·0075	13·5*	12·6*	0·9*			20·6*	19·7*
288.13		258·0	256·2	22 4 44·1	-43 26 48	—							
288.14		300·3	256·1	22 9 4·5	-43 25 34	—							
288.15	288 G 40	246·6	275·0	22 3 31·0	-43 6 14	—	16·4*	15·6*	0·7*			24·4*	23·9*
342.02	342 G 36	224·6	117·8	21 19 2·2	-41 0 39	1·017*	15·1*	14·0*	1·1*			18·9*	16·6*
342.03		239·9	124·2	21 20 32·0	-40 52 51	—							
343.07	343 G 28	216·3	232·0	21 44 18·3	-38 56 42	1·015*	15·7*	14·9*	0·8*			22·2*	20·6*
410.01		297·0	19·5	0 34 10·7	-32 50 57	—							
410.02	410 G 5	57·8	41·0	0 12 58·3	-32 27 19	—	14·9*	14·0*	0·9*			22·9*	22·3*
410.03		302·2	63·0	0 34 30·9	-32 2 4	1·031							
410.04	410 G 18	271·5	116·8	0 31 43·2	-31 3 3	1·005	14·0*	13·4*	0·7*				
410.05		285·9	172·8	0 32 50·2	-29 59 24	—							
410.06		304·7	177·8	0 34 26·6	-29 53 22	—							
410.07		324·0	202·6	0 36 3·2	-29 24 42	1·024	17·4	16·8	0·6	-16·9-17·5		23	22
410.08		295·6	232·6	0 33 34·8	-28 52 2	—	17·3	16·2	1·1			25	24·5
410.09		293·8	251·6	0 33 22·2	-28 31 54	—							
410.10		285·4	262·8	0 32 38·0	-28 19 35	—							
410.11	410 G 12	204·4	267·9	0 25 48·1	-28 15 31	—	16·1*	15·5*	0·6*			22·3*	20·5*
410.12		222·6	284·4	0 27 18·3	-27 56 25	—							
410.13	409 IG 27	7·9	298·7	0 9 15·2	-27 38 48	—	17·9*	17·7*	0·2*			23·1*	22·6*
410.14	410 G 11	164·9	304·9	0 22 26·9	-27 34 11	1·035	17·1*	16·4*	0·8*			23·3*	22·4*

object	ESO-Upp	x	y	r.a.	dec.	$1+z$	b	r	$b-r$	B	R	$(S_B)_0$	$(S_R)_0$
					...continued...								
412.01		291·0	19·0	1 19 35·3	-32 50 56	1·023							
412.02		60·0	37·0	0 59 9·9	-32 32 22	—	18·3	17·1	1·2			23·5	22
412.04	352 G 23	203·0	39·0	1 11 45·3	-32 30 49	1·017	16·6*	15·9*	0·6*			20·8*	21·0*
412.05	413 G 3	323·0	42·0	1 22 22·0	-32 24 49	1·021	16·2*	15·4*	0·8*			22·8*	22·0*
412.06		119·0	54·0	1 4 22·1	-32 13 42	1·036							
412.07		122·0	51·0	1 4 39·8	-32 17 22	—							
412.08		230·0	68·0	1 14 8·3	-31 58 9	—							
412.09		225·5	78·5	1 13 44·8	-31 46 3	—							
412.10		236·0	110·0	1 14 39·2	-31 10 25	1·036							
412.11		131·0	136·0	1 5 26·8	-30 41 52	—							
412.12		326·0	169·0	1 22 16·9	-30 2 10	1·031							
412.13	412 G 12	176·0	196·5	1 9 21·0	-29 33 45	—	16·6*	15·6*	1·0*			23·2*	21·9*
412.14		109·0	270·0	1 3 41·3	-28 10 53	1·020							
412.15		111·0	290·0	1 3 50·8	-27 48 35	—							
412.16		300·0	297·0	1 19 43·8	-27 39 36	—							
412.17		287·0	318·0	1 18 36·4	-27 17 28	1·054	16·0	15·0	1·0	-20·1-21·1		22	21

yielded only five objects, four of these found in the EUC search, and three of these four being members of our catalogue.

All of these objects not in our catalogue were examined on the appropriate SERC Schmidt plates. Only one of these was found which came close to our selection criteria, though its nucleus was too "large and dark" for it to be included. Hence we do not appear to have missed any ESO-Uppsala objects which satisfied our criteria.

3.3 Observations

Spectra were taken using the blue and red photon counting arrays on the Double Beam Spectrograph (DBS) at the ANU's 2.3m reflector at Siding Spring, N.S.W., on 23/24 August 1990 and the nights of 22/23, 23/24, 24/25 October 1990. These were obtained for 55 of the objects in fields 286-288, 410 and 412, as well as for 6 objects in other fields.

Helium-argon, iron-argon and neon arcs were taken at the beginnings and ends of the nights as well as once or twice in between. The FIGARO data reduction package was used for calibrating the arcs, image arithmetic and fitting of the calibrated arcs to the object spectra. Using Norlén (1973) and Stathakis *et al.* (1982) as a check and backup to the FIGARO list of arc lines, the arcs were fitted with on average a 0·3Å standard deviation from a linear fit. Rows in the images containing the object spectra were added and series of nearby rows (considered to be sky background) were subtracted from these sums. This gave the object spectra, which were smoothed with a Gaussian of half-width 3 pixels and matched with the calibrated arcs. A number of these are displayed in Figure 3.1.

Emission lines in H_α and [O II] were found with a signal-to-noise of around 2:1 to 5:1 for 23 of the objects in fields 286-288, 410 and 412 and for object 237.09. In addition the H_β line was found in objects 286.05, 286.07 and 288.12, and the H and K absorption lines were found in objects 287.02 and 412.17. Wavelengths of emission lines were read off printouts with a ruler and pencil. This is accurate to about 5 Angstroms, giving the redshifts correct to $\pm 0{\cdot}001$, which is easily sufficient for the purposes of the survey. These redshifts are listed in Table 3.2.

Photometry was carried out using a GEC p8603 578×416 CCD on the ANU's 40-inch reflector at Siding Spring, N.S.W. on the night of 9/10 November 1990. A B_J filter developed at MSSSO which has slightly higher quantum efficiency than a standard B_J filter and an R filter were used. Standards from Menzies *et al.* (1989) (in regions SA114 and SA98) were observed at intervals throughout the night. The night was photometric but the seeing (FWHM) was about 5 *arcsec.*

Figure 3.1: Calibrated and smoothed spectra of objects 286.05, 287.02, 288.09, 410.07, 410.08, 412.02 and 412.17. Units of flux are photons /sec/pixel, with arbitrary scale; wavelengths are observed wavelengths in Angstroms. Emission and absorption lines from which redshifts were calculated are designated. A sky spectrum is also plotted for comparison.

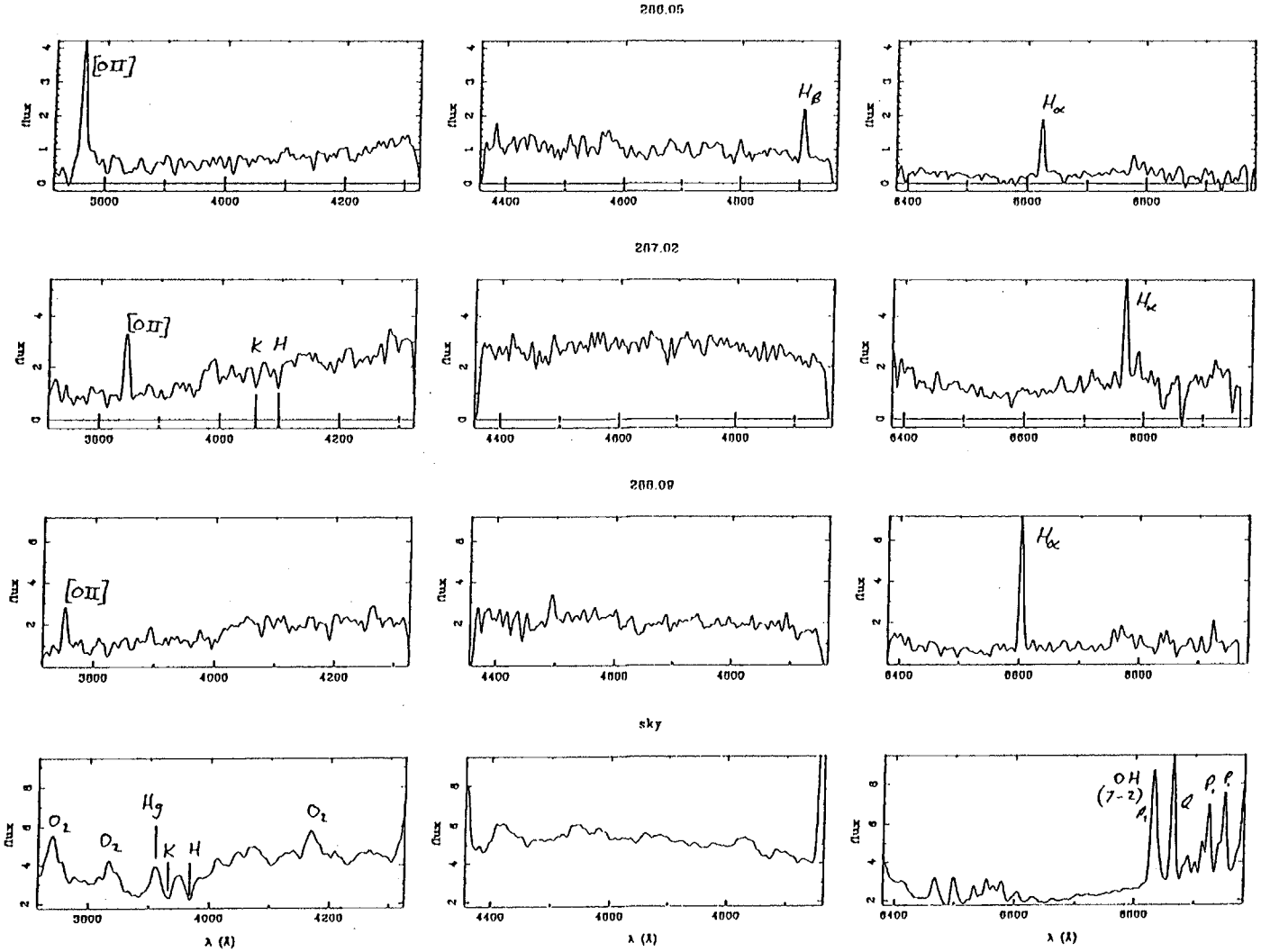
206.05
[OII]
Hβ
Hα
207.02
[OII]
K H
Hα
206.09
[OII]
Hα
sky
O2
O2
Hg
K
H
O2
OH (7-2)
flux
λ (Å)

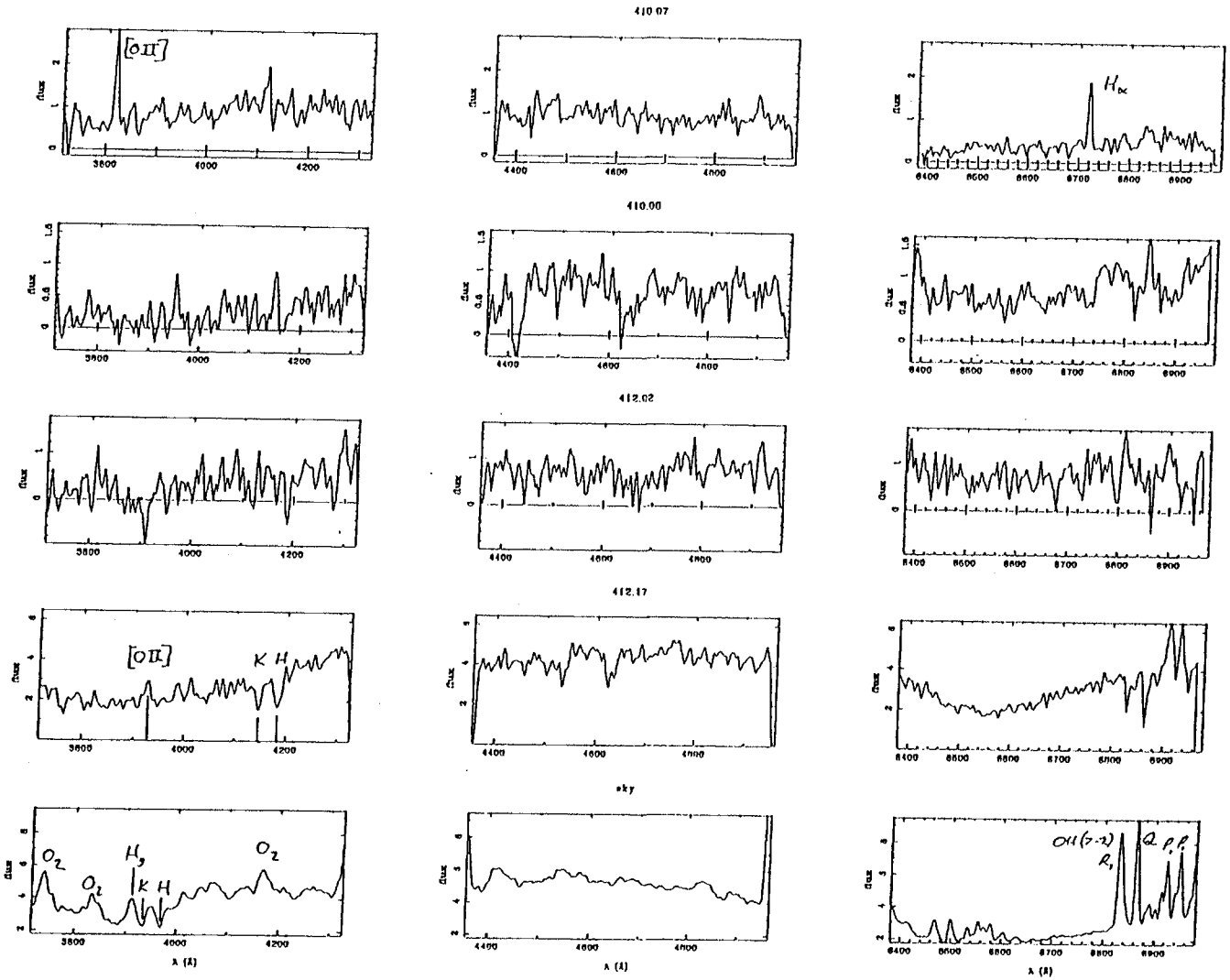
410.07
[OII]
Hα
410.00
412.02
412.17
[OII]
K H
sky
O2
O2
H
K
H
O2
OH(7-2)
R1
Q.P.
λ (Å)
λ (Å)
λ (Å)

Seven objects were imaged in both wavebands: 286.05, 287.02, 288.09, 410.07, 410.08, 412.02 and 412.17.

The images were bias-subtracted and flat-fielded using IRAF image processing software. Total magnitudes were found by summing up the light in regions containing the objects, excluding light due to cosmic rays. The isophotes corresponding to the edges of these regions vary, but lie in the ranges $26{\cdot}7 \pm 0{\cdot}8\, B\, mag\, arcsec^{-2}$ and $25{\cdot}6 \pm 1{\cdot}4\, R\, mag\, arcsec^{-2}$. Zero points, extinction and colour terms were calculated using the Menzies *et al.* (1989) standards in Johnson-Cousins B and R, enabling total magnitudes to be correct to $0{\cdot}1\, mag$. Surface brightness profiles were calculated by finding the surface brightness in successive circular annuli around the centres of the objects, with areas containing bright stars or cosmic rays excluded from the analysis. No more than about 5% of the area was excluded for any object.

These surface brightness profiles are plotted in Figure 3.2. The projected central surface brightnesses calculated from these plots (from linear fits to the outer regions), as well as apparent magnitudes, colours and absolute magnitudes (for $H_0 = 100\, kms^{-1}\, Mpc^{-1}$) are listed in Table 3.2.

3.4 Space Number Density of LSBG's

Given the small number of galaxies for which we have both redshifts and magnitudes, a V/V_{max} method (Schmidt, 1968, Binggeli *et al.*, 1988) of correcting for incompleteness cannot be applied. However, a simple estimate of the space number density of our sample can be made as follows. Suppose that the sample is complete in redshift to some redshift, z_{compl}, less than the maximum redshift in the sample. Suppose that these objects do form a population which is uniformly distributed throughout space to this redshift. Then the number of objects per redshift interval is proportional to $(1+z)^3\, dV/dz \times dz$ (i.e., $\approx z^2$ for $z < z_{compl}$). Figure 3.3 compares our data against the function $(1+z)^3\, dV/dz$ integrated over the corresponding redshift intervals for a range of normalisations. From this figure, it can be seen that the value of z_{compl} would be about $z = 0{\cdot}02$. This corresponds to a distance of $60h^{-1}Mpc$. ($h \equiv H_0/100 km\, s^{-1} Mpc^{-1}$.)

We then have to make a correction for the number of objects for which we did not obtain redshifts. Let us suppose that the objects for which we have redshifts are a representative sample of all the objects which were found in the five fields 286-288, 410 and 412. Then, for these plates, the ratio of the number of objects with (measured) redshifts less than $z = 0{\cdot}02$ to the total number of objects with (measured) redshifts should be the same as the ratio of the total

Figure 3.2: Surface brightness profiles of galaxies for which photometry was obtained. Surface brightnesses in B (left) and R (right) in $mag\,arcsec^{-2}$ are plotted against radius in arcseconds for galaxies 286.05, 287.02, 288.09, 410.07, 410.08, 412.02 and 412.17. These are values average over circular annuli. The plots for 286.05 and 288.09 also plot data from the ESO-Uppsala Surface Photometry Catalogue, plotted as plus symbols.

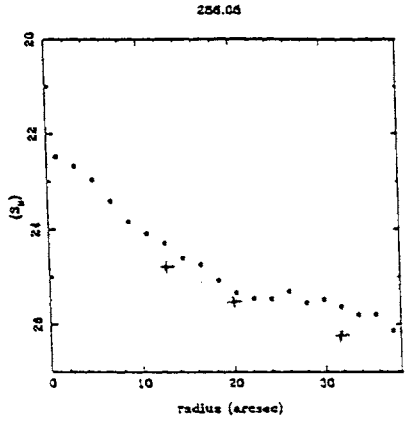
256.05
20
22
24
26
(B_M)
0
10
20
30
radius (arcsec)

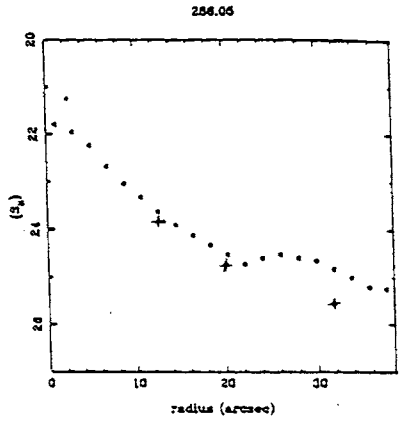
256.05
20
22
24
26
(B_M)
0
10
20
30
radius (arcsec)

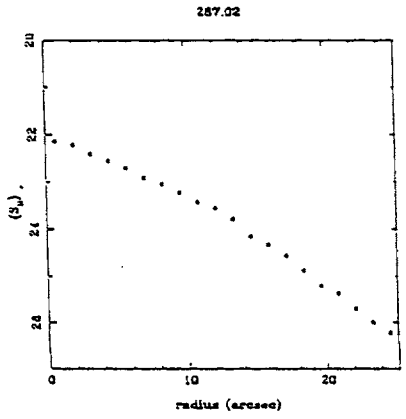
257.02
20
22
24
26
(B_M)
0
10
20
radius (arcsec)

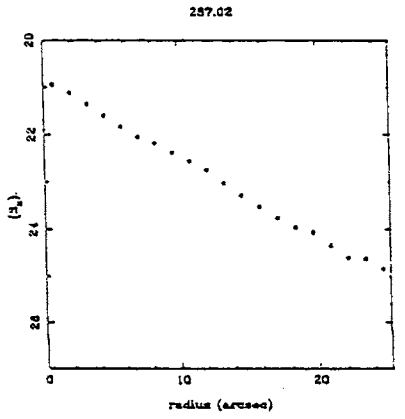
257.02
20
22
24
26
(B_M)
0
10
20
radius (arcsec)

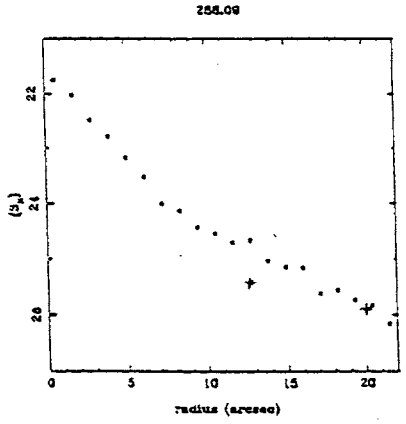
256.09
22
24
26
(B_M)
0
5
10
15
20
radius (arcsec)

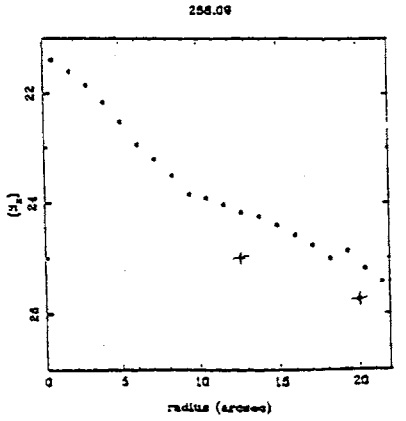
256.09
22
24
26
(B_M)
0
5
10
15
20
radius (arcsec)

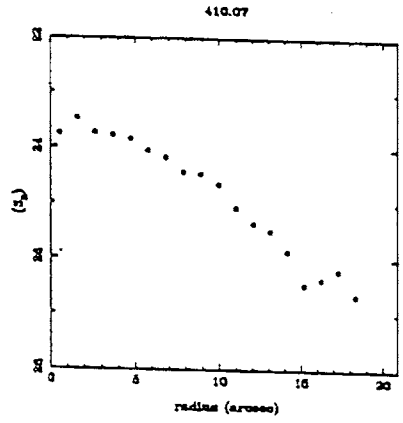
410.07
radius (arcsec)

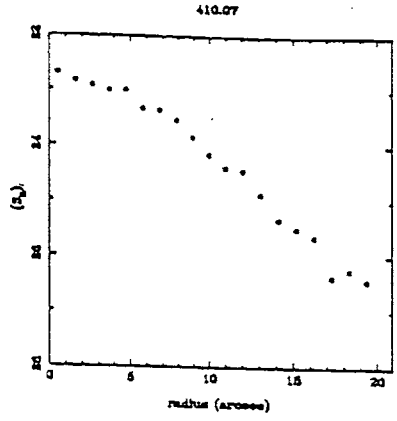
410.07
radius (arcsec)

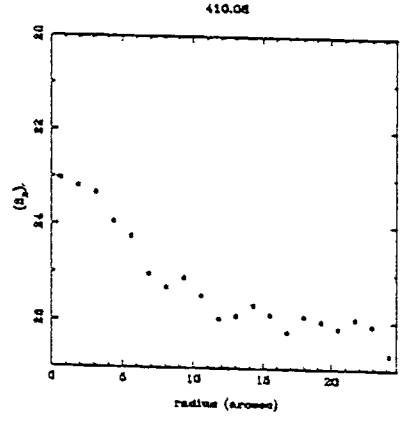
410.06
radius (arcsec)

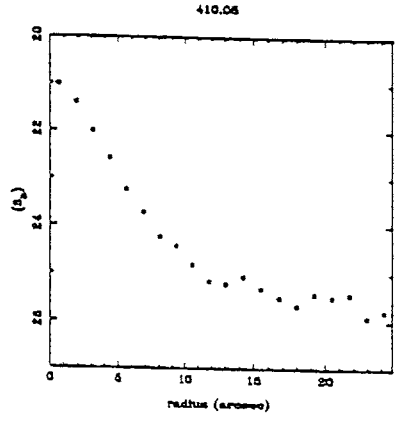
410.06
radius (arcsec)

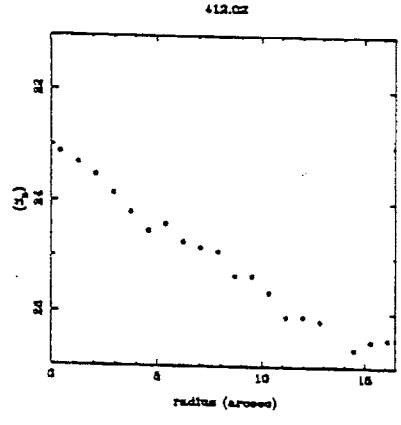
412.02
radius (arcsec)

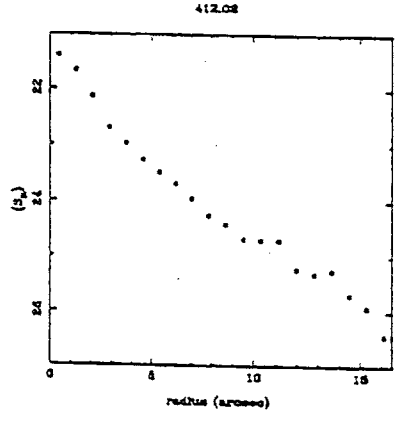
412.02
radius (arcsec)

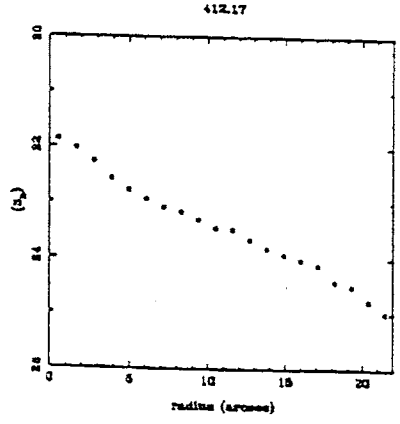
412.17
radius (arcsec)

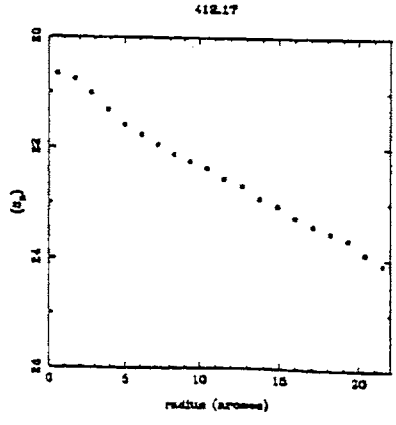
412.17
radius (arcsec)

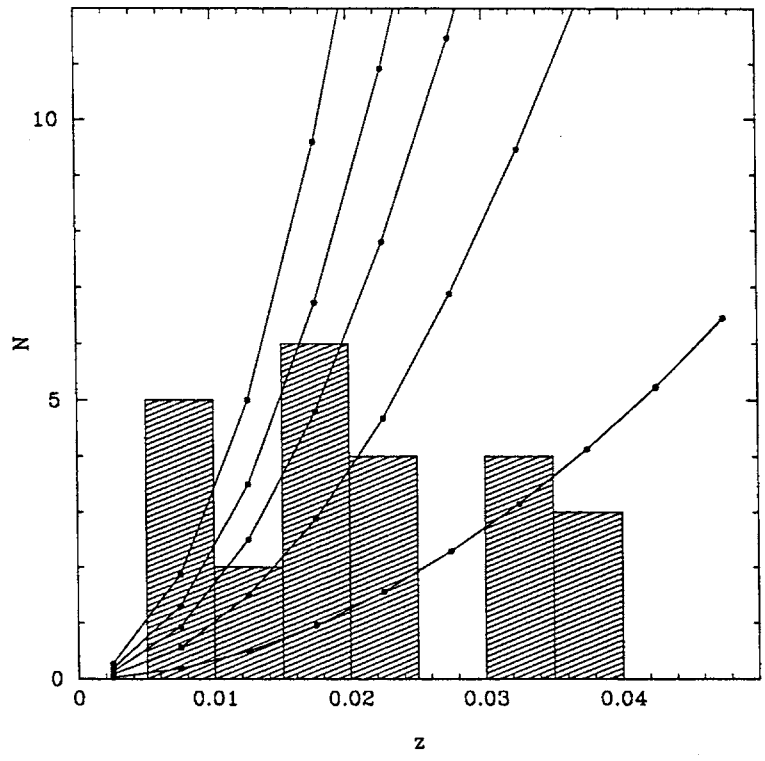

Figure 3.3: Redshift distribution of LSBG's, number per bin against redshift. Bin size is $\Delta z = 0{\cdot}005$. Lines with solid circles indicate $\int (1+z)^3\, dV/dz$ integrated over the same bins as for the data, with a range of normalisations, for $q_0 = 0{\cdot}5$. (The corresponding curves for lower values of q_0 would be virtually indistinguishable on the scale of this figure.)

number of objects closer to us than $z = 0{\cdot}02$ (whether redshifts were measured or not) to the total number of objects found on these plates (redshifts measured or not). This gives the number of objects on these plates closer to us than $z = 0{\cdot}02$ to be $\frac{13}{24}\times 65 = 35{\cdot}2$. If we assume the errors to be Poissonian, then $\sqrt{N}$ errors give a standard deviation error of 21, i.e., 35 ± 21 objects.

Each of the five plates is about $6{\cdot}5°$ square, there are overlaps between 286 and 287, and 287 and 288, of about $1{\cdot}5° \times 6{\cdot}4°$ each, and these angles are small enough to calculate solid angles simply by multiplying the one-dimensional angles. This gives the solid angle of these five plates to be $0{\cdot}058 \pm 0{\cdot}02\, ster$. The volume (comoving, in length units at t_0) to $z = 0{\cdot}02$ in this solid angle is $V = (4{\cdot}0 \pm 0{\cdot}1)\times 10^3 h^{-3} Mpc^3$. Hence the number density of this population of LSBG's is

$$n_{LSBG} \approx (9 \pm 5)\times 10^{-3} h^3 Mpc^{-3}. \tag{3.1}$$

3.5 Discussion

As this galaxy sample has been detected subjectively, it is necessary to quantify the selection criteria. As discussed below (§3.5.1, there is approximate correspondence between subjective and objective surface brightness criteria for the small number of objects with both, but those of lower surface brightness also turn out to have lower total luminosity, so that our sample does not find objects in a different part of the $(S_B)_0 - b$ plane to the dwarfs found in the Virgo and Fornax surveys. However, we still choose to compare the space density of our objects to that of the general luminosity function (§3.5.2), we discuss the possibility that the objects in our sample could be low redshift counterparts of the excess faint galaxies (Tyson, 1988) (§3.5.3) and mention the contribution of our sample to the mass density of the Universe (§3.5.4).

3.5.1 Selection Criteria

The range of the values of $(S_B)_0$ for the objects with CCD photometry shows that this subsample is comparable with the LSBG's found in the Virgo and Fornax clusters by the abovementioned authors, though not quite as faint. All of the objects on fields 410, 286, 287 and 288 originally had $(S_B)_0$ estimated by eye from the plate copies by comparison with objects of known surface brightness. For the five objects on these plates for which we have our own photometry, these estimates are a mean of $0{\cdot}6\, mag\, arcsec^{-2}$ fainter than the measured values and give an r.m.s. error $1{\cdot}1\, mag\, arcsec^{-2}$. This suggests that the (subjective) surface brightness criterion used in selection of the total sample was approximately satisfied, with a bias of about half a magnitude towards estimating $(S_B)_0$ as fainter than the measured values. However, we can take advantage of the central projected surface brightnesses available from the ESO-Uppsala Surface Photometry Catalogue (SPC). Combining these values with our own measured values, we can calculate the bias in our eye-estimated values from this larger set of seventeen objects. This shows that our eye-estimates are a mean of $0{\cdot}9\, mag\, arcsec^{-2}$ fainter than the measured values with an r.m.s. error of $1{\cdot}2\, mag\, arcsec^{-2}$.

Figure 3.4 compares the distribution of the values of $(S_B)_0$ measured by us, listed in the SPC, and estimated by eye, for galaxies in fields 410, 286, 287 and 288. Given the biassing of about a magnitude just described in the eye-estimated values of $(S_B)_0$, it is likely that our full set of eye-estimates is biassed by about this amount. If we correct for this bias in Fig. 3.4, then it is clear that the distribution of objects for which we have observed values of $(S_B)_0$ are a representative sample of all our eye-estimated objects in these four fields. It is also clear that our sample

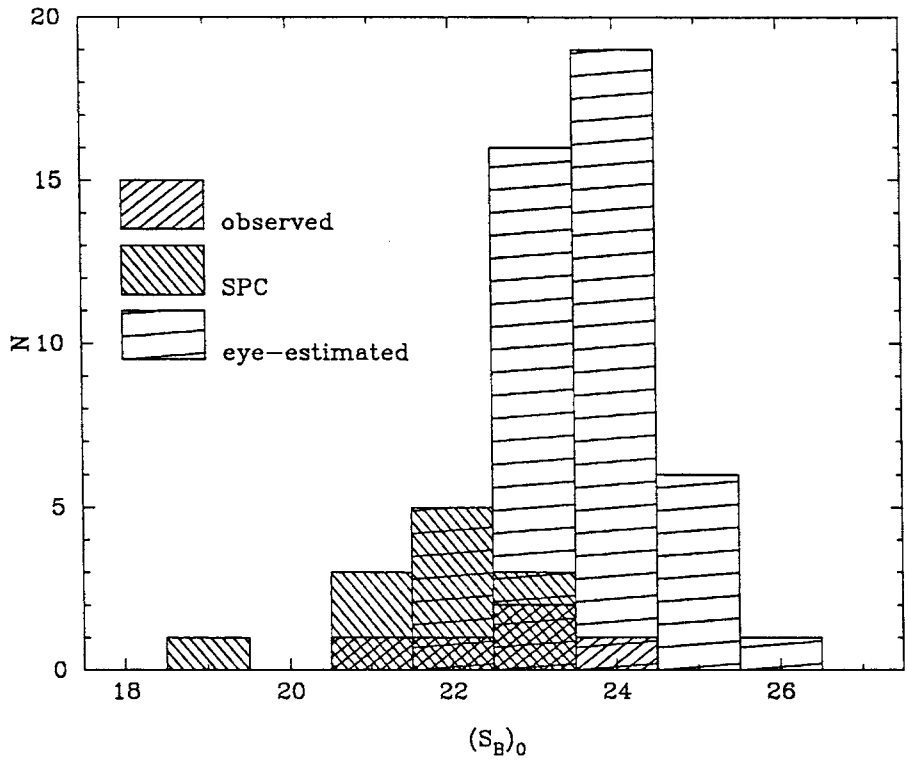

Figure 3.4: Distributions of $(S_B)_0$ for objects in fields 410, 286, 287 and 288. The distributions of values which we have from photometry, from the SPC and that we have estimated by eye are plotted as histograms.

goes about a magnitude fainter than the SPC in $(S_B)_0$.

Given that the set of objects for which we have photometry is a representative sample of the total (and extending this to field 412), we can use this set to indicate how our sample relates to other observations in the full $(S_B)_0 - b$ plane.

In Figure 3.5 the objects with both projected central surface brightness and redshifts (hence absolute magnitudes) are plotted in comparison to previous surveys of low surface brightness or low total luminosity galaxies in the $(S_B)_0 - b$ plane. SPC data was used in combination with ours where available for comparison. The previous surveys include Virgo dwarfs observed by Caldwell, (1983), Binggeli *et al.* (1984) and Ichikawa *et al.* (1986), Fornax dwarfs observed by Caldwell & Bothun (1987), the Virgo low surface brightness survey by Impey *et al.* (1987) and the dwarf Spheroidals in the Local Group (Faber & Lin, 1983). The compilation of these sources by Impey *et al.* (1987) has been used. This includes shifting the non-Virgo galaxies to the distance of Virgo assuming that Virgo is 25% further from us than Fornax, that the Virgo distance modulus is 31·7 and

using the dwarf Spheroidal distances given in Faber & Lin (1983). The points for the objects in our survey also assume distance modulus of Virgo of 31·7, and a Hubble constant of $H_0 = 100\,kms^{-1}Mpc^{-1}$ has been used.

This figure shows that the distribution of our sample, as indicated by the five points for which we have both photometry and redshifts, is consistent with that of dwarfs and the faint end of the "normal" galaxy population. The surface brightnesses of the brighter galaxies is in agreement with Thuan & Seitzer's (1979) finding that the Freeman (1970) result of constant central projected surface brightness holds for galaxies brighter than $M_{pg} \lesssim -19{\cdot}0$. Our sample has therefore turned out to be a sample of field galaxies of low total luminosity (dwarfs) rather than a set of field galaxies of ordinary total luminosity which have significantly lower $(S_B)_0$ values than other observations to date. As in Fig. 3.4, the distribution of our galaxies for which SPC data is available can be seen to be brighter in $(S_B)_0$ than our full sample; and also brighter in absolute magnitude.

3.5.2 Significance of Galaxy Number Density

The galaxy number density calculated above (eqn (3.1)) does not appear to be large in comparison to the present number density of galaxies known from recent redshift surveys and described by the standard Schechter (1976) luminosity function,

$$\int_{L=L_{min}}^{\infty} \phi(L)d(L/L^*) = \phi^* \int_{L=L_{min}}^{\infty} (L/L^*)^{\alpha} e^{-(L/L^*)}\, d(L/L^*),$$

although it is large enough that it should not be ignored.

This integral can be evaluated as follows. From the calibration of Efstathiou *et al.* (1988), let us use $\alpha = -1{\cdot}1$, $M_B^* = -21{\cdot}1$ and $\phi^* = 1{\cdot}56 \times 10^{-2}h^3Mpc^{-3}$. Binggeli *et al.* (1988, pp537, 538) consider $\alpha = -1{\cdot}25$ as the likely value for cluster luminosity functions and $\alpha \approx -1{\cdot}0$ as a likely (but as yet uncertain) value for field galaxies; let us also consider these as extremum values. Some of our LSBG's do appear to lie in distant clusters, so this should give a realistic range of appropriate faint end slopes. As our galaxy sample includes galaxies ranging from about $M_B = -14$ to $M_B = -20$ (see Table 3.2), it is relevant to consider the integral of the Schechter function from $M_B = -14$ to $M_B = -20$ as well as the total integral from $M_B = -14$ to $M_B = \infty$. These values are listed in Table 3.3.

This gives the survey number density to be $7 \pm 4\%$ of the previously accepted number density in the magnitude range $-14 \geq M_B \geq -20$ for $\alpha = -1{\cdot}1$, $11 \pm 6\%$ for the field slope $\alpha = -1{\cdot}0$ and $4 \pm 2\%$ for the cluster slope $\alpha = -1{\cdot}25$. Exactly what proportion of galaxies comparable to those in our survey are represented in evaluations of the general galaxy luminosity function (e.g. Binggeli *et al.*, 1988)

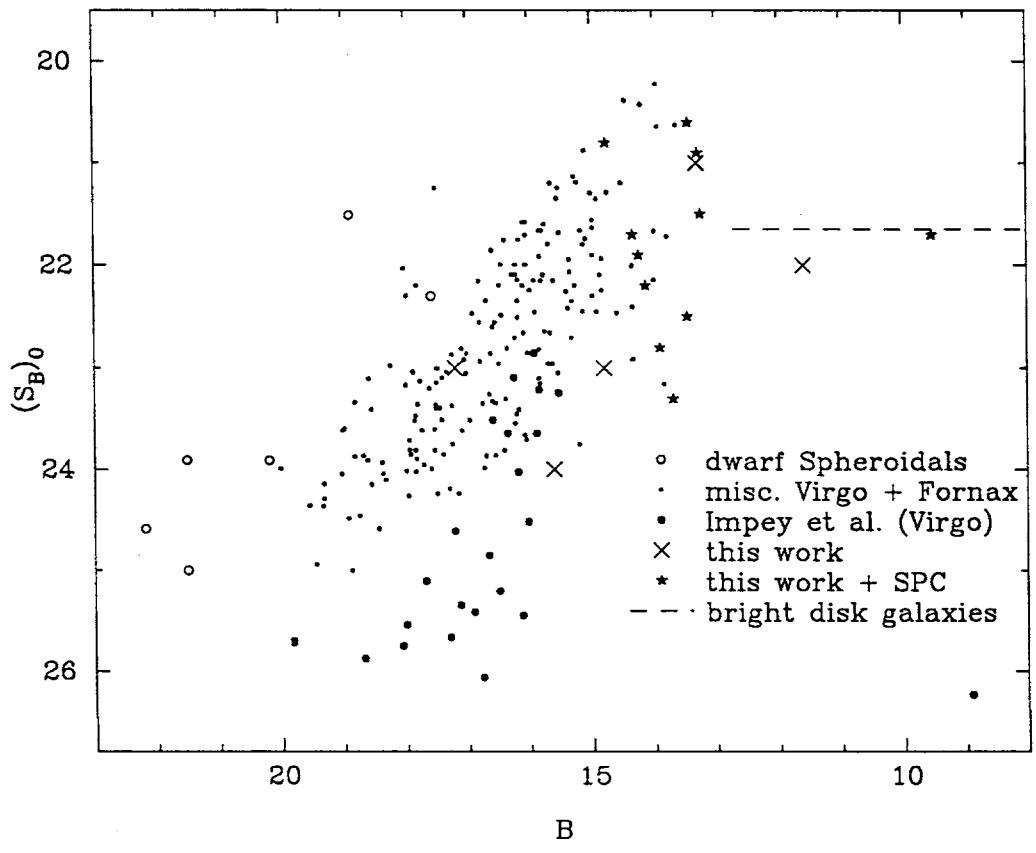

Figure 3.5: Plot of central projected surface brightness ($(S_B)_0$) versus apparent magnitude of galaxies (B) at the distance of the Virgo cluster. Discussion of the various samples is made in the text. The symbol for miscellaneous Virgo and Fornax dwarfs combines the Caldwell, (1983), Binggeli *et al.* (1984), Ichikawa *et al.* (1986) and Caldwell & Bothun (1987) samples. The Impey *et al.* (Virgo) sample refers to Impey *et al.* (1987). The line indicating the central projected surface brightness of the disks of bright disk galaxies uses the value $(S_B)_0 = 21{\cdot}65$ (Freeman, 1970) for galaxies brighter than $B \approx -19{\cdot}0$ (Thuan & Seitzer, 1979, using $M_{pg} \approx M_B$).

$\frac{L_{min}}{L^*}$	$\frac{L_{max}}{L^*}$	$M_{B_{max}}$	$M_{B_{min}}$	α	$\int_{\frac{L_{min}}{L^*}}^{\frac{L_{max}}{L^*}} \phi(\frac{L}{L^*})\, d(\frac{L}{L^*})$
					(in units $h^3 Mpc^{-3}$)
$10^{-2\cdot8}$	$10^{-1\cdot6}$	-14	-20	$-1\cdot1$	$1\cdot2\times10^{-1}$
$10^{-2\cdot8}$	∞	-14	$-\infty$	$-1\cdot1$	$1\cdot3\times10^{-1}$
$10^{-2\cdot8}$	$10^{-1\cdot6}$	-14	-20	$-1\cdot0$	$8\cdot1\times10^{-2}$
$10^{-2\cdot8}$	∞	-14	$-\infty$	$-1\cdot0$	$9\cdot3\times10^{-2}$
$10^{-2\cdot8}$	$10^{-1\cdot6}$	-14	-20	$-1\cdot25$	$2\cdot3\times10^{-1}$
$10^{-2\cdot8}$	∞	-14	$-\infty$	$-1\cdot25$	$2\cdot4\times10^{-1}$

Table 3.3: Integrals of the luminosity function.

is not straightforward to determine quantitatively as redshift surveys are not normally published with projected central surface brightness values.

However, consider, for example, the AARS survey (Peterson *et al.*, 1986). The limiting isophotes for the galaxies chosen for the survey are $23\cdot6\, B_J\, mag\, arcsec^{-2}$. From Fig. 3.4, keeping in mind the bias of our eye-estimates of $(S_B)_0$ of about $0\cdot9\, mag\, arcsec^{-2}$, it can be inferred that about half of our sample has $(S_B)_0 \lesssim 22\cdot5$. That is, about half our sample has projected central surface brightnesses at least a magnitude greater than the survey limiting isophote. If objects similar to these had been observed in the AARS survey, loss of light below the $23\cdot6\, B_J\, mag\, arcsec^{-2}$ isophote would have caused at most about a magnitude loss in the estimate of their total magnitudes (see Figure 4a, Peterson & Yoshii, 1992). In contrast, any objects similar to those of our galaxies in the fainter half of our sample would either have drastic magnitude loss or be totally omitted from the survey.

Hence, our sample would appear to add to the presently accepted faint end of the galaxy luminosity function as represented by the Peterson *et al.* (1988) survey, though by a small amount.

3.5.3 Faint Galaxy Excess Candidature

An original motivation for this study was to see if LSBG's could contribute to the population of "faint blue galaxies" as observed by Tyson (1988), Cowie *et al.* (1990), Lilly *et al.* (1991) and others, as well as the observations described in Chapter 4. A simple numerical calculation indicates that our LSBG's do not appear to form part of the excess population as observed by these authors.

Suppose we take a "typical" redshift of our LSBG's to be $z = 0\cdot02$. Cowie *et al.* (1991) find that the galaxy excess above no-evolution models at $23 < B < 24$ has $z \approx 0\cdot25$. The excess above evolution models at $23 < B < 24$ is of course less than

that above no-evolution models (e.g. Yoshii & Peterson, 1991), but Cowie *et al.* (1991) consider the excess population to be anywhere from 30-80% of the total population in this magnitude interval. (Their median redshift for galaxies in the interval is $z \approx 0{\cdot}4$.) Consider, then, that our "typical" LSBG has been displaced to $z = 0{\cdot}25$. The following show that (a) its total magnitude is consistent with that of the "faint blue galaxy" excess, but that (b) its diameter is not. (Due to the small galaxy size and noise per pixel of our own faint galaxy sample (Chapter 4), it seems more robust to compare diameters rather than central projected surface brightnesses.)

(a) Most of our galaxies have $16 \lesssim B \lesssim 18$. If galaxies similar to these occur at $z = 0{\cdot}25$ instead of $z = 0{\cdot}02$, then their total magnitudes are fainter by $5{\cdot}5\,mag$ due to the increase in distance. (A full luminosity distance calculation with $q_0 = 0{\cdot}5$ corrects this by only $0{\cdot}11\,mag$.) Due to the fact that the light is redshifted, a "K-correction" dependent on the shape of the spectrum is also needed; and to take spectral evolution of the galaxy into account, an "E-correction" is needed. However, the K- and E-corrections are dependent on galaxy type, the LSBG's may not have star formation histories similar to "standard" spirals and ellipticals, and the $B - R$ colours of our LSBG's range from 0·5 to 1·2, spanning the whole range of normal galaxy colours (e.g., see Table 1 or Table 2 of Yoshii & Peterson, 1991), so there is no clearly correct single value to use here. A reasonable estimate would be to take the combined (E + K)-corrections plotted in Figure 4 of Yoshii & Peterson, 1991 for the $q_0 = 0{\cdot}5$ model—these lie between about $0{\cdot}3\,mag$ and $0{\cdot}8\,mag$ over a full range of galaxy types.

If we take an (E + K)-correction of $0{\cdot}5\,mag$, the total magnitude of one of our LSBG's displaced to $z = 0{\cdot}25$ would be in the range $22 \lesssim B \lesssim 24$, which is consistent with the population from which we chose $z = 0{\cdot}25$ to start off with.

(b) Although for low redshifts ($z \ll 1$) surface brightness is to a very good approximation independent of distance for a fixed point on a galaxy, for higher redshifts surface brightness starts decreasing due to the decrease in energy per photon of $(1 + z)$, the time delay effect of $(1 + z)$, a $(1 + z)$ increase in the diameter (over what would be expected in a static universe) and the E- and K-corrections. The total of this is a decrease in surface brightness by a factor of $(1 + z)^4$ in addition to the E- and K-corrections. This needs to be kept in mind in considering the diameters of galaxies at high redshifts. It is also relevant for the possibility that the surface brightness of the outer parts of a galaxy drops so low that a significant part of the luminosity of a galaxy falls outside of the threshold isophote, in which case the measured galaxy magnitude is fainter than its "true" total magnitude. However, in our case this loss is only about $0{\cdot}2\,mag$

for an elliptical or $0{\cdot}3\,mag$ for a spiral (using Figure 4 of Peterson & Yoshii, 1992 and the isophotes calculated below).

To account for this surface brightness dimming, we transform the limiting isophotes to which the faint galaxies are measure to what those isophotes would be at $z = 0{\cdot}02$, assuming that they have in fact been measured at $z = 0{\cdot}25$.

Our faint galaxy sample (Chapter 4) is in the V band rather than B, but given that the galaxies range from $B - V \approx 0{\cdot}4$ to $B - V \approx 1{\cdot}0$ (e.g. see Mitton, 1976) this can be taken into account. We consider galaxies with $23 < B < 24$ in the region labelled R_2, which has a detection threshold of 14·0 counts per pixel, i.e., $27{\cdot}6\,V\,mag\,arcsec^{-2}$, i.e., between $28{\cdot}0\,B\,mag\,arcsec^{-2}$ and $28{\cdot}6\,B\,mag\,arcsec^{-2}$ depending on galaxy type. From a scatter plot of galaxy areas against magnitudes, it can be seen that this population has diameters in the range $4{\cdot}5 \pm 0{\cdot}8\,arcsec$.

Surface brightness dimming of $10\,log_{10}(1{\cdot}25/1{\cdot}02) = 0{\cdot}9\,mag\,arcsec^{-2}$ relative to $z = 0{\cdot}02$ and an (E + K)-correction of 0·3 to $0{\cdot}8\,mag\,arcsec^{-2}$ means that the isophote used corresponds to an isophote at $z = 0{\cdot}02$ between extreme limits of $26{\cdot}3\,B\,mag\,arcsec^{-2}$ and $27{\cdot}4\,B\,mag\,arcsec^{-2}$.

Take the centre of this range to be an isophote of $26{\cdot}8B\,mag\,arcsec^{-2}$. We then need to examine the diameters of the seven LSBG's in Fig. 3.2 at this isophote. These diameters turn out to have a mean and standard deviation of $66 \pm 22\,arcsec$. (Note that this is nearly exactly $1{\cdot}0mm$ on the SERC plates. An analysis of the originally estimated visual diameters shows that these occurred at an isophote of about $25{\cdot}1 \pm 0{\cdot}3\,mag\,arcsec^{-2}$.)

We then shift these diameters back to $z = 0{\cdot}25$ for comparison with those of the faint galaxies. At $z = 0{\cdot}25$, the LSBG diameters are reduced by a factor of $0{\cdot}25/0{\cdot}02 = 12{\cdot}5$ (and by an additional factor of 1·05 if the full luminosity distance calculation is used) but expanded by 1·25 due to the redshift. This gives a range of $6{\cdot}3 \pm 2{\cdot}1\,arcsec$ if our LSBG's were shifted to $z = 0{\cdot}25$. While this range certainly includes the range of diameters of our faint objects, it is much larger. If there were many LSBG's like ours at $z = 0{\cdot}25$, then there would be many of them with $23 \lesssim B \lesssim 24$ with diameters larger than $6{\cdot}3\,arcsec$, i.e., more than $2{\cdot}25\sigma$ greater than the $4{\cdot}5\,arcsec$ which is the mean in our data. These do not appear in our data, so as a population they either did not exist at $z = 0{\cdot}25$, or they have significantly evolved in either luminosity or size since that epoch.

Hence, considering both their (a) total magnitudes and (b) diameters, our sample objects do not appear likely to account for the excess of faint galaxies, as they are too large. This is, of course, based on Cowie *et al.*'s (1991) typical redshift of an excess faint galaxy. Moving our displaced LSBG to a higher redshift

$\frac{L_{min}}{L^*}$	$\frac{L_{max}}{L^*}$	$M_{B_{max}}$	$M_{B_{min}}$	α	$\int_{\frac{L_{min}}{L^*}}^{\frac{L_{max}}{L^*}} \frac{M}{L} L^* \phi(\frac{L}{L^*})\, d(\frac{L}{L^*})$	
					(in units $M_\odot h^3 Mpc^{-3}$)	(in units ρ_c)
$10^{-2\cdot8}$	$10^{-1\cdot6}$	-14	-20	$-1\cdot1$	$2\cdot1\times10^{9}$	$7\cdot6\times10^{-3}h$
$10^{-2\cdot8}$	∞	-14	$-\infty$	$-1\cdot1$	$6\cdot0\times10^{9}$	$2\cdot2\times10^{-2}h$
$10^{-2\cdot8}$	$10^{-1\cdot6}$	-14	-20	$-1\cdot0$	$1\cdot7\times10^{9}$	$6\cdot2\times10^{-3}h$
$10^{-2\cdot8}$	∞	-14	$-\infty$	$-1\cdot0$	$5\cdot7\times10^{9}$	$2\cdot0\times10^{-2}h$
$10^{-2\cdot8}$	$10^{-1\cdot6}$	-14	-20	$-1\cdot25$	$3\cdot0\times10^{9}$	$1\cdot1\times10^{-2}h$
$10^{-2\cdot8}$	∞	-14	$-\infty$	$-1\cdot25$	$6\cdot9\times10^{9}$	$2\cdot5\times10^{-2}h$

Table 3.4: Total mass densities.

would reduce its diameter and make its magnitude fainter, possibly bringing these into agreement with those of the excess faint galaxies.

3.5.4 Mass Contribution

As the number density of our LSBG's is not large compared to the general galaxy population and our LSBG's presumably have typical mass-to-luminosity ratios, it wouldn't be expected that they significantly contribute to the mass density of the Universe. If we use a constant mass-to-light ratio of, say, $M/L = 10$ and integrate mass over the luminosity function for the same parameters as done above in the number density calculation, then we have the values listed in Table 3.4.

Hence the contribution to Ω_0 according to the standard luminosity function and assuming $M/L = 10$ for the magnitude range corresponding to our LSBG's is $(8^{+3}_{-1})\times10^{-3}h$. (The integrated contribution across the whole magnitude range is $(2\cdot2 \pm 0\cdot3)\times10^{-2}h$.) Since our sample forms about $7 \pm 4\%$ of the galaxies in their magnitude range, if we assume that the detailed number distribution with respect to magnitude is proportional to that of other galaxies, then their mass density is $7 \pm 4\%$ of $(8^{+3}_{-1})\times10^{-3}h$, i.e., $6 \pm 4\times10^{-4}h$. This is small relative to the total baryonic component of Ω_0.

3.6 Conclusions

Our conclusions from this preliminary survey for low surface brightness galaxies (LSBG's) in the field can be summarised as follows.

Of 60 objects for which we obtained spectra, 24 have emission lines (mostly H_α and [O II]) and two also have H and K absorption lines. The redshifts indicated

by these lines extend up to $z \approx 0{\cdot}05$, and under the assumption that the sample is complete to about $z = 0{\cdot}02$, a number density of $(9 \pm 5){\times}10^{-3}h^3Mpc^{-3}$ was derived. The absolute magnitude range of the sample is about $-14 \geq M_B \geq -20$. If we use a Schechter (1976) luminosity function having parameters $\alpha = -1{\cdot}1$, $M_B^* = -21{\cdot}1$ and $\phi^* = 1{\cdot}56 \times 10^{-2}h^3Mpc^{-3}$ (Efstathiou *et al.*, 1988), then our galaxy sample comprises only about $7 \pm 4\%$ of the number density of the galaxies represented in this magnitude range by this luminosity function.

Though we only have photometry for a small number of objects, by combining this with data from the ESO-Uppsala Surface Photometry Catalogue we found that those objects for which we have photometry were representative of the full sample. These indicate that the galaxies of lower (central projected) surface brightness were also of lower total luminosity, occupying a similar part of the $(S_B)_0 - b$ plane to that occupied by dwarfs/LSBG's found in a range of surveys in the Virgo and Fornax clusters. Comparison with a determination of the general galaxy luminosity function such as the Peterson *et al.* (1986) survey indicates that about half our sample would be included in such a survey while the other half would either have total luminosity severely underestimated by several magnitudes or be totally omitted. Hence, the overall luminosity function in the magnitude range $-14 \geq M_B \geq -20$ would be only increased by about half of $7 \pm 4\%$, or $4 \pm 2\%$. As the slope of the luminosity function may be between $\alpha = -1{\cdot}0$ and $\alpha = -1{\cdot}25$, this is not a significant contribution.

Even supposing that the number density was higher, a comparison of magnitudes and diameters of our objects to those of the excess of faint galaxies (Tyson, 1988) showed that while the magnitudes are consistent, the diameters of our objects are about 50% too large. This comparison took account $(1+z)^4$ and E- and K-correction surface brightness dimming and used Cowie *et al.*'s (1991) typical redshift of the excess galaxies of $z = 0{\cdot}25$.

As our sample doesn't contribute much to the number density, it doesn't contribute much to the mass density in the Universe either. Assuming a mass-to-light ratio of 10, the contribution to Ω_0 is only $6 \pm 4{\times}10^{-4}h$.

Chapter 4

The Observed Correlation Function of Faint Galaxies

Abstract

Measurements of the two-point angular autocorrelation function of galaxies down to median magnitudes of $V \approx 24{\cdot}5$ from observations of a field containing Tyson & Seitzer's (1988) SGP field are described. While the uncertainties are large, these measurements suggest that the amplitude of the angular correlation function continues to decrease with decreasing median magnitude as has been observed for brighter samples. The measurements do not confirm Neuschaefer *et al.*'s (1991) amplitudes which increase for magnitudes fainter than $V \approx 24{\cdot}5$. They are consistent within the calculated uncertainties with Efstathiou *et al.*'s (1991) result, but within the calculated uncertainties they are also consistent with a totally uncorrelated distribution.

However, if the uncertainties are assumed to have been greatly overestimated, then the values of the amplitude would be significantly lower than Efstathiou *et al.*'s, and these measurements would then indicate that clustering growth is faster than it would be if clustering was fixed in proper coordinates. This result is consistent with both N-body model predictions (Melott, 1992, Yoshii *et al.*, 1993) and an observational measurement of the growth rate of the spatial correlation function (Warren *et al.*, 1993).

4.1 Introduction

The two-point angular autocorrelation function ($w(\theta)$) has recently been measured for faint limiting magnitudes by several authors (Koo & Szalay, 1984, Efstathiou *et al.*, 1991, Neuschaefer *et al.*, 1991, Couch *et al.*, 1992, Roche *et al.*, 1992), as it provides an alternative to total number counts as a deep probe into the structure of the galaxy distribution over our past time cone.

As for brighter magnitudes, these results are consistent with power law expressions for the correlation function, i.e.,

$$w(\theta) = A_w \left(\frac{\theta}{\theta_0}\right)^{1-\gamma}, \quad 1-\gamma \approx -0{\cdot}8. \tag{4.1}$$

The amplitudes, A_w, for the brighter median magnitudes are found to fall on a nearly straight line in the $\log(A_w)$-magnitude plane (Fig. 4.9, consistent with a scaling relation, e.g., Groth & Peebles (1977). This scaling with the depth of the sample can be easily thought of as being due to two factors. For galaxies separated by a fixed angle, the greater the distance these galaxies are from the observer, the greater will be their separation perpendicular to the line of sight. As the correlation function decreases with separation, galaxies further away will therefore be less correlated for a given angle, hence the amplitude will be lower. The second effect decreasing the amplitude is that galaxy slices at large separations along the line of sight will be uncorrelated with respect to each other, so in projection their individual correlations will be diluted.

The two faintest sets of observations apart from ours are those of Neuschaefer *et al.* (1991) and Efstathiou *et al.* (1991). The former finds a dramatic rise in the amplitude for very faint magnitudes, while the data point of the latter suggests that the slope of this relation decreases slightly. We discuss these in comparison to our results below.

These amplitudes of the measured correlation functions have been compared to the expected amplitudes of the correlation function as a function of limiting or median magnitude, calculated according to descriptions of the evolution of the spatial correlation function ($\xi(r)$) and to different universe geometries. Efstathiou *et al.* (1991) find that unless the majority of the faint blue galaxies belong to a weakly clustered, intrinsically faint, new population, either $\xi(r)$ evolves faster than predicted by CDM N-body models or an $\Omega_0 = 1$, $\lambda = 0$ geometry is ruled out.[1]

On the other hand, Yoshii *et al.* (1993) find that for CDM N-body predicted evolution of $\xi(r)$, the observations are consistent with an $\Omega_0 = 1$, $\lambda_0 = 0$ geometry,

[1] $\lambda_0 = (\Lambda c^2)/(3H_0^2)$ is the normalised cosmological constant.

as well as with an $\Omega_0 = 0{\cdot}2$, $\lambda_0 = 0{\cdot}8$ geometry.

The processes of reducing the CCD data, synthesising an image from the mosaic, detecting objects and calculating the correlation function vary between authors, so these are discussed in detail in this chapter. I discuss our observations and detection of images in § 4.2, the definition and method of calculating the correlation function in § 4.3 the resulting correlation functions in § 4.4 and I compare these results to previous observations and model values in § 4.5.

4.2 Observations

The images were taken by B.A. Peterson and J.Silk during a dark night, 18/19 April 1991, on the Anglo-Australian Telescope at Siding Spring, N.S.W., Australia, with a Thompson 1024x1024 pixel CCD. The F/1 prime focus was used so that the CCD covered a square field of about 17 arcminutes on a side. In order to improve flatfielding of the data, observations were made in several positions slightly offset from one another. There are seven of these positions: a central position which includes Tyson & Seitzer's (1988) "SGP" field and six positions displaced from this one by about 3 arcminutes in different directions in approximately a hexagonal shape. Five 400s exposures were made in each of the displaced positions and nine 400s exposures were made in the central position. The individual exposures within each position were offset from each other by several pixels. This resulted in a total of thirty nine separate images. Exposures on the E1, E2 and E9 standard UBVRI stars from Graham (1982) bracketted these observations and were used for photometric calibration.

The combination of these individual images can be desribed as follows.

A median flat is created using one image from each of the seven positions. Each of the thirty nine individual images is bias-subtracted and then divided by this median flat. The images resulting from this have flat backgrounds, although at high contrast, wings of bright stars extend many arcminutes. The seeing was about $1{\cdot}75''$. As each of these five (or nine) resultant images has been slightly offset from one another, these are shifted in order to have objects at matching positions. The shifting is determined by comparing the positions of bright and medium bright stars in the different images. These slightly shifted images are then combined by taking a median at each pixel. Because of the shifts, the averaging process effectively occurs over physically different pixels. A side effect of this process is that for the image resulting at this stage at any of the seven positions, there are edge regions which are not the intersection of all five (nine) exposures. These edge regions are trimmed off. This results in seven trimmed

images. Each of these is copied into a larger blank image with its position within the blank determined by comparing the positions of bright and medium bright stars in different images, as for the earlier object matching.

This results in a new set of seven images. Each of these is the same size and contains a blank area around the region with data, and any astronomical objects appearing in any of the images now appear at the same pixel position in each of the images which has data at that position. The final "mosaic" image is then created by assigning to each pixel the mean of the pixels in all the images which have a nonzero value at the position of that pixel.

This resulting mosaic image, (Figure 4.1) has good signal-to-noise at its centre, but worsening signal-to-noise moving outwards towards the edges due to the pixels being combinations of less total observing time and fewer images. As described in the following section, I chose different subregions of this final processed image for image analysis.

4.2.1 Detection of Galaxies

Four regions of this mosaic image were chosen for detailed analysis, which I label R_0, R_1, R_2, R_3. The first of these, R_0, corresponds approximately to Tyson & Seitzer's (1988) "SGP" field, ($\approx 2{\cdot}6' \times 4{\cdot}7'$), R_1 is the region in which the fields in all seven positions overlap, ($9{\cdot}6' \times 8{\cdot}7'$), R_2 is the rectangular region in which at every point images from at least three positions overlap, ($16{\cdot}6' \times 16{\cdot}9'$), while R_3 is a large rectangular region ($24' \times 2l'$) taking up about 90% of the total area of the master image but avoiding some of the edge regions with the worst noise. The areas of regions R_0 to R_3 are 0·0034, 0·02, 0·078 and 0·14 square degrees respectively.

R_0 was chosen for the purpose of comparison with Tyson & Seitzer's field (further analysed by Tyson, 1988); R_1 was chosen as the area with the optimal signal-to-noise (due to effective exposure of 15600 seconds); R_3 was chosen as the largest region which excluded the noisiest edges of the mosaic; while R_2 was chosen as a compromise between exposure time and area.

For each of these regions, APM image processing software (Irwin, 1985) was used to flatten large-scale variation in the backgrounds (program FLAT) and to find all objects above a given minimum pixel area (area threshold) and above a given number of counts above the sky (intensity threshold), deconvolving overlapped objects in the process (program IMAGES). Flattening was found to work best for our purposes with a pixel background analysis size of eight pixels and the sky was reset to zero.

Figure 4.2 shows the region R_1 after the flattening process. As is clear from

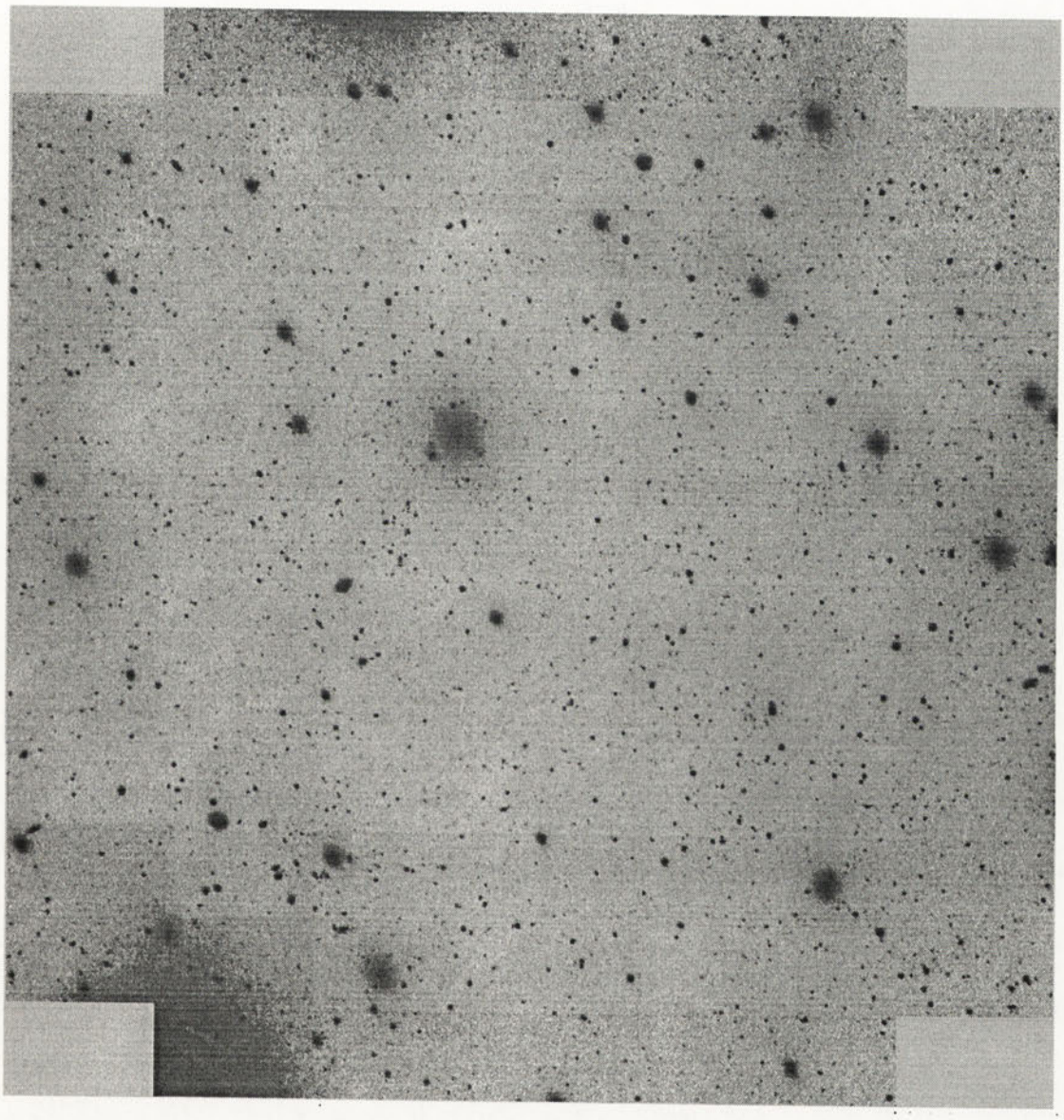

Figure 4.1: Grey-scale plot of the final mosaic image obtained by the mosaicing process. The overlaps can be seen at the outer edges due to different noise levels and presence or absence of wings from bright stars in images in different positions. Plate scale: 23.9'×25.1'.

this figure, although the background in this image is very flat, the flattening process has damaged some of the images of the brightest objects. However, this is not a problem as we remove areas around these and other bright objects (§4.3.3).

Objects were detected using isophotal intensities. The signal-to-noise ratio of detection of the faintest objects is a combination of the area and intensity thresholds. If the intensity threshold is $I\sigma$ (where σ is the noise per pixel) and the area threshold is A pixels, then total signal-to-noise is

$$(A\,I\sigma)/(\sqrt{A\,\sigma^2}) = \sqrt{A}\,I. \tag{4.2}$$

For a fixed value of A, reducing I increases detection of lower surface brightness objects; while for a fixed value of I, reducing A increases detection of more compact objects. The balance between the two chosen, $A = 3$ and $I \approx 1{\cdot}5$ appears to be a reasonable compromise. Various area and intensity thresholds were tried and the output isophotal plots of objects found compared to grey-scale images both on paper and on workstation screens to reach this compromise. The fixed circular aperture and smoothed data options of IMAGES were not used.

Intensity thresholds used for the different regions were (in photons/400s) 50, 50, 70 and 115 for R_0, R_1, R_2 and R_3 (equivalently, $28{\cdot}0\,mag\,arcsec^{-2}$, $28{\cdot}0\,mag\,arcsec^{-2}$, $27{\cdot}6\,mag\,arcsec^{-2}$ and $27{\cdot}1\,mag\,arcsec^{-2}$) respectively. For R_0 and R_1 these correspond to about 1·5 times the mean noise (per pixel) within those regions. For R_2 this intensity threshold is about 1·5 times the noise in the edge regions, in which fewer data images have been combined than in the centre. For R_3 the threshold is about 1·5 times the noise in the corners, which are the noisiest regions of R_3.

4.2.2 Reality of Objects

The reality of the objects detected in this way is tested by two methods, detection of troughs (as opposed to peaks) in the data and comparison of the analysis of R_0 with objects detected in Tyson & Seitzer's (1988) data. If objects being detected are in reality Poisson noise from the sky background, they should appear as troughs as often as they appear as peaks. Hence, the number of troughs detected should be about the same as the number of noise objects misconstrued to be astronomical objects. The IMAGES program was run with detection of such troughs ("negative objects") switched on. For example, in the region R_0, 284 objects were found in total, 32 of these being negative, so that about 220 would be expected to be real, and in the region R_1, 2037 objects were found in total, 177 negative, hence about 1683 real objects. In Figure 4.3 the number counts for

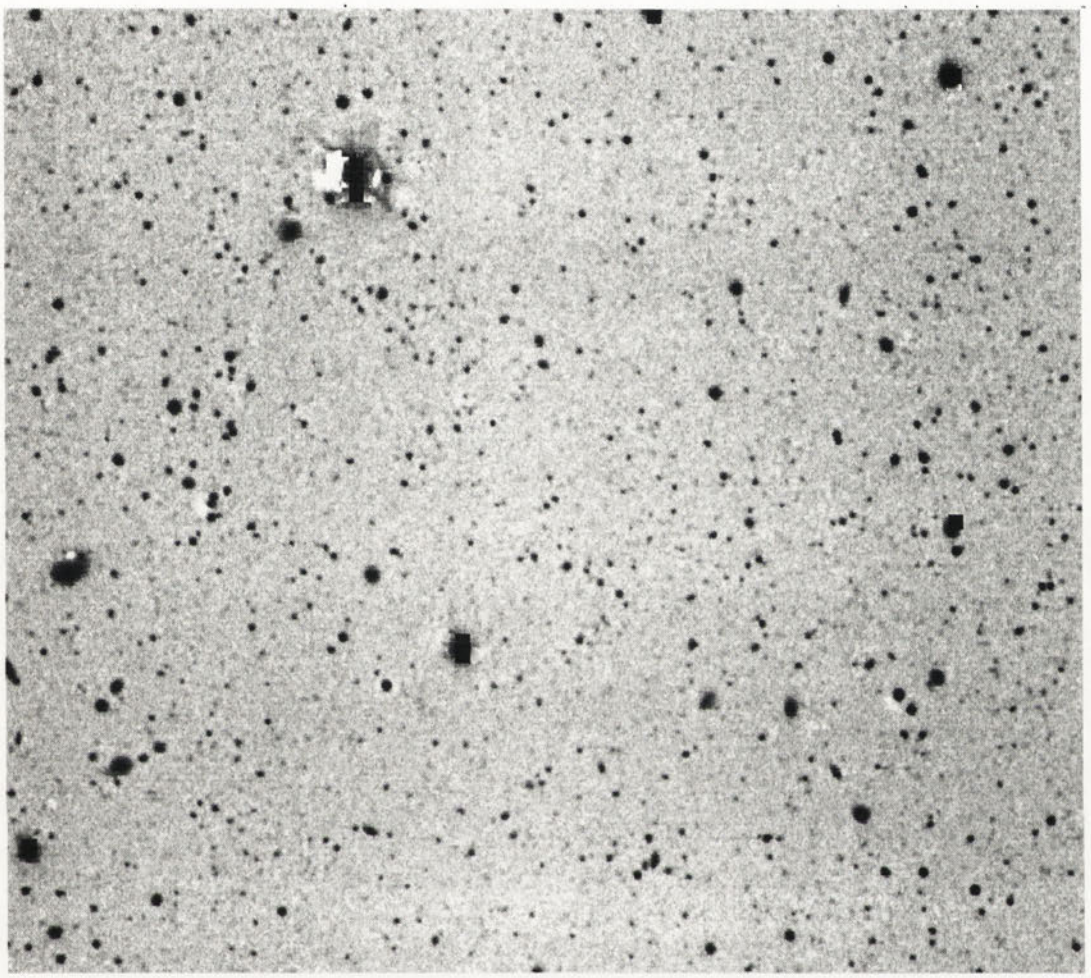

Figure 4.2: Grey-scale plot of region R_1, after removal of large scale variations in sky background (program FLAT). Because this flattening process was chosen to optimise detection of faint objects, it damages some of the images of the brightest objects, as is clear from the bright star near the top left corner.
Plate scale: 9.6' × 8.7'.

R_1 are plotted, with corrections for negative objects detected also plotted. This shows that contamination by noise objects does not appear to be significant until fainter than $V = 25$. In the $25{\cdot}5 \leq V < 26{\cdot}0$ bin the contamination is about 20%, while for the $26{\cdot}0 \leq V < 26{\cdot}5$ bin the contamination has reached 60%. Hence a magnitude limit of about $V = 25{\cdot}5$ to $V = 26{\cdot}0$ can be sensibly used.

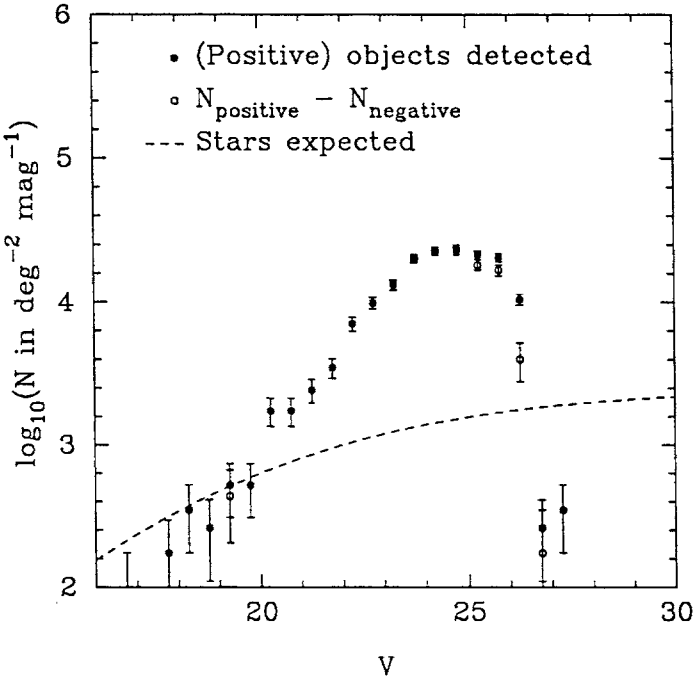

Figure 4.3: Number of objects detected in region R_1 as a function of V apparent magnitude, in 0·5 magnitude bins, with correction for "negative objects." Solid circles are for the number of (positive) objects; hollow circles are for the number of positive objects minus the number of negative (i.e., noise) objects, dashed line indicates star density expected from Bahcall & Soneira (1980) (§ 4.2.3). Error bars are Poisson errors.

Tyson & Seitzer's (1988) data covers a much smaller field than ours, and has smaller pixels, so that an area threshold of three pixels in their data covers a smaller solid angle than for our data. Hence, any object detected by us at the three-pixel limit in our data should be better resolved in their data as either a real or spurious object, and of course any random noise objects in our data will not (except rarely) appear in theirs. Using the reduced images of the SGP field kindly made available by Tyson, we combine Tyson & Seitzer's J and R fields, simply by taking the mean of the two, both normalised to an exposure time of 7200s. We analyse the "pseudo-V-band" image thus obtained using the APM software as for our own data.

In this image, at an area threshold of (again) $A = 3$ pixels and an intensity

threshold of about $I = 1{\cdot}25$ times the noise level, 648 objects were found, i.e., more than twice as many as in the same area in our data. Excluding a border area of width 5 pixels in this pseudo-V-band image, the fraction of R_0 which falls into this image is 73%, i.e., one would expect 208 of the objects in R_0 to appear in it. The position of each object found in R_0 was transformed into the coordinates of the pseudo-V-band image (a slight rotation was necessary) and a search was made for any counterparts in this image within 2·5 pixels. This process found counterparts for 195 objects, i.e., 94% of the expected 208 objects were found. Five extra counterparts to R_0 objects were found, and thirteen R_0 objects did not have counterparts according to the automatic search. A close examination of the two image plots showed that most of these eighteen R_0 objects were resolved into two separate objects in the pseudo-V-band image, explaining why either two or zero counterparts were found. Only five objects in (our) R_0 had no obvious counterparts in the pseudo-V-band image.

This is a better success rate than expected from the numbers of negative objects detected. From the 32 negative objects detected in R_0, one would expect 73% of this number, i.e., 23, positive spurious objects in the region in R_0 to lie in the Tyson & Seitzer pseudo-V-band image. If we consider all 13 R_0 objects that had no Tyson & Seitzer counterparts within 2·5 pixels to be spurious objects, then this is significantly lower than 32. However, the distance for identifying objects between R_0 and the pseudo-V-band image can conceivably have been made too large. A tighter identification criterion of a separation of 1·5 or 2 pixels would increase the number of objects considered spurious. In any case, we choose to be conservative, considering the numbers of negative objects detected as our estimate of numbers of spurious objects.

4.2.3 Star Removal

The criterion for separating stars and galaxies was determined by plotting for each object the ratio of its peak intensity to the intensity per pixel of the sky, I_{pk}/I_{sky}, against apparent magnitude, where the peak intensity is defined as the maximum intensity of any pixel within the isophote of an object. Stars are only spread by the point spread function (seeing) rather than by geometrical extension at the source, so this ratio should be higher for stars than for galaxies.

Figure 4.4 shows such a plot of peak intensities for the region R_3. In this figure a sharp, linear band of stars from about $V = 17$ to $V = 19$ is clearly visible. This clarity disappears at fainter magnitudes and for $V \gtrsim 23$ the whole relation loses its linearity. We therefore choose to remove objects above the cutoff line brighter

than $V = 22$, i.e., objects having

$$V < 22, \quad log_{10}\left(\frac{I_{pk}}{I_{sky}}\right) \geq -0{\cdot}39(V - 18{\cdot}65) \tag{4.3}$$

are removed. (The value I_{sky} corresponds to $21{\cdot}0\, V\, mag\, arcsec^{-2}$.)

The sharpness of the star band from $V = 17$ to $V = 19$ is not only due to a higher stellar density, but also due to the exclusion of objects in squares around large objects (§4.3.3). For a given magnitude, galaxies have larger isophotal areas than stars, hence are more likely to be excluded, leaving a mainly stellar locus. The decrease in the magnitude of the slope of the relation at fainter magnitudes is explainable as an increase in Poisson noise. Smaller numbers of photons mean that more pixels have fractionally higher and lower values relative to the overall flux from an object. The peak intensity is only a function of the highest value per pixel, not the mean value per pixel, and hence becomes a higher fraction of total flux, resulting in the change in slope. Another artefact of the observing process in this figure is that at the faint end of the distribution, a separation is visible between objects detected at the area limit of three pixels and those detected as being four pixels in area. This is simply due to the discretisation of objects with respect to pixels, i.e., they are forced into having integer numbers of pixels.

In Fig. 4.3, the number of stars expected from standard galactic star distribution models at $b^{II} = -90°$ (Bahcall & Soneira, 1980, Fig. 4a,4b) is plotted as a dashed line. This shows that the number of stars fainter than $V = 22$ that are not removed are not likely to be more than about 5% to 10% of the total sample.

4.3 Correlation Functions

In the practical calculation of the angular correlation function for samples of faint limiting magnitude (Koo & Szalay, 1984; Efstathiou *et al.*, 1991, Neuschaefer *et al.*, 1991, Couch *et al.*, 1992, Roche *et al.*, 1992), the calculation of the correlation function is corrected for a bias in the number density due to having samples over finite regions. Below, a derivation of this correction is given. We also describe the exclusion of areas affected by bright objects and describe our uncertainty estimates.

4.3.1 Biassing Correction for Finite Areas

The two-point angular autocorrelation function is commonly defined as in Peebles (1980, eqn (45.3)):

$$\delta P = \mathcal{N}_t^2 \delta\Omega_1 \delta\Omega_2 [1 + w(\theta_{12})] \tag{4.4}$$

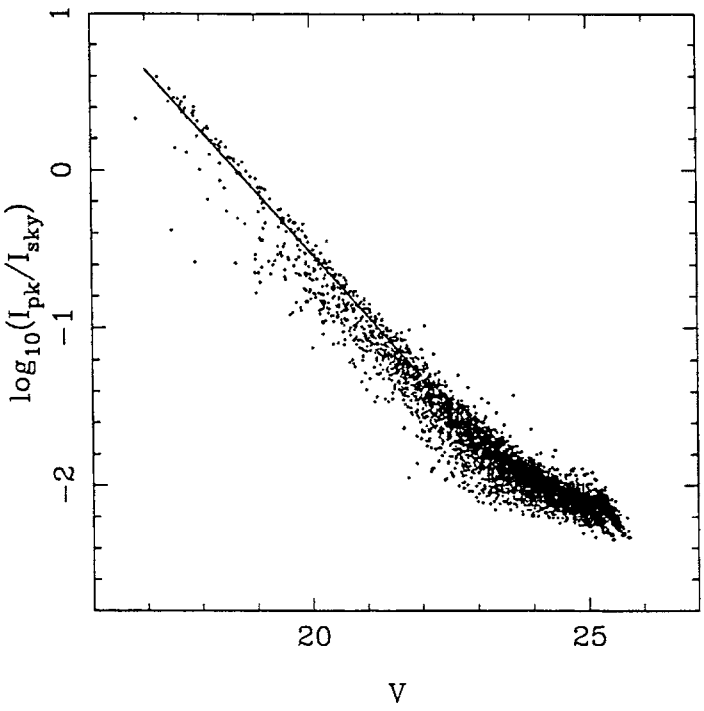

Figure 4.4: Star-galaxy separation. Logarithms of the ratio of the maximum intensity of any pixel in an object to the sky intensity are plotted against apparent V magnitude of objects in region R_3. Objects lying in square regions surrounding objects of large isophotal area are excluded as described in §4.3.3.

where $d\Omega_1$ and $d\Omega_2$ are two elements of solid angle separated by angle θ_{12}, δP is the expected number of pairs of galaxies having one galaxy in each of the two solid angle elements (also termed the "joint probability of finding objects in both of the elements of solid angle"), $w(\theta_{12})$ is the angular correlation function and $\mathcal{N}_t$ is defined as the mean number density of this and similarly sized regions over a series of many observations hypothesised to exist under the fair sample hypothesis (Peebles, 1980, §30).

However, as is indicated by the methods of calculation used by those who have recently measured $w(\theta)$ for faint limiting magnitudes, (Koo & Szalay, 1984, Efstathiou *et al.*, 1991, Neuschaefer *et al.*, 1991, Couch *et al.*, 1992 and Roche *et al.*, 1992) this definition is considered biassed if the actual number density for a finite region is used. A simple way to see the problem is to obtain the total number of pairs of objects, N_{pairs}, in a (finite) region by integrating eqn (4.4):

$$\begin{aligned} N_{pairs} &= \int_\Omega \int_\Omega \delta P \\ &= \int_\Omega \int_\Omega \mathcal{N}_t^2 \, d\Omega_1 d\Omega_2 (1 + w(\theta_{12})) \end{aligned}$$

$$= \mathcal{N}_t^2 \left(\int_\Omega \int_\Omega d\Omega_1 d\Omega_2 + \int_\Omega \int_\Omega w(\theta_{12}) d\Omega_1 d\Omega_2 \right)$$

$$= \mathcal{N}_t^2 \left(\Omega^2 + \int_\Omega \int_\Omega w(\theta_{12}) d\Omega_1 d\Omega_2 \right) \tag{4.5}$$

$$= \mathcal{N}_t^2 \Omega^2 \left(1 + \frac{\int_\Omega \int_\Omega w(\theta_{12}) d\Omega_1 d\Omega_2}{\Omega^2} \right). \tag{4.6}$$

Dividing both sides by Ω^2 gives

$$\mathcal{N}_t^2 = \frac{\frac{N_{pairs}}{\Omega^2}}{\left(1 + \frac{\int_\Omega \int_\Omega w(\theta_{12}) d\Omega_1 d\Omega_2}{\Omega^2} \right)}. \tag{4.7}$$

But if N is the number of objects in the region, then the number of pairs of objects is $N(N-1) \approx N^2$ and if we define the number density for the region to be $\mathcal{N}_e$ ("estimated" number density), then we have

$$N_{pairs} = \mathcal{N}_e^2 \, \Omega^2 \tag{4.8}$$

so that

$$\mathcal{N}_e^2 = \mathcal{N}_t^2 \left(1 + \frac{\int_\Omega \int_\Omega w(\theta_{12}) d\Omega_1 d\Omega_2}{\Omega^2} \right). \tag{4.9}$$

Hence, if the correlation function $w(\theta)$ is nonnegative at all separations, then the number density in the region is higher than what is considered to be the true number density. If we consider $\mathcal{N}_t$ to be a limit of $\mathcal{N}_e$ as the area of the region increases without bound; if we assume that the correlation functions for finite regions w_e defined by

$$\delta P = \mathcal{N}_e^2 \delta\Omega_1 \delta\Omega_2 (1 + w_e(\theta_{12})) \tag{4.10}$$

approach w in some limiting sense as the area of the region increases without bound; and if we assume that $w(\theta) \to 0$ as $\theta \to \infty$; then the above definition (4.4) would appear to make sense.

In any finite region, one can then think of the point distribution being composed of an uncorrelated distribution having number density $\mathcal{N}_t$ plus a correlated distribution on top of this which takes the total number density to $\mathcal{N}_e$. The function w then describes the number of pairs of objects in excess to that expected in an uncorrelated distribution of number density $\mathcal{N}_t$, not of number density $\mathcal{N}_e$. One can show this in the definition by substituting eqn (4.9) into eqn (4.4) to get

$$\delta P = \frac{\mathcal{N}_e^2 \delta\Omega_1 \delta\Omega_2 (1 + w(\theta_{12}))}{1 + \left(\int_\Omega \int_\Omega w(\theta_{12}) d\Omega_1 d\Omega_2 \right) / \Omega^2}. \tag{4.11}$$

The way the correlation function is actually calculated from the data is to count $N_{gg}(\theta)$, the number of pairs of data points within a bin of separation θ to

$\theta + \delta\theta$, and compare this to the number of pairs $N^e_{rr}(\theta)$ within the same bin found in a uniform random simulation, i.e.,

$$w_e(\theta) = \frac{N_{gg}(\theta)}{N^e_{rr}(\theta)} - 1. \tag{4.12}$$

The uniform random simulation here has either the same number density as the sample ($\mathcal{N}_e$) or has the number of pairs counted scaled so that it corresponds to the number of pairs that would occur if the number density was the same as that in the sample, hence the superscript "e".

However, to find w rather than w_e, one needs to scale the number density of the random sample to $\mathcal{N}_t$ rather than to $\mathcal{N}_e$, i.e.,

$$w(\theta) = \frac{N_{gg}(\theta)}{N^t_{rr}(\theta)} - 1. \tag{4.13}$$

By eqn (4.9),

$$N^t_{rr} = N^e_{rr}\left(1 + \frac{\int_\Omega \int_\Omega w(\theta_{12}) d\Omega_1 d\Omega_2}{\Omega^2}\right)^{-1}, \tag{4.14}$$

so that

$$\begin{aligned} 1 + w(\theta) &= \frac{N_{gg}(\theta)}{N^e_{rr}(\theta)}\left(1 + \frac{\int_\Omega \int_\Omega w(\theta_{12}) d\Omega_1 d\Omega_2}{\Omega^2}\right) \\ &= (1 + w_e(\theta))\left(1 + \frac{\int_\Omega \int_\Omega w(\theta_{12}) d\Omega_1 d\Omega_2}{\Omega^2}\right). \end{aligned} \tag{4.15}$$

Hence, strictly speaking, to find $w(\theta)$ for a finite region one needs to calculate $w_e(\theta)$ from the data in the usual manner and then solve this integral equation for $w(\theta)$. However, the second factor on the right hand sides of eqn (4.15) is a constant with respect to θ. If we label this factor

$$B_k^{-1} \equiv \left(1 + \frac{\int_\Omega \int_\Omega w(\theta_{12}) d\Omega_1 d\Omega_2}{\Omega^2}\right), \tag{4.16}$$

then eqn (4.15) gives

$$w(\theta) = (1 + w_e(\theta))\, B_k^{-1} - 1 \tag{4.17}$$

$$= (B_k^{-1} - 1) + B_k^{-1} w_e(\theta). \tag{4.18}$$

This value B_k^{-1} is then the correction factor used by Koo & Szalay (1984), Neuschaefer *et al.* (1991) and Couch *et al.* (1992). Koo & Szalay assume that w has the form of a $-0{\cdot}8$ power law as found for samples of brighter limiting magnitude (eqn (4.1)). Hence they simply solve eqn (4.17) for a value of B_k^{-1} which makes w take this form. Their values of B_k^{-1} (Table 2A, Koo & Szalay,

1984) are in the range $1{\cdot}025 - 1{\cdot}000$, this value decreasing as the limiting magnitude becomes fainter. The samples with fainter limiting magnitudes for any fixed field also have lower values of A_w (as expected). By eqn (4.16), since the set of pairs of elements of area $\{(\delta\Omega_1, \delta\Omega_2)\}$ in the field is fixed, if w satisfies eqn (4.1) and A_w decreases, then the value of B_k^{-1} should decrease. Hence the values of B_k^{-1} found by Koo & Szalay are consistent with their solutions for w. (They actually give B_k, which increases with decreasing A_w.)

Neuschaefer *et al.* (1991), on the other hand, only assume that $w(\theta)$ takes a power law form, allowing the slope of w, $1 - \gamma$, to be a free parameter in addition to A_w and B_k^{-1}. By minimising χ^2 they find that the slope must be in the range $-0{\cdot}6$ to $-0{\cdot}8$. Their three values of B_k^{-1} which are not equal to unity (Table 1, Neuschaefer *et al.*, 1991) also decrease with decreasing A_w, which is again self-consistent. For high values of A_w, although B_k^{-1} should also be high, it becomes small compared to A_w so that ignoring it (setting it equal to unity) is a good approximation, hence Neuschaefer *et al.*'s other three solutions, which have $B_k^{-1} = 1$, also make sense.

Couch *et al.* (1992) assume that $1 - \gamma = -0{\cdot}8$, as do Koo & Szalay. However, their values of B_k are greater than unity, i.e., their values of B_k^{-1} are less than unity. These would make sense if the values tabulated are in fact those of B_k^{-1}, but then the values of B_k^{-1} decrease with decreasing A_w for one field (F249) but increase for decreasing A_w for their other field (SGP). This would still make the values of B_k^{-1} for the SGP field hard to interpret.

An alternative approach to using eqn (4.16) is that if $w(\theta)$ is fairly small, then B_k^{-1} is not much greater than unity, so

$$\begin{aligned} w(\theta) &= (B_k^{-1} - 1) + w_e(\theta) + (B_k^{-1} - 1) w_e(\theta) \\ &\approx (B_k^{-1} - 1) + w_e(\theta) \end{aligned} \tag{4.19}$$

since the third term is the product of two small numbers. Again with the assumption that w takes the form of a $-0{\cdot}8$ power law, one can solve this equation to find $B - 1$ as an additive correction factor. This is the approach taken by Efstathiou *et al.* (1991) and Roche *et al.* (1992). They find that the assumption of a $1 - \gamma \approx -0{\cdot}8$ power law gives self-consistent results. This doesn't, of course, show that this assumption gives a unique solution, so this is not justified without recourse to other results given in the literature.

Here we choose the first of these two methods and, as in Neuschaefer *et al.* (1991) find that the assumption of a $1 - \gamma \approx -0{\cdot}8$ power law is reasonable.

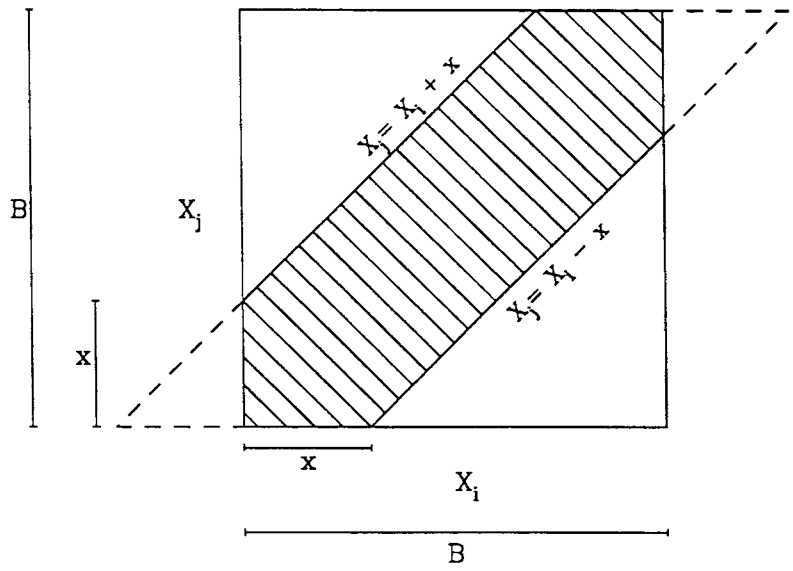

Figure 4.5: Distribution of pairs $\{(x_i, x_j : i \neq j)\}$ for a one-dimensional uniform random distribution over the interval $[0; B]$. The shaded area indicates the region in which pairs of points satisfy $|x_i - x_j| \leq x$. The dashed extensions are simply an aid to calculating the area of this shaded region.

4.3.2 Analytical Calculation of Number of Random Pairs per Bin

If one uses the whole area of the field for the correlation calculation, then it can be relatively easy to analytically calculate N_{rr}^{e} for a bin θ to $\theta + \delta\theta$. For example, for a small enough solid angle one can ignore curvature and calculate the analytical probability distribution of pair separations for a rectangle.

To see how to derive this, first consider the probability density for a one-dimensional situation. That is, consider a set of points $\{x_i\}$ uniformly randomly distributed over the interval $[0; B]$ where B is the length of the interval. Imagine plotting the set of points $\{(x_i, x_j : i \neq j)\}$. These fall within a square of side length B and are distributed uniformly randomly over this square if the original set of points $\{x_i\}$ is uncorrelated as intended. This square is plotted in Figure 4.5.

Given some distance $x < B$, points (x_i, x_j) for which $|x_i - x_j| \leq x$ lie in the shaded region in this diagram. The area of this shaded region is $(2x)(B) - 2[0{\cdot}5(x)(x)] = 2xB - x^2$ (e.g., the area of the parallelogram minus that of the two triangles indicated by the dashed lines). Since points are spread evenly over the region in this figure, the probability that the separation between two points

$\Delta\theta_X$ is less than x is therefore the ratio of this shaded region to the total, i.e.,

$$\begin{aligned} P(\Delta\theta_X < x) &= \frac{2xB - x^2}{B^2} \\ &= 2\left(\frac{x}{B}\right) - \left(\frac{x}{B}\right)^2. \end{aligned} \tag{4.20}$$

The probability density is therefore

$$\frac{dP(\Delta\theta_X < x)}{dx} = \frac{2}{B} - 2\frac{x}{B^2}. \tag{4.21}$$

This extends to a two-dimensional case by observing that the probability densities with respect to the X and Y directions should be independent. If we label the length of the side in the Y direction to be C, we therefore get that the two-dimensional probability density function is

$$\frac{d^2P(\Delta\theta_X < x, \Delta\theta_Y < y)}{dx\,dy} = \frac{1}{B}\left(2 - 2\left(\frac{x}{B}\right)\right)\frac{1}{C}\left(2 - 2\left(\frac{y}{C}\right)\right), \tag{4.22}$$

where $\Delta\theta_X$ and $\Delta\theta_Y$ are the separations between pairs in the X and Y directions respectively. This expression can then be easily integrated to give

$$BC\ P(\sqrt{x^2+y^2} < \theta) =$$

$$\begin{cases} \pi\theta^2 - \frac{4}{3}\left(\frac{1}{B} + \frac{1}{C}\right)\theta^3 + \frac{1}{2BC}\theta^4, \\ \qquad\qquad 0 \le \theta \le B \\ 2\theta^2\left[\alpha + \frac{\sin 2\alpha}{2}\right]_{\alpha=0}^{\alpha=\arcsin(B/\theta)} - \frac{4}{3B}\theta^3 + \frac{4}{3B}(\theta^2 - B^2)^{3/2} - \frac{B}{C}\theta^2 + \frac{B^3}{6C}, \\ \qquad\qquad B \le \theta \le C \\ C\left(2\sqrt{\theta^2 - C^2} - \frac{1}{B}(\theta^2 - C^2)\right) + 2\theta^2\left[\alpha + \frac{\sin 2\alpha}{2}\right]_{\alpha=\arcsin[(\theta^2-C^2)/\theta]}^{\alpha=\arcsin(B/\theta)} \\ \quad - \frac{B}{C}\theta^2 + \frac{B^3}{6C} + \frac{4}{3B}(\theta^2 - B^2)^{3/2} + \frac{2}{C}\theta^2\sqrt{\theta^2 - C^2} - \frac{2}{3C}(\theta^2 - C^2)^{3/2} - \frac{4C^3}{3B} \\ \quad - \frac{1}{BC}\theta^2(\theta^2 - C^2) + \frac{1}{2BC}(\theta^2 - C^2)^2, \\ \qquad\qquad C \le \theta \le \sqrt{B^2 + C^2} \end{cases} \tag{4.23}$$

where $B \le C$ without loss of generality. The value of N_{rr}^e is then given by

$$N_{rr}^e = N_e^2\left[P(\sqrt{x^2+y^2} < \theta + \delta\theta) - P(\sqrt{x^2+y^2} < \theta)\right]. \tag{4.24}$$

4.3.3 Correction for Bright Objects

While this analytical calculation is valid for a continuous rectangular region, in our data we need to invalidate areas of the region around bright objects. In

our data, the fainter objects are close enough to one another that brighter objects are likely to hide some of the fainter ones, i.e., the approximation of galaxies as points no longer holds. Additionally, the fact that bright stars or galaxies are, by definition, bright, means that the Poisson noise in their wings is high, so that spurious objects are more likely to be detected close to them. To avoid these problems, we exclude from the correlation analysis any object whose isophotal area on the sky is more than a fixed limit, which we choose to be 100 pixels. The areas behind and around these objects need also to be excluded, so for each object removed, we remove a square centred on the object and having sidelength equal to twice the square root of the isophotal area of the object. This removal of squares involves removing not only the object which generated the removal of the squares, but also removing any data or uniformly distributed random points from the squares.

To evaluate the expected number of random pairs for this more complex region, we could, in principle, perform an analytical calculation similar to that described in the previous section. However, this is not expected to be trivial, so we instead choose to use a Monte Carlo technique.

We randomly distribute points according to a uniform probability distribution, exclude any points which fall in the squares around large objects and add more random points until the total number of points in valid regions equals the number of points in the data set which lie in the valid region. If m realisations of this distribution are made, each time counting the number of pairs in each separation bin, then the limit as $m \rightarrow \infty$ would give the analytically expected number of pairs in that bin. As in practice we have to use a value of $m < \infty$, this introduces a calculational uncertainty into the value of $w(\theta)$. We evaluate this using the standard error in the mean of the number of pairs in any fixed separation bin over the different realisations. The resulting uncertainties are propagated to uncertainties in $w(\theta)$ and are plotted as solid error bars on the points representing $w(\theta)$ in our plots of $w(\theta)$. For R_1 and R_2 we have $m = 100$ realisations; for R_3, $m = 10$ realisations are sufficient.

4.3.4 Uncertainties

As just explained, use of random simulations introduces calculational uncertainties. To calculate the *intrinsic* uncertainties in $w(\theta)$, one can also use the random simulations. These intrinsic uncertainties can't simply be found by taking the Poisson errors in the number of pairs in a bin, since the pairs are interdependent. However, for values of $w(\theta) \ll 1$, we can make use of the standard deviation among the different random realisations of the number of pairs in any

fixed separation bin.

This standard deviation signifies the variation that one would get for a set of totally uncorrelated points. An ideal way to calculate the variation in $w(\theta)$ would stem from knowing $w(\theta)$ *a priori* and being able to generate an underlying probability distribution which has $w(\theta)$ as the mean value of its correlation function. One could then distribute points randomly according to the underlying distribution many times, bin the number of pairs in each realisation and take standard deviations for each bin. As is common in science, if one doesn't want to assume the function $w(\theta)$ *a priori,* one often does the next best thing, which is to apply the same process with the measured values of $w(\theta)$ substituting for the *a priori* known or assumed values.

However, making random distributions which generate a given correlation function is a non-trivial task. But when the value of $w(\theta) \ll 1$, a uniform random distribution is in fact a good approximation to the correlated distribution as far as the total number of pairs per separation bin is concerned, since the extra or "correlated" numbers of pairs are $\ll 1$. Hence one can use the standard deviation of the number of pairs in any fixed bin among the uniform random simulations as an indicator of the intrinsic variation in the data. This is the approach chosen here. These standard deviations are plotted as dashed or variegated error bars in the plots of $w(\theta)$. The magnitudes of these standard deviations are in fact close to Poissonian. (They are within around $\pm 20\%$ of $\sqrt{N}$ where N is the number of pairs in the bin.)

As is obvious from the figures in the following section, the individual points of $w(\theta)$ for different bins are well within one or two of these standard deviations from zero correlation. However, as also explained in the following section, these sets of points do show negative slopes which can fit $-0{\cdot}8$ power laws for credible amplitudes. This suggests that the process just described overestimates the uncertainty, though no flaw in this process is obvious.

As we calculate the amplitude of the angular correlation function from each of the subsamples, we need an estimate of the uncertainty in this overall amplitude. To combine the error bars for the individual bins used for the four points for each correlation function would be difficult to do precisely (apart from just saying that they're approximately Poisson errors and that therefore the combination should also be roughly Poissonian), because the points are not independent. For example, many objects in the sample are members of pairs of objects represented in all four of the bins. Removing or changing the position of any such object could therefore affect all four bins simultaneously. Hence the error bars we choose come from the standard deviation in the number of pairs in the uniform random simulations as

described previously, but using the total number of pairs across all four bins.

4.4 Results

Following the discussion in §4.2.2, we conservatively choose a faint magnitude limit of $V \leq 25{\cdot}5$ for the region R_1. For the regions R_2 and R_3 the corresponding faint magnitude limits for the same signal-to-noise ratio are $V \leq 25{\cdot}1$ and $V \leq 24{\cdot}6$ respectively. For a comparison with Efstathiou *et al.*'s (1991) calculation of the correlation function for $24 < B_J < 26$, we therefore consider the range $23{\cdot}5 < V < 25{\cdot}5$ for the region R_1. Given the small numbers of objects at the brighter magnitudes, we choose a bright magnitude limit of $V \geq 21$, so we also evaluate the correlation function over R_1 for $21 < V < 25{\cdot}5$. To get some values for brighter ranges, we calculate the correlation function for the region R_2 for the two ranges $21 < V < 25{\cdot}1$ and $21 < V < 24$.

We also calculate the correlation function for the largest region, R_3, even though this is biassed by the excessive noise in the outermost regions, and we calculate the correlation function to a faint magnitude limit at which severe incompleteness has set in, i.e., the range $21 < V < 26{\cdot}5$ for the region R_2.

In binning the pairs in any calculation of the correlation function we have to choose relatively large bin sizes in order to minimise the uncertainties. The binning chosen is as follows. The minimum pair separation is $10''$. This avoids distances close to the size of the actual objects and is slightly below the mean inter-object separation in the subsamples just mentioned. The maximum size is the length of the smaller side of the region. This range is first divided into eighteen bins at equal logarithmic intervals. To reduce the uncertainties, each set of three adjacent bins is summed into a single bin, making a total of six bins. Since pairs at separations comparable to the size of the whole region are not averaged over a large enough region, we then remove the two largest bins. This leaves four bins, covering a mininum separation $10''$ and a maximum separation 15% to 25% of the length of the smaller side of the region.

Figure 4.6 shows the uncorrected and corrected correlation functions (w_e and w respectively) for the region R_1. The corrected w is obtained as follows. For various values of B_k^{-1}, a line is least squares fit to the values $B_k^{-1}(w_e + 1) - 1$ for the four bins in $\log(w) - log(\theta)$ coordinates. This gives a power law with an amplitude and a slope. A slope of around $-0{\cdot}8$ to $-1{\cdot}0$ is consistent with minimum values of χ^2 with respect to varying B_k^{-1} to give these different power laws. We therefore choose the value of B_k^{-1} which gives the slope closest to $-0{\cdot}8$ to be the corrected correlation function. Figure 4.7 shows the full set of corrected

correlation functions, while Table 4.1 lists the parameters involved in each of the different subsamples.

Region	range in V	V_{med}	$A_w(1')$	B_k^{-1}	N_{gal}
R_1	$21 - 25{\cdot}5$	24·13	$-2{\cdot}21$	1·004	1340
R_1	$23{\cdot}5 - 25{\cdot}5$	24·5	$-2{\cdot}46$	1·0076	963
R_2	$21 - 24$	23·2	$-1{\cdot}84$	1·0165	1697
R_2	$21 - 25{\cdot}1$	23·85	$-2{\cdot}16$	1·008	3060
R_2	$21 - 26{\cdot}5$	24·28	$-2{\cdot}07$	1·0175	4058
R_3	$21 - 24{\cdot}6$	23·4	$-1{\cdot}38$	1·054	3339

Table 4.1: Details of subsamples used in calculating correlation functions.

While Fig. 4.6 shows that our fitting procedure does not give a perfect fit for the subsample with the faintest median magnitude, we prefer to leave this as it is rather than improve the fit without good justification. We illustrate this faint sample with a plot of the isophotes of the objects within their region, i.e., the objects having $23{\cdot}5 < V < 25{\cdot}5$ in the region R_1 (Figure 4.8).

The amplitudes of these correlation functions, $w(1')$, are shown in Figure 4.9 in comparison with previous authors' results. The magnitudes which the amplitudes are plotted against in Fig. 4.9 are the median V values of each magnitude range. Neuschaefer *et al.*'s (1991) data is already given against median Gunn g magnitude, as well as transformations from other bands to Gunn g. We approximate Gunn $g \approx V$. For other transformations, we use $B - V \approx 0{\cdot}7$ as a median value, e.g. Couch *et al.*'s (1992) transformation $VR = V - 0{\cdot}29(B - V) - 0{\cdot}10$ (eqn (1), Couch *et al.*, 1992) gives $V \approx VR + 0{\cdot}3$. To get median magnitudes from the various magnitude ranges involved we find the median V magnitude in our data for the appropriate magnitude range in V.

We expect the points for R_2, $21 < V < 26{\cdot}5$ and R_3, $21 < V < 24{\cdot}6$ to suffer systematic errors due to incompleteness at the faint end and inclusion of noise in the outer regions respectively, so it is the other four points which are of main interest. Unfortunately, though, the error bars in Fig. 4.9 show that all but the brightest of these four points are consistent with zero at the 1σ level. Given the fact that the four main points appear close to (but slightly below) a linear extension of all the previous authors' points with brighter median magnitudes, it is possible, as mentioned earlier, that the method of estimating the uncertainties has given overestimates of the errors.

In any case, the four points do suggest that the correlation function amplitude continues to decrease at these faint magnitudes in a similar way to the way it decreases for brighter magnitudes, at least to first order.

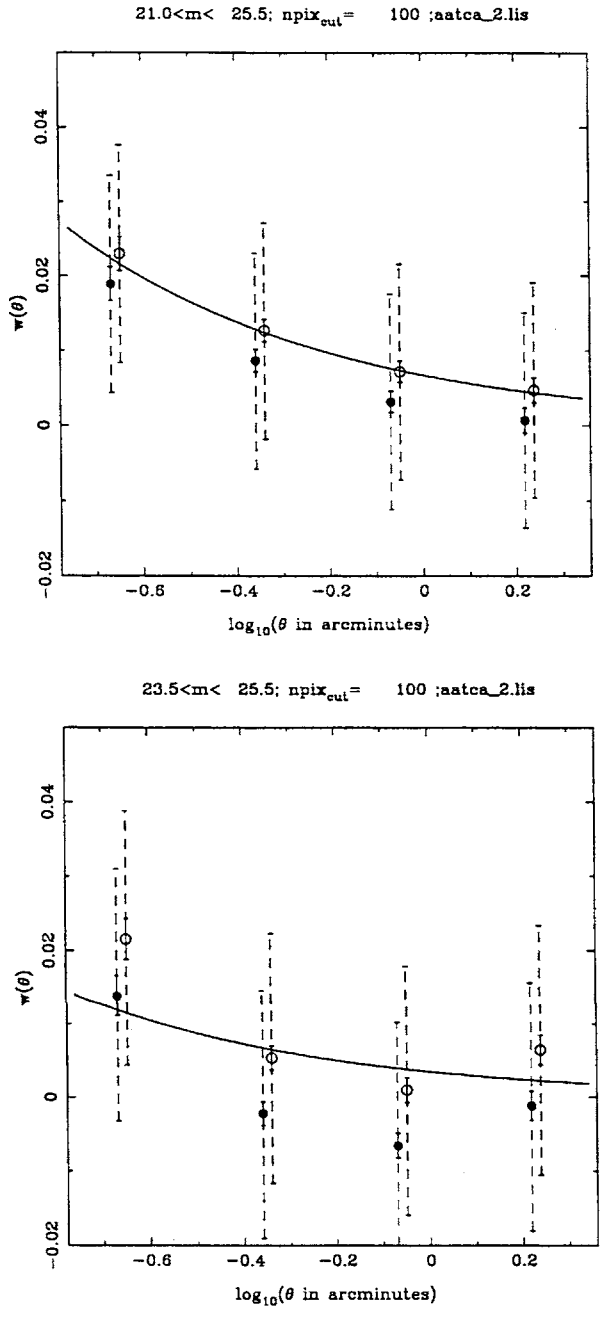

Figure 4.6: Two-point angular autocorrelation function for objects in region R_1 having $21 < V < 25{\cdot}5$ and $23{\cdot}5 < V < 25{\cdot}5$ (upper and lower respectively). As can be seen in Fig. 4.8, square regions around large objects have been cleared of objects. The solid points represent the correlation function of the raw data, the hollow points represent the correlation of the B_k^{-1}-corrected data and the solid curves represent the fitted correlation functions. The dashed error bars show the standard deviation between the sets of random points, while the error bars on the data points represent standard errors in the mean due to using random points to calculate N_{rr} rather than an exact calculation of N_{rr}.

4.5 Discussion

While Fig. 4.9 does indicate consistency to first order with previous results at brighter median magnitudes, it does not confirm Neuschaefer *et al.*'s (1991) finding of an increase in the amplitude for magnitudes fainter than about $V_{median} \approx 24{\cdot}5$. However, as Neuschaefer *et al.* clearly state, these values are obtained for subsamples which are seriously incomplete. While Neuschaefer *et al.* do put in a correction for weighting, it is hard to see how this weighting can recapture the information lost by missing galaxies. For example, consider the following two plots of artificial populations (Figure 4.10). These show a bright population of galaxies, a faint "observed" population and two differing possibilities for a faint "unobserved" population. The observed populations are the same in both plots. With any weighting scheme whatsoever, the "corrected" correlation function derived from the observed objects in both plots will therefore have to be the same. However, the correlation function for the total (observed plus unobserved) data sets is clearly very different, with a higher correlation on the right.

This makes it hard to see how any weighting scheme can sensibly cope with data which is seriously incomplete. A simple explanation of Neuschaefer *et al.*'s faint points would be that their weighting scheme tends to be equivalent to assuming that the unobserved population is more similar to the right-hand plot than the left-hand one.

The other value at a faint magnitude to compare with is that of Efstathiou *et al.* (1991). Within our calculated errors, our result does agree with theirs. If we have overestimated the errors, then there could be a disagreement. If we consider our values to be the true values, then the disagreement is that their value is about a factor of three or four higher.

One difference between the two sets of observations is that the Efstathiou *et al.* point is for the B_J band rather than V. Efstathiou *et al.* argue for a marginally significant increase of the amplitude as the waveband becomes redder. If real, this effect would only worsen the disagreement slightly. The agreement between different bands at brighter magnitudes also suggests that such an effect should be small.

Another difference is that their point comes from a total of 13 separate fields over a total area of $0{\cdot}04\,deg^2$ while each of our four points comes from a single field (though perforated by areas obscured by bright objects) with an area of $0{\cdot}08\,deg^2$ (the two brighter points) or $0{\cdot}02\,deg^2$ (the two fainter points). Of the twelve Tyson & Seitzer (1988) fields which Efstathiou *et al.* use, five are at lower galactic latitudes than $|b^{II}| \approx 45°$, while a total of nine are at lower galactic latitudes than

$|b^{II}| \approx 60°$. (Their thirteenth field, SA68, also has a galactic latitude as low as $|b^{II}| \approx 45°$ (Pickering & Kapteyn, 1918).) However, according to the model indicated in Fig. 4a of Bahcall & Soneira (1980), the stellar density at $|b^{II}| = 50°$ is not much greater than at $|b^{II}| = 90°$, though at $|b^{II}| = 30°$ it is greater than at $|b^{II}| = 90°$ by about a factor of four. As only two of the twelve Tyson & Seitzer fields are lower than $|b^{II}| \approx 30°$, this means that not much effect from stellar contamination is likely.

Calculational differences between Efstathiou *et al.* and ours include detection software; choices of areas to exclude due to bright objects; Efstathiou's use of N_{gr} rather than N_{rr} (which should subtract off any correlations due to density gradients across fields, making their result smaller than or equal to what it would be if the density gradient were not corrected for, as in our calculation); and Efstathiou's use of an additive rather than multiplicative $\mathcal{N}_e/\mathcal{N}_t$ correction factor (as derived in eqn (4.19)). None of these give any obvious explanation of the difference.

Supposing that our error estimates are in fact greatly overestimated and that our amplitudes are in fact very close to the true values, what would this tell us about the properties of the faint galaxies or the geometry of the Universe? As with the differential number counts, the angular correlation function comes from an integral over the (three-dimensional) spatial volume of our past time cone. Therefore effects of the geometry of the Universe, evolution of galaxy number density and luminosity density (i.e., evolution in the luminosity function) and evolution of the spatial correlation function are all combined to effect the angular correlation function.

The first two of these effects have already been discussed with regards to the faint galaxy number counts. We therefore introduce here a discussion on the third, evolution of the spatial correlation function.

4.5.1 Evolution of Spatial Correlation Function with Redshift

Groth & Peebles (1977) and Efstathiou *et al.* (1991) parametrise evolution of the two-point spatial auto-correlation function by

$$\xi(r, z) = \left(\frac{r_0}{r}\right)^{\gamma} (1+z)^{-(3+\epsilon)} \tag{4.25}$$

where r (and r_0) are in proper coordinates and the values $r_0 \approx 5h^{-1}\,Mpc$ and $\gamma \approx 1{\cdot}8$ are expected to be constant. As mentioned by Efstathiou *et al.* and Couch *et al.* (1992), a value of $\epsilon = -1{\cdot}2$ in this expression means that ξ is constant in comoving coordinates. This is equivalent to conservation of galaxy numbers and

constancy of galaxy positions in comoving coordinates, which is expected to occur on length scales over which the density perturbation amplitudes are still in the linear regime and so are still expanding with general universe expansion, i.e., on length scales greater than many *Mpc* at $z = 0$.

At smaller scales, it is useful to imagine virialised clumps of galaxies at early epochs which conserve their size and number density. As also mentioned by Efstathiou *et al.* and Couch *et al.* (1992), this corresponds to a value of $\epsilon = 0$. This is derived by Phillipps *et al.* (1978) but can be easily thought of as follows.

Consider the correlation function in the form $\xi = (N_{gg}/N_{rr}) - 1$, where N_{gg} is the number of pairs of galaxies in the sample at separation r to $r + \delta r$ and N_{rr} is the expected number of pairs of galaxies in the same separation range for a uniform random distribution containing the same total number of galaxies as the sample. Consider a sample of galaxies at $z = 0$ to be composed of clusters of diameter r_1 separated by $r \gg r_1$ with a uniform distribution of "field" galaxies in between. At an earlier epoch in the Universe, consider the same (proper) volume. The total number of galaxies is then greater by a factor of $(1 + z)^3$. Hence the total number of pairs is greater by the square of this, $(1 + z)^6$, so N_{rr} for any pair separation bin is greater by $(1 + z)^6$.

The clusters at the earlier epoch have the same diameters, fixed at r_1, and the distributions within these diameters are also fixed. However, the clusters are closer to one another at the earlier epoch by a factor of $(1 + z)$, so the total number of clusters is greater by a factor of $(1 + z)^3$. Provided that $\xi \gg 1$ and that most clusters are already greater than r_1 apart at the earlier epoch, the only pairs separated by $r < r_1$ are intracluster pairs. The number of pairs, N_{gg}, therefore only increases by the increase in the total number of clusters, $(1 + z)^3$.

Hence, ξ scales as $(1 + z)^3/(1 + z)^6 = (1 + z)^{-3}$ and $\epsilon = 0$ if the clustering is fixed in proper coordinates.

However, if clusters are to contract at all in proper coordinates, i.e., if the density perturbations on cluster scales are to become seriously nonlinear, then the density of objects and hence density of pairs of objects at a fixed proper separation must increase, so ξ must increase faster than $(1 + z)^{-3}$. That is, the value of ϵ has to be greater than zero. Recent N-body simulations do in fact predict values of ϵ which are significantly greater than zero (Melott, 1992, Yoshii *et al.*, 1993).

Melott calculates a value for the Efstathiou *et al.* (1991) point of about $4{\times}10^{-3}$, for an $\Omega_0 = 1$, $\lambda_0 = 0$ geometry, without specifying the luminosity function evolution. This would correspond to a value of $log_{10}(A_w(1')) \approx -2{\cdot}6$, which is in fact slightly lower than that which our measured four points would indicate,

though of course within the error bars.

Yoshii *et al.*, however, would appear to predict a value of the amplitude much closer to Efstathiou *et al.*'s value. They model the luminosity function as in Yoshii & Peterson (1991), involving evolutionary population synthesis and a present day standard Schechter function (Efstathiou, Ellis & Peterson, 1988). The closest of their models to our point would be their mildly biassed, $\Omega_0 = 1$, $\lambda_0 = 0$, CDM post-recombination perturbation spectrum model.

In either case, if our measured values are closer to the true values than should be expected according to our calculated error estimates, this would appear to support a value of $\epsilon > 0$.

A recent preliminary result of measuring the growth of the spatial correlation function directly is that of Warren *et al.* (1993) for elliptical galaxies. Warren *et al.* state that their result is consistent with $\epsilon = 0$, though they don't rule out $\epsilon > 0$, which is in fact the value which their data appear to indicate. This would therefore also appear to be consistent with our result.

4.6 Conclusion

In summary, we have made deep observations (to a total of 15600s in the centre of the mosaic) of the SGP field in the V band and derived the two-point angular correlation function for different subsamples of the resulting data. Our reduction techniques, choice of subregions and method of detecting galaxies have been described. A derivation of the $\mathcal{N}_e/\mathcal{N}_t$ correction and an analytical calculation of the expected number of pairs per bin in a uniform random distribution in a rectangle have been presented.

The subsamples of the sets of galaxies obtained go down to median magnitudes of $V \approx 24{\cdot}5$. The resulting angular correlation functions have amplitudes decreasing with median magnitude similarly to the decrease at brighter median magnitudes and are assumed to be power laws of slope $-0{\cdot}8$, which is consistent with the data.

Within these uncertainties, Neuschaefer *et al.*'s (1991) amplitudes which rise with increasing magnitude are not supported (though not strictly speaking ruled out either) but Efstathiou *et al.*'s (1991) amplitude is confirmed. However, our fainter values are also formally consistent with zero, i.e., a totally uncorrelated distribution.

If we have greatly overestimated these uncertainties, then these results would indicate that clustering growth is faster than if it were fixed in proper coordinates, i.e., $\epsilon > 0$. This is consistent with both N-body model predictions (Melott, 1992,

Yoshii *et al.*, 1993) and an observational measurement of the growth rate of the spatial correlation function (Warren *et al.*, 1993). However, these results would also then be inconsistent with those of Efstathiou *et al.*, with no obvious explanation for this inconsistency, though differences in wavebands, galactic latitudes and the details of data reduction and calculation would appear to be possible candidates for an explanation.

A followup to see whether this contingent result would still hold would be to observe to this same limiting magnitude over a much larger area, thereby guaranteeing that these uncertainties are reduced.

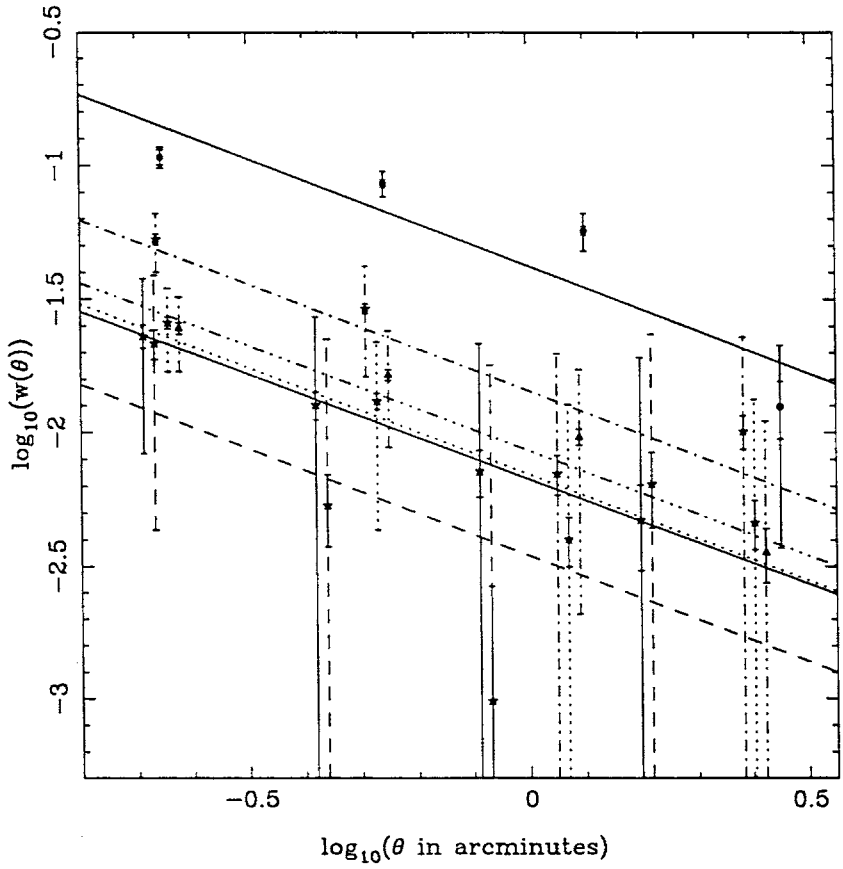

Figure 4.7: Two-point angular autocorrelation functions (with B_k^{-1} correction) - corrected data and fitted correlation functions. Slight horizontal offsets of 0·02 are used for clarity between some of the data points. The small, solid error bars indicate calculational uncertainties (due to using random simulations rather than analytical calculations) while the larger, variegated error bars indicate the intrinsic uncertainty calculated from standard deviations in the random simulations. The different subsamples can be identified by the symbol type as follows. The solid circles are, in order of increasing amplitude of the fitted function, calculated over the region and magnitude ranges R_1, $23{\cdot}5 < V < 25{\cdot}5$; R_1, $21 < V < 25{\cdot}5$; R_2, $21 < V < 25{\cdot}1$ and R_2, $21 < V < 24$ respectively. The solid triangles are for the region R_2, magnitude range $21 < V < 26{\cdot}5$, while the solid circles are for the region R_3, magnitude range $21 < V < 24{\cdot}6$. The line style of the intrinsic error bars for a subsample is the same as that of the fitted correlation function for that subsample.

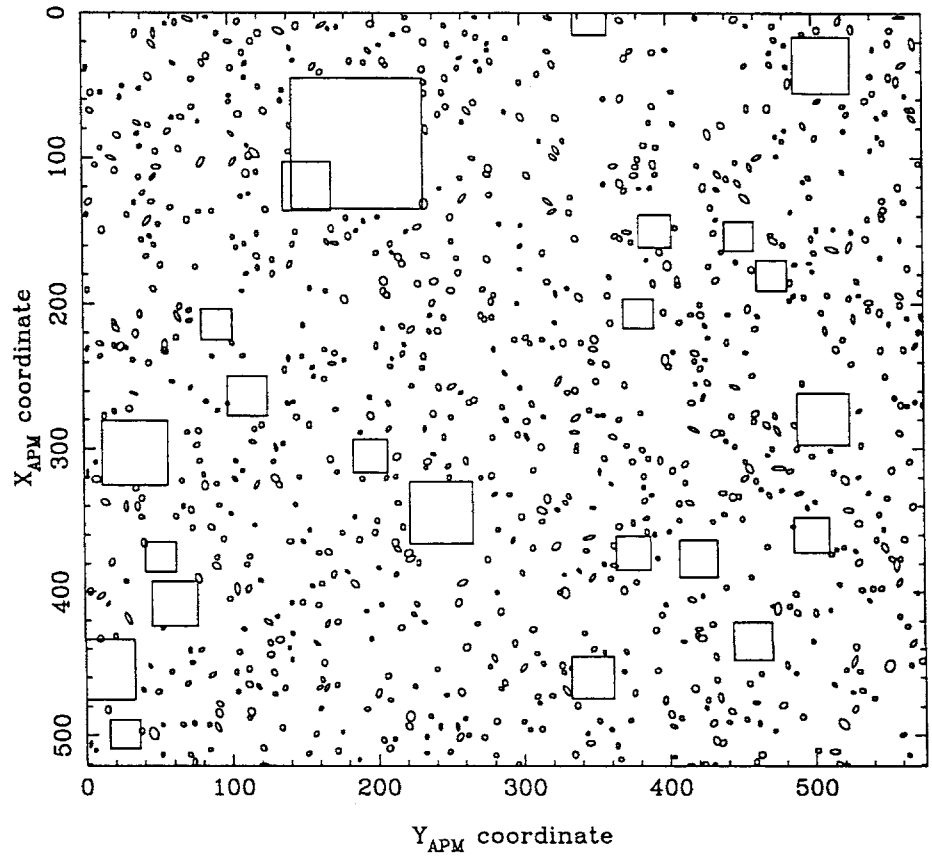

Figure 4.8: Representative isophotes of images detected in region R_1 having $23{\cdot}5 < V < 25{\cdot}5$ and not in squares surrounding objects of isophotal area greater than 100 pixels. Fig. 4.6 shows the correlation of these objects.

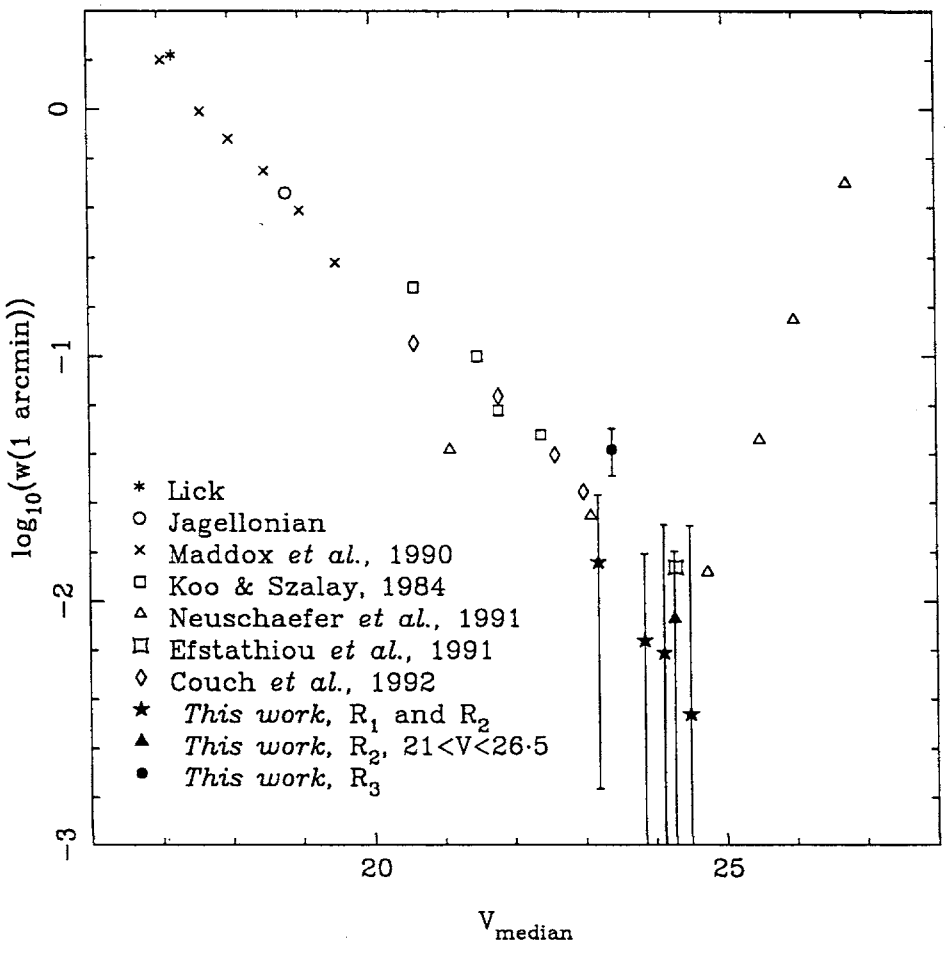

Figure 4.9: Comparison of previous authors' amplitudes of the two-point angular autocorrelation function with our results. The amplitudes are plotted as $\log_{10}(w(1'))$ as a function of median V magnitude, with transformations between wavebands mentioned in the text. The solid symbols represent our data. The solid stars represent, in order of increasing magnitude, calculations over the region and magnitude ranges R_2, $21 < V < 24$; R_2, $21 < V < 25{\cdot}1$; R_1, $21 < V < 25{\cdot}5$ and R_1, $23{\cdot}5 < V < 25{\cdot}5$ respectively. The solid triangle is for the region R_2, magnitude range $21 < V < 26{\cdot}5$, so is severely incomplete at the faint end, while the solid circle is for the region R_3, magnitude range $21 < V < 24{\cdot}6$, and includes some noise objects in its outer regions, so both of these measurements suffer systematic errors.

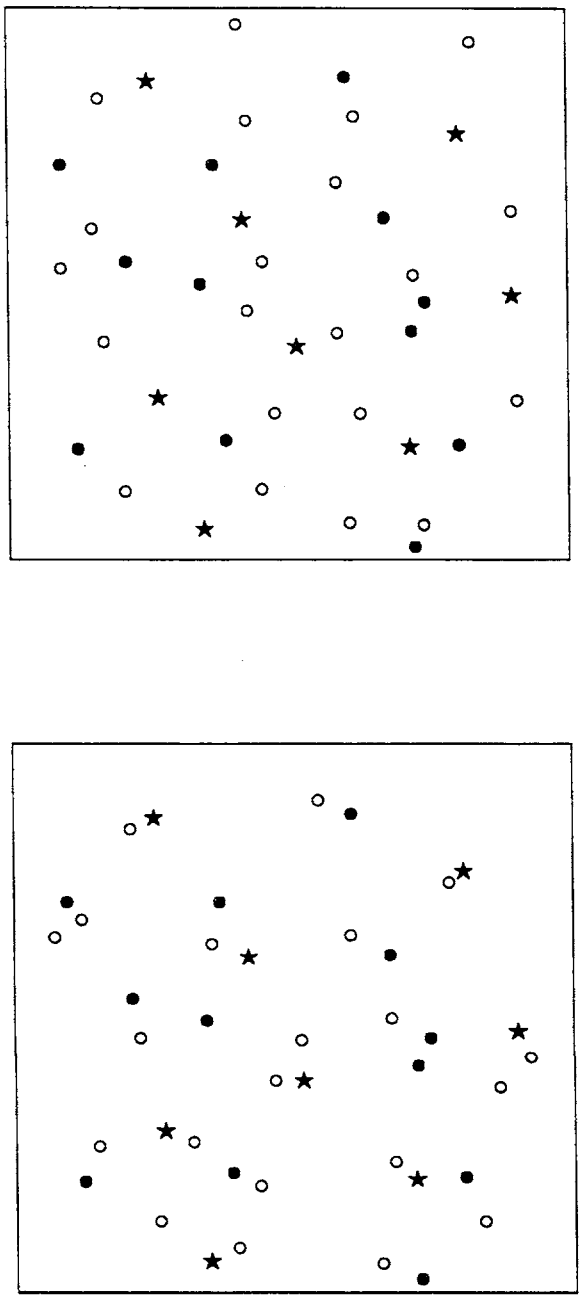

Figure 4.10: Plots of artificial populations showing problem with trying to estimate correlation function from incomplete data. The solid stars in each plot represent an "observed" bright population, the solid circles in each plot represent the "observed" part of a faint population, while the hollow circles represent two possibilities for an "unobserved" portion of the faint population. The "observed" points are identical in the two plots.

Chapter 5

Luminosity Function Evolution of Merging/Accreting Galaxies - Models

Abstract

Gravitational physics, stellar formation physics and stellar evolutionary physics are used to model galaxy evolution. Gas dynamics are not included.

Cosmological N-body simulations run by Warren *et al.* (1992) for a range of initial power spectra are searched for mass density peaks. As the dark haloes of galaxies are much more massive than the visible parts of galaxies, these density peaks are considered as galaxy haloes rather than just galaxies. For each model a galaxy halo merging history representing each halo over a range of time steps from initial formation to the present is determined. A certain fraction of the mass of each halo is considered as potentially star-forming material. From the merging histories the rate at which these haloes merge as well as the rates at which uncondensed matter is accreted onto the haloes is examined.

Bruzual's (1983) galaxy evolutionary population synthesis code is used to evolve the potentially star-forming material for each halo. Either an exponentially decaying star formation rate (SFR), a burst of star formation at each merging event or a combination of the two are used as the SFR. The bursts are parametrised by an SFR of

$$\psi(t) = \psi_0 \frac{\sum_{i \neq 1} M_i^{gal}}{M_0^{tot}} \frac{\sum_{\mathrm{all}\, i} M_i^{gas}}{2M_0^{gas}}$$

for a period of

$$t^{burst} = \frac{t_0^{burst}}{\sqrt{\frac{\rho^{gal}}{\rho_0}}}$$

where $\psi_0 = 50 M_\odot yr^{-1}$, $M_0^{gas} = 10^{10} M_\odot$, $M_0^{tot} = 10^{12} M_\odot$, $\rho_0 = 8{\times}10^6 M_\odot kpc^{-3}$, $t_0^{burst} = 2{\times}10^8 yr$; M_i^{gal} and M_i^{gas} are the total mass and gas mass respectively of the i^{th} most massive galaxy halo involved in the merger and ρ^{gal} is the density of the most massive galaxy halo involved in the merger.

Total masses, gas masses and stellar populations of the predecessors of a merger are added together to make the product of the merger.

The details of these models are described in this chapter.

5.1 Introduction

The purpose of the work discussed here is to examine an important aspect of the physics of galaxy evolution by linking the gravitational growth of density peaks and merging histories available from N-body simulations with evolutionary population synthesis techniques. Gas hydronamics are not used, so it is not expected that this work will provide a complete modelling of the processes involved. However, it is interesting to see how much this gravitational-evolutionary-population-synthesis combination does in fact give results matching observations.

In the context of this thesis, the intention is to model the evolution of the luminosity function, in order that we can model the faint galaxy number counts using an evolving luminosity function which includes both luminosity and number evolution in a realistic way. This chapter describes the models, while the following chapter shows the results.

The physics under examination in these models involves both merging and accretion of uncondensed material and the conversion of material into stars. It combines gravitational physics, stellar formation physics and stellar evolutionary physics. While the first of these is generally accepted as well understood both theoretically and observationally, the third still has significant uncertainties in the later and pre-main-sequence stages of stellar evolution, and the second appears a long way from having a good match between theory and observation. But it is the star formation rate (SFR), primarily via starbursts which are presumed to occur on merging, which is the new input physics involved in this combination. Hence, contingent upon the correctness of the other elements in the combination, comparison of the results with observational constraints such as the galaxy luminosity and correlation functions enable this new element to be tested.

The gravitational input physics is calculated theoretically via the N-body simulations. These N-body simulations are discussed in §5.2, while the algorithm used to search for density peaks in these simulation is described in §5.3.

In order to represent the evolution of these galaxies, merging histories are created. This is described in §5.4.

The stellar formation physics input to the models involves both the initial mass function (IMF) and the SFR. As no well accepted theory of stellar formation is yet available, the IMF and SFR are assumed to be separable, which empirically seems acceptable, though not well established. The IMF input is based on Scalo's (1986) review of various observational evidence, while the SFR is the function in which the gravitational physics of merging and accretion are connected with stellar formation physics. In the results presented here, the default SFR is an

exponentially decaying one, inspired by the idea that whatever the details of stellar formation are, the overall rate in an isolated galaxy should be proportional to the overall amount of gas remaining in the galaxy.

The stellar evolutionary physics involved is a combination from numerous sources, compiled by Bruzual (1983) and incorporated in the form of stellar evolutionary tracks in his evolutionary population synthesis code.

The theoretical and observational physics used to model the SFR on merger-induced starbursts is described in §5.5, while the connection between Bruzual's code and the merging history trees is described in §5.6.

A demonstration of the results of this model and possible effects on faint galaxy number counts are discussed in the following chapter.

Throughout this chapter and the following, a value for the Hubble constant of $H_0 = 50\, kms^{-1}\, Mpc^{-1}$ is used and the models are for an $\Omega_0 = 1{\cdot}0, \Lambda = 0$ universe.

5.2 N-body Models of Matter Density

The models of evolution of matter density in the Universe via gravity which we use are some of the N-body cosmological simulations run by Warren *et al.*, 1992. These were intended for examining the dynamical properties of haloes, such as angular momentum, so the correlation function, for example, was optimised for this purpose rather than for cosmological purposes. So, while not optimal for the study of the evolution of matter density in the Universe, the physics simulated in these models remains valid and is sufficient for a start to an examination of the models of interest in this thesis.

The present model analysed uses a 128 by 128 by 128 initial particle mesh. Particles are placed on this mesh, making a cube of $\sim 2{\times}10^6$ particles, with side length of the cube 10000 length units in comoving coordinates. The models with power law perturbation spectra imposed are of course scale-free in some senses, but a convention for scaling the units is chosen. This convention chooses 1 kpc for the length unit, $10^{10} M_\odot$ for the mass unit and 1 Gyr for the time unit, making the velocity unit close to 1 $km\, s^{-1}$ and the gravitational constant close to $4{\times}10^4$ in these units. (From hereon values are cited according to this convention unless otherwise mentioned.)

An initial perturbation spectrum, e.g., a power law with slope $n = 0$ (i.e., white noise), is imposed on this cube by "Fourier transforming the initial complex amplitudes" from the perturbation spectrum and using the the Zel'dovich "growing mode" method (Warren *et al.* 1992) on this Fourier transform and the 128^3 particle mesh. Particles more than 5000 kpc from the centre of the cube

are then trimmed off the particle set, resulting in a sphere of $\sim 1{\cdot}1{\times}10^6$ particles perturbed according to the perturbation spectrum.

This is then evolved forward gravitationally via a tree-code (e.g., see Barnes & Hut, 1986), initially with roughly logarithmic time steps up to $0{\cdot}3\,Gyr$, after which equal time steps of $0{\cdot}03\,Gyr$ are used, with every hundredth time step being stored on disk. It is these time steps which are available for peak analysis.

5.3 Peak Searching Algorithm

The simulation data are searched for density peaks at each time step by the following algorithm, known as an "oct-tree" method.

Conceptually, the sphere of particles is surrounded by a cube concentric to it and having side length the diameter of the sphere. This cube is divided into two in each dimension, making eight subcubes. If any of these subcubes has more than one particle in it, it is itself subdivided into eight subcubes. This process is repeated to a depth of n_{levels} levels below the original cube, unless all the cubes have one or zero particles in them (though this could not occur with this $1{\cdot}1{\times}10^6$-particle model). In the results presented here, we use $n_{levels} = 6$ and $n_{levels} = 9$ for $r_{thresh} = 5$ and $r_{thresh} = 1000$ (described in the following paragraph) respectively. In our model default units this makes the side length of the smallest cube $174\,kpc$ and $20\,kpc$ respectively at $z = 0$. The detection at the higher threshold finds peaks with smaller radii, hence the higher resolution is appropriate.

Any of the cubes at the deepest level which is more than r_{thresh} as dense as the mean density of particles in the sphere then has the list of particles it contains recorded as a primary density peak. The results presented here are for $r_{thresh} = 5$ and $r_{thresh} = 1000$. If we assume that the rotation curve of the Galaxy is flat at about $220\,km\,s^{-1}$ and that the circular velocity curve of the Galaxy is identical to the rotation curve, then the cumulative mass within a radius is proportional to the radius, and the density is $\rho(r) = 1{\cdot}2{\times}10^7\rho_c r^{-2}$ for H_0 as above and r in kpc. This makes our cutoff densities correspond to about $1500\,kpc$ and $110\,kpc$ respectively. The latter is a reasonable value for the size of the halo, while the former is about an order of magnitude greater than the largest values claimed for the radius of the Galaxy.

The next section of the algorithm first orders the primary density peaks by mass, from largest to smallest. An "incremental radius", r_{inc}, is defined as 1·1 times half of the largest diagonal of the cube used to determine the primary density peaks. A search is then made for any (primary) peak whose centre is less than $r_{inc} + r$ from the centre of the first peak, where r is the maximum radius

of the first peak. Whenever such a peak is found, it is joined to the first peak and the radius of the first peak is recalculated, so that subsequent comparisons are between the new, larger peak and further primary peaks. When this process has finished for the first peak, it is repeated for the next largest peak which has not already been joined to the first peak, searching for primary peaks (smaller than itself) which are less than r_{inc} from its maximum radius and joining any such peaks to itself. This process is repeated for each successive peak remaining unjoined.

After each primary peak has either had other (less massive) primary peaks joined to it or itself been joined to a (more massive) primary peak, a secondary list of density peaks results, corresponding to peaks inside isodensity contours for the value of r_{thresh} used.

5.4 Creation of History Tree

A history tree of peak merging is then obtained as follows.

Peak lists for a series of time stages of the model are obtained by the algorithm just described, each with the same n_{levels} and r_{thresh}. Then for each pair of successive times, t_1, t_2, the peaks in the two times are compared as follows. Two arrays, a_1, a_2, each with as many elements as the number of particles in the simulation, are created. For each element j of array $a_i (i = 1, 2)$, the number k identifying the peak that particle j is a member of is assigned to $a_i(j)$, where this is a peak according to the peak list for t_i. If the particle is not a member of any peak, a null value is assigned. A sort (into increasing arithmetical order) is performed on array a_2, swapping the elements of a_1 according to this same order. This means that any consecutive series of the same peak number in a_2 has the peak numbers of the corresponding particles at t_1 at the same positions in a_1, i.e., for the particles in any peak at t_2, a list of which peaks those particles were in at t_1 is obtained.

For any such peak at t_2, if more than 50% of the particles in any of the peaks at t_1 which contribute to the peak at t_2 are present in the peak at t_2, then the peak at t_2 is considered a "descendant" of the peak at t_1 and the peak at t_1 is an "ancestor" of the peak at t_2. These links are represented in a number of arrays. Due to the nature of this algorithm, no peak can have more than one descendant, though it can certainly have more than one ancestor, which is allowed in the array storage.

Applying this across each pair of successive times obtains a representation of the peak merging history.

The merging history tree plots are obtained by choosing a range of peaks at a certain time stage (usually the last time stage) and tracing back all their ancestors. The radii of the circles in any one plot are a logarithmic transformation of the peak masses. This is monotonic, so that the bigger the circle radius, the bigger the mass, but the normalisation is not necessarily the same in each plot. The vertical axis indicates time/redshift, while the horizontal axis is only used to separate individual peaks. The latter doesn't directly indicate space positions, although there should be some correlation between how close two peaks are in the plot and how close they are in space.

The line segments joining the circles are the key feature of the plots. These indicate that the peak at the earlier time is considered to merge into the peak at the later time according to the above algorithm.

Much information on the merging process is represented in these tree plots. The ones presented here (Figs 6.8–6.22) start with a range of final peaks and trace backwards. However, the reader should be aware that any peaks which have no descendant at the final time stage are therefore not represented here. As described in the following chapter, for the $n = 0(b)$ model about 5% to 10% ($r_{thresh} = 5$) or 10% to 30% ($r_{thresh} = 1000$) of the peaks at each time stage have no descendants at the following time stage, while in the $n = -2(b)$ model the same fraction is about 20% to 30% ($r_{thresh} = 5$) or 30% to 50% ($r_{thresh} = 1000$). This can be easily understood due a large fraction of the halo evaporating in the merging process and the merged halo therefore failing to pass the merging criterion defined here. Typically, about $25\% \pm 25\%$ of a halo evaporates (e.g., in tails) or forms in low-density "atmospheres" in close-up looks at N-body simulations of interacting galaxies (Quinn, 1992). These tails or atmospheres are likely to fall below the density detection threshold.

So, for any time stage in one of these plots, only those peaks which end up in the chosen range of final peaks are shown.

5.5 Modelling Starbursts to Occur on Merging

We represent star formation physics via an initial mass function (IMF) and a star formation rate (SFR). The separability of these two is not guaranteed *a priori*, though observation and theory do suggest that it is a reasonable assumption. The IMF is discussed in the §5.6, while this section describes our modelling of the SFR, based on starbursts.

For the purpose of this first-order examination of the effect of merger-induced starbursts on galaxy spectral evolution, we only use very simple models of the

starbursts. The following are observational and theoretical indications of what models appear realistic.

An early observational model of a starburst, but not necessarily one caused by a merger, is that of Rieke *et al.* (1980).

Rieke *et al.* (1980) model the starburst in the nucleus of M82 via evolutionary population spectral synthesis. They find that instantaneous (Dirac delta function) and constant star formation rate models fail to produce the observed spectrum, but exponential decay SFR models with an IMF with a lower mass cutoff well above a solar mass are necessary. Their best models (say, D and F) have the e-folding time in the SFR $t_0 = 2{\times}10^7 yr$ and $t_0 = 1{\times}10^8 yr$ and run for $t = 5{\times}10^7 yr$ and $t = 1{\cdot}6{\times}10^7 yr$ respectively. Both have IMF's with $\alpha = 2$ and the mass range $3{\cdot}5 - 31 M_\odot$. The mass turned into stars is $\approx 1{\cdot}5 - 2{\times}10^8 M_\odot$, this being constrained to be less than the total mass in the nucleus, estimated as $3{\times}10^8 M_\odot$ by Rieke *et al.* This constraint is considered the major reason for the need for a high lower mass cutoff. That is, if a normal lower mass cutoff is used, then more mass than is actually present in the nucleus is required to generate the necessary luminosity, which of course is physically unreasonable.

Rieke (1991) describes more recent observational constraints on the models for M82, finding that the above conclusion still holds using more modern stellar evolutionary tracks in the models.

Scoville & Soifer (1991) argue from IRAS far-infrared data that "virtually all of the strong *global* starbursts occur in ... starburst-infrared galaxies," defined as "those with L_{IR}/M_{H_2} significantly higher than in normal galaxies," which correlate highly with "the occurrence of a recent [galaxy-galaxy] interaction." They argue that such global starbursts require the progenitor galaxies to be of comparable mass in order to generate such activity.

While this result doesn't necessarily imply the converse, i.e., that all mergers of similarly sized galaxies induce major global starbursts, it does imply that it is a reasonable exploration of parameter space to assume that this converse is correct. With the assumption of this converse, Scoville & Soifer find that the high luminosity end of the infrared (galaxy) luminosity function from the IRAS survey is consistent with 0·2% of all spiral galaxies undergoing global starbursts at the present with lifetimes equal to the dynamical times of large galaxies, $\sim 1{-}2{\times}10^8 yr$. For the most IR-luminous galaxies they find SFR's of $10{-}100 M_\odot yr^{-1}$. They don't find a high lower mass cutoff necessary for their models to fit the observations.

Norman (1991), citing the models of merging gas-rich disk galaxies of Hernquist and Barnes, (Barnes, 1990, equal mass galaxies, Hernquist, 1989, differing

mass galaxies), describes a qualitative three-phase model to take into account gas falling into the galaxy centre. The three phases essentially correspond to proportions of the gas having fallen to the centre. Actual star formation models following these three phases separately are not mentioned in the article, but if this is done in the future, such models could be incorporated in the code discussed here.

Norman (1991) also argues that constant SFR models of starbursts satisfy an observed sparsity of post-starburst galaxies relative to starburst galaxies, but that instantaneous SFR models predict too many post-starbursts.

Hence, for these first-order models, a starburst with a constant SFR is chosen.

For pairwise mergers, the following canonical values are chosen. We normalise the rate of the starburst for a "typical" large galaxy merger product to be an SFR of $\psi_0 = 50 M_\odot yr^{-1}$ as per the models of Scoville & Soifer (1991). The lower mass cutoff in the IMF used here ($0{\cdot}08 M_\odot$, see eqn 5.4) is consistent with Scoville & Soifer's value of $0{\cdot}1 M_\odot$.

We consider this to be the remnant of two large galaxies each of gas mass $M_0^{gas} = 10^{10} M_\odot$, total mass $M_0^{tot} = 10^{12} M_\odot$ and halo radius $50\,kpc$. This gives a dynamical time $t_{dyn} \equiv (G\rho_0)^{-1/2} \approx 2{\times}10^8 yr$, where the mean density of either galaxy to its halo radius is $\rho_0 = 8{\times}10^6 M_\odot kpc^{-3}$. The modelling by Barnes (1990), Hernquist (1989) or earlier non-gaseous N-body models such as those of Quinn & Goodman (1986) find that the merger takes place over only a few dynamical times. This is why Scoville & Soifer (1991) chose burst durations of dynamical time scales. So the choice of progenitor galaxies here gives a t_{dyn} matching Scoville & Soifer's burst duration of $t_0^{burst} = 2{\times}10^8 yr$, which is chosen as the canonical burst duration.

In this canonical case, 50% of the total gas mass is used up in the burst. To sum up, we have

$$\psi_0 = 50 M_\odot yr^{-1}$$

$$M_0^{gas} = 10^{10} M_\odot$$

$$M_0^{tot} = 10^{12} M_\odot$$

$$\rho_0 = 8{\times}10^6 M_\odot kpc^{-3}$$

$$t_0^{burst} = 2{\times}10^8 yr \qquad (5.1)$$

The canonical values are then scaled for different situations. To first order it

seems reasonable that the kinetic energy available for generating star formation should be proportional to the mass of the smaller galaxy and that the SFR should also be proportional to the total amount of gas available. Hence we scale the SFR by the mass of the smaller galaxy times the ratio of combined gas mass to $2M_0^{gas}$.

Since we consider the duration of the starburst to be the order of a dynamical time, t^{burst} is scaled by $\rho^{-1/2}$, where ρ is the density of the larger galaxy.

Note that both of these scalings are also reasonable for galaxies of similar masses.

Given a coarse time resolution in the merging histories, each merger is identified by the code as one multiple merger—e.g., seven galaxies merge to one—instead of as a series of several individual pairwise mergers. If we consider the approximation that each of the pairwise mergers is with the largest progenitor galaxy, then we can choose the following compromise.

Have a single burst with the above normalisation. Scale the SFR by the sum of the masses of each of the smaller galaxies (i.e., all but the largest) and by the ratio of the combined gas mass from all progenitor galaxies (i.e., including the largest) to $2M_0^{gas}$, giving

$$\psi(t) = \psi_0 \frac{\sum_{i \neq i_{max}} M_i^{gal}}{M_0^{tot}} \frac{\sum_{\text{all } i} M_i^{gas}}{2M_0^{gas}} \tag{5.2}$$

where $\psi(t)$ is the star formation rate (in $M_\odot yr^{-1}$), the progenitor galaxies are labelled by i, and i_{max} is the label of the progenitor galaxy of greatest mass. (For the present version of peak selection, $i_{max} = 1$.)

Scale the starburst duration as above, by $\rho^{-1/2}$, where ρ is the density of the largest galaxy, giving

$$t^{burst} = \frac{t_0^{burst}}{\sqrt{\frac{\rho^{gal}}{\rho_0}}}. \tag{5.3}$$

Two modifications may have to be applied in some situations. Firstly, where the starburst at this rate uses up more gas than is actually available, it is truncated in time at the point of having zero mass of gas left. Secondly, if the duration of the starburst is longer than the time interval to the next time step, it is truncated at that next time step.

While this modelling of multiple merger-induced starbursts with large time steps may make the spectral evolution more temporally discrete than it should be, it does conserve physical quantities in line with the observational and theoretical constraints discussed above.

5.6 Connection with Galaxy Evolutionary Population Synthesis (GEPS)

We use galaxy evolutionary population synthesis to combine star formation and stellar evolutionary physics. A version of Bruzual's GEPS code (Bruzual, 1983) which is essentially that of 1983, but with some updating and conversion to UNIX, is used. In the interactions of my own programs with this code, the star formation history (star formation rate, SFR) and masses of galaxies and gas in galaxies are determined outside of the Bruzual routines or by amended versions of the Bruzual routines. The return of gas from supernovae to a galaxy was turned off for test purposes but otherwise left on. The loss of this supernova gas from a galaxy was not invoked, neither was the option allowing infall of gas to a galaxy.

The initial mass function (IMF) used was the default IMF chosen by the code, after Scalo (1986) (e.g., Fig. 16 in Scalo, 1986). Where $f(m) \propto m^{-(1+x)}$ is the number of stars born per unit (linear) mass in a given mass range, the IMF slopes used are

$$x = \begin{cases} -2{\cdot}60, & 0{\cdot}05 \leq M \leq 0{\cdot}08 M_{\odot} \quad \text{(brown dwarfs)} \\ -2{\cdot}60, & 0{\cdot}08 \leq M \leq 0{\cdot}18 M_{\odot} \\ 0{\cdot}01, & 0{\cdot}18 \leq M \leq 0{\cdot}42 M_{\odot} \\ 1{\cdot}75, & 0{\cdot}42 \leq M \leq 0{\cdot}62 M_{\odot} \\ 1{\cdot}08, & 0{\cdot}62 \leq M \leq 1{\cdot}18 M_{\odot} \\ 2{\cdot}50, & 1{\cdot}18 \leq M \leq 3{\cdot}5 M_{\odot} \\ 1{\cdot}63, & 3{\cdot}50 \leq M \leq 75 M_{\odot}. \end{cases} \tag{5.4}$$

The Bruzual code works without introducing numerical effects (e.g., rounding errors) in the star formation history (SFR) of a galaxy by using only simple analytical forms of the SFR. Numerical effects do of course come in when the galaxy spectral energy distribution (SED) is calculated, since only finitely many points representing different stellar ages are present for each of the finitely many mass tracks.

However, this has the disadvantage that one cannot simply stop the code after a certain time step, save the population data, start up the program from scratch, read in the saved population data and continue on as if the program had never stopped. The population data could be stored and later read back in, but this would round each star's age to the appropriate stellar evolution track age at every time step, making cumulative errors. The alternative technique chosen was to numerically store the SFR at each time step. An array of time points from one time step to the following time step and the corresponding array of integrals of the SFR are stored. These integrals of the SFR are the total number of stars created since the first star formation in any of the predecessor peaks which end

up in the present peak being worked on. Because I use the integral of the SFR, the errors are not cumulative, and in the present version are $\sim 0{\cdot}1\%$.

Hence the program which applies GEPS to the merging histories, **evolve.f**, stores an SFR for each peak as it is evolved quiescently to the next time step, adds these together for merged peaks, and from that point on the effect of GEPS is the same as if all the stars in the contributing peaks had been in the same peak, but a nonsimple numerical SFR had operated in that peak.

For the present modelling, GEPS is applied by optionally having an exponentially decreasing SFR between mergers and optionally having starburst SFR's commencing at each merger. Gas masses and total masses are by default conserved, i.e., the gas and total masses of a galaxy are the respective sums of the gas and total masses of predecessor galaxies, except that matter accreting directly onto the density peaks is added as gaseous mass. If both exponential and burst star formation are turned on simultaneously (considered the most realistic model) the SFR's are simply added together, conserving the number of stars created.

5.7 Summary

The above form a brief description of the ingredients and algorithms used in our galaxy evolutionary models.

We model gravity by 1·1 million particle N-body simulations; we search for density peaks according to some density threshold above the mean universe density (i.e., at some iso-density contour); we consider these objects to be (dark plus luminous) galaxy haloes; we calculate and represent their merging histories (as merging history trees); we insert an observationally inspired star formation rate due to merger-induced starbursts; and we combine all of this with the initial mass function and stellar evolution modelled in Bruzual's (1983) evolutionary population synthesis code.

The results of these models are described in the following chapter.

Chapter 6

Luminosity Function Evolution of Merging/Accreting Galaxies - Results

Abstract

The results of the galaxy evolutionary (merger-induced evolutionary population synthesis, or MIEPS) models described in the previous chapter are discussed. Information on the peaks considered as massive objects (galaxy haloes) and as luminous objects (galaxies) is presented. The runs of the model discussed are for initial perturbation power spectra of slope $n = 0$ and $n = -2$, for peak detection at thresholds of 5 and 1000 times the mean universe density in an $\Omega_0 = 1{\cdot}0, h = 0{\cdot}5, \lambda_0 = 0$ universe.

Resultant evolution of the luminosity function and how this may affect the faint galaxy number counts is shown.

6.1 Introduction

The software described in the previous chapter has been applied to both an $n = 0$ and an $n = -2$ power law initial perturbation spectrum N-body model (labelled n0b, n-2b by Warren *et al.*, 1992). Table 6.1 shows redshifts and cosmological times for the timesteps available for these two models. The negative redshifts correspond to future times with the default model units (§5.2). If the time units chosen are different to the default, then these latter time stages can be moved into the past or the present.

Peaks are detected in both of these models at thresholds of both $r_{thresh} = 5$ and $r_{thresh} = 1000$ times the mean universe density. The latter is the more physically reasonable of these two detection thresholds. The peaks detected, their mass

$redshift$	$t(Gyr)$	$timestep$	
		$n=0$	$n=-2$
11·2	0·31	40	(15)
3·2	1·51	–	55
1·5	3·3	140	115
0·62	6·3	240	215
0·25	9·3	340	315
0·039	12·3	440	415
−0·10	15·3	540	515
−0.203	18·3	640	615

Table 6.1: Parameters of Time Stages Used

functions and merging histories are discussed in §6.2 and §6.3. The two-point autocorrelation functions of the peaks, which should be used to check (primarily) the time scaling of the simulations, are discussed in §6.4. Mass-to-mass and mass-to-light ratios are discussed in §6.5.

The luminosity functions which result from the full models and rescaling of model mass and length units are discussed in §6.6. Plots of faint number counts derived from these luminosity functions are shown in §6.7.

6.2 Peaks

The number of peaks found (with $r_{thresh} = 5$) for each of these time steps is shown in Table 6.2. In the $n = -2$ model, matter has not yet collapsed into peaks at $t = 0{\cdot}31\,Gyr$, hence the $t = 1{\cdot}5\,Gyr$ time step was used instead.

$t(Gyr)$	$r_{thresh} = 5$		$r_{thresh} = 1000$	
	$n=0$	$n=-2$	$n=0$	$n=-2$
0·3	4296	–	238	–
1·5	–	2023	–	412
3·3	1598	2009	4214	1421
6·3	1090	1214	2695	1516
9·3	858	856	2121	1176
12·3	732	673	1891	923
15·3	647	523	1674	790
18·3	607	460	1524	672

Table 6.2: Number of peaks found for the different power spectra and detection thresholds.

The reality of these peaks is verified visually by rectilinear projections of a sample of the points for each peak plotted with differing symbols for different peaks; by radial particle count profiles; and by an interactive program which

plots a sampling of all the points, optionally colouring a range of peaks in a third colour to the particle colour and the black background and allows real time rotation of the image to give an intuitive feel of the three-dimensional shape of the data. (This latter program is **magnum**, written by P. Quinn.) Figure 6.1 shows a projection plot for the analysis of the final time stage of the $n = 0$ model, while Figures 6.2 and 6.3 show the radial particle count profiles for the four biggest peaks (by number) and for four smaller peaks. The profiles are simply numbers of particles per spherical shell, hence the fact that they quickly decrease to zero shows that the density falls off much faster than r^2. Note that in Fig. 6.3 one profile has two maxima, neither at its centre. This is because, as a closer investigation of the peaks with magnum shows, a small proportion of the smaller "peaks" are in fact fairly close binary peaks rather than single peaks as desired. These binaries are usually quite uneven in size, so consideration of the peak as a single peak is still a good approximation.

For each time stage, a peak at time t_i is considered to merge into a peak at the following time stage t_{i+1} (or retain its identity) if and only if more than 50% of the particles of the peak at time t_i are present in the peak at time t_{i+1}. Table 6.3 shows the means and standard deviations of what fraction of a peak at time t_i is present in a peak at time t_{i+1}. By definition, these fractions are constrained to be greater than 50%.

$t(Gyr)$	$r_{thresh} = 5$		$r_{thresh} = 1000$	
	$n = 0$	$n = -2$	$n = 0$	$n = -2$
0·3	$96 \pm 8\%$	–	$90 \pm 11\,\%$	–
1·5	–	$87 \pm 15\%$	–	$76 \pm 12\,\%$
3·3	$92 \pm 9\%$	$84 \pm 14\%$	$78 \pm 12\,\%$	$74 \pm 12\,\%$
6·3	$92 \pm 9\%$	$81 \pm 14\%$	$79 \pm 12\,\%$	$71 \pm 11\,\%$
9·3	$93 \pm 8\%$	$82 \pm 13\%$	$81 \pm 12\,\%$	$72 \pm 10\,\%$
12·3	$93 \pm 8\%$	$82 \pm 13\%$	$82 \pm 11\,\%$	$72 \pm 11\,\%$
15·3	$94 \pm 8\%$	$84 \pm 12\%$	$84 \pm 11\,\%$	$74 \pm 10\,\%$
18·3	–	–		

Table 6.3: Statistics of fraction of peak at time stage listed here contained in peak at following time stage

Figures 6.4, 6.5 6.6 and 6.7 show the mass functions of these peaks. These figures suggest that with the detection threshold of $r_{thresh} = 5$, for either spectral index the overall halo merging rate from $t = 3{\cdot}3\,Gyr$ (i.e., for $z \approx 1{\cdot}5$,) to the present is little more than about $3 - 10$ for galaxies below about $10^{10} M_{\odot}$. While this merging goes on, the number of large haloes in the largest bin in the $n = 0$ model increases somewhat until the last time step. Depending on the average

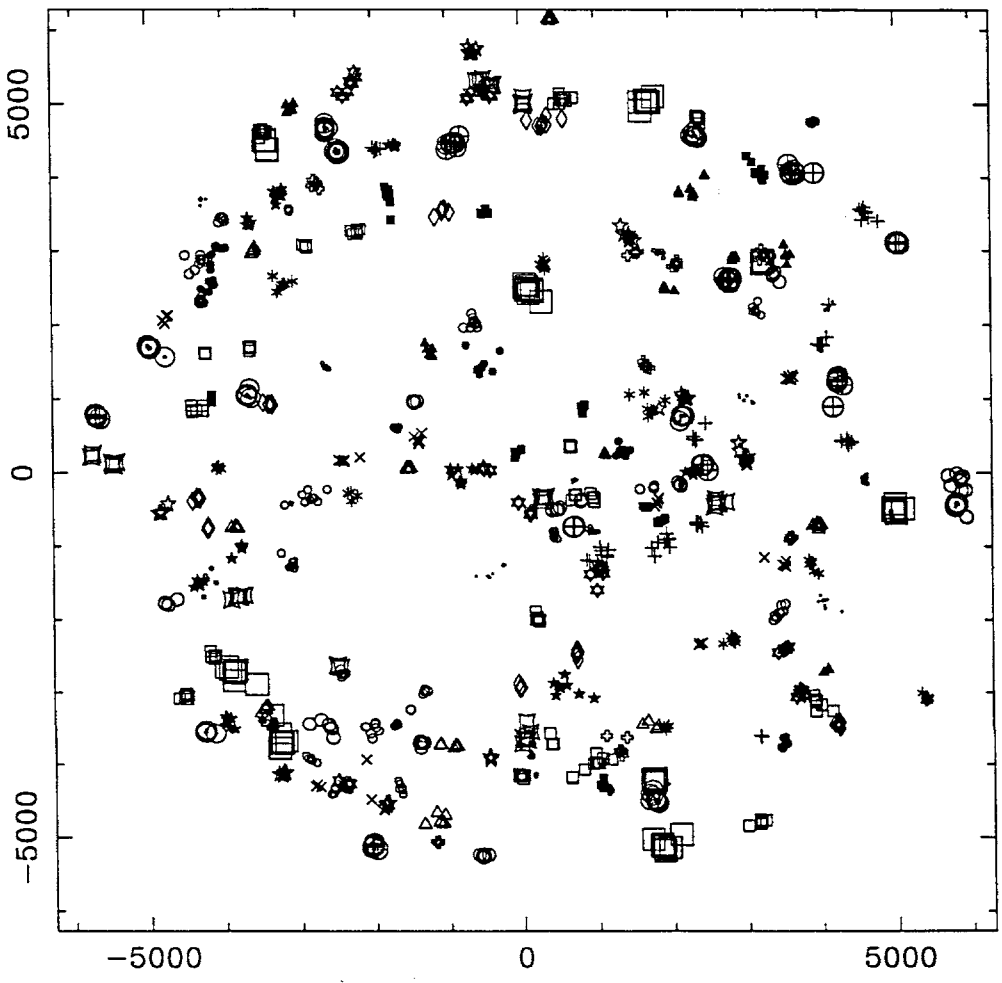

Figure 6.1: Rectilinear projection of set of peaks found in time stage 640 of the $n = 0$ model with $r_{thresh} = 5$. For each peak, a maximum of 10 particles in the peak are plotted, using one of the 23 available symbols. In a few cases, separate peaks with identical symbols are projected close to one another.

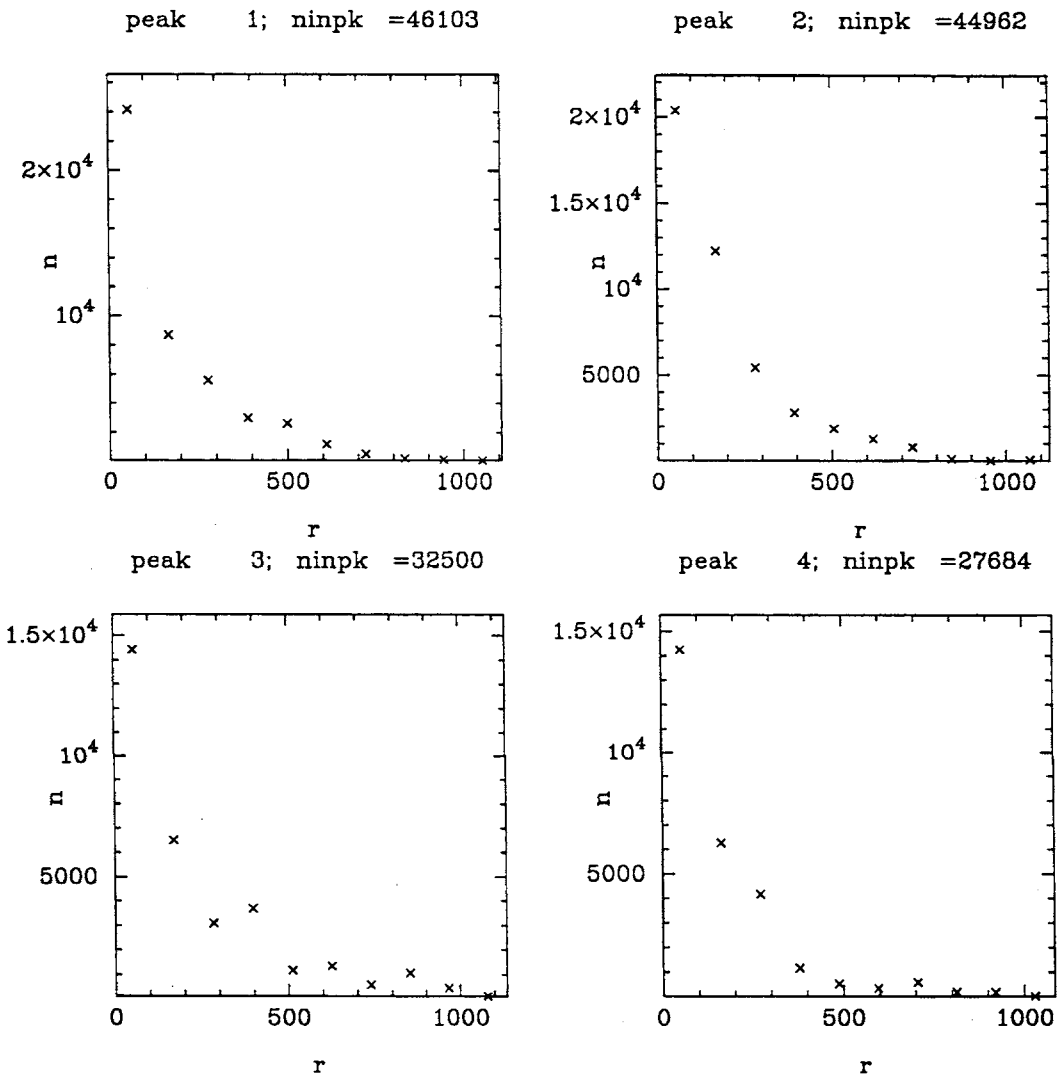

Figure 6.2: Peak profiles: number of particles in spherical shells are plotted for peaks $1-4$ of time stage 640 in the $n=0$ model for $r_{thresh}=5$.

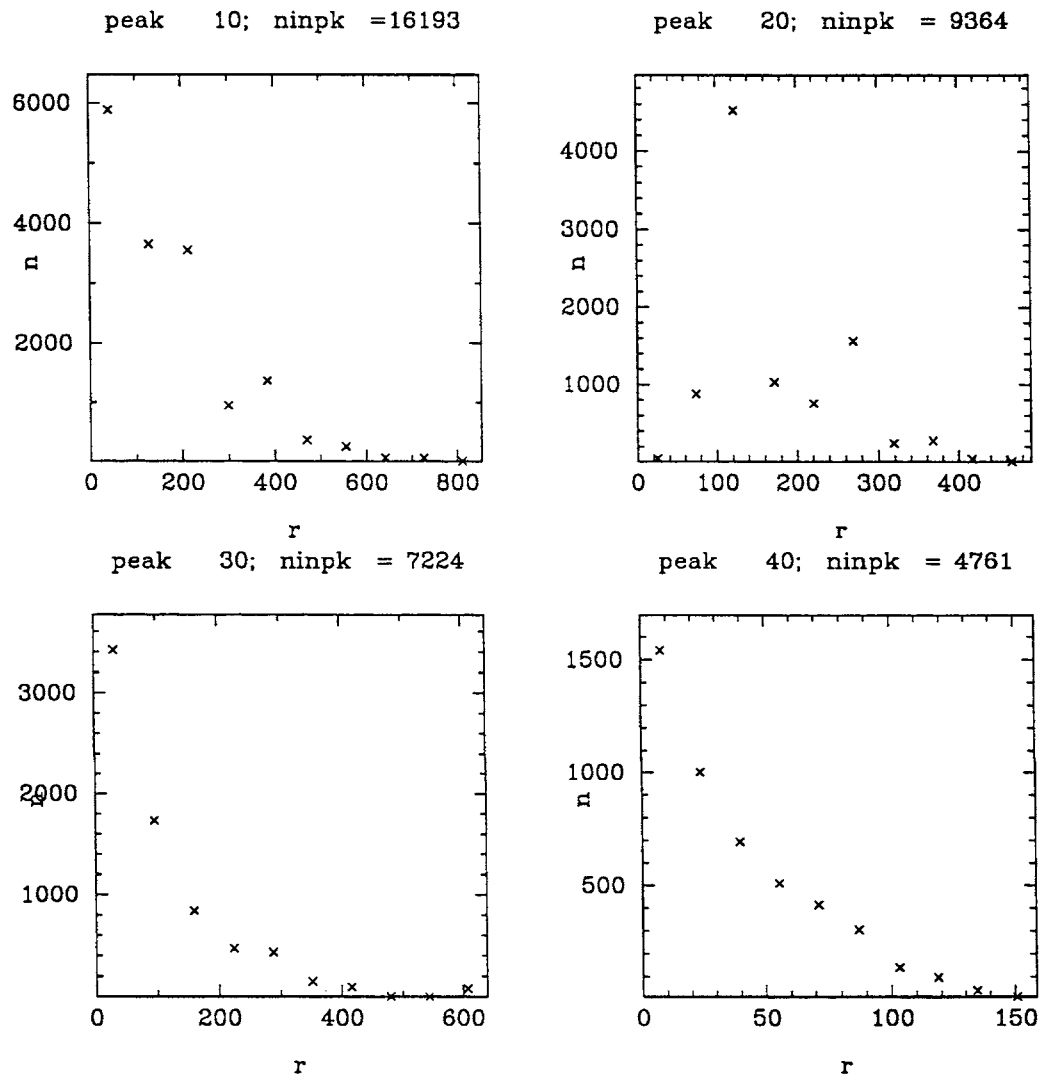

Figure 6.3: Peak profiles: number of particles in spherical shells are plotted for peaks 10, 20, 30 and 40 of time stage 640 in the $n = 0$ model for $r_{thresh} = 5$.

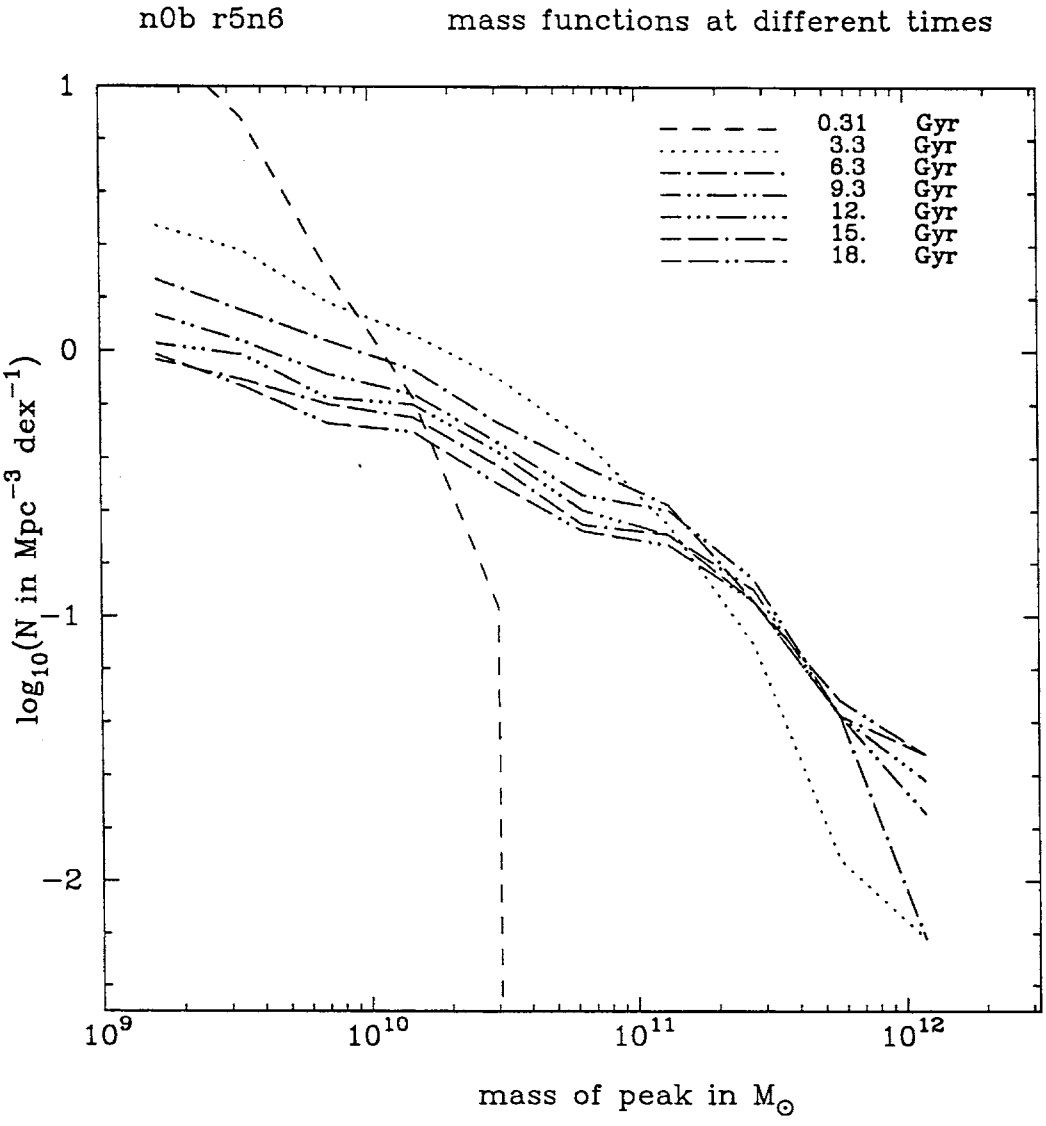

Figure 6.4: Mass functions for $n = 0$ model for $r_{thresh} = 5$.

number of small haloes which merge into a single large one, the increase in the number of large haloes would appear at first sight to be explained by the decrease in the number of smaller ones, consistent with a merging ratio of about $3 - 10$. Though the large mass end of the $n = -2$ mass function is noisy, there still are enough increases at the large end to interpret this mass function evolution similarly.

These plots show a significant dependence on detection threshold and a weak dependence on n. For the peaks detected at the more realistic threshold of $r_{thresh} = 1000$, the merging is much weaker than for $r_{thresh} = 5$. For the same density field, objects detected at the higher threshold consist of the dense cores of

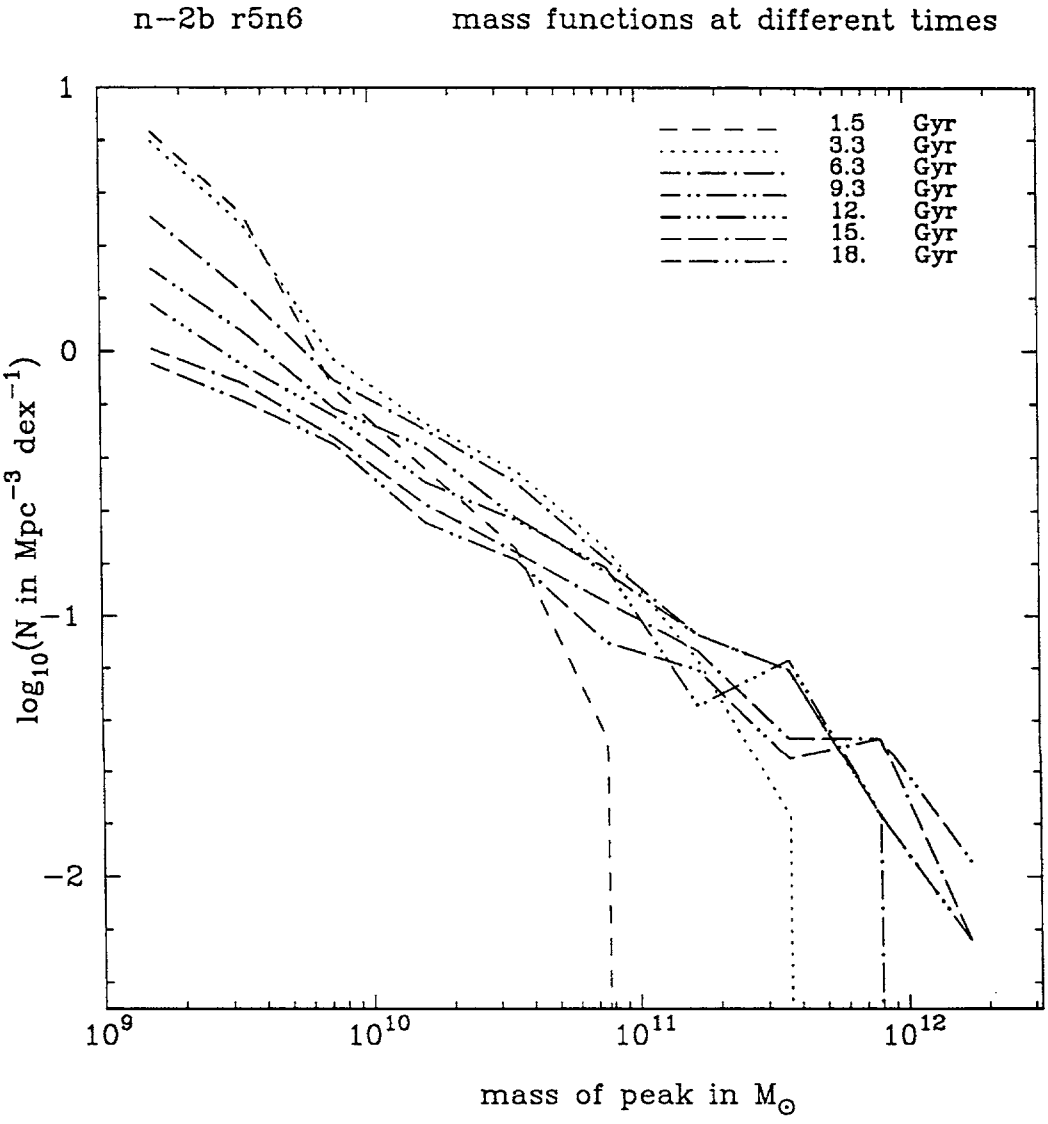

Figure 6.5: Mass functions for $n = -2$ model for $r_{thresh} = 5$.

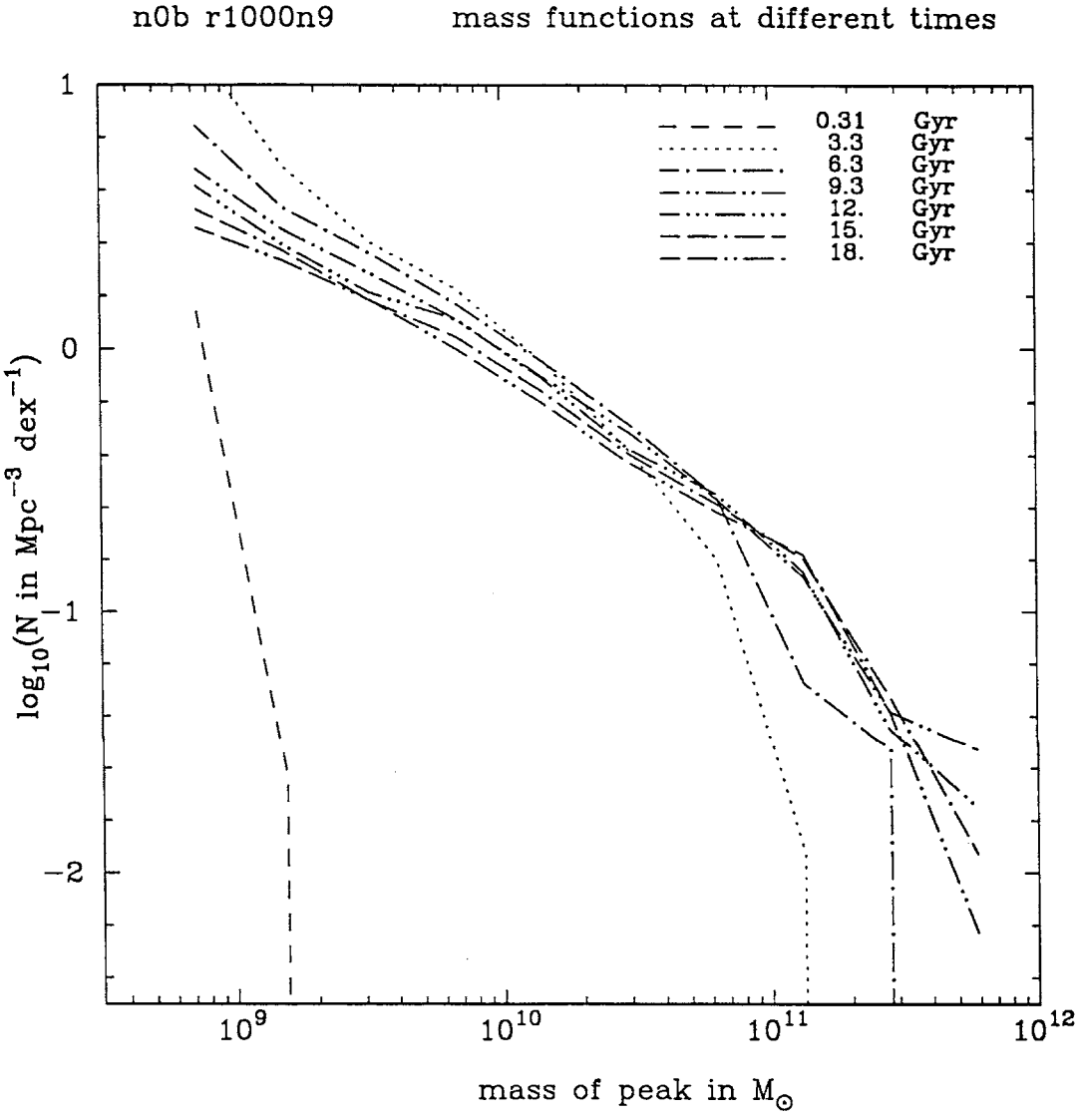

Figure 6.6: Mass functions for $n = 0$ model for $r_{thresh} = 1000$.

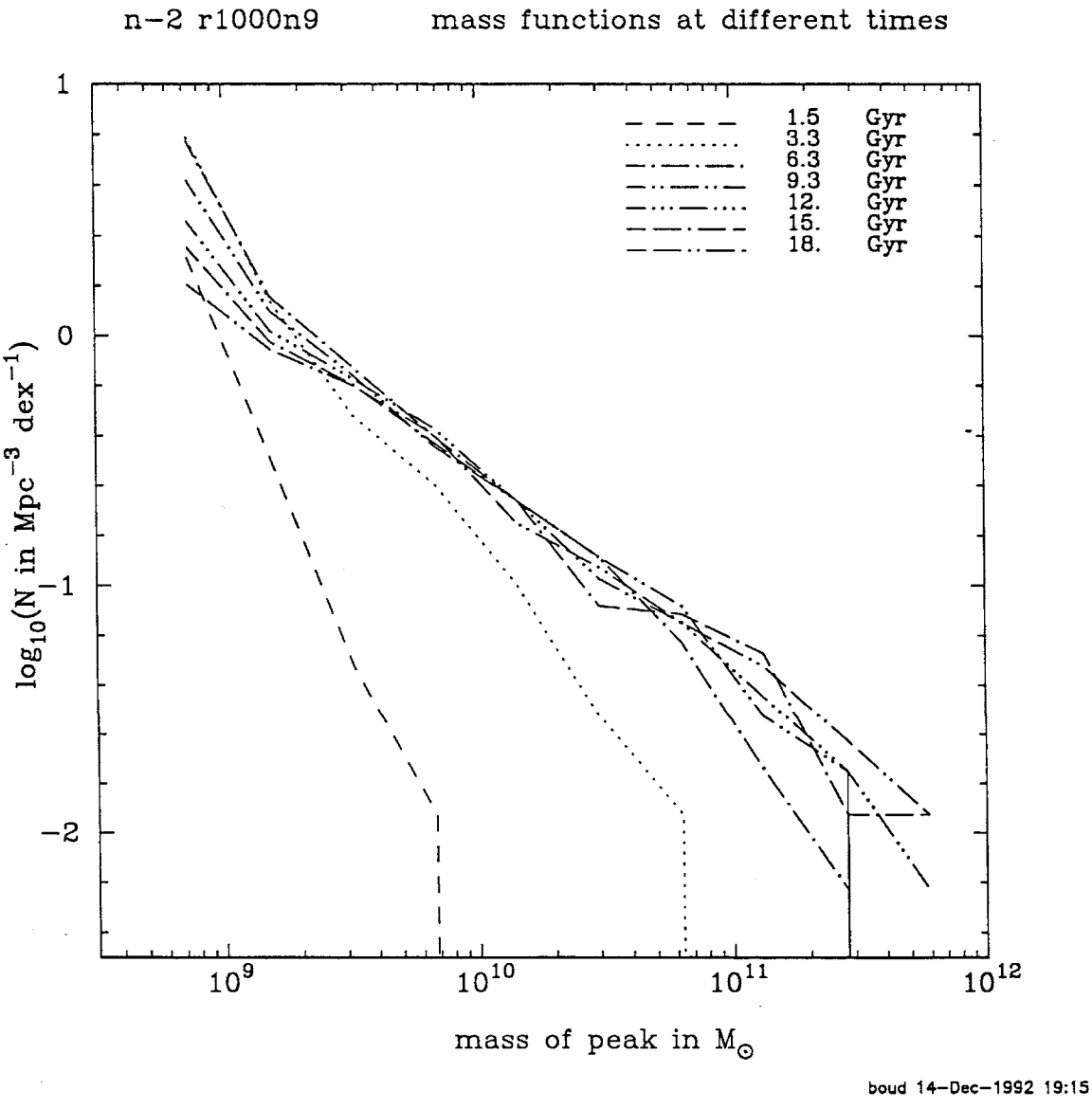

Figure 6.7: Mass functions for $n = -2$ model for $r_{thresh} = 1000$.

the objects detected at the lower threshold. Hence, a simple explanation for the weaker merging is that if the low density envelopes merge, the cores don't necessarily do so, but if the cores merge, the large low density envelopes are almost certainly going to merge.

Some simple statistics show that the merging history is not as simple as has just been described for the $n = 0$, $r_{thresh} = 5$ model.

Table 6.4 shows the fraction of the peaks at each time stage that have no descendants, i.e., the fraction of the peaks for which no more than 50% of their particles appear in any single peak at the following time stage. The fact that these are nonzero (from about 5% for $n = 0$, $r_{thresh} = 5$ to $30\% - 50\%$ for $n = -2$, $r_{thresh} = 1000$) shows that many peaks are destroyed in the sense that more than 50% of their particles may have been pulled into an "atmosphere" of a large peak at a density lower than the threshold density or possibly thrown out of the peak or pulled into another peak. This means that the peak number density does not only decrease by merging, it also decreases by this peak destruction. Hence, for example, if the overall number ratio is 4 : 1 but one in four haloes terminates, then the underlying ratio of haloes actually merging is only 3 : 1. Of course, this distinction is dependent on the definition of halo identity as described above.

$t(Gyr)$	$r_{thresh} = 5$		$r_{thresh} = 1000$	
	$n = 0$	$n = -2$	$n = 0$	$n = -2$
0·3	5%	–	11%	–
1·5	–	15%	–	32%
3·3	8%	24%	32%	40%
6·3	8%	30%	26%	49%
9·3	7%	29%	23%	46%
12·3	7%	24%	20%	44%
15·3	4%	21%	15%	36%
18·3	–	–	–	–

Table 6.4: Fraction of peaks which have no descendants at following time stage

More direct statistics are those of the overall history of the peaks detected at the final time stage. The mean (and standard deviation) of the overall number of peaks which originally collapse to above the threshold density (either at the first time stage or at a later time stage) and end up in a final peak is shown in Table 6.5.

While these mean values are in the range $3-10$ estimated above for $r_{thresh} = 5$, the standard deviations show that many final peaks come from as many as 20 or more original peaks. In fact, the maximum number of peaks that any final

	$n = 0$	$n = -2$
$r_{thresh} = 5$	7·4 ± 20·7	5·0 ± 16·9
$r_{thresh} = 1000$	3·2 ± 6·5	2·6 ± 6·2

Table 6.5: Numbers of original peaks which end up in a peak detected at the final time stage.

peak originates from is 233 for the $n = 0$ model and 259 for the $n = -2$ model (for $r_{thresh} = 5$). For $r_{thresh} = 1000$, the overall rate is lower, and the maximum numbers of peaks per any final peak are 88 and 95 for $n = 0$ and $n = -2$ respectively.

As already suggested by the number of haloes which terminate, throwing matter back out into the background, the amount of matter which "rains" or accretes onto haloes directly rather than first collapsing into smaller density peaks is non-negligible. For the $n = 0$, $r_{thresh} = 5$ model, $32 \pm 26\,\%$ (mean±st. dev.) of the mass of the final peak comes from such accretion, while for the $n = -2$, $r_{thresh} = 5$ model this value is $23 \pm 28\,\%$. The corresponding values for $r_{thresh} = 1000$ are similar, i.e., $36 \pm 25\,\%$ and $29 \pm 32\,\%$ respectively.

Much of both merging and accretion occurs from the first to the second time stages, but these processes do continue throughout the peaks' histories. To get a much more detailed, though not directly quantitative measure of these processes, I have plotted the sections of the merging history trees as described in §5.4 and discussed in the next section.

6.3 Merging History Trees

The plots from the merging history trees are shown in Figs 6.8–6.22. Figs 6.8, 6.9, 6.10, 6.15, 6.19 and 6.21 show that merging ratios of $3 - 10$ occur for many of the most massive haloes at low redshifts, while as indicated by the maximum number of original peaks for any final peak, the merging ratio from the first to second time stages can be much higher, as high as a few hundred in several cases for $r_{thresh} = 5$. For the smaller peaks, (Figs 6.11, 6.12, 6.13, 6.16 6.20 and 6.22), very little merging occurs apart from the earliest one or two time stages. And for the smallest peaks, Figs 6.14 and 6.18 show that many of these have either only recently collapsed or are unmerged objects which have formed well after the first time stage. Fig. 6.17 shows a case intermediate between the latter two.

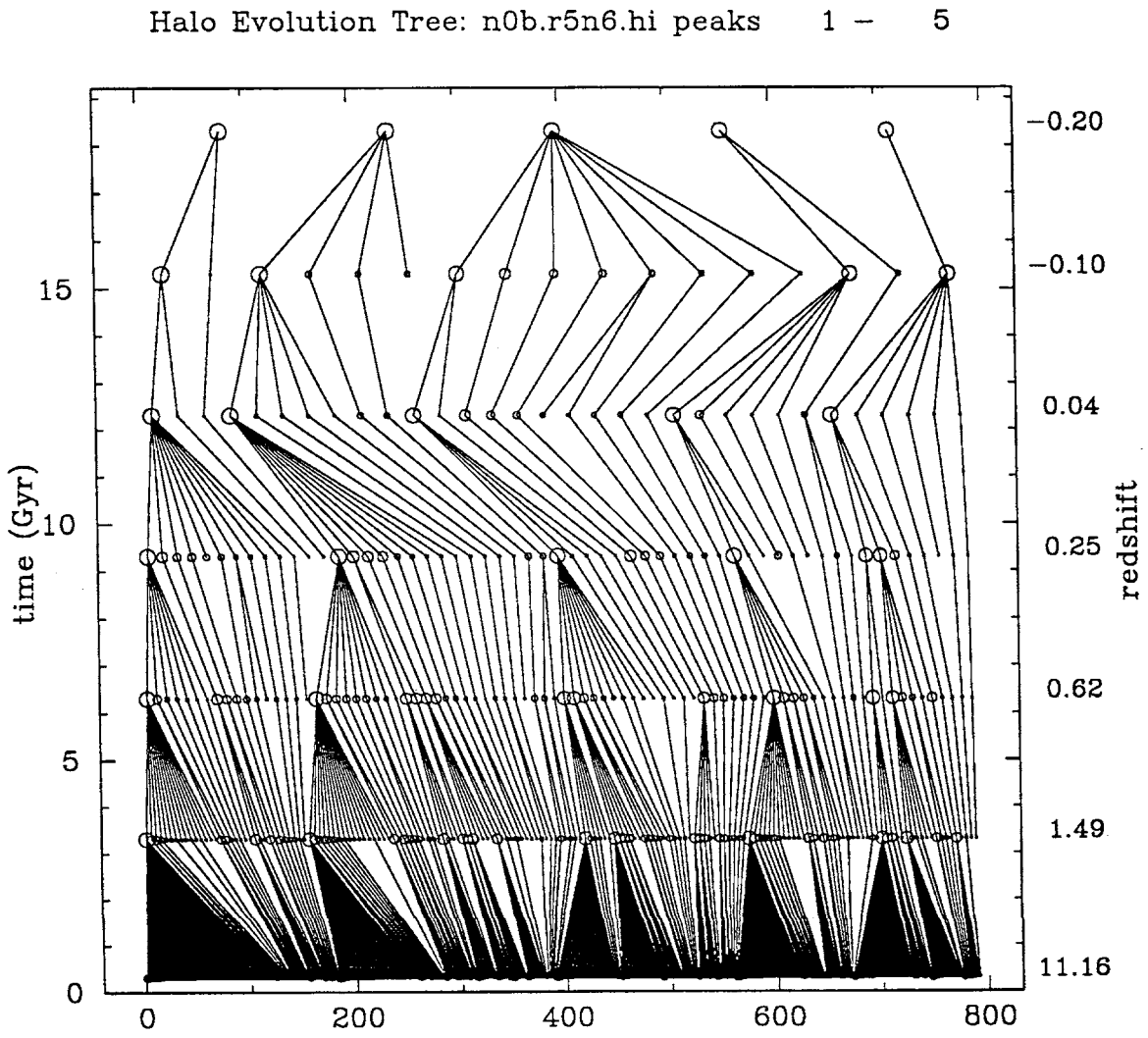

Figure 6.8: Merging History: $n = 0$, $r_{thresh} = 5$, peaks $1 - 5$. This and the following plots show peaks detected at different points in time-space connected according to the criterion described in §5.4, i.e., showing which peaks merge into which. The horizontal axis separates individual peaks, while the vertical axis indicates time/redshift. (Negative redshifts indicate future times.) Circles indicate peaks, with radii a logarithmic transformation of the peaks masses (differs between separate plots for display purposes) and line segments indicating the merging connections. The peaks at the latest time stage, and the set of predecessors of any peak, are ordered by mass decreasing to the right. Numbering on the horizontal axis indicates the maximum number of peaks in the figure for any time stage.

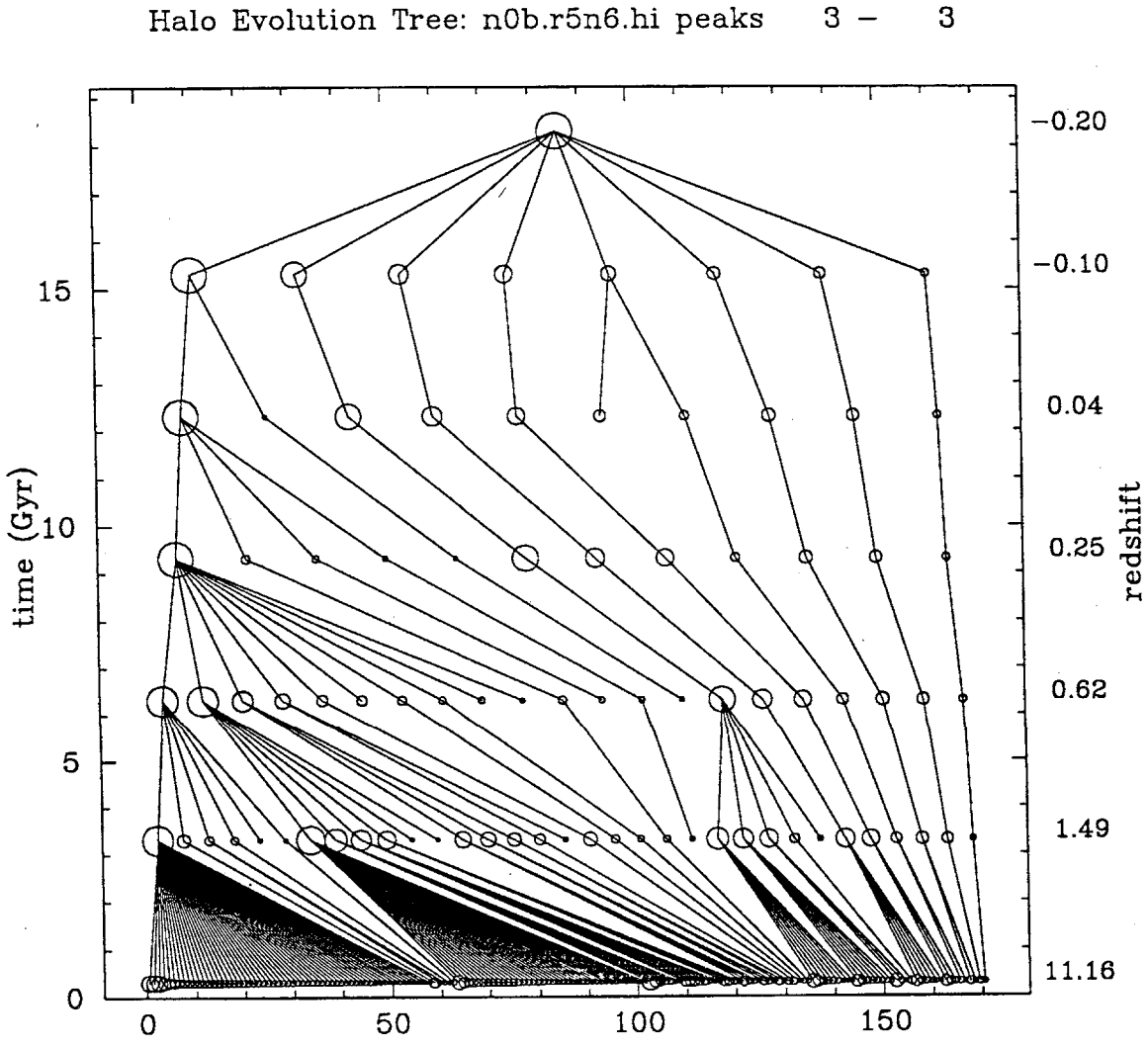

Figure 6.9: Merging History: $n = 0$, $r_{thresh} = 5$, peak 3

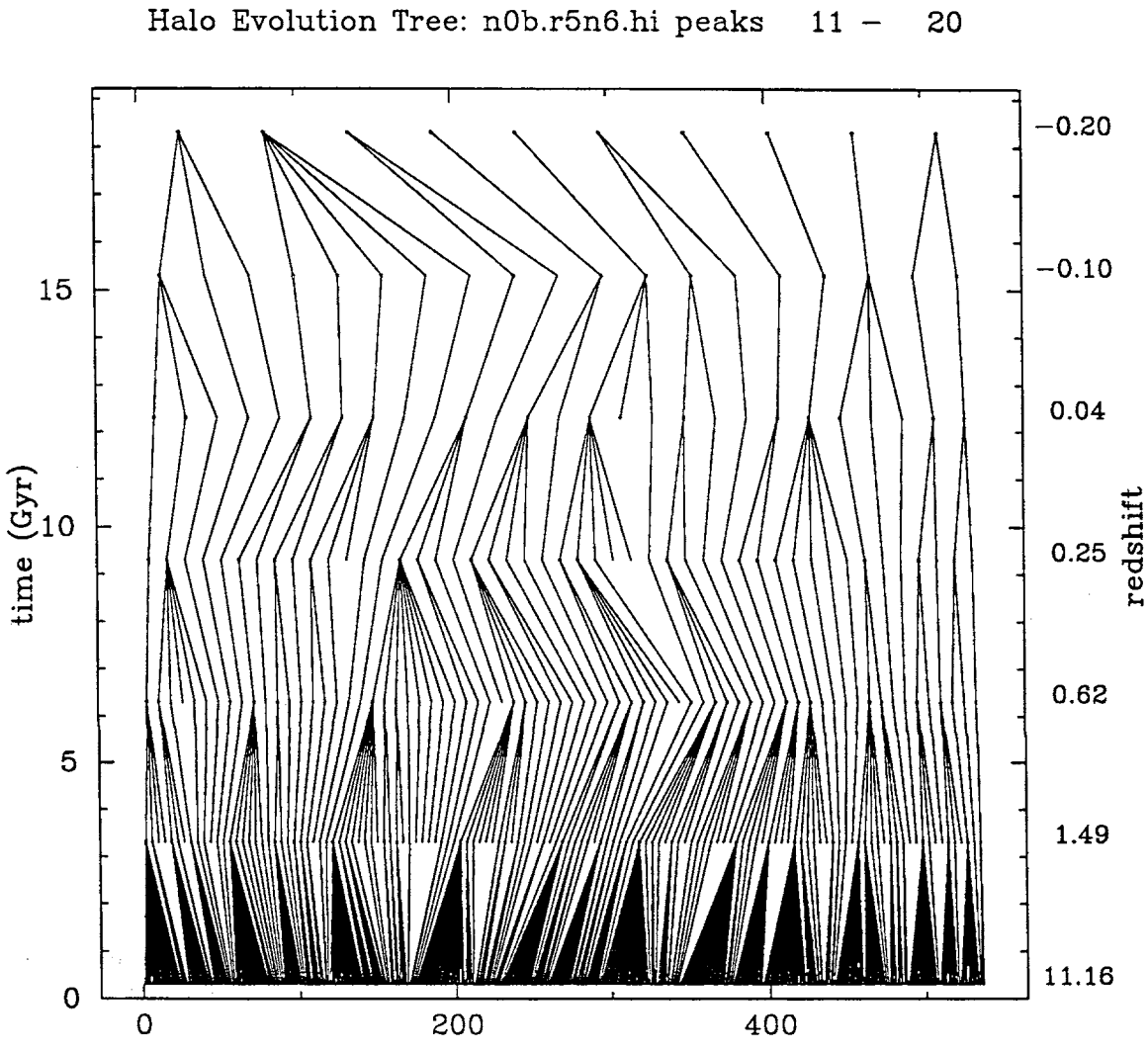

Figure 6.10: Merging History: $n = 0$, $r_{thresh} = 5$, peaks $11 - 20$

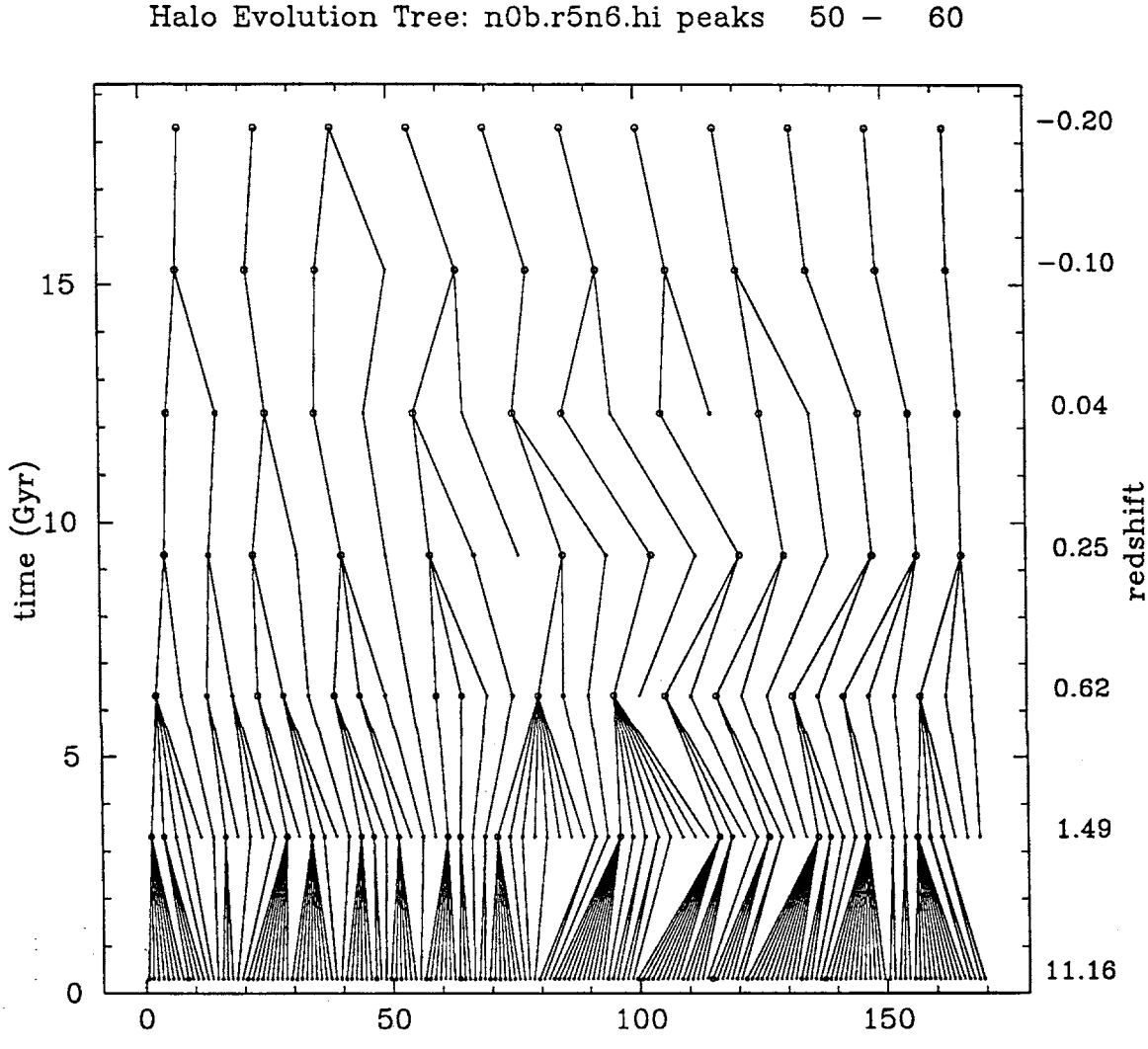

Figure 6.11: Merging History: $n = 0$, $r_{thresh} = 5$, peaks $50 - 60$

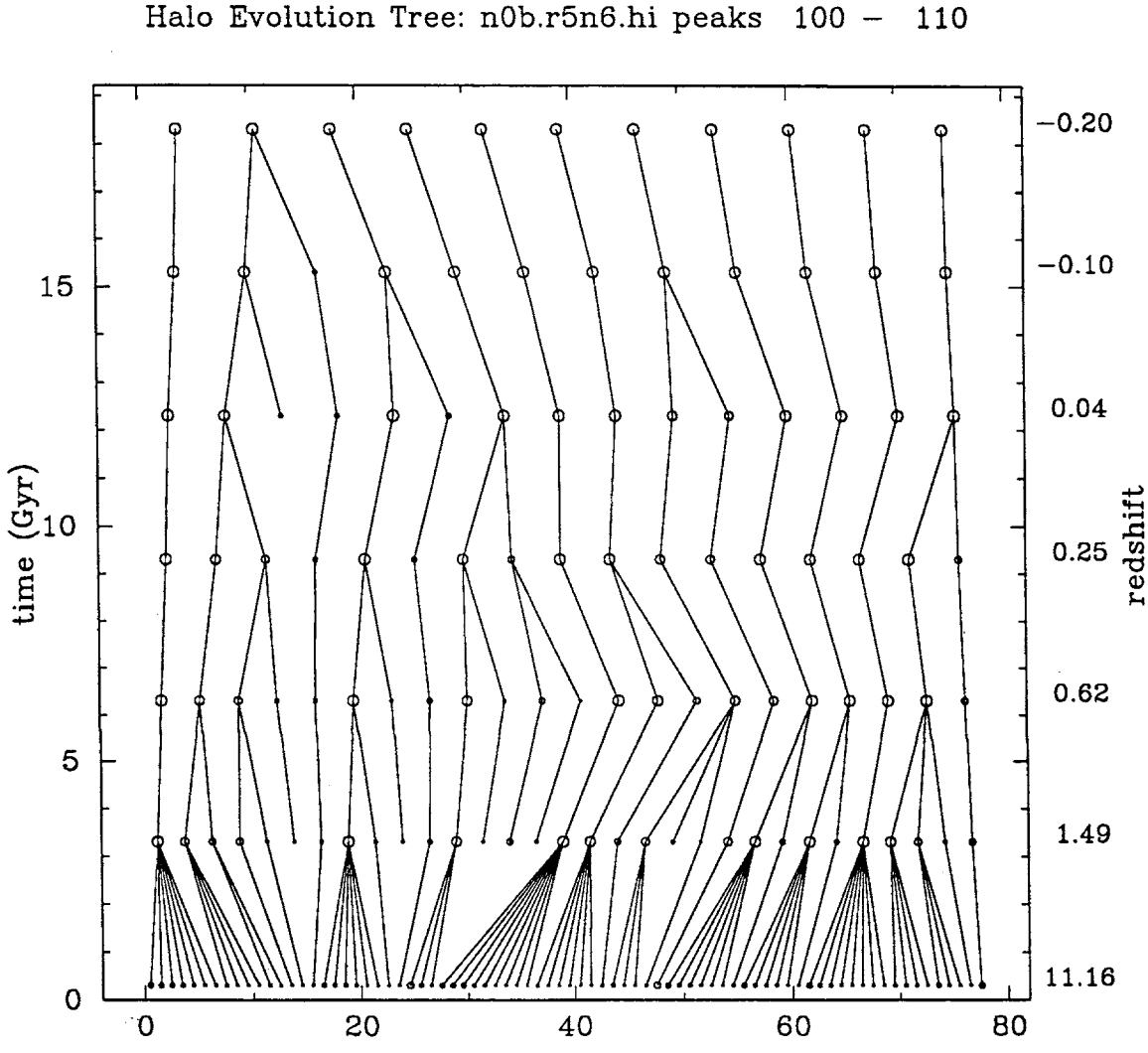

Figure 6.12: Merging History: $n = 0$, $r_{thresh} = 5$, peaks $100 - 110$

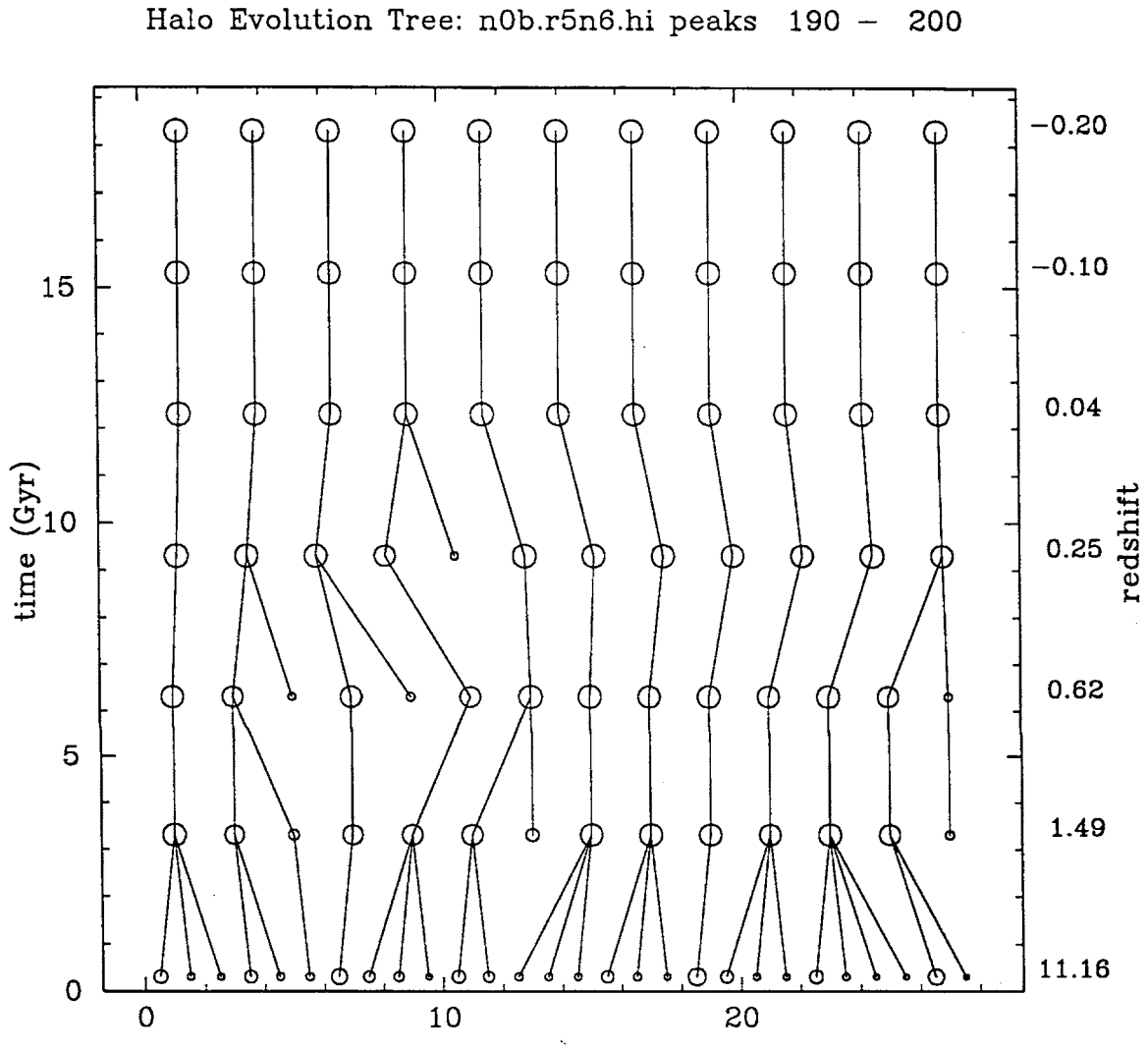

Figure 6.13: Merging History: $n = 0$, $r_{thresh} = 5$, peaks $190 - 200$

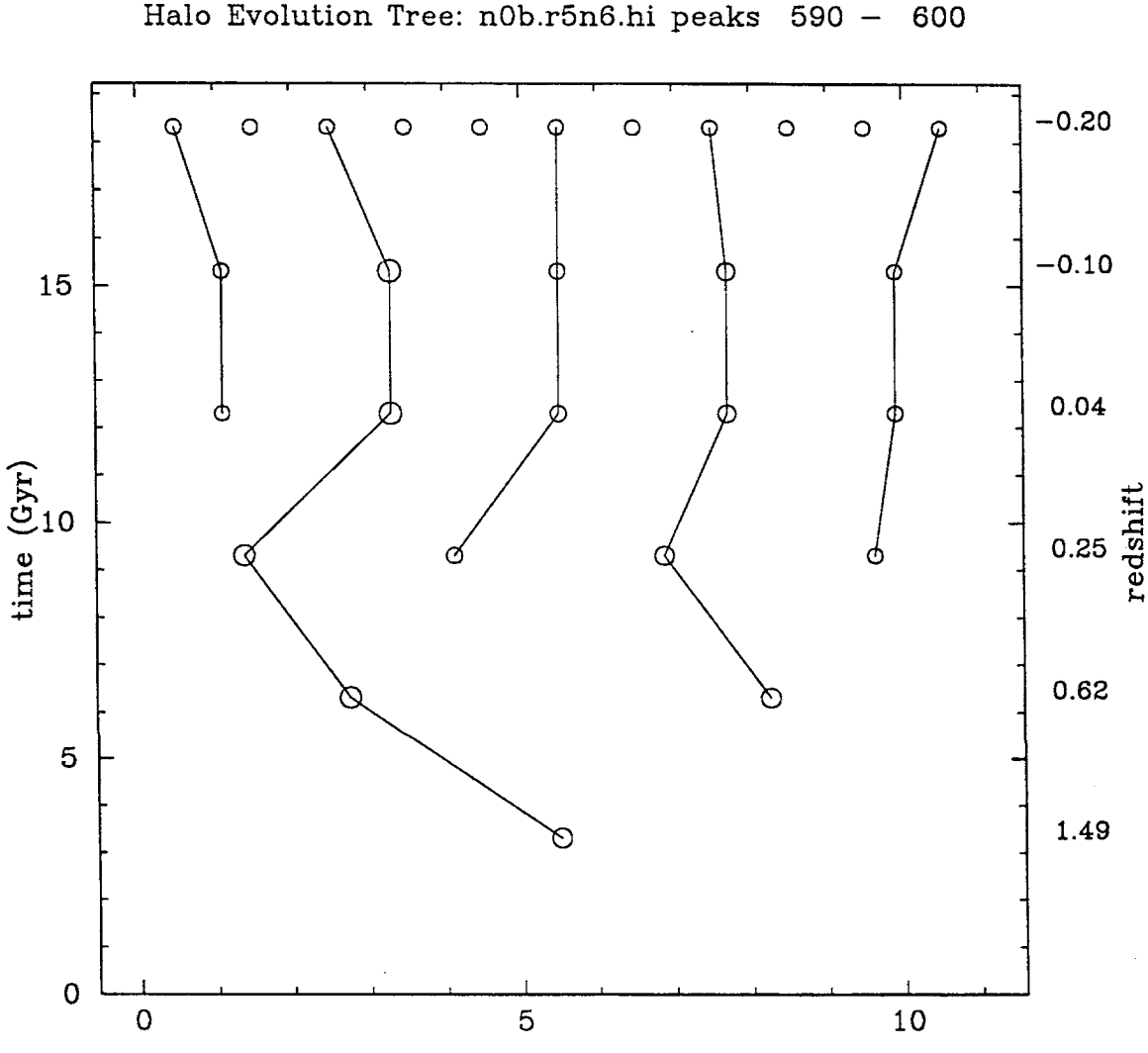

Figure 6.14: Merging History: $n = 0$, $r_{thresh} = 5$, peaks $590 - 600$

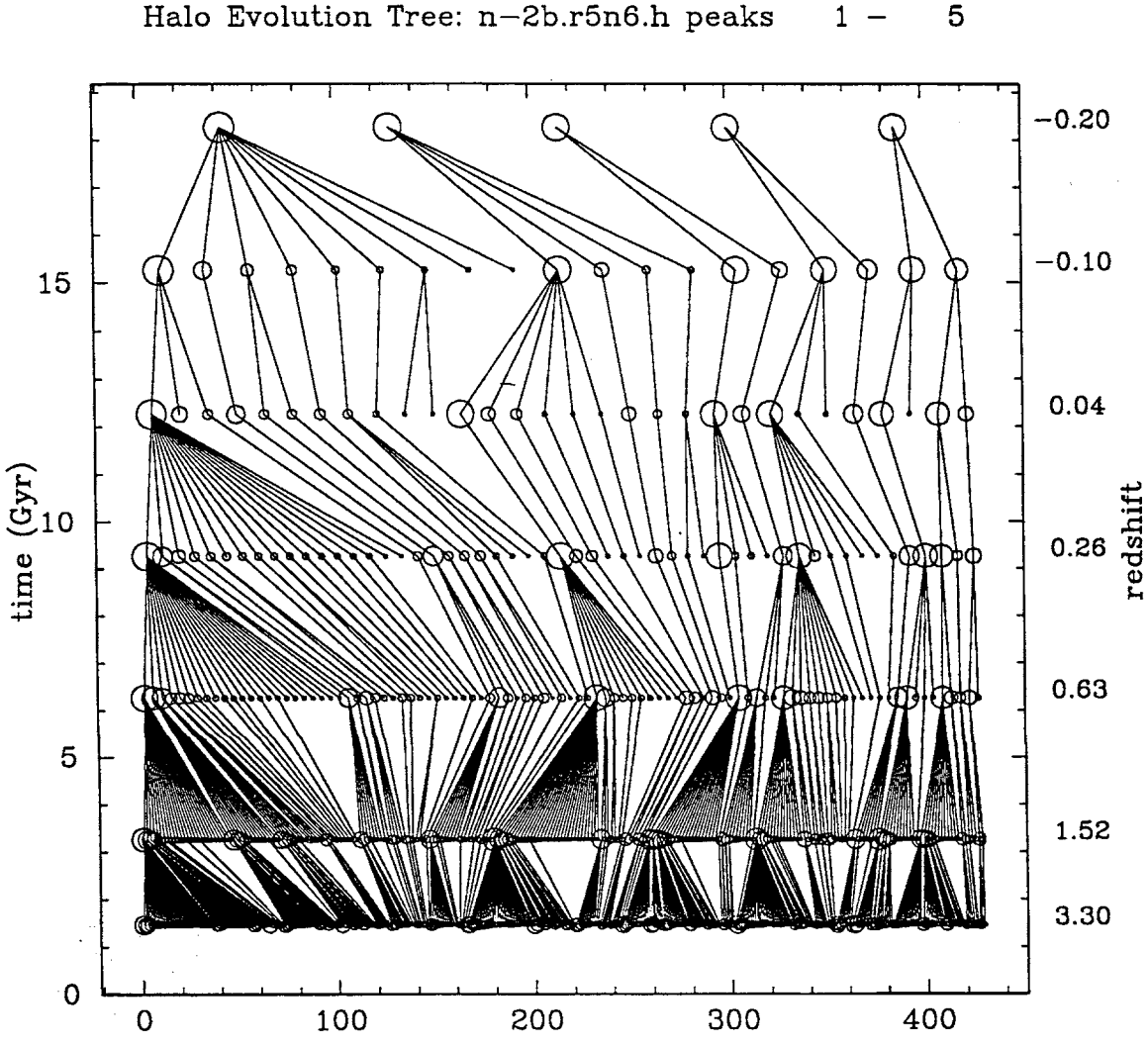

Figure 6.15: Merging History: $n = -2$, $r_{thresh} = 5$, peaks $1 - 5$

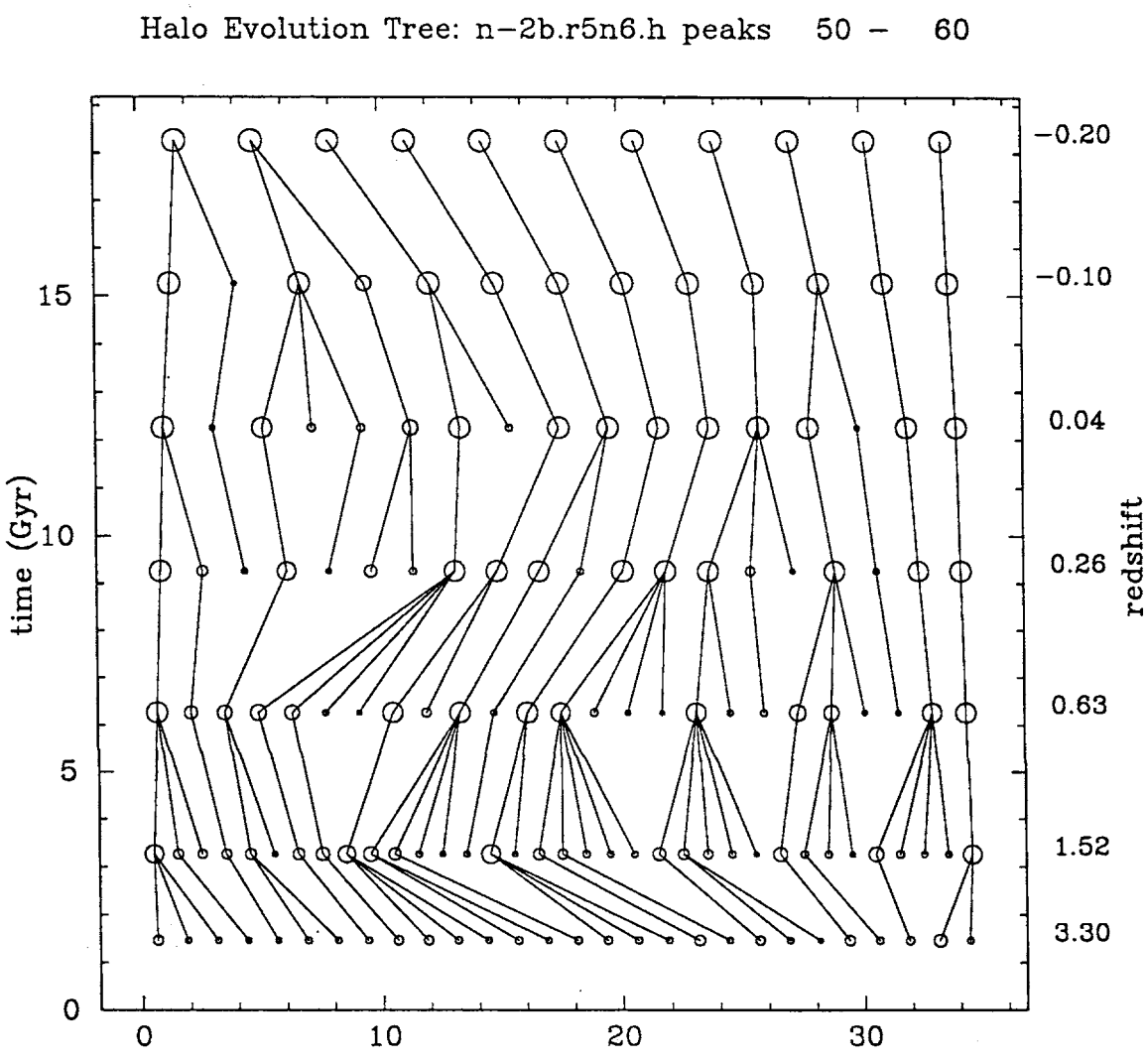

Figure 6.16: Merging History: $n = -2$, $r_{thresh} = 5$, peaks $50 - 60$

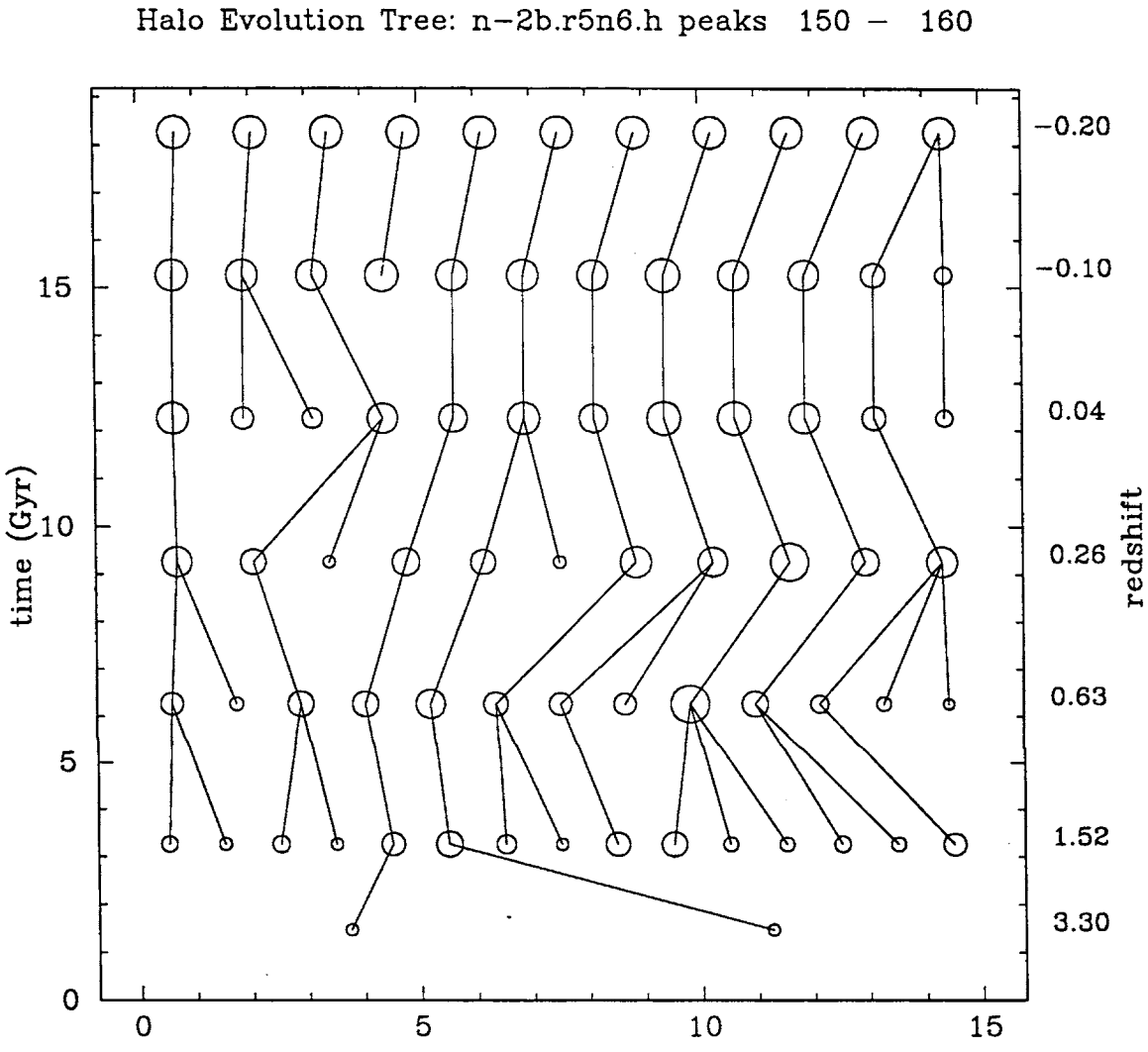

Figure 6.17: Merging History: $n = -2$, $r_{thresh} = 5$, peaks $150 - 160$

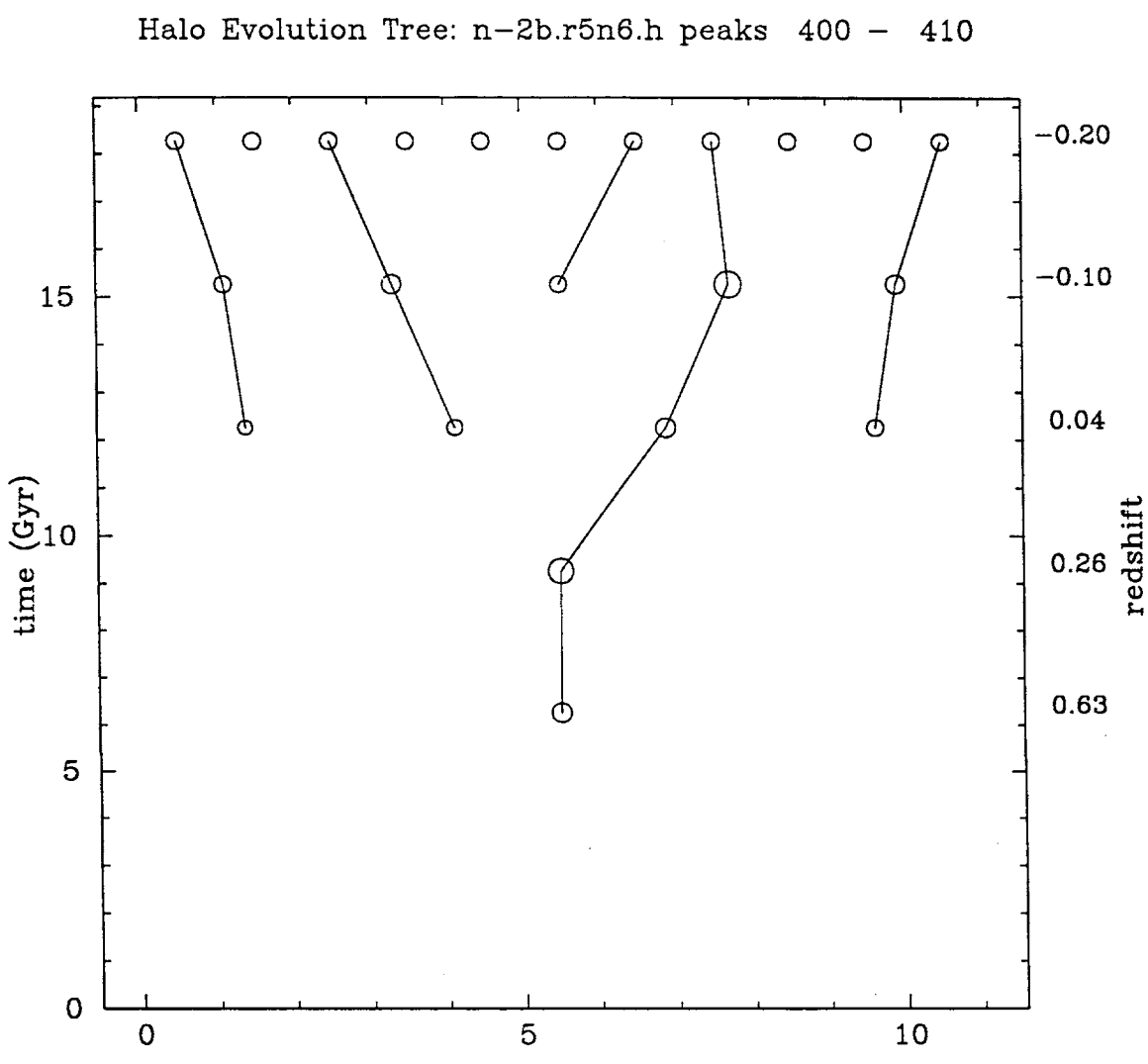

Figure 6.18: Merging History: $n = -2$, $r_{thresh} = 5$, peaks $400 - 410$

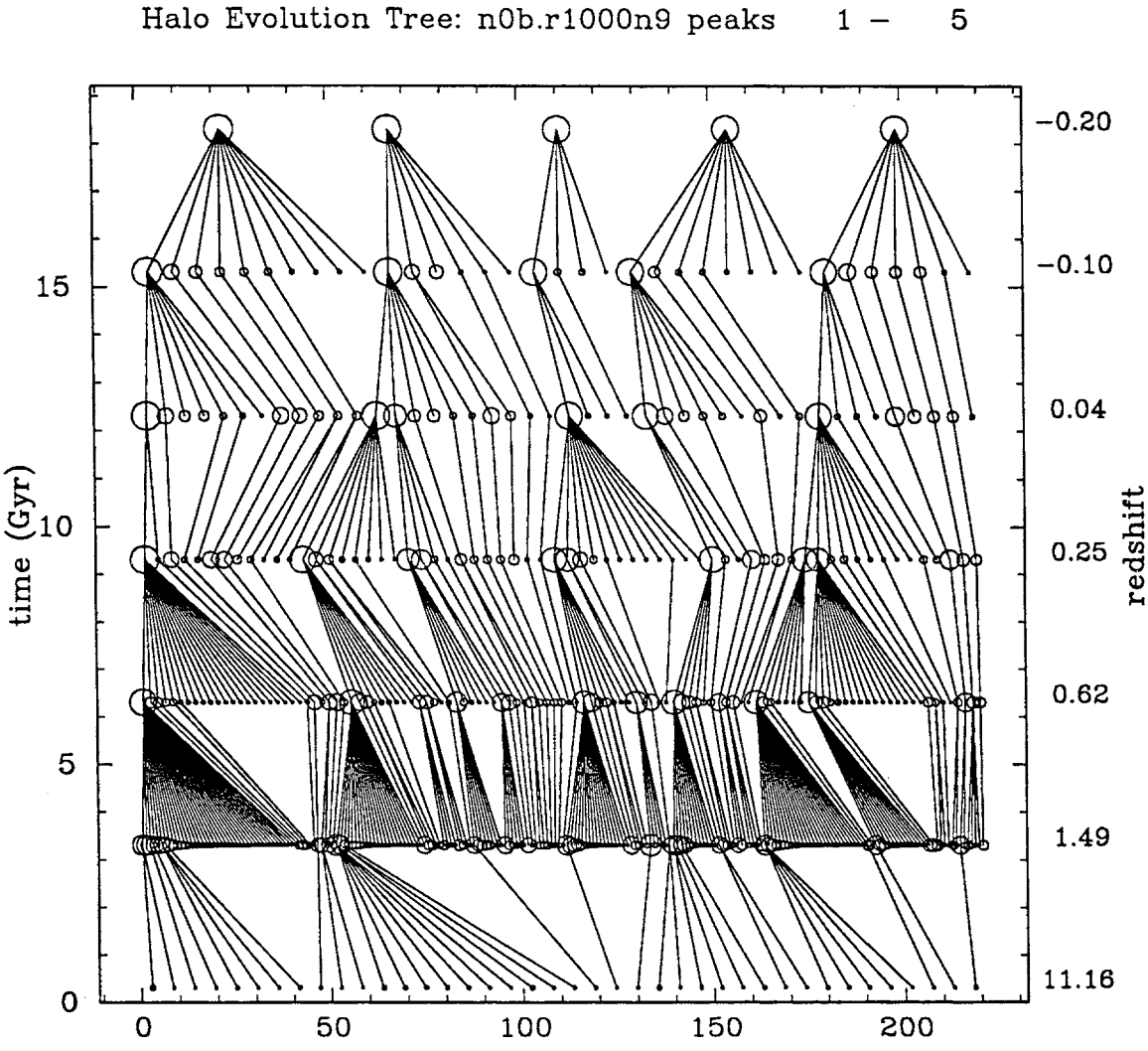

Figure 6.19: Merging History: $n = -2$, $r_{thresh} = 1000$, peaks $1 - 5$

The obvious conclusion to make from these plots is that the larger a galaxy halo is, the more original peaks it is likely to have been created from, and at any time in general, the more massive a galaxy halo is the more peaks are likely to be merging into it.

6.4 Halo Correlation Functions

Before looking at the actual results of applying GEPS (galaxy evolutionary population synthesis), we need to look at the spatial two-point auto-correlation function, $\xi(r)$, of the haloes. The amplitude of the power spectrum which goes

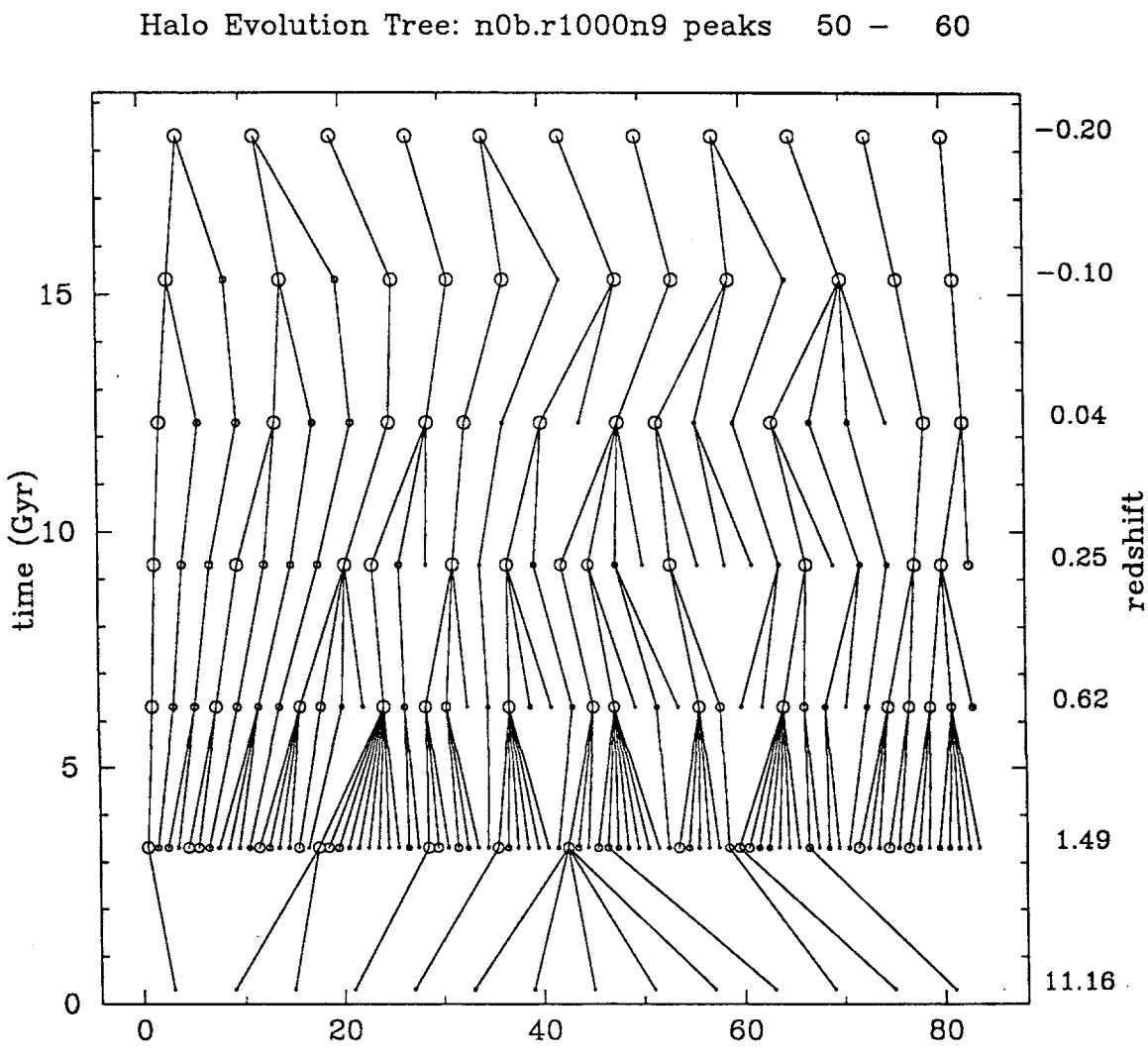

Figure 6.20: Merging History: $n = -2$, $r_{thresh} = 1000$, peaks $50 - 60$

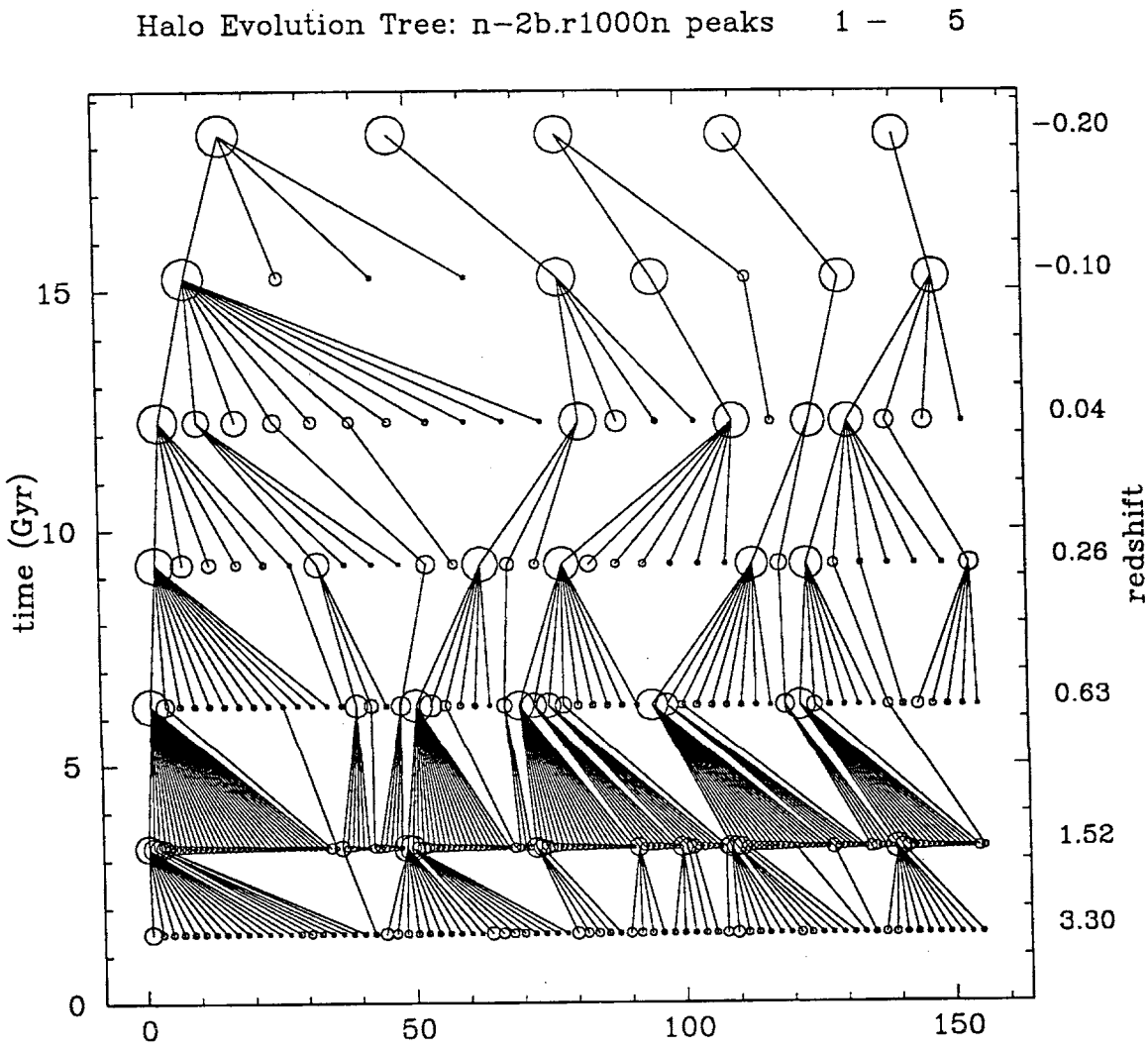

Figure 6.21: Merging History: $n = -2$, $r_{thresh} = 1000$, peaks $1 - 5$

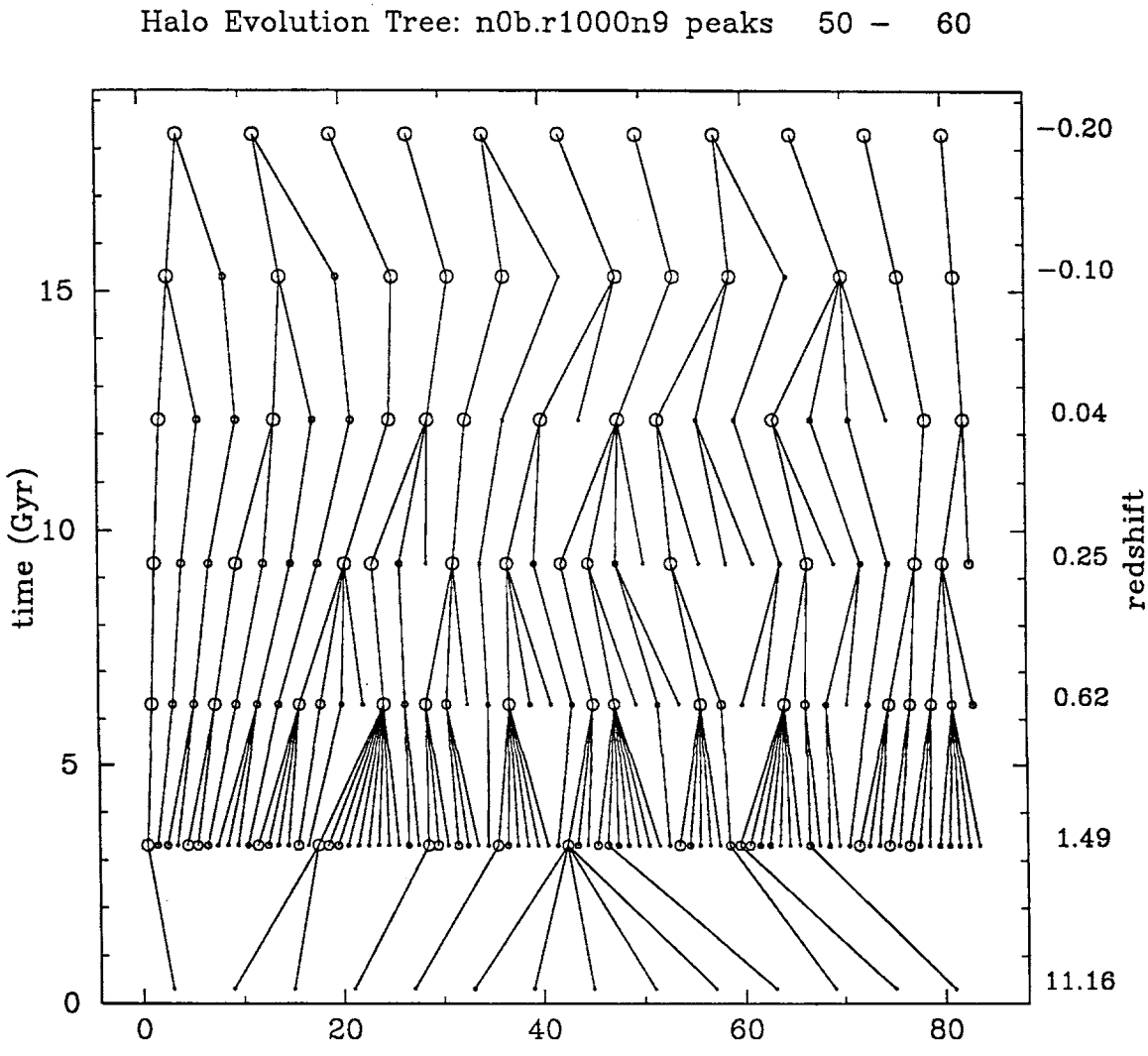

Figure 6.22: Merging History: $n = -2$, $r_{thresh} = 1000$, peaks $50 - 60$

into the initial conditions is calculated such that the correlation amplitude predicted in the linear modelling of the growth of density perturbations is well below the observed amplitude at the present. Specifically, the amplitude was chosen such that linear modelling predicts $(\delta M/M)(r = 0{\cdot}5h^{-1}Mpc) = 2{\cdot}0$ at $z = 0$, where $(\delta M/M)(r)$ is the r.m.s. value of the excess mass (over uniform density) in spheres of radius r (Warren *et al.* 1992). This is, of course, a lot lower than that derived from observation, i.e., for which $(\delta M/M)(r) = 1{\cdot}0$ at $8h^{-1}Mpc$ for $z = 0$. The intention of this was to make the density peaks about the same size for different values of n, which has indeed been the result. This is useful for the purposes for which these simulations were designed, but for the purposes of merger-induced evolutionary population synthesis (MIEPS) modelling means that to relate these simulations directly to a realistic cosmology would require a rescaling of the units.

Figure 6.23 shows the correlation functions for the peaks detected for $n = 0$, $r_{thresh} = 5$. The slopes of these are consistent with that observed for galaxies, i.e.,

$$\xi(r) \approx \left[\frac{r}{(r_0 = 5h^{-1}\,Mpc)}\right]^{-1{\cdot}8}, \tag{6.1}$$

e.g., Peebles (1980). The correlation functions for the other three models are similar to those in Fig. 6.23, except that the $-1{\cdot}8$ slope continues right up through to the smallest bin rather than flattening as in this figure, and one or two of the earliest correlation functions for the $r_{thresh} = 1000$ models are noisy.

This is consistent with the results of Davis *et al.* (1985) for cold dark matter (CDM) initial perturbation spectra, while for the power law initial perturbation spectra of Efstathiou *et al.* (1988), this appears to be consistent in the $n = -2$ case but not the $n = 0$ case. As the CDM spectrum has a slope of approximately $n = -2$ on galaxy scales, it is reasonable that these simulations agree with each other and the data presented here in having slopes of $\gamma \approx -1{\cdot}8$. The disagreement between our $n = 0$ case (which does give $\gamma \approx -1{\cdot}8$) and Efstathiou *et al.*'s $n = 0$ case (which doesn't give $\gamma \approx -1{\cdot}8$) may be explainable by the fact that Efstathiou *et al.* plot correlation functions for all their particles rather than for peaks detected according to a density threshold, although why this effect would affect $n = 0$ but not $n = -2$ is not obvious.

Suto & Suginohara (1991) show correlation functions both for all their particles and for peaks, for a CDM initial perturbation spectrum. The peaks are detected at an early time stage and retain their identity throughout the simulation; while the detection density threshold applies to the total density of a peak, not to the local density at the boundary of a peak. The slopes for the all-particle

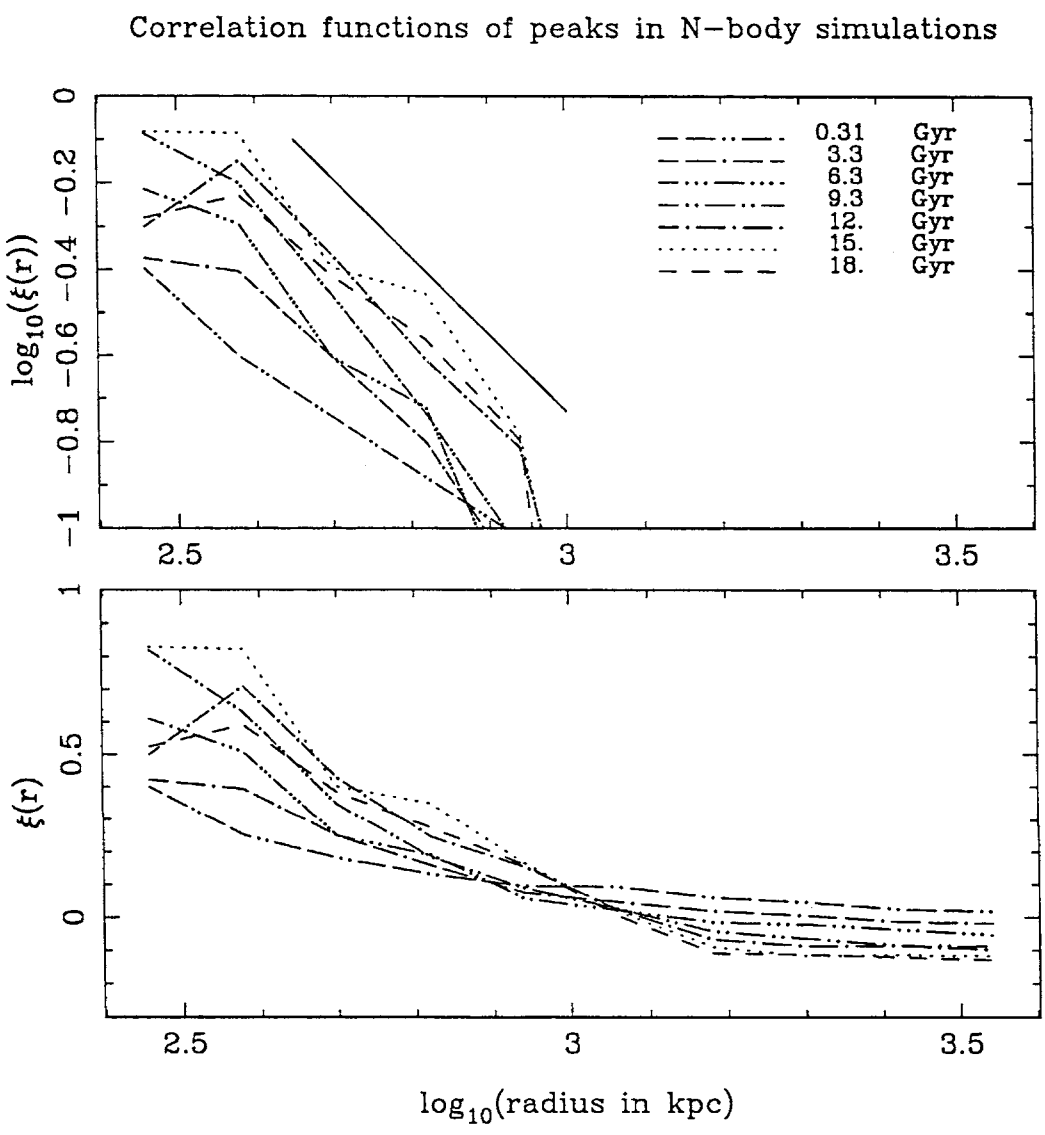

Figure 6.23: Spatial two-point autocorrelation functions of density peaks (haloes) in $n = 0$, $r_{thresh} = 5$ model. $log_{10}(\xi(r))$ (upper plot) and $\xi(r)$ (lower plot) are plotted against $log_{10}(r)$ where r is the comoving radius in *kpc*. A solid line with slope of $\gamma = -1{\cdot}8$ is shown in the upper plot for comparison.

correlation functions[1] are close again to $\gamma = -1{\cdot}8$, in agreement with the other results just discussed. The slopes of the correlation functions for their peaks are slightly steeper than $-1{\cdot}8$. Suginohara & Suto (1991) show correlation functions for a number of power law initial perturbation spectra. The slopes for $n = -2$ are very close to $-1{\cdot}8$ and for $n = 0$ they are slightly steeper than this, again consistent with our results.

In order to scale our results, we would need to know how the amplitude of the correlation function evolves. Figure 6.24 shows this evolution, described in terms of $\xi(5h^{-1}Mpc)$ (which assumes that ξ retains its slope of $\gamma = -1{\cdot}8$ outside the domain measured). The points for the $n = 0$ model fit reasonably well to a power law growth in $(1+z)$, with the amplitude increasing as a function of time. The slopes are $\alpha = 0{\cdot}6 \pm 0{\cdot}1$ and $\alpha = 0{\cdot}8 \pm 0{\cdot}3$ for $r_{thresh} = 5$ and $r_{thresh} = 1000$ respectively, where the variable α is that used by Melott (1992); or equivalently $\epsilon = -0{\cdot}6 \pm 0{\cdot}1$ and $\epsilon = -0{\cdot}4$. (α just represents a conversion between comoving and proper coordinates, and can be related to eqn (4.25) via $\epsilon = \alpha - 3 + \gamma$.) This is a similar result to that of Melott (1992), except that the slopes are less steep. (From Melott's Fig. 1, the slope for $n = 0$ is $\alpha \approx 1{\cdot}5 \pm 0{\cdot}1$.) Melott doesn't say whether or not his correlation functions were calculated for individual particles or for density peaks, hence presumably they are for the former. If his points are indeed for particles rather than peaks, this would correspond in our models to an extremely high density threshold of detection (and correspondingly extremely small resolution size). As the slope becomes steeper with higher detection threshold in our data, this could be consistent with Melott's data if this relationship were extrapolated. However, given the above summary of different results for correlation functions of particles and peaks, this may not be a sufficient explanation.

The growth rates for the $n = -2$ model are not consistent with a power law in $(1+z)$ across all redshifts. The amplitude decreases initially before increasing again once $(1+z)$ is close to unity. This may be explained by merging, as the overall merging rate is very high at early epochs and merging decreases the amplitude of the correlation function at the point of time at which it happens. Once the overall merging rate has dropped, the usual increase in the correlation amplitude due to clustering scales reaching the turnaround radius takes over, and presumably continues.

We make the assumption here that the growth in amplitude at the lowest redshifts (specifically, we choose the four lowest redshifts) is according to a power

[1]Here we refer to correlation functions in real space, not redshift space, which Suto & Suginohara (1991) do in fact also consider.

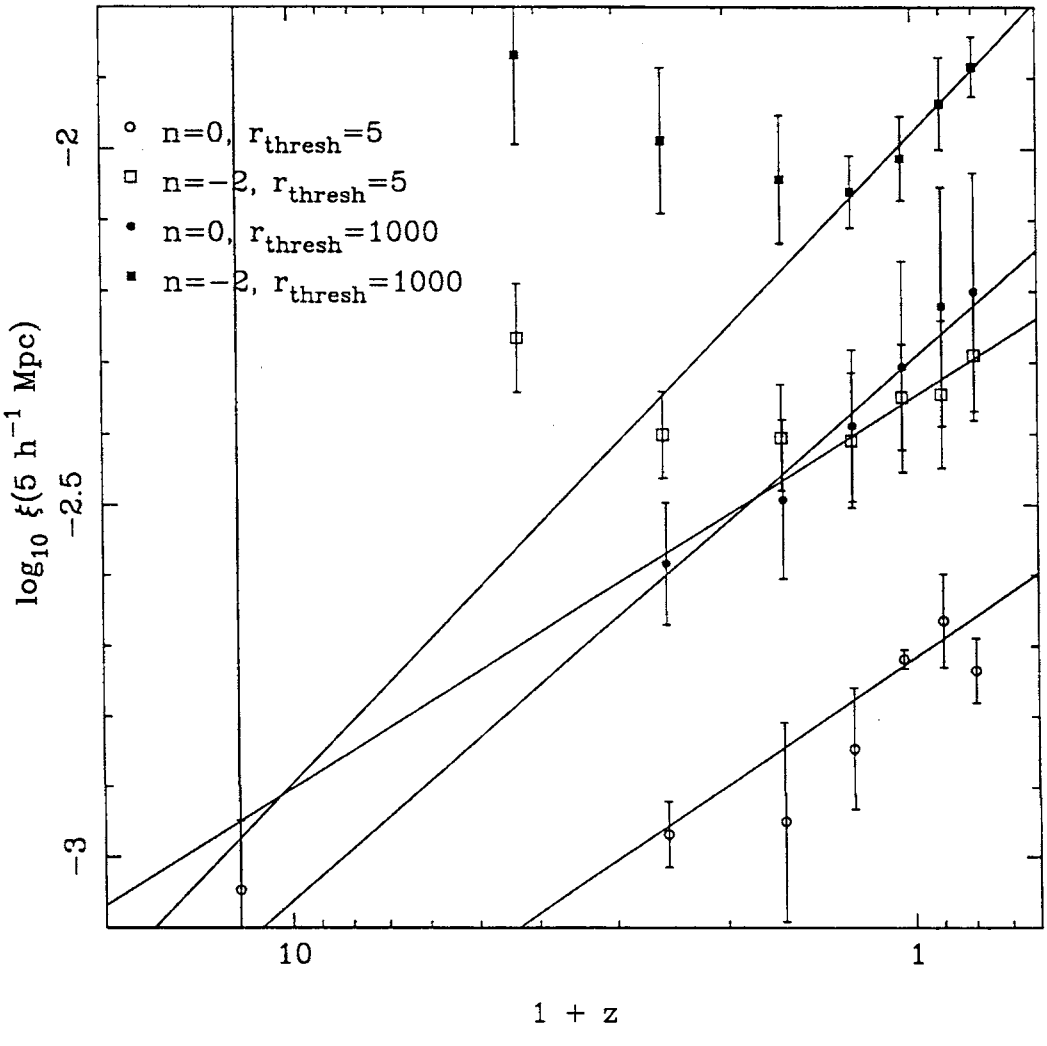

Figure 6.24: Evolution of spatial two-point autocorrelation function. The correlation functions for the different models all have slopes very close to $\gamma = -1{\cdot}8$, so the amplitudes of these extended to $5h^{-1}Mpc$ in comoving coordinates are shown against redshift $(1 + z)$. (The highest redshift correlation function for $n = 0$, $r_{thresh} = 1000$ is too noisy to fit a line of slope $\gamma = -1{\cdot}8$ and so is excluded.) Lines fitted to all but the highest z point for $n = 0$ and to the four points with lowest z for $n = -2$ are also plotted.

law in $(1+z)$ and we fit lines to these points. This assumption gives slopes of $\alpha = 0{\cdot}6 \pm 0{\cdot}6$ and $\alpha = 0.9 \pm 0{\cdot}3$, equivalently $\epsilon = -0{\cdot}6 \pm 0{\cdot}6$ and $\epsilon = -0{\cdot}3 \pm 0{\cdot}3$, for $r_{thresh} = 5$ and $r_{thresh} = 1000$ respectively. While these uncertainties are high because of the small number of points involved, they suggest a result that the slope of the growth rate, once growth has started, is more dependent on the density threshold at which the peaks are detected than on the value of n! This is consistent with the plots of Suginohara & Suto (1991), which show little dependence on n. If we consider the high density threshold detection to be the closest to that of Melott's (1992) presumable use of all-particle correlation functions, then this is marginally consistent with his result, since for r_{thresh} the slope for $n = -2$ is slightly greater than that for $n = 0$.

If we suppose that this power law evolution continues forwards in time, we can rescale the time units so that the N-body results we have here represent gravitational evolution early in the Universe. Our best rescaling in this case would be for the $n = -2$, $r_{thresh} = 1000$ model, since it has the fastest rate of growth, $\alpha = 0{\cdot}9$, as well as the greatest amplitude. With this slope, and the $1+z = 1$ value $\xi(5h^{-1}Mpc) = 10^{-1{\cdot}98}$, $\xi(5h^{-1}Mpc)$ would reach unity at $1+z = 7{\cdot}0{\times}10^{-3}$. Rescaling time units to have $\xi(5h^{-1}Mpc)$ equal to unity at $1+z = 1$ would therefore make the time step presently labelled with $1+z = 1$ occur at a redshift of $1+z = 143$. Since we do have data labelled $1+z = 0{\cdot}8$, we could use this as our latest time step, which would then be relabelled $1+z = 114$, though this is not much help to us. These redshifts are way too high to be useful to us for the purposes here, and the earliest steps in the N-body simulations are likely to pushed into the pre-recombination and radiation-dominated eras, in which case the calculations are not likely to remain valid.

If we rescale mass and length, as will be suggested in later sections, this time rescaling might not need to be this harsh. As it turns out, mass and length rescaling is nowhere near enough to make the time rescaling sensible, so we choose not to rescale time. So, while the amplitude of the correlation function may not be a problem for the purposes of Warren *et al.* (1992), it remains a problem for the purposes discussed here.

6.5 Mass-to-mass and Mass-to-light Ratios

Before discussing the results of evolutionary population synthesis applied to these merging histories, the various mass-to-mass and mass-to-light ratios need to be considered, as the models described here assume that all the mass in a halo is gas available for forming stars, and that as $t \rightarrow \infty$ all the mass approaches

being turned into stars. The mass-to-mass and mass-to-light ratios show how the models run here fit more closely to reality.

From a known stellar population, the amount of mass contained in those stars can be calculated. The amount of mass in stellar remnants or gas ejected by the stars can also be calculated from the stellar population, though with less certainty. In these models, there is also mass in a galaxy which is considered to be gas which has not yet been turned into stars. Let us denote the total mass in stars or stellar remnants by $\mathcal{M}_*$, the total mass in either fresh or recycled gas by $\mathcal{M}_{gas}$ and the total luminosity in waveband W (e.g., $W = B$) by L_W.

Let us then denote the total amount of matter available for turning into stars, i.e., $\mathcal{M}_{gas}$ plus $\mathcal{M}_*$, as $\mathcal{M}_{lum}$. While not all this matter is in fact luminous optically, any gas is at least visible at 21cm, or if hot enough as in galaxy clusters it can be visible in X-rays. Finally, let us denote any other mass (detectable only dynamically) as $\mathcal{M}_{dk}$ and the total amount of mass as $\mathcal{M}_{tot}$.

In summary, we then have

$$\begin{aligned} \mathcal{M}_{tot} &= \mathcal{M}_{dk} + \mathcal{M}_{lum} \\ \mathcal{M}_{lum} &= \mathcal{M}_{gas} + \mathcal{M}_* \\ \mathcal{M}_* &\quad \text{generates } L_W. \end{aligned} \tag{6.2}$$

The ratios in which we are interested are $\mathcal{M}_{tot}/\mathcal{M}_{lum}$, and $\mathcal{M}_{lum}/L_W$ $(= \mathcal{M}_{lum}/\mathcal{M}_* \times \mathcal{M}_*/L_W)$. The first of these ratios appears to be roughly constant according to many authors, and hence is an observational input, while the second is that which is output by the models discussed here. The models here, by default, output K-corrected luminosities in chosen wavebands, as these are closer to observational quantities than luminosities at rest-frame wavelengths are.

Freeman (1987) finds a value of the ratio $\mathcal{M}_{disk}/L_{disk,B}$ in the range $2 - 7\,M_\odot L_\odot^{-1}$ derived from the inner part of the optical/HI rotation curves of disk galaxies without bulges. This is consistent with stellar population values, e.g., Larson & Tinsley (1978). If we consider $\mathcal{M}_{disk}$ to be a good approximation to the total mass (counting any gas potentially available for star formation) in that part of the galaxy, then since most of the luminosity at the location of the disk comes from the disk, then the ratio $\mathcal{M}_{disk}/L_{disk,B}$ corresponds to $\mathcal{M}_{lum}/L_B$, so we have $\mathcal{M}_{lum}/L_B \approx 2 - 7\,M_\odot L_\odot^{-1}$. Explaining the outer parts of the rotation curves as due to dark matter, Freeman (1987) then gives $\mathcal{M}_{halo}/\mathcal{M}_{disk}$ ratios of $2-7$. Since the galaxies observed are considered not to have bulges, this ratio corresponds to $\mathcal{M}_{tot}/\mathcal{M}_{lum} - 1$. That is, $\mathcal{M}_{tot}/\mathcal{M}_{lum} - 1 \approx 2 - 7$, or $\mathcal{M}_{tot}/\mathcal{M}_{lum} \approx 3 - 8$.

For the Galaxy, Freeman (1987) gives $\mathcal{M}_{halo}/\mathcal{M}_{lum}$ to be 1·5 out to a Holmberg radius or possibly as much as 15 in total. Again this can be interpreted as

$\mathcal{M}_{tot}/\mathcal{M}_{lum} - 1 \approx 1{\cdot}5 - 15$ or $\mathcal{M}_{tot}/\mathcal{M}_{lum} \approx 2{\cdot}5 - 16$.

From the masses inferred from X-ray emission in ellipticals, Canizares (1987) gives $\mathcal{M}_{tot}/L_B$ to be about $20 - 30\, M_\odot L_\odot^{-1}$ within a radius of about $30 - 40\, kpc$, with possible extremes of $5\, M_\odot L_\odot^{-1}$ and $100\, M_\odot L_\odot^{-1}$. For whole clusters he gives values of $\mathcal{M}_{tot}/L_B$ ranging from $120\, M_\odot L_\odot^{-1}$ to $400 - 600\, M_\odot L_\odot^{-1}$. Also from X-ray data, Sarazin (1987) finds $\mathcal{M}_{tot}/\mathcal{M}_{lum} \approx 4$, where $\mathcal{M}_{lum}$ includes both stellar mass and X-ray emitting gas.

Blumenthal's (1988) summary is consistent with these values. He gives $\mathcal{M}_{tot}/L_B$ ratios of about $30 - 300\, M_\odot L_\odot^{-1}$ from dwarf spheroidals to the Galaxy to small galaxy clusters to the cores of large galaxy clusters. He corrects these for the variation in values of $\mathcal{M}_{lum}/L_B$ due to differences in stellar populations (i.e., exactly what is obtainable from the models discussed here) and due to consideration of X-ray emitting gas in rich clusters. This gives

$$\mathcal{M}_{tot}/\mathcal{M}_{lum} \approx constant \approx 10 \tag{6.3}$$

over the whole range of mass scales (a range of $\sim 10^9$)! This is consistent with Freeman's values.

Since we stay below cluster scales, it would appear reasonable to use this value if we accept that as $t \to \infty$ all the mass approaches being turned into stars.

The mass-to-light ratios, $\mathcal{M}_{lum}/L_{IIIaJ}$, of the presently run models appear quite high, at least in comparison to, say, a Galactic population as mentioned above. Figure 6.25 shows the mass-to-light ratios $\mathcal{M}_{lum}/L_{IIIaJ}$ using rest frame values of L_{IIIaJ} (i.e., no K-corrections) for a run on the $n = 0$, $r_{thresh} = 5$ model with exponential and burst evolution both turned on and Bruzual's SFR parameter $\mu = 0{\cdot}15$. (The parameter μ is the proportion of gas turned into stars in a (nonmerging) galaxy within $1\, Gyr$.)

6.6 Luminosity Functions

From the mass functions (Figs 6.4, 6.5, 6.6 and 6.7), it is obvious that with the scaling of mass, length and time units mentioned in §5.2, the number of haloes per cubic Megaparsec is too high. The mass scale covers a realistic range of halo masses. If all these haloes are converted to galaxies with the right range of luminosities by a monotonic function, then in comparison with a standard Schechter function (Schechter, 1976) these mass functions have around $10 - 100$ too many haloes per cubic Megaparsec. Hence both the correlation function and mass functions indicate that a rescaling of some of the units would be appropriate for making the results compatible with observation.

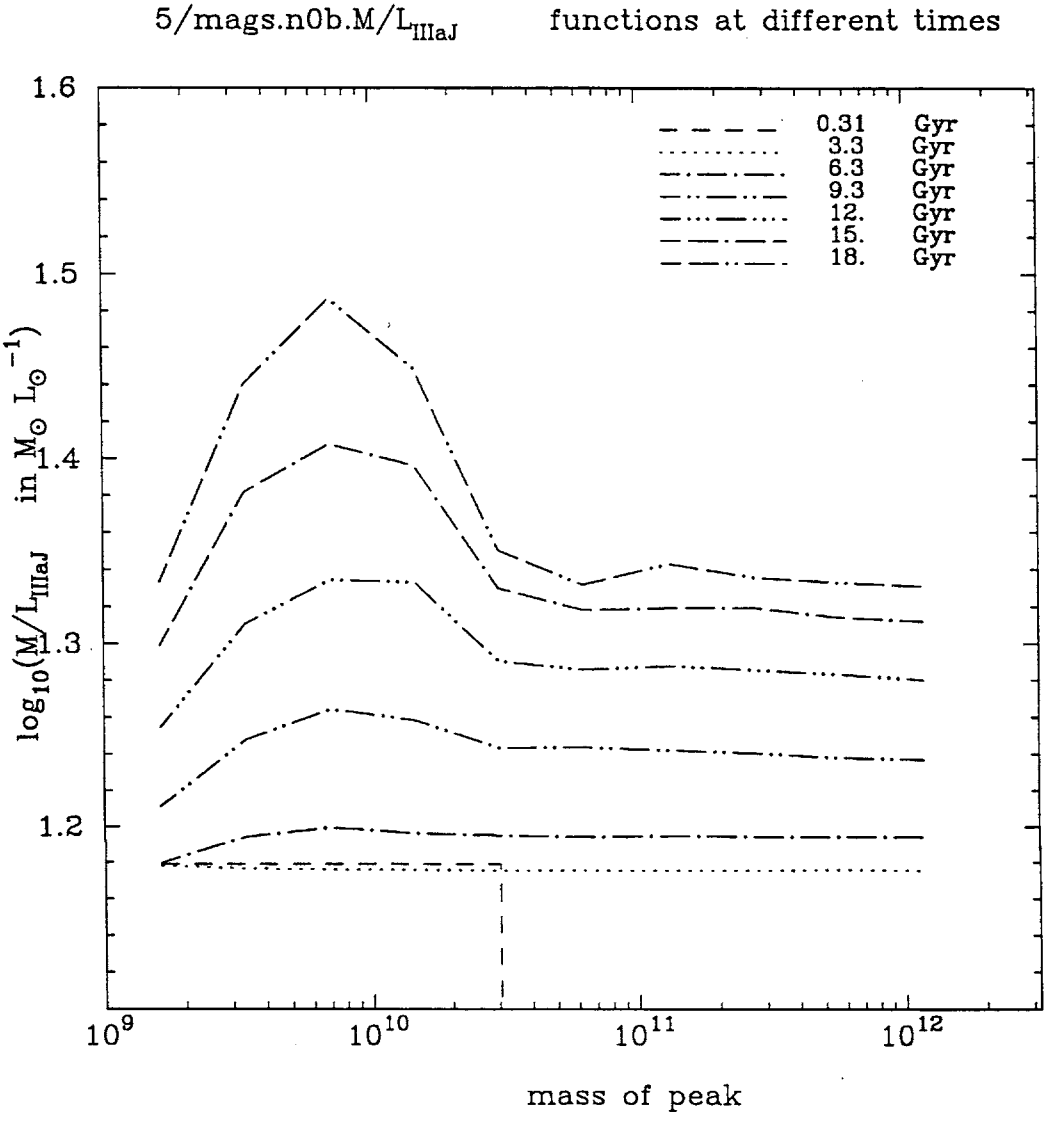

Figure 6.25: $\mathcal{M}_{lum}/L_{IIIaJ}$ for rest frame values of L_{IIIaJ} for a run on the $n = 0$, $r_{thresh} = 5$ model merging history with exponential and burst evolution turned on and Bruzual's SFR parameter $\mu = 0{\cdot}15$. The masses detected at the time stage t_i and the luminosities resulting at the end of the interval $[t_i, t_{i+1}]$ are used to obtain $\mathcal{M}_{lum}/L_{IIIaJ}$ values labelled t_i in this figure.

Of course, the luminosity function of galaxies is much better known than the mass function of galaxy haloes, so *it* will be used as a constraint rather than the mass function.

We therefore choose to rescale the mass and length units which apply to the N-body simulations. We also introduce a realistic $\mathcal{M}_{tot}/\mathcal{M}_{lum}$ ratio. Mass and length have to be rescaled simultaneously in order to keep density the same. This introduces a free parameter, provided that N-body models with "scale-free" power law initial perturbation spectra are used, while the $\mathcal{M}_{tot}/\mathcal{M}_{lum}$ ratio is an observational input as mentioned in §6.5, so we treat this as fixed.

The mass-length scaling clearly applies to the model before GEPS is applied. If we assume that the $\mathcal{M}_{tot}/\mathcal{M}_{lum}$ scaling is due to nonbaryonic matter, for example, or any other matter which does not form stars at all, then it, too, applies in these models before GEPS is applied.

Figures 6.27, 6.28, and 6.29 show the (unscaled) luminosity functions obtained for the $n = 0$, $r_{thresh} = 5$ models when either exponentially decaying or burst SFR's or both are turned on. An example SFR (for the $n = 0$, $r_{thresh} = 5$ exponential-plus-burst model) is shown in Figure 6.26.

Before considering the scalings just mentioned, the shapes of these functions are obviously of interest. While a detailed understanding requires looking at the population and luminosity evolution of individual galaxies, the overall shapes of the luminosity functions are clearly a strong constraining factor on the models. Figure 6.30 shows a standard Schechter function (Schechter, 1976) with the parameters $\phi^* = 1{\cdot}56{\times}10^{-2}h^3Mpc^{-3}$, $M^* = -21{\cdot}1$ and $\alpha = -1{\cdot}1$ (Efstathiou *et al.*, 1988),[2] on the same vertical and horizontal scales as the other model luminosity functions apart from a vertical offset.

The $n = 0$, $r_{thresh} = 5$ exponential-plus-burst and exponential-only models are very similar, as the rate of the exponential SFR alone is enough to use up most of the gas, leaving little for the bursts. In general, these are too steep and straight to match well to a Schechter function. Brighter than $M \approx -18$, the shape of the $12{\cdot}3Gyr$ luminosity function (LF) could conceivably match the bright end of the Schechter function, but there would remain a peak above a Schechter shape in the range $-18 \geq M \geq -16$. However, this is not very promising. The sudden drop fainter than $M \lesssim -15$ can be reasonably attributed to the low mass end of the resolution of the models; and the observations of this end of the galaxy luminosity function (LF) are still not well determined in any case.

The exponential-plus-burst and exponential-only models similarly are too steep for the other three combinations of n, r_{thresh}.

[2] see eqn 2.2

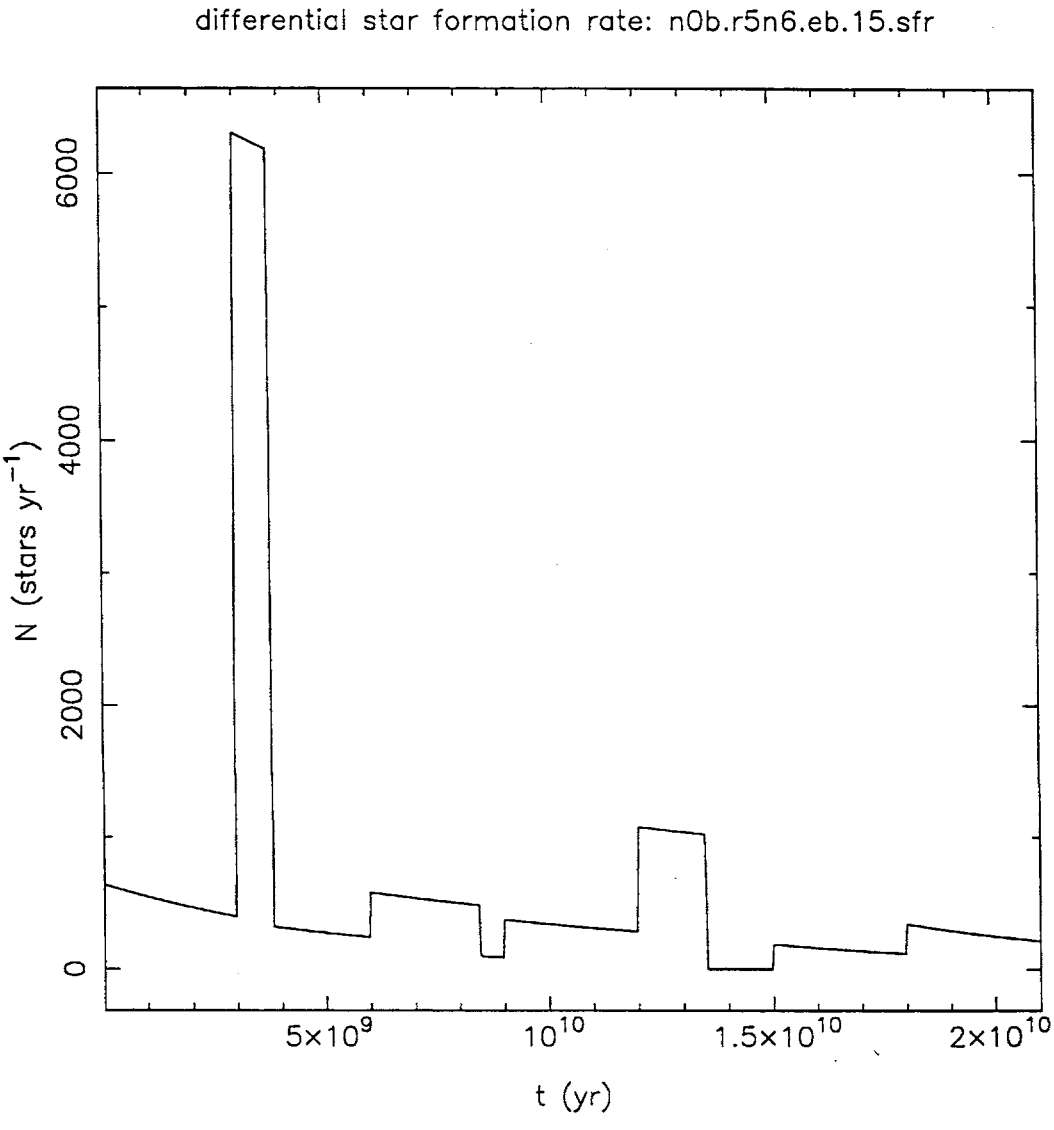

Figure 6.26: Star formation rate (SFR) for $n = 0$, $r_{thresh} = 5$, exponential+burst model, $\mu = 0{\cdot}15$.

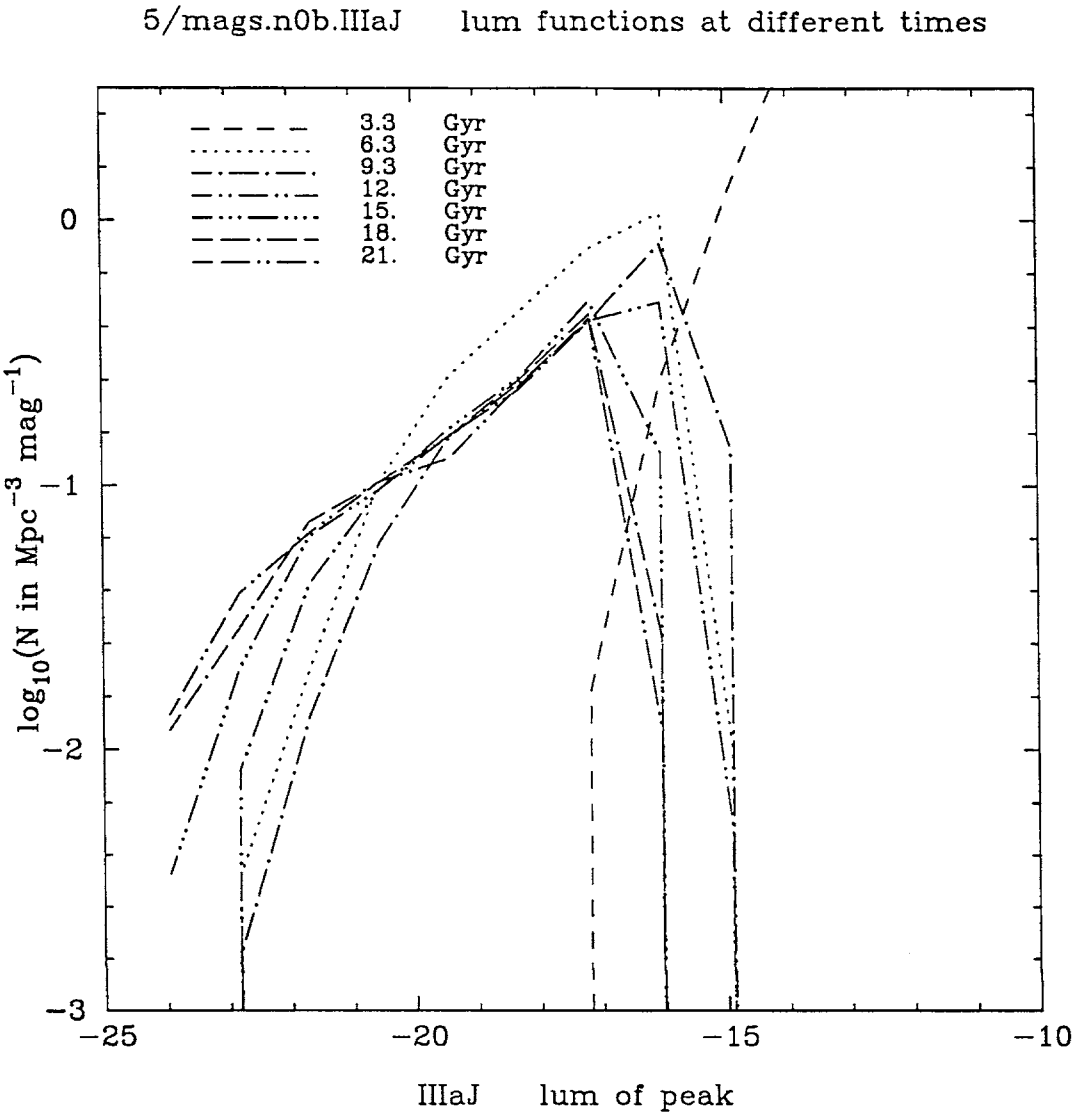

Figure 6.27: IIIaJ luminosity functions for $n = 0$, $r_{thresh} = 5$ model, exponential decay SFR only, Bruzual's SFR index $\mu = 0{\cdot}15$. Luminosities are expressed in absolute magnitudes, $\mathcal{M}_{IIIaJ}$, densities in $\log_{10}(N \text{ in } Mpc^{-3}mag^{-1})$, where the Mpc are in comoving coordinates. Note that the times with which the luminosity functions are labelled are later than the ones listed in Table 6.1. This is because each luminosity function calculated is that at the end of a period of star formation, i.e., each period of merger-induced star formation occurs over the interval $[t_i, t_{i+1})$, (where the interval after the last time stage is of duration $3Gyr$) and the luminosity information is output for that at $t = t_{i+1}$, or strictly speaking, it is the luminosity information in the limit as $t \to t_{i+1}^-$. Hence, we label the times as $t = t_{i+1}$.

The following plots show the same quantities for different models.

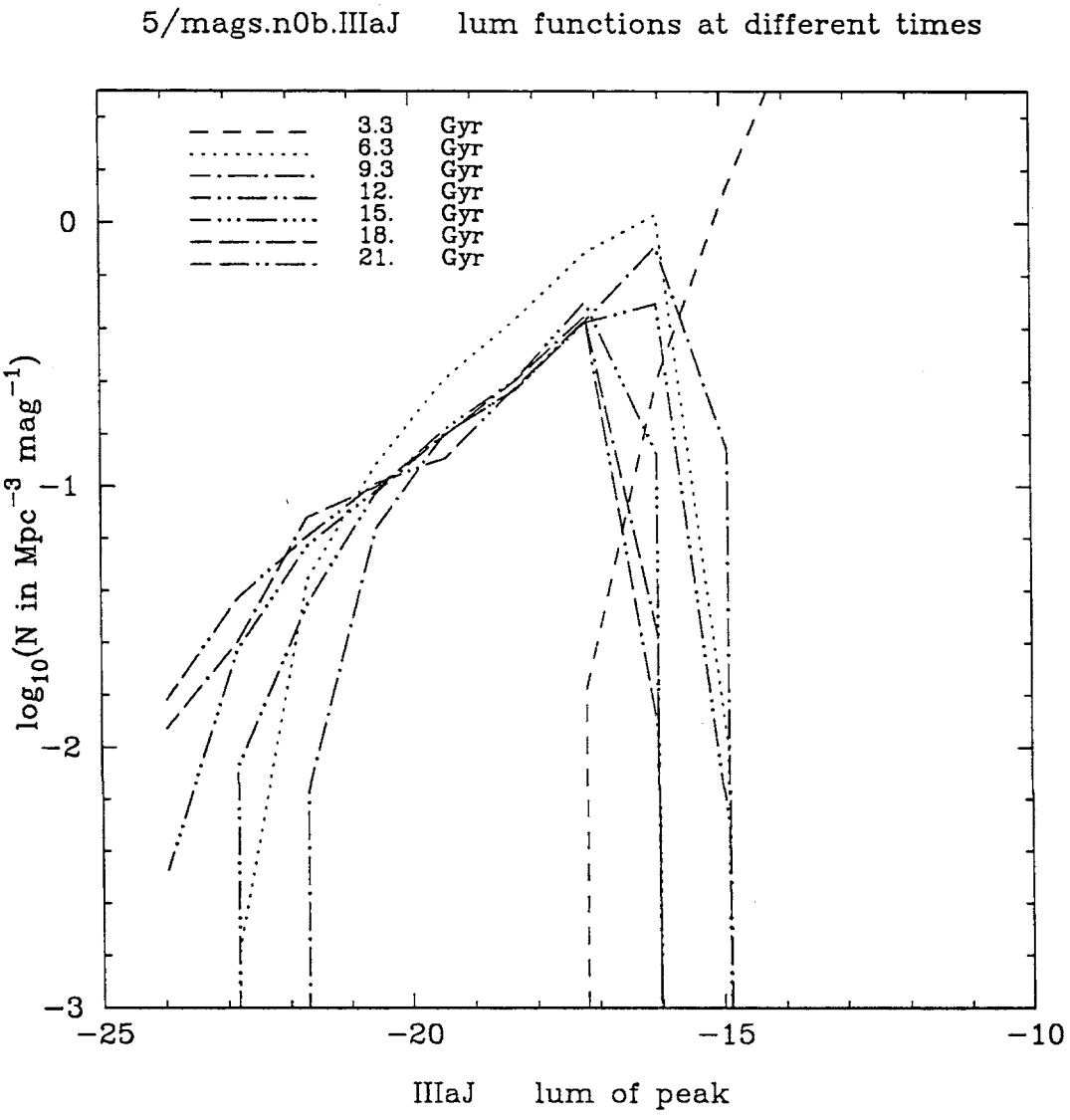

Figure 6.28: IIIaJ luminosity functions for $n = 0$, $r_{thresh} = 5$ model, (exponential decay + burst) SFR, Bruzual's $\mu = 0{\cdot}15$.

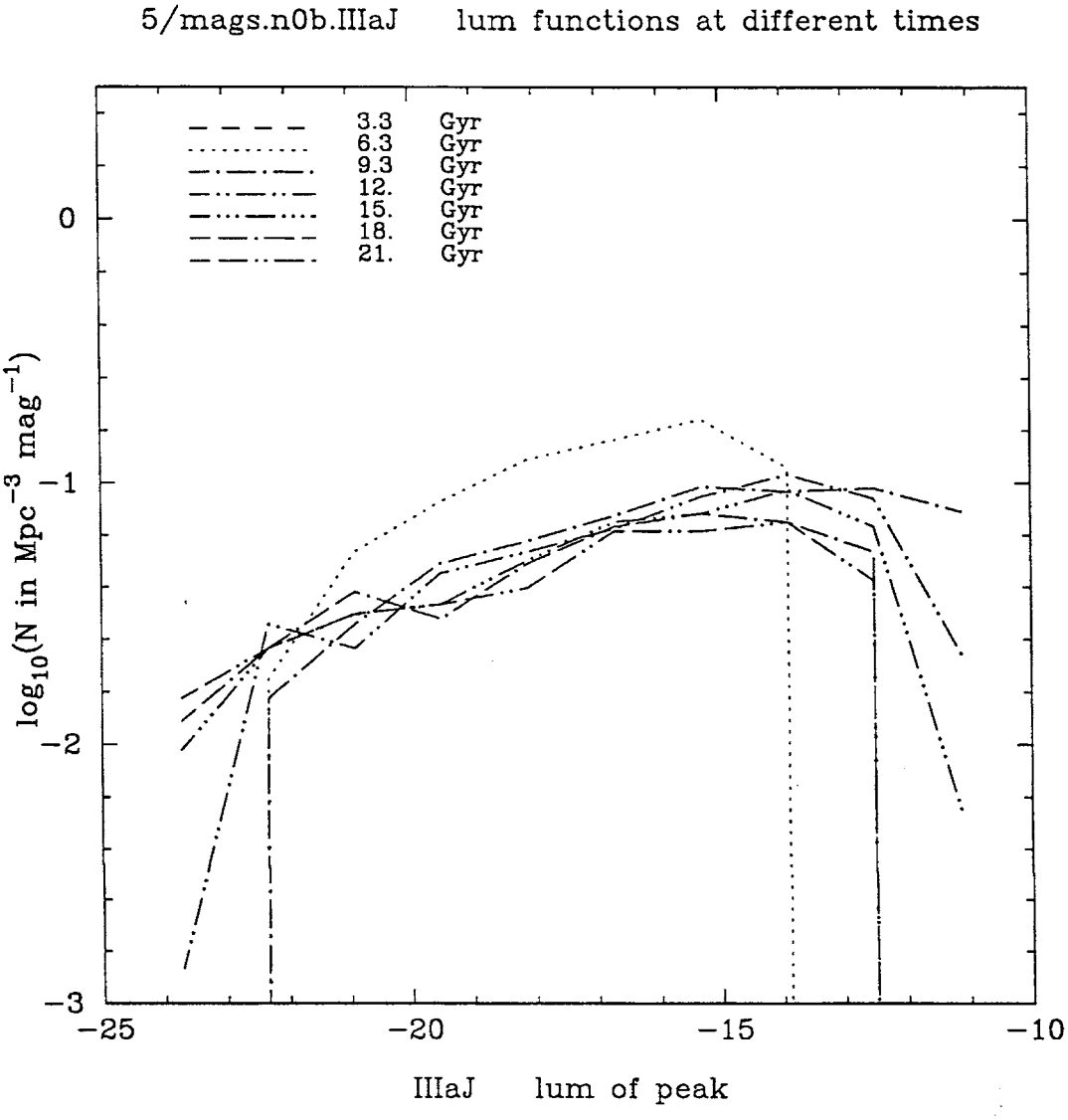

Figure 6.29: IIIaJ luminosity functions for $n = 0$, $r_{thresh} = 5$ model, burst-only SFR. In this and the following plots of the luminosity function for burst-only models, the luminosity functions at $t = 3{\cdot}3\,Gyr$ are missing. This is a property of the model: stars are only formed when mergers occur, which first occurs at the second time stage in this model, so that at this time stage ($t = 3{\cdot}3\,Gyr$) the galaxies still have no stars, hence they have zero luminosities and the luminosity function is meaningless.

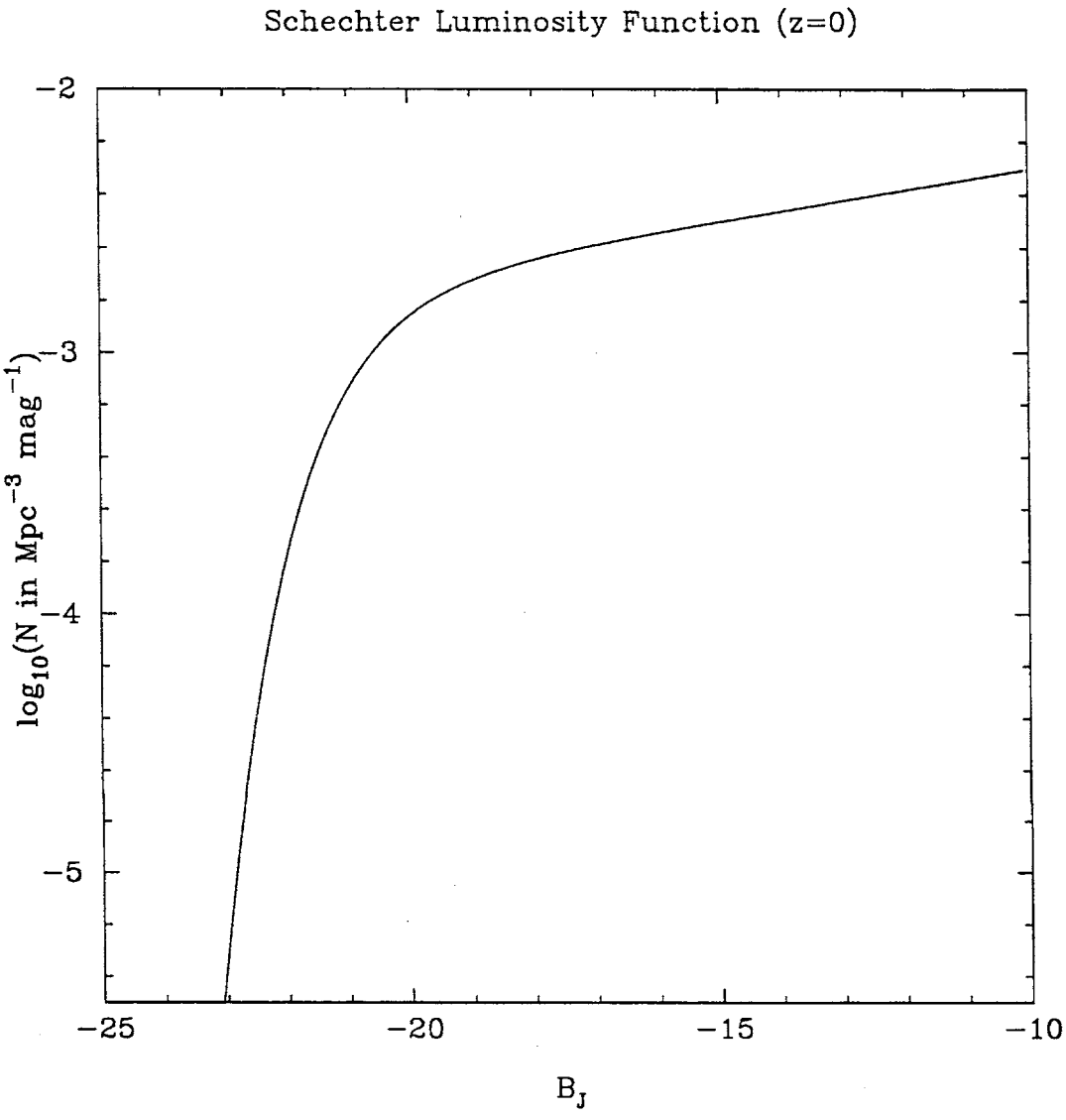

Figure 6.30: Schechter (1976) luminosity function of galaxies in the B_J (similar to IIIaJ) band, for Efstathiou *et al.* (1988) parameters: $\phi^* = 1{\cdot}56{\times}10^{-2}h^3Mpc^{-3}$, $M^* = -21{\cdot}1$ and $\alpha = -1{\cdot}1$.

The $n = 0$, $r_{thresh} = 5$ burst-only model, on the other hand, appears to match the faint end of the Schechter LF quite well (Fig. 6.29), with a shallow enough slope. The bright end of a few of these, in particular, the time stage labelled $t = 12{\cdot}3Gyr$, does in fact have a steep drop as in the Schechter function. While due to the scale-free nature of the models there should be no obvious reason to pick out this time stage, a default choice for scaling the LF's is to choose the time stage closest to the present epoch, $t_0 \approx 13Gyr$ (for our model values $q_0 = 0{\cdot}5$, $h = 0{\cdot}5$).

In both of these cases, the time stage closest to t_0 is in fact the $12{\cdot}3\,Gyr$ time stage, which provides about the best fit to a Schechter function for the model. We therefore use this time stage in each case.

The other three burst-only models (Figures 6.31, 6.32 and 6.33) also have fairly shallow slopes, but the $n = 0$, r_{thresh} burst-only model provides the best fit. As the similarity in the mass functions and merging history trees (Figs 6.5 - 6.7, 6.15 - 6.22) for these other three models indicate, the luminosity functions are also similar. As the $n = -2$ slope is close to the popular CDM model and $r_{thresh} = 1000$ is close to a realistic detection threshold, we choose to examine the results of rescaling on the $n = -2$, r_{thresh} burst-only model in addition to the $n = 0$, $r_{thresh} = 5$ burst-only model.

We parametrise the scaling as follows.

Let the units for mass and length be $L^3.10^{10}\mathcal{M}_\odot$ and $L\,kpc$, with the time unit remaining $1\,Gyr$, where $L > 1$. This way matter density and time are unchanged, so that the cosmological and gravitational physics remain unaffected, apart from the length scales at which resolution and boundary effects take place changing by a factor of L. The mass of gas considered to be star-making material for a halo is therefore a factor of L^3 greater than previously assumed, while any set of haloes in the simulation now occupies L^3 times the volume, decreasing the halo number density as required. As has been assumed here, the IMF is independent of total mass going into stars, so the evolutionary population synthesis simply underestimates the numbers of stars of any age or mass by the same factor, L^3. Hence the SED of the galaxy associated with the halo is increased in amplitude by this factor and the magnitude is decreased (brightened) by

$$7{\cdot}5log_{10}(L). \tag{6.4}$$

Incorporating the $\mathcal{M}_{tot}/\mathcal{M}_{lum}$ ratio applies in the same way, so that the final luminosity function is shifted to brighter magnitudes by

$$2{\cdot}5log_{10}(L^3\mathcal{M}_{lum}/\mathcal{M}_{tot}), \tag{6.5}$$

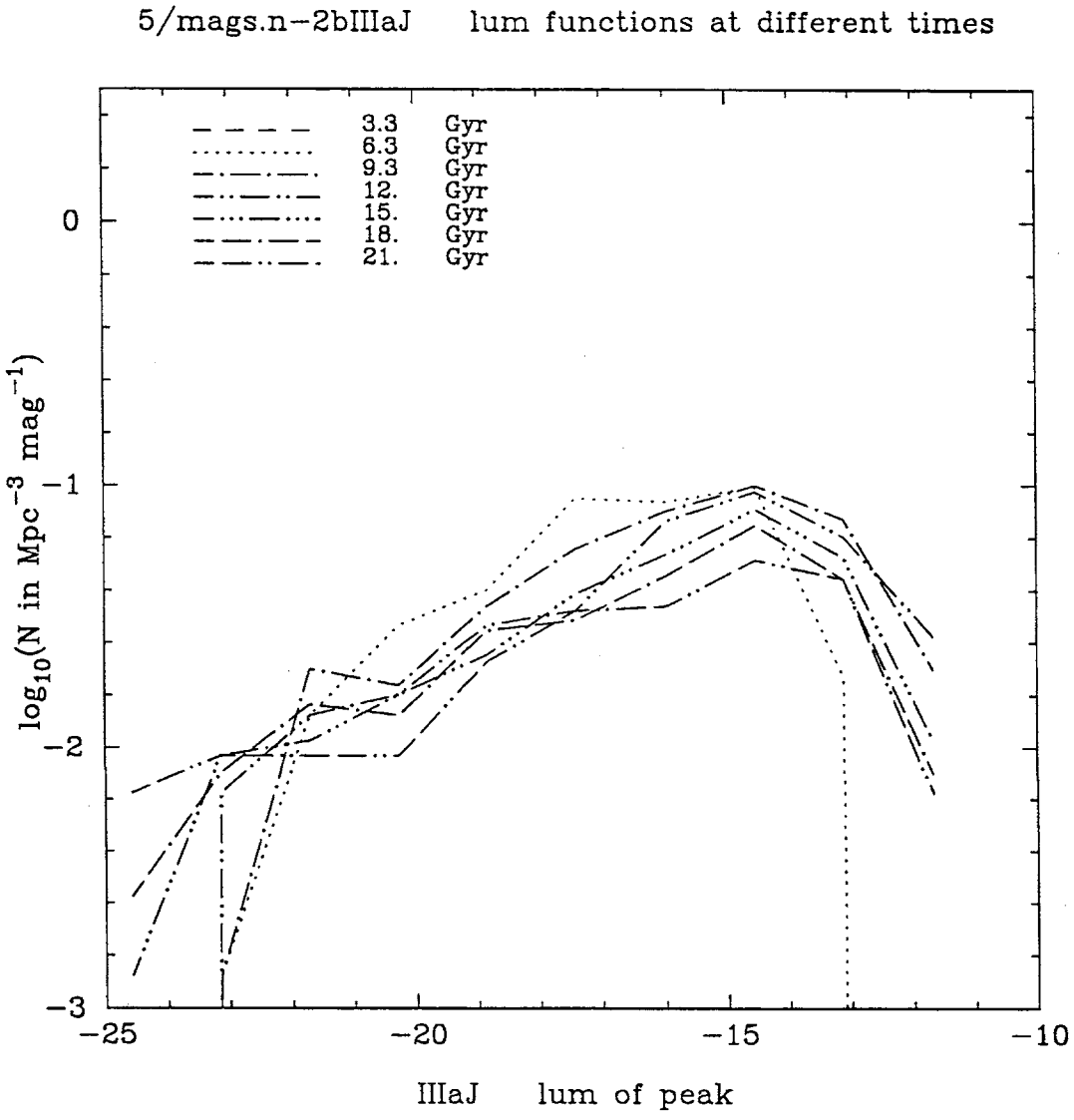

Figure 6.31: IIIaJ luminosity functions for $n = -2$, $r_{thresh} = 5$ model, burst-only SFR.

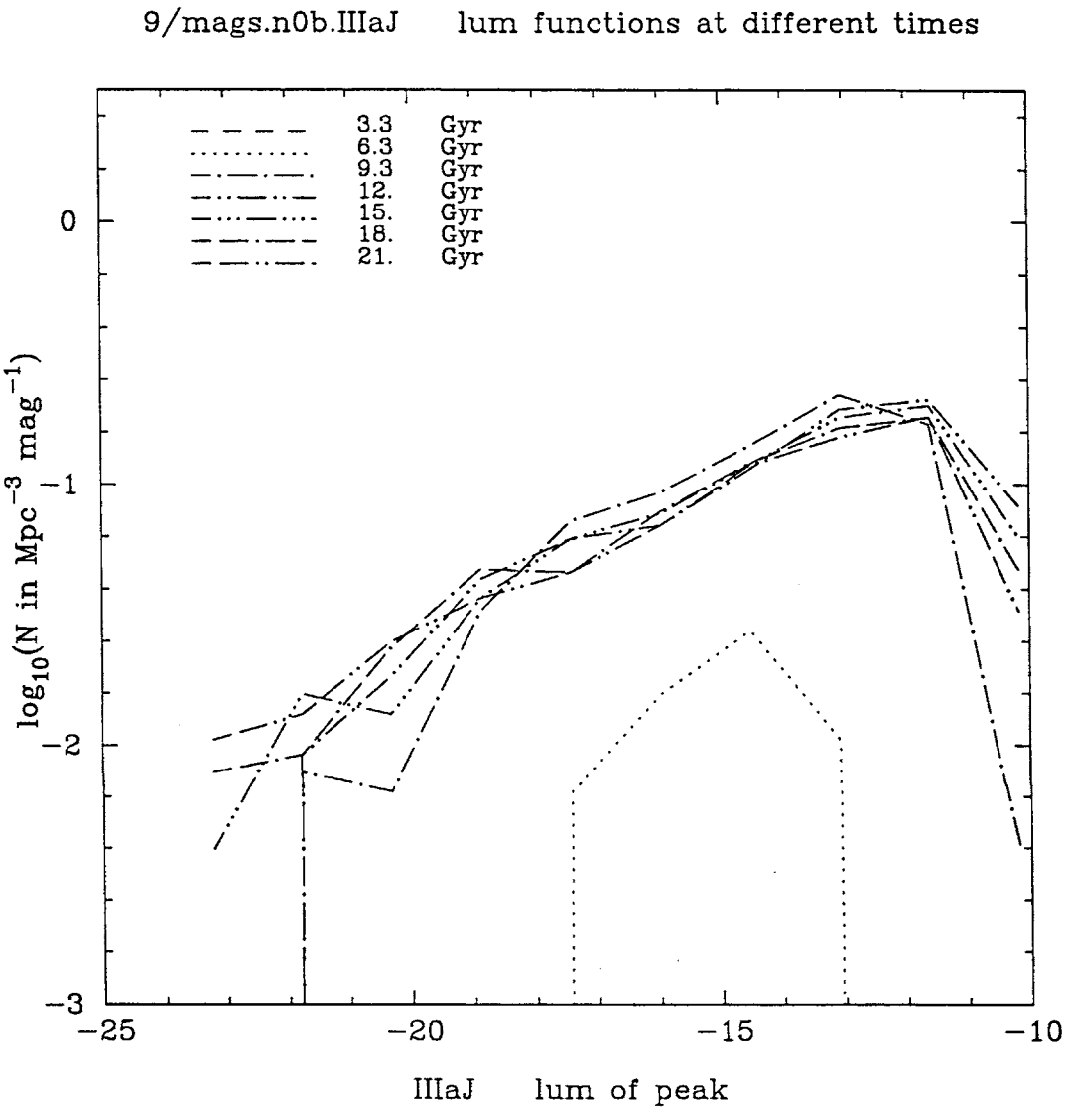

Figure 6.32: IIIaJ luminosity functions for $n = 0$, $r_{thresh} = 1000$ model, burst-only SFR.

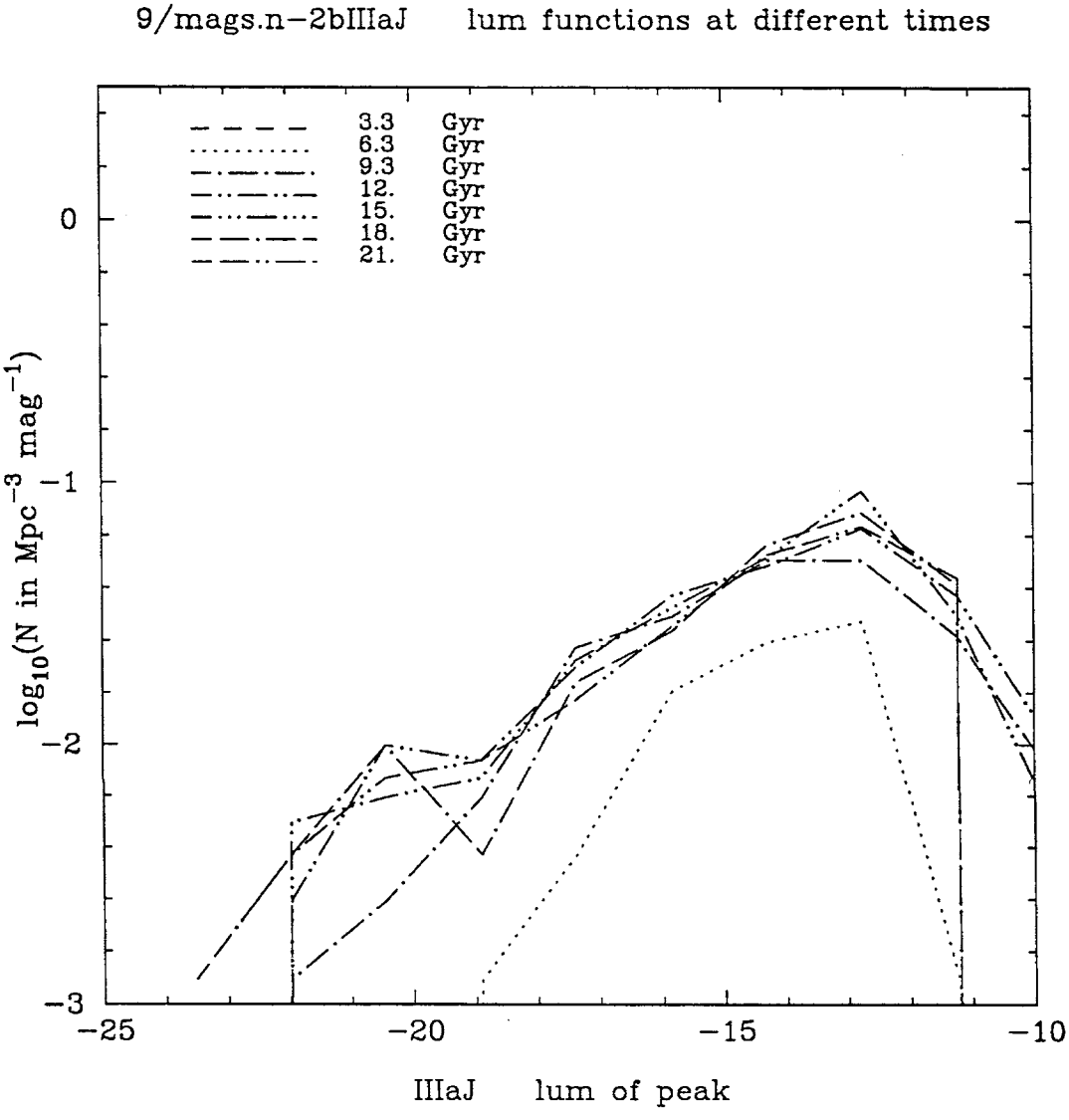

Figure 6.33: IIIaJ luminosity functions for $n = -2$, $r_{thresh} = 1000$ model, burst-only SFR.

as well as being shifted down in $log_{10}(\psi)$ by

$$3log_{10}(L). \tag{6.6}$$

If we take $\mathcal{M}_{tot}/\mathcal{M}_{lum} \approx 10$ (eqn 6.3) as fixed, then this leaves us with only one free parameter, L, to satisfy three constraints, ϕ^*, M^* and α, where ϕ^*, M^* and α are the parameters of the Schechter (1976) function.

Figures 6.34 and 6.35 show the best attempts to use these scalings to make the luminosity functions fit a Schechter function. These show the luminosity functions for the $t = 12{\cdot}3\,Gyr$ time stage (i.e., for $t \approx t_0$) for the $n = 0$, $r_{thresh} = 5$ and $n = -2$, $r_{thresh} = 1000$ burst-only models. The arrow portrays the direction any point on the luminosity function moves if L is altered. With the (observational) input of $\mathcal{M}_{tot}/\mathcal{M}_{lum} = 10$, the best fit for the $n = 0$, $r_{thresh} = 5$ model is found for $L = 3{\cdot}2$. Clearly the bright end of this LF doesn't match a Schechter function for any value of L. On the other hand, the $n = -2$, $r_{thresh} = 1000$ LF has a much better average fit, with $L = 2{\cdot}2$, though the slope of the faint end really is too steep, unless one generously allows this to be noise.

These scalings are not large enough for the time rescaling mentioned in section §6.4 to become reasonable. For example, if we use the value $L = 2{\cdot}2$ for the $n = -2$, $r_{thresh} = 1000$ model and the projected (power law) growth rate of the amplitude of the correlation function mentioned in §6.4, we get the (unscaled) t_0 pushed back to a redshift of $1 + z = 30$, which is still far too high for our purposes.

In spite of this, we can at least examine how this simple model would affect the galaxy counts. This is described in the following section. However, because the $n = 0$, $r_{thresh} = 5$ time stage which we have fitted still does not fit a Schechter function, and the threshold $r_{thresh} = 5$ is extremely low, we introduce an additional factor for this model.

If we assume that the mass density in the galaxy falls off as r^{-2} (which is implied by the flatness of the observed rotation curve) then the detection threshold of $r_{thresh} = 5{\cdot}0$ gives a radius for the halo of the Galaxy of about at least $1500kpc$, much larger than any claimed radius for the halo of the Galaxy. The flatness of the rotation curve also implies that the total mass inside any radius is proportional to the radius, so that the total mass in our Galaxy would be overestimated by about an order of magnitude. Hence, although the merging physics as represented here would not be expected to change simply according to a proportionality factor, we attempt to model this change by allowing a factor, A, which decreases the total amount of light, or equivalently increases the $\mathcal{M}_{tot}/\mathcal{M}_{lum}$ ratio.

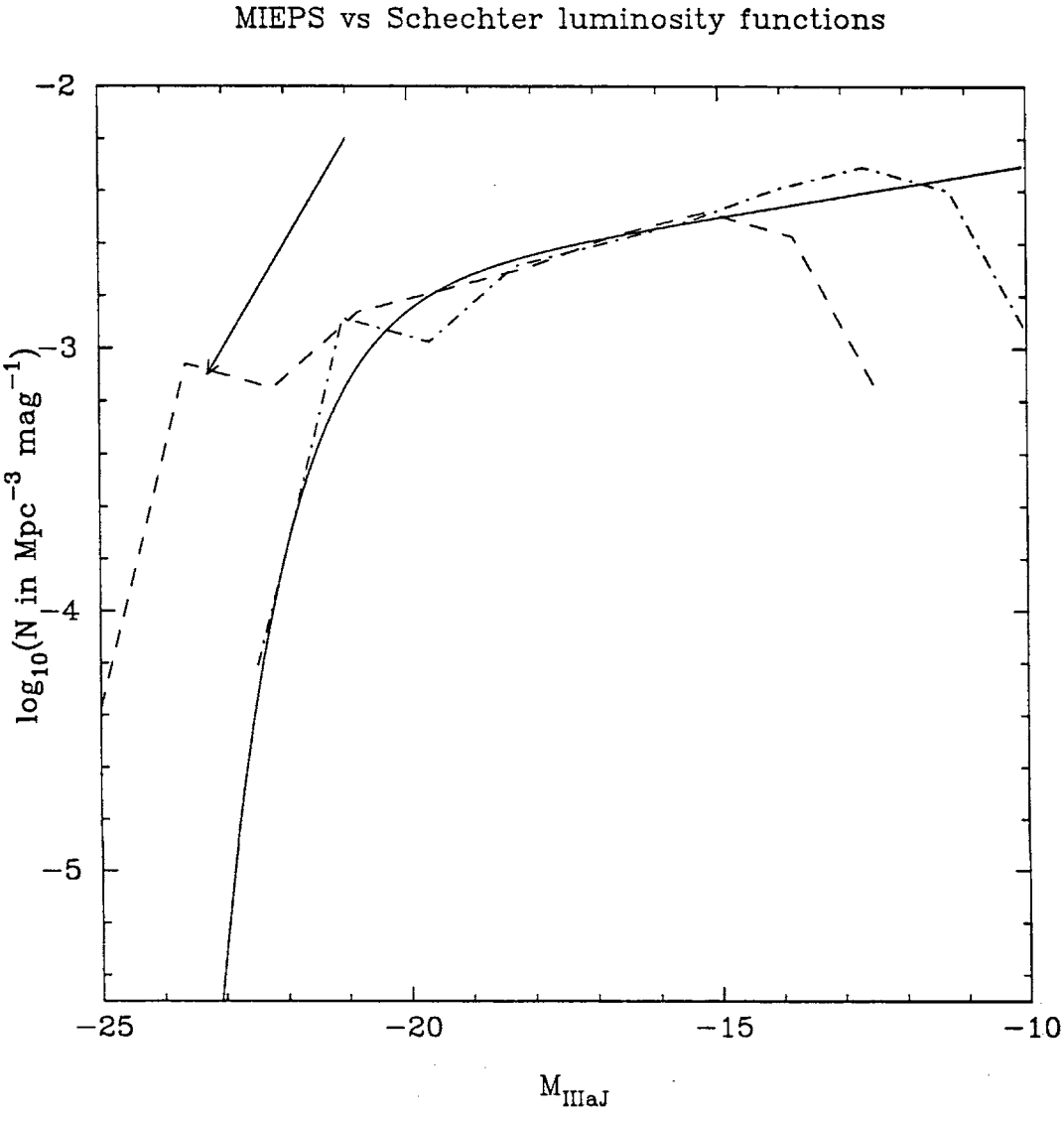

Figure 6.34: IIIaJ luminosity function for $n = 0$, $r_{thresh} = 5$ burst-only model, with scalings $L = 3{\cdot}2$ and $(L = 2{\cdot}8, A = 7)$ shown as dashed and dash-dotted lines respectively, in comparison to Schechter function shown as solid line (Fig. 6.30). $\mathcal{M}_{tot}/\mathcal{M}_{lum} = 10$ is used in both cases. The arrow denotes the direction any point on the luminosity function will move if L alone is altered.

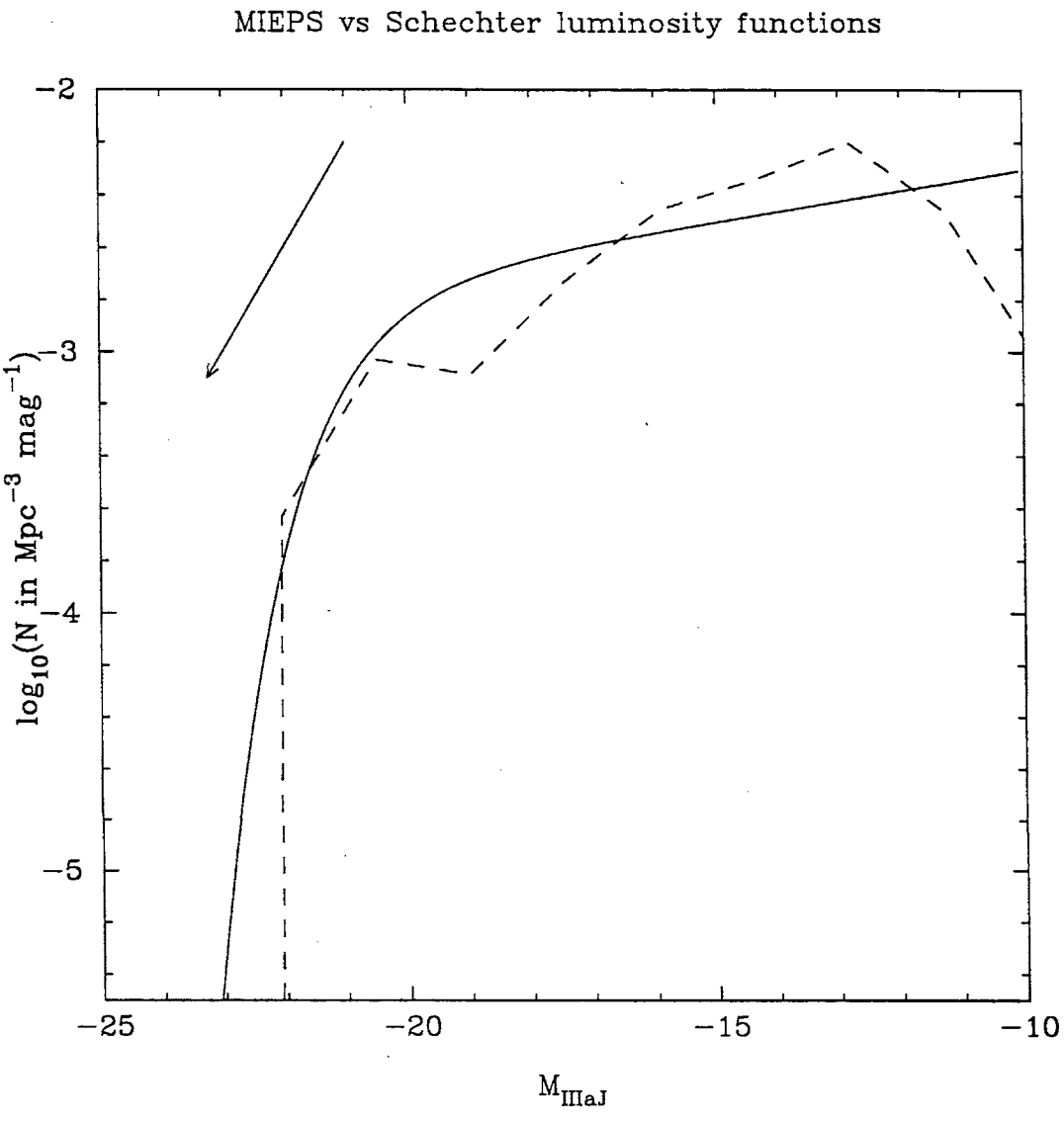

Figure 6.35: IIIaJ luminosity function for $n = -2$, $r_{thresh} = 1000$ burst-only model, with scaling $L = 2{\cdot}2$. The dashed line is for our model, the solid line for a Schechter function. $\mathcal{M}_{tot}/\mathcal{M}_{lum} = 10$ is used. The arrow denotes the direction any point on the luminosity function will move if L is altered.

The $n = 0$, $r_{thresh} = 5$ $t = 12{\cdot}3Gyr$ time stage is then fitted with the combination ($L = 2{\cdot}8, A = 7$) (Fig. 6.34). This factor $A = 7$ is indeed about an order of magnitude, so this attempted compensation factor may be more realistic than expected.

A radius of $1500kpc$ from the Galactic Centre would essentially include most of our Local Group. To compensate for treating all of these as a single galaxy, one should not only have to decrease the amount of mass available for the galaxy to turn into stars, but one should also have to account for the greater number of galaxies actually inside this radius and make them have extra bursts of star formation to account for their interactions with one another. The factor $A = 7$ brings the $1500kpc$ radius down to $200kpc$, which is a much more reasonable value. But then our companion galaxies in the Local Group would be missed (continuing this analysis as if our Galaxy is a typical galaxy) and no star formation would have been caused in the Galaxy by other Local Group members. Some overall increase in the normalisation of the luminosity function and a shift brightwards should therefore be necessary. This cannot have been absorbed into the length scaling factor, L, as an increase in normalisation of the luminosity function requires a decrease in L, which implies a shift faintwards of the luminosity function.

The $n = 0, r_{thresh} = 1000$ burst-only model does detect these smaller galaxies ("halo substructure") and results in a luminosity function which is slightly too steep (Fig. 6.32). The better fitting $n = 0$, $r_{thresh} = 5$ burst-only model therefore achieves this better fit by assuming that all the galaxies in this group are really a single galaxy, and then correcting for the overestimate in mass of this single galaxy caused by the method of ignoring the other galaxies. If gas-dynamical processes had the effect of decreasing star formation activity in galaxy groups, while allowing star formation due to major mergers, this could conceivably explain this result. This might be the case if intra-group velocities are too low to provide enough kinetic energy to start star formation. The star formation input to the MIEPS models described in this thesis (§5.5) ignores velocity information, even though the inspiration for the parametrisation is in fact that the energy for star formation should to first order be proportional to the kinetic energy available. Hence, inclusion of velocity information, i.e., using a proper kinetic energy term, would not only be consistent with the ideas behind these models, it may also improve the fit.

6.7 Effects on Number Counts

A useful method of seeing the effect of our models on the faint galaxy number counts would be to see if some simple transformation of the Schechter function can be used to describe the luminosity functions we have here. However, most of the luminosity functions in Figs 6.29 and 6.33 are not as Schechter-like as the time stages which we have fitted, and even these two are only approximate matches. So, matching these other time stages to Schechter functions would seem less justified than for the stages which we have fitted. Additionally, the whole point of the full-scale merger-induced evolutionary population synthesis described here is to model the evolution of the galaxy population in greater detail than has previously been done, so it may be an intrinsic property of this population that it is not always Schechter-like.

We therefore choose to use the luminosity functions plotted directly. We fitted the 12·3 Gyr time stage to the Schechter function, so we use this time stage and all the available luminosity functions previous to this. No luminosity function exists for the first time stage in the models for any star formation rate, since galaxies can't be luminous when stars have not yet formed. In the burst-only models, no stars form until the first merger occurs, i.e., at the second time stage. Hence, the first of our discrete time stages at which a galaxy has stars is the third time stage. As we do not rescale time, this means we only have two luminosity functions previous to the 12·3 Gyr time stage, i.e., the 6·3 Gyr and 9·3 Gyr time stages. We interpolate linearly to the intervening time stages and extrapolate backwards to $t = 3{\cdot}3Gyr$, having zero-valued luminosity functions previous to this. As far as luminosity is concerned, the formation time is therefore $t = 3{\cdot}3Gyr$, i.e., $z = 1{\cdot}5$. This is quite low, but is a property of the model as described in this thesis.

We do rescale length, and for the $n = 0$, $r_{thresh} = 5$ allow the low-threshold correction factor A. That is, we use $(L = 2{\cdot}8, A = 7)$ for the $n = 0$, $r_{thresh} = 5$ model and $L = 2.2$ for the $n = -2$, $r_{thresh} = 1000$ model. These same scalings apply to all the time stages previous to the ones fitted, of course. $(\mathcal{M}_{tot}/\mathcal{M}_{lum} = 10$ is used for both models.)

The resultant number counts are shown in Figures 6.36 and 6.37. Neither model supplies the excess faint galaxies required to fit the data.

The $n = 0$, $r_{thresh} = 5$ model fits fairly well at the bright end, but is too low at the faint end. However, the luminosity evolution only model with the same formation redshift ($z_f = 1{\cdot}5$) shows an even worse deficit of faint galaxies, so relative to the luminosity evolution only model, our model (which combines luminosity and number evolution) contains more galaxies at these fainter magnitudes. The

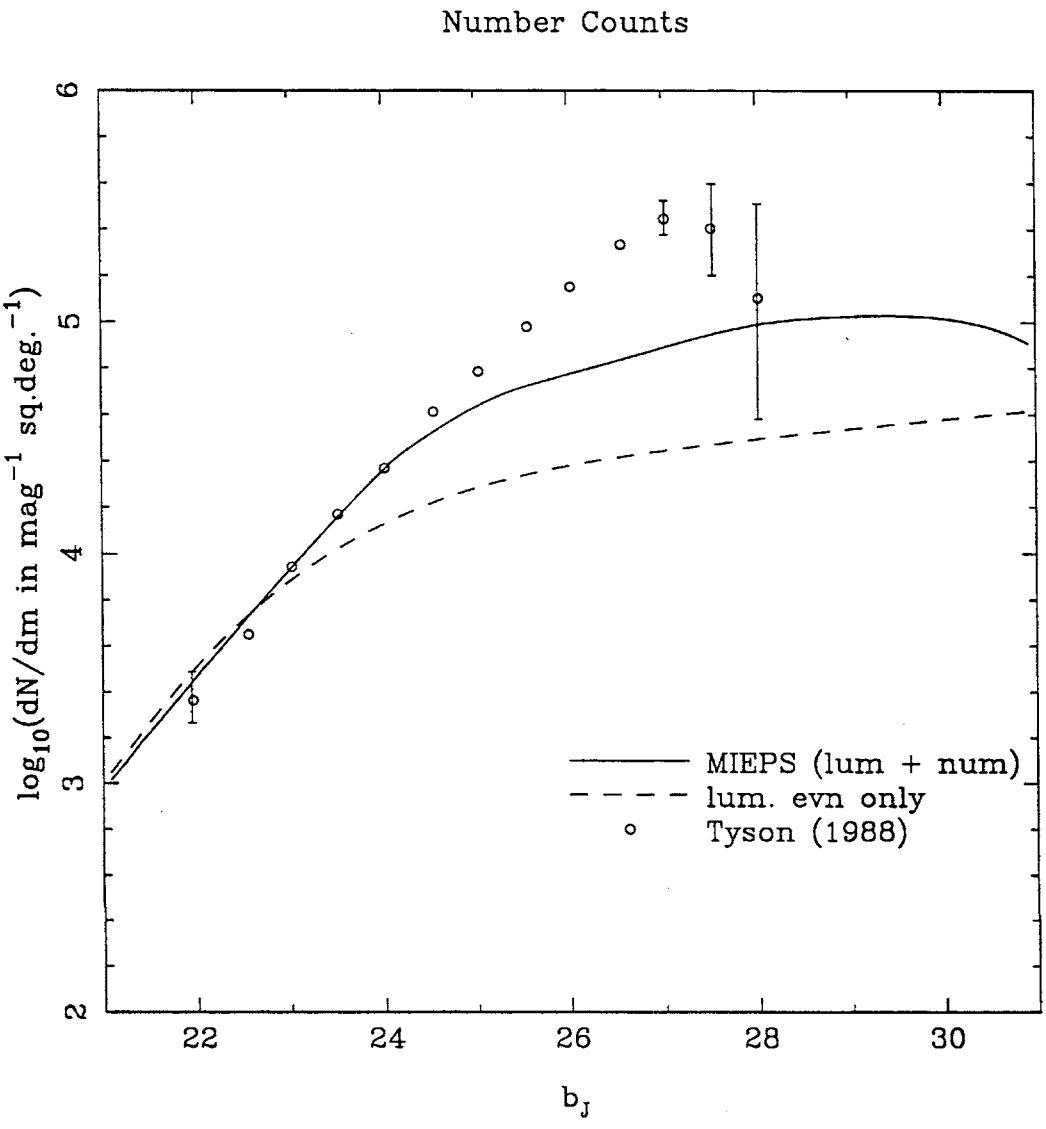

Figure 6.36: Number counts ($d^2N(< m)/d\Omega\, dm$) for $n = 0$, $r_{thresh} = 5$ burst-only model. The scaling ($L = 2{\cdot}8, A = 7$) and $\mathcal{M}_{tot}/\mathcal{M}_{lum} = 10$ have been applied to all time stages, the luminosity function is zero before $t = 3{\cdot}3Gyr$, no time rescaling has been applied, and non-model time stages have been interpolated/extrapolated linearly from model time stages. These counts are indicated by the solid line ("luminosity plus number evolution"). A dashed line indicates the counts for a model involving (K+E)-corrections for $q_0 = 0{\cdot}5, h = 0{\cdot}5, z_f = 1{\cdot}5$ ("luminosity evolution only").

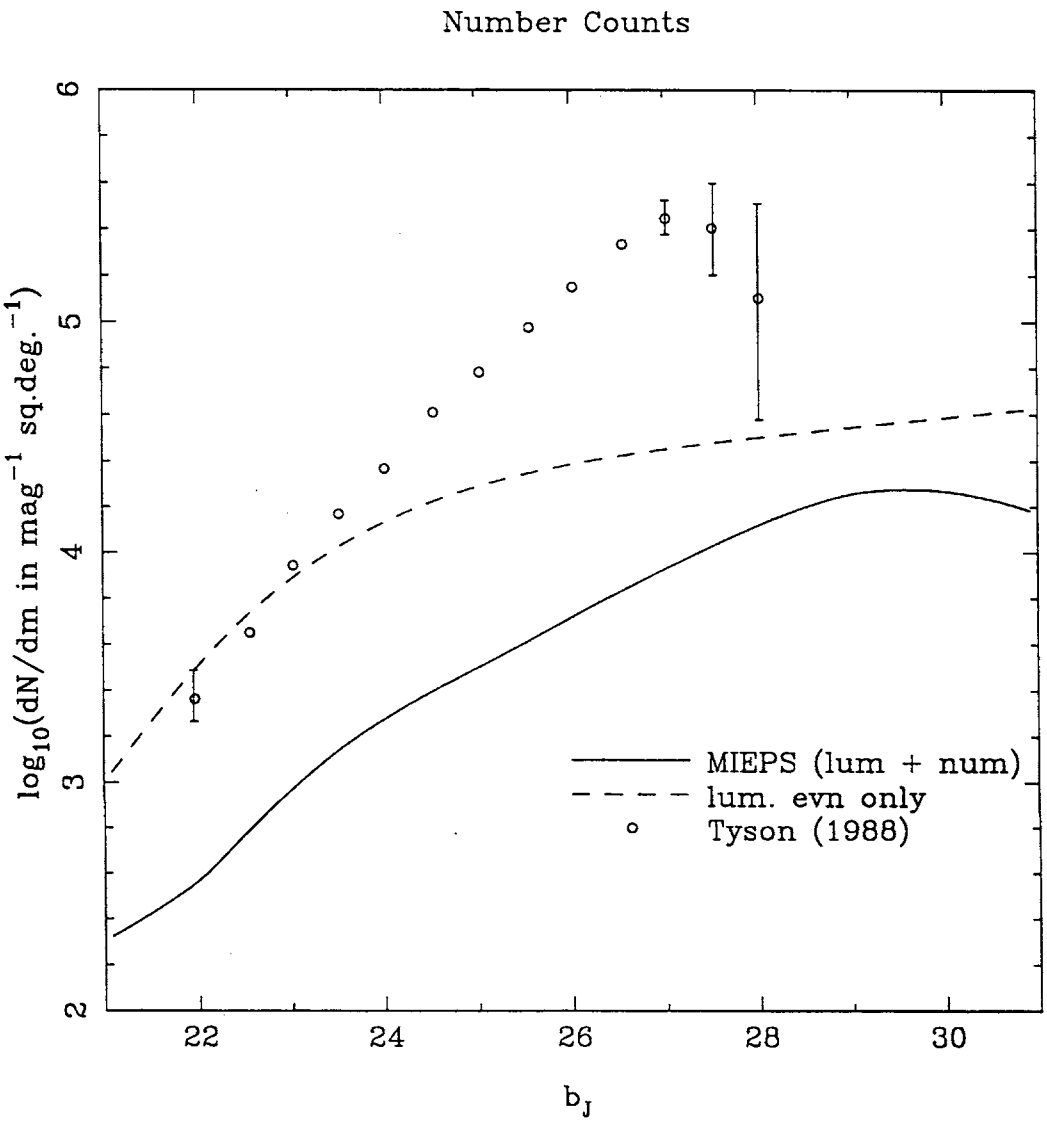

Figure 6.37: Number counts for $n = -2$, $r_{thresh} = 1000$ burst-only model. Use of the models and plotting is same as for Fig. 6.36 except that the scaling $L = 2{\cdot}2$ and $\mathcal{M}_{tot}/\mathcal{M}_{lum} = 10$ have been used (and A has not been used).

reason for this can be seen in Fig. 6.29, which shows that the only time stage at which the luminosity function is significantly different from the rest (apart from the bright and faint ends) is that at the earliest time stage at which the luminosity function is nonzero. The fact that the luminosity function at this time stage has a higher amplitude than the others means that the amplitudes of the luminosity function at those times between the first time of merging ($t = 3{\cdot}3Gyr$ in this model) and the second time of merging are higher still, since we linearly extrapolate backwards into this time interval (in log(N)). This shows the origin of the greater number of galaxies in our model.

The $n = -2$, $r_{thresh} = 1000$ model, on the other hand, is way too low to fit the counts, and way lower than the luminosity evolution only model. Fig. 6.33 shows that the $t = 6{\cdot}3\,Gyr$ time stage is lower in amplitude than the later time stages. Hence, the luminosity function at all times between $t = 3{\cdot}3Gyr$ and $t = 9{\cdot}3Gyr$ are lower than the Schechter-fitted luminosity function, showing the origin of the deficit of faint galaxies in this model.

6.8 Conclusion

The techniques and results discussed above show that this method of exploring galaxy evolutionary physics is feasible and that luminosity functions and number counts comparable to observational values are obtained for some combinations of the model parameters chosen. We have shown results for basic models; i.e., those having $n = 0$ or $n = -2$ power law initial perturbation power spectra and $r_{thresh} = 5$ or $r_{thresh} = 1000$ overdensity detection thresholds.

The merger-induced luminosity evolution does not flatten the slopes of the low mass ends of the mass functions enough to match a Schechter function (Schechter, 1976) if exponentially decreasing star formation rates are used. However, with burst-only star formation rates, the merger-induced luminosity evolution does flatten the low mass end slopes significantly.

The model with a physically reasonable detection threshold ($r_{thresh} = 1000$) and a perturbation spectrum slope which is close to that of the popular cold dark matter (CDM) model at galaxy scales ($n = -2$) results in a luminosity function at the present epoch for burst-only merger-induced luminosity evolution which is somewhat too steep, but which can be fitted to a Schechter function (Schechter, 1976) if length and mass units are rescaled (with $L = 2{\cdot}2$). However, because of the lateness of formation of galaxies (Table 6.2), the earliest luminosity function in this model is very low, so that the faint galaxy number counts derived from this (scaled) model are far below the observed faint galaxy counts.

The luminosity function close to the present epoch in the model with a physically unreasonable detection threshold ($r_{thresh} = 5$) and a white noise perturbation spectrum slope ($n = 0$) fits the faint end of the Schechter function very well with a length-mass rescaling of $L = 3{\cdot}2$, i.e., the faint end slope is that of a Schechter function. This still leaves the drop in the luminosity function at too bright a magnitude in comparison to a Schechter function. A factor which attempts to crudely compensate for the physically unreasonable threshold, essentially by increasing the $\mathcal{M}_{tot}/\mathcal{M}_{lum}$ ratio, allows a better fit to be obtained (with ($L = 2{\cdot}8$, $A = 7$)). However, the faint galaxy number counts derived from this (scaled) model are in fact much better than for the previously mentioned model, though they don't fit the faint end of the observed number counts as hoped.

To paraphrase this, a model with expected parameters gives a luminosity function which roughly fits a Schechter function at $t \approx t_0$ but gives number counts which clearly don't fit the observations, while a model with less likely parameters gives a luminosity function which has the slope of a Schechter function and fits a Schechter function overall if a compensatory factor is allowed, and in that case

the number counts fit reasonably well to the observations, apart from the faint end. The inclusion of velocity information in the star formation rates of the bursts in future work may show that the reason this latter model works is that galaxies within groups have too low relative kinetic energies to cause as much star formation as galaxies colliding from larger distances.

However, two important caveats need to be kept in mind in interpreting these results.

Firstly, the amplitude of the two-point autocorrelation function is far too low, though it does fit well to a $\gamma = -1{\cdot}8$ power law at all time stages in all models where the data is significant. If we suppose the amplitude to increase according to a power law fitted to all but the first time stage in the $n = 0$ models or to the last four time stages in the $n - 2$ models, this does not reach the observed amplitude until a redshift factor of greater than order of 10^2 into the future. That is, if we rescale time in order that the projected correlation function has the observed amplitude at the present, then the latest time stage for which we have N-body information would correspond to a redshift of $1 + z \sim 10^2$, which of course would be likely to invalidate the initial conditions of the N-body models.

This correlation function is calculated for galaxy haloes, rather than galaxies. In reality, dissipation is likely to mean that when haloes merge the galaxies inside them have previously collapsed so that they fail to merge when their overlying haloes merge. This would increase the galaxy correlation function with respect to the halo correlation function. However, the whole aim of the models here is to examine what aspects of galaxy properties can be explained using these simple models which assign one galaxy to each halo and ignore dissipation. If we introduce a factor which stops galaxies merging in some of the cases in which their respective haloes merge, then the models as described here would no longer apply.

The second caveat is the that the intervals between the time stages used from the N-body models are sparsely spaced and few in number, so the effective luminous galaxy formation epoch of the burst-only models is $z = 1{\cdot}5$, which is an artefact of the time stages chosen to be stored on running the N-body models. The fact that the number counts in the rescaled $n = 0$, $r_{thresh} = 5$ model are greater than those for a luminosity evolution only model for this artificial formation redshift, indicate that use of a higher, more realistic redshift would lead to number counts which are likely to be high enough to explain the observed number counts, as the difference between these two models is at least as large as the difference between the observed counts and luminosity evolution only models at the faint end of the observed range.

The other interesting results from this galaxy evolutionary modelling are that the individual merger rates can be very different from the average merger rates and that the fraction of mass coming from accretion can be quite high. For example, for the $n = 0$, $r_{thresh} = 5$ model, the mean number of peaks which collapse from the intergalactic medium at any time stage and end up in a peak at the final time stage is 7·4 while the standard deviation in this quantity is 20·7 (Table 6.5), and the maximum is 233; and the fraction of mass in the final peaks coming from accretion is $32 \pm 26\%$. (For the other three models, the merger numbers go down to about half the corresponding values, while the accretion percentages are about the same.)

Chapter 7

Conclusion

In this thesis I have described observations and theory which contribute to our understanding of faint galaxy populations.

In chapter 2 it was shown that d_L, dV/dz, q_0, z_f, the K- and E- corrections, ϕ^*, M^*, α, and η all affect the faint number counts, though not independently, while the effect of H_0 is small. It was also shown that conservation of comoving number density with a standard Schechter luminosity function requires a low q_0, high z_f cosmology. However, as pointed out in the Introduction, redshift information makes a merging scenario more likely to explain the faint galaxy number counts, with the possibility of the existence of an excess dwarf population at the present epoch also remaining.

The search for low surface brightness galaxies described in Chapter 3 gave unpromising results, with a number density to $z \approx 0{\cdot}05$ of $n \approx (9 \pm 5) \times 10^{-3} h^3 Mpc^{-3}$, which is about $7 \pm 4\%$ of the number density for normal galaxies in the corresponding magnitude range of $-14 \geq M_B \geq -20$ represented in a Schechter (1976) luminosity function having parameters $\alpha = -1{\cdot}1$, $M_B^* = -21{\cdot}1$ and $\phi^* = 1{\cdot}56 \times 10^{-2} h^3 Mpc^{-3}$ (Efstathiou *et al.*, 1988). Only about half of this low surface brightness galaxy population is likely to be excess to that represented in the Schechter function. The diameters of the population observed are inconsistent with the hypothesis that they are the low-redshift counterparts of the excess faint galaxies if the latter are assumed to have a typical redshift of $z = 0{\cdot}25$ at $B \approx 24$ (as in Cowie *et al.*, 1991), though their magnitudes are consistent.

The angular two-point correlation function data of the faint galaxies also gave a result which was numerically low, but in this case more interesting. The clustering of these faint galaxies was shown to be as low as that found by Efstathiou *et al.* (1991), but Neuschaefer *et al.*'s (1991) rising correlation function amplitudes as a function of median sample magnitude was not found. The former implies that clustering growth is faster than it would be if clustering were fixed in proper

coordinates, i.e., $\epsilon > 0$ (eqn (4.25)). If for some reason we have overestimated the uncertainties in our measurements, this result would be even stronger. Efstathiou *et al.* feel that $\epsilon > 0$ is unlikely, so their favoured explanation is that the weakness in clustering is due to the excess faint galaxies being an intrinsically faint, low redshift, more weakly clustered than normal population. The N-body models used in this thesis here do in fact predict $\epsilon < 0$ in agreement with Efstathiou *et al.* (§6.4), but they also have an amplitude (of the spatial correlation function) which is far lower than cosmological amplitudes, so this does not seriously overrule the N-body results of Melott (1992) or Yoshii *et al.* (1993) or the observational data of Warren *et al.* (1993), which all indicate that $\epsilon > 0$. Instead, it provides a constraint with which to check future N-body simulations which are normalised with the intention of having correlation functions at a cosmological scale.

A followup observational project indicated by this result is to observe to the same limiting depth over a larger area, in order to reduce the error bars and see if the continuation of linearity in the relation between correlation function amplitude and median magnitude to our limiting median magnitude was merely a coincidence or not.

The results of the merger-induced evolutionary population synthesis (MIEPS) models (Chapters 5, 6), with the two caveats on the problem with the spatial correlation function of the simulations and the size of the time interval between time stages used, are that these models look like a good candidate for explaining the faint counts, as expected. Burst-only star formation rate models are found to be necessary, as exponentially decaying star formation rates do not flatten the faint end of the mass function enough in converting it into a luminosity function. The burst-only models with initial perturbation spectra as power law spectra with indices of $n = 0$ and $n = -2$ and detection thresholds of $r_{thresh} = 5$ and $r_{thresh} = 1000$ then have the following interesting result.

The model with the most expected parameters ($n = -2$, $r_{thresh} = 1000$) gives a luminosity function which roughly fits a Schechter function at $t \approx t_0$, but gives number counts which clearly don't fit the observations; while a model with less likely parameters ($n = 0$, $r_{thresh} = 5$) gives a luminosity function which has the slope of a Schechter function and fits a Schechter function overall if the compensatory factor A is allowed, in which case the number counts fit reasonably well to the observations apart from the faint end. An increase in time resolution of the N-body output is likely to improve the fit of the latter model more than that of the former.

Hence, these models favour a white-noise-like initial perturbation spectrum

($n \approx 0$) with a low detection threshold ($r_{thresh} \approx 5$) and a correction factor $A = 7$ as a candidate for explaining the excess of faint galaxies. A CDM-like spectrum on these scales ($n \approx -2$) appears less likely. This is unexpected, because it has been found in earlier N-body simulations (Quinn *et al.*, 1986) that the flatness of observed galaxy rotation curves imply a value of $n \approx -2$ on galaxy scales.

The Warren *et al.* (1992) team is continuing to run N-body simulations, including several normalised to cosmological conditions and with order of 10^7 particles. It is planned to use these new simulations to investigate whether or not these results hold up with the cosmologically scaled spatial correlation functions, as well as with the use of finer time resolution.

It is also planned to consider using velocity information in the inputs to the star formation bursts, as this may explain why the corrected $n = 0$, $r_{thresh} = 5$ burst-only model gives a better fit to the Schechter function than the $n = -2$, $r_{thresh} = 1000$ model.

The other main result from the N-body galaxy evolutionary modelling is that the individual merger rates can be very different from the average merger rates and that the fraction of mass coming from accretion can be quite high. For example, for the $n = 0$, $r_{thresh} = 5$ model, the mean number of peaks which collapse from the intergalactic medium at any time stage and end up in a peak at the final time stage is 7·4, while the standard deviation in this quantity is 20·7. While this result is likely to quantitatively change with the new N-body simulations, qualitatively it is unlikely to.

To sum up, the results of this thesis are that a population of low surface brightness objects appears to be an unlikely candidate for explaining the excess faint galaxy counts; that the clustering of these faint galaxies is low, which is consistent with a flat universe either with fast clustering growth ($\epsilon > 0$) as several authors expect or an intrinsically faint weakly clustered population as Efstathiou *et al.* (1991) favours; and that a realistic model of the evolution of the luminosity function which combines gravity (from N-body models, Warren *et al.*, 1992) and star formation and evolution (from galaxy evolutionary population synthesis, Bruzual, 1983) has been performed and indicates that the observed faint galaxy counts are likely to be consistent with a flat universe, where star formation occurs primarily in merger-induced bursts in a universe with a white-noise-like post-recombination density perturbation spectrum.

References

Arimoto, N. & Yoshii, Y., 1986. *Astr.Ap.*, **164**, 260

Arimoto, N. & Yoshii, Y., 1987. *Astr.Ap.*, **173**, 23

Bahcall, J.N. & Soneira, R.M, 1980. *ApJSupp*, **44**, 73

Barnes, J., 1990. In *Dynamics and Interactions of Galaxies.* Heidelberg, Germany: Springer-Verlag

Barnes, J. & Hut, P., 1986. *Nature*, **324**, 446

Binggeli, B., Sandage, A. & Tammann, G.A., 1988. *Ann.Rev.Astron.Astrophys.*, **26**, 509

Blumenthal, G., 1988. In *The Santa Fe TASI-87.* Singapore: World Scientific Publishing

Bothun, G., Impey, C. & Malin, D., 1991. *Ap.J.*, **376**, 404

Bothun, G., Impey, C., Malin, D. & Mould J., 1987. *A.J.*, **94**, 23

Broadhurst, T.J., Ellis, R.S. & Shanks, T., 1988. *MNRAS*, **242**, 570

Broadhurst, T.J., Ellis, R.S. & Glazebrook, K., 1992. *Nature*, **355**, 55

Bruzual, G., 1983. *Ap.J.*, **273**, 105

Bruzual, G., 1981. *Ph.D. thesis, University of California, Berkeley*

Caldwell, N., 1987. *A.J.*, **94**, 1116

Caldwell, N. & Bothun, G., 1987. *A.J.*, **94**, 1126

Canizares, C.R., 1987. In *IAU Symposium 117, 1985, p165.* Dordrecht, Holland: D.Reidel

Colless, M.M., Ellis, R.S., Broadhurst, T.J., Taylor, K. & Peterson, B.A., 1992. *Faint Blue Galaxies: High or Low Redshift?* MNRAS, **261**, 19

Colless, M.M., Ellis, R.S., Taylor, K. & Hook, R.N., 1990. *MNRAS,* **244,** 408

Couch, W. ., Jurcevic, J.S. & Boyle B.J., 199 . *Evolution of Galaxy Clustering: New data on the Angular Correlation Function of Faint Galaxies* MNRAS 260, 241

Cowie, L.L., Gardner, J.P., Lilly, S.J. & McLean, I.S., 1990. *ApJ,* **360,** L1

Cowie, L.L., Lilly, S.J., Gardner, J. & Mclean, I.S., 1988. *ApJ,* **332,** L29

Cowie, L.L., Songaila, A. & Hu, E.M.,1991. *Nature,* **354,** 460

Davies, J.I., Phillipps, S., Cawson, M.G.M., Disney, M.J. & Kibblewhite, E.J., 1988. *MNRAS,* **232,** 239

Davis, M., Efstathiou, G., Frenk, C.S. & White, S.D.M., 1985. *Ap.J.,* **292,** 371

Disney, M.J., Phillipps, S. & Davies, J.I., 1990. *MNRAS,* **244,** 385

Ellis, R.S., 1990. In *The Evolution of the Universe of Galaxies, p248.* Utah, U.S.A.: Ast.Soc.Pacific

Efstathiou, G., Bernstein, G., Katz, N., Tyson, J.A. & Guhathakurta, P., 1991. *Ap.J.,* **380,** L47

Efstathiou, G., Ellis, R.S. and Peterson, B.A.,1988. *MNRAS,* **232,** 431

Efstathiou, G., Frenk, C.S., White, S.D.M. & Davis, M., 1988. *MNRAS,* **235,** 715

Freeman, K.C., 1970. *Ap.J.,* **160,** 811

Freeman, K.C., 1987. In *IAU Symposium 117, 1985, p119.* Dordrecht, Holland: D.Reidel

Graham, J.A., 1982. *P.A.S.P.,* **94,** 244

Groth, E.J. & Peebles, P.J.E., 1977. *Ap.J.,* **217,** 385

Guhathakurta, R., Tyson, J.A. & Majewski, S., 1990. *ApJ,* **357,** L9

Guiderdoni, B. & Rocca-Volmerange, B., 1990. *Astr.Ap.,* **227,** 362

Guiderdoni, B. & Rocca-Volmerange, B., 1987. *Astr.Ap.,* **186,** 1

Hernquist, L., 1989. *Nature,* **340,** 687

Impey, C. & Bothun, G., 1989. *Ap.J.,* **341,** 89

Impey, C., Bothun, G. & Malin D., 1988. *Ap.J.*, **330**, 634

Irwin, M.J., 1985. *MNRAS*, **214**, 575

Jones, L.R., Fong, R., Shanks, T., Ellis, R.S., Peterson, B.A., 1991. MNRAS 249, 481

Koo, D.C., 1990. In *The Evolution of the Universe of Galaxies, p268.* Utah, U.S.A.: Ast.Soc.Pacific

Koo, D.C. & Szalay, A.S., 1984. *Ap.J.*, **282**, 390

Lacey, C.G., Guiderdoni, B., Rocca-Volmerange, B. & Silk, J., 1993. *Tidally Triggered Galaxy Formation,* *Ap.J.*, 402, 15

Lacey, C.G. & Silk, J., 1991. *ApJ*, **381**, 14

Larson, R.B. & Tinsley, B., 1978. *Ap.J.*, **219**, 46

Lauberts & Valentijn, 1990. *Surface Photometry Catalogue of the ESO-Uppsala Galaxies (SPC)*

Lauberts, 1982. *ESO-Uppsala Catalogue of Galaxies (EUC)*

Lilly, S.J., Cowie, L.L. & Gardner, J.P., 1991. *Ap.J.*, **369**, 79

Melott, A.L., 1992. *ApJ*, **393**, L45

Menzies, J.W., Marang, J., Laing, J.D., Coulson, I.M. & Engelbrecht, C.A., 1989. *MNRAS*, **248**, 642

Misner, C.W., Thorne, K.S. & Wheeler, J.A., 1970. In *Gravitation.* San Francisco, U.S.A.: W.H.Freeman

Mitton, S., 1976. In *Exploring the Galaxies, Ch. Scribner's Sons.* London: Faber & Faber

Neuschaefer, L.W., Windhorst, R.A. & Dressler, A., 1991. *Ap.J.*, **382**, 32

Norlén, G., 1973. *Physica Scripta*, **8**, 249

Norman, C.A., 1991. In *Massive Stars in Starbursts.* Britain: Cambridge Univ. Press

Peebles, P.J.E., 1980. In *The Large-Scale Structure of the Universe.* Princeton, N.J., U.S.A.: Princeton University Press

Peterson, B.A., Ellis, R.S., Efstathiou, G., Shanks, T., Bean, A.J., Fong, R. and Zou, Zhen-Long, 1986. *MNRAS*, **221**, 233

Peterson, B.A. & Yoshii, Y., 1992. *Faint Galaxies: The Limiting Isophote and the Redshift Distribution, (preprint)*

Phillips, S., Fong., R., Ellis, R.S., Fall, S.M. & MacGillivray, H.T., 1978. *MNRAS,* **182,** 673

Pickering, E.C. & Kapteyn, J.C., 1918. *Harv.Ann.,* **101,**

Quinn, P.J., 1992. *personal communication*

Quinn, P.J. & Goodman, J., 1986. *Ap.J.,* **309,** 472

Quinn, P.J., Salmon, J.K. & Zurek, W.H., 1986. *Nature,* **322,** 329

Rieke, G.H., 1991. In *Massive Stars in Starbursts.* Britain: Cambridge Univ. Press

Rieke, G.H., Lebofsky, M.J., Thompson, R.I., Low, F.J. and Tokunaga, A.T., 1980. *Ap.J.,* **238,** 24

Rocca-Volmerange, B., 1989. *MNRAS,* **236,** 47

Rocca-Volmerange, B. & Guiderdoni, B., 1990. *MNRAS,* **247,** 166

Roche, N., Shanks, T., Metcalfe, N. & Fong, R., 1993. *The Angular Correlation Function of $B \sim 25^m$ Galaxies*

Sarazin, C.L., 1987. In *IAU Symposium 117, 1985, p183.* Dordrecht, Holland: D.Reidel

Schechter, P., 1976. *Ap.J.,* **203,** 297

Schmidt, M., 1968. *ApJ,* **151,** 393

Scoville, N. & Soifer, B.T., 1991. In *Massive Stars in Starbursts.* Britain: Cambridge Univ. Press

Silk, J. & Lacey, C.G., 1990. *Birth of Galaxies*

Stathakis, R.A., Hunstead, R.W., Johnston, H. & Robinson, R.D., 1982. *Guides to Wavelength identification for Comparison Lamps Used with the AAT Spectrograph*

Suginohara, T. & Suto, Y., 1991. *Ap.J.,* **371,** 470

Suto, Y. & Suginohara, T., 1991. *Ap.J.,* **370,** L15

Thuan, T.X. & Seitzer, P.O., 1979. *Ap.J.*, **231**, 680

Tremaine, S., 1980. In *NATO Conference: The Structure and Evolution of Normal Galaxies.* Cambridge, U.K.

Tyson, J.A., 1988. *A.J.*, **96**, 1

Tyson, J.A. & Seitzer, P., 1988. *Ap.J.*, **552**, 583

Warren, M., Quinn, P.J., Salmon, J. & Zurek, W.H. 1992. *Ap.J.*, **399**, 405

Warren, S.J., Iovino, A., Hewett, P.C. & Shaver, P.A.,1993. *The Evolution of the Elliptical-Galaxy Correlation Function*

Weinberg, S., 1972. In *Gravitation and Cosmology.* New York: Wiley

Yoshii, Y. & Peterson, B.A., 1991. *Ap.J.*, **372**, 8

Yoshii, Y., Peterson, B.A. & Takahara, F., 1993. *On the Angular Function of Faint Galaxies, to appear in Ap.J.Lett.*, **414**

Yoshii, Y. & Takahara, F., 1988. *Ap.J.*, **326**, 1